

SOLID STATE CHEMISTRY OF SELECTED
FULLERENES

By
Craig Brown

SUBMITTED IN FULFILLMENT OF THE
REQUIREMENTS FOR THE DEGREE OF
DOCTOR OF PHILOSOPHY
AT THE
UNIVERSITY OF SUSSEX
FALMER
BRIGHTON
BN1 9QJ
NOVEMBER 1998

Table of Contents

Table of Contents	iii
List of Tables	iv
List of Figures	vii
Acknowledgements	xxii
1 Introduction	1
1.1 Molecular and Solid C ₆₀	1
1.2 Fullerenes	8
1.3 Purposes of the Thesis	16
2 Experimental and Practical Aspects	18
2.1 Introduction	18
2.2 Basics	19
2.2.1 Crystal Packing	19
2.2.2 The Lattice and Unit Cell	21
2.2.3 Crystal Planes, Reciprocal Lattice and Diffraction	24
2.3 Production and Characteristics of Radiation	34
2.3.1 Neutrons	35
2.3.2 X-ray tubes	37
2.3.3 Synchrotron	38
2.3.4 Muons	39
2.4 Instrumentation and Experiments	41
2.4.1 Powder Diffraction	41
2.4.2 Inelastic Neutron Scattering	48
2.4.3 μ^+ SR	52

2.5	Data Treatment and Analysis	55
2.5.1	Powder Diffraction	55
2.5.2	Structure Refinement	63
2.5.3	Rietveld Refinement	64
2.5.4	Inelastic Scattering	67
2.5.5	μ^+ SR	75
3	Azafullerene	84
3.1	Introduction	84
3.2	High Pressure Experiments	86
3.3	Pure Azafullerene	95
4	Crystallography of Barium Fullerides	110
4.1	Introduction	110
4.2	Ba ₄ C ₆₀ : X-ray Diffraction	114
4.2.1	<i>Immm</i> Space Group	118
4.2.2	<i>Pnnm</i> Space Group	125
4.2.3	Low Temperature	128
4.3	Ba ₄ C ₆₀ : Neutrons	139
4.4	Effects of Pressure	141
4.4.1	Ba ₆ C ₆₀	142
4.4.2	Ba ₄ C ₆₀	151
4.5	Conclusion	161
5	Ammoniated Fullerides	164
5.1	Introduction	164
5.2	Neutron Diffraction	167
5.3	μ^+ SR studies of (NH ₃)K ₃ C ₆₀	171
5.4	Inelastic Neutron Scattering of (NH ₃)K ₃ C ₆₀ and (ND ₃)K ₃ C ₆₀	178
5.4.1	Experimental and Data Reduction	179
5.4.2	Rotational Tunnelling	183
5.4.3	Molecular and Lattice Vibrations	187
5.5	Conclusions	198
6	Alkali Metal Fullerides	200
6.1	Introduction	200
6.2	Sodium Fullerides	202
6.2.1	Polymeric Na ₂ RbC ₆₀	207
6.2.2	Na ₂ Rb _{0.5} Cs _{0.5} C ₆₀	227

6.3	Lithium Fullerides	237
6.3.1	Inelastic Neutron Scattering of $\text{Li}_2\text{CsC}_{60}$	238
6.3.2	Inelastic Neutron Scattering of $\text{Li}_{2-x}\text{CsC}_{60}$	248
6.4	CsC_{60}	258
6.4.1	Inelastic Neutron Scattering of CsC_{60}	262
6.5	Conclusion	278
7	Conclusion	282
7.1	Background	282
7.2	Overview and Future Directions	284
	Bibliography	293

List of Tables

2.1	Selected properties of the muon	40
3.1	Le Bail refinement parameters for $(C_{59}N)_2$ at 0.8 and 18.5 GPa	90
3.2	Structural data for solid $(C_{59}N)_2$ at different temperatures (space group $C2/m$)	100
3.3	Refinement data for $(C_{59}N)_2$ at 278 K. Atomic coordinates are for the optimised dimer structure.	107
4.1	Histogram details for the BM16 data of Ba_4C_{60} collected at 295 K.	118
4.2	Structural Information for the Rietveld refinement of Ba_4C_{60} in space group $Immm$. The data were collected at 295 K on the BM16 diffractometer.	120
4.3	A description of closest contacts of barium in Ba_4C_{60} for the two distinct sites at 295 K. All distances are in Å. The numbers in brackets refer to the standard deviation of the measurement, giving a quantification of the distribution of bond lengths.	124
4.4	Structural Information for the Rietveld refinement of Ba_4C_{60} (295 K) in space group $Pnnm$	125
4.5	Histogram details for the SNBL data of Ba_4C_{60} collected at 10 and 5 K.	129
4.6	Structural Information for the Rietveld refinement of Ba_4C_{60} (space group $Immm$) at 10 K.	134
4.7	Structural Information for the Rietveld refinement of Ba_4C_{60} (space group $Immm$) at 5 K.	136

4.8	A description of closest contacts of barium in Ba_4C_{60} for the two distinct sites at 10 and 5 K. All distances are in Å. The numbers in brackets refer to the standard deviation of the measurement, giving a quantification of the distribution of bond lengths.	137
4.9	Histogram and phase contributions for Ba_4C_{60} neutron data collected at 2.5 K on D2B.	141
4.10	Summary of the refined parameters for the Rietveld analysis of the diffraction profiles of Ba_6C_{60} at 0.01, 1.45 and 6.19 GPa.	146
4.11	Summary of refined parameters for the diffraction profiles of Ba_4C_{60} at 0.04, 1.49 and 2.64 GPa. For the peak shape values, the numbers in square brackets show the values for Ba_3C_{60}	153
4.12	A description of closest contacts of barium in Ba_4C_{60} for the two distinct sites at 0.04 and 2.64 GPa. All distances are in Å. The numbers in brackets refer to the standard deviation of the measurement, giving a quantification of the distribution of bond lengths.	159
5.1	INX Correction Parameters for $(\text{NH}_3)\text{K}_3\text{C}_{60}$ on IN5	180
5.2	INX Correction Parameters for $(\text{NH}_3)\text{K}_3\text{C}_{60}$ on IN6	181
5.3	INX Correction Parameters for $(\text{ND}_3)\text{K}_3\text{C}_{60}$ on IN6	182
5.4	Multiphonon Correction Parameters used with the FITDEN5 program for $(\text{NH}_3)\text{K}_3\text{C}_{60}$	188
5.5	Multiphonon Correction Parameters used with the FITDEN5 program for $(\text{ND}_3)\text{K}_3\text{C}_{60}$	189
6.1	The INX correction parameters used for the IN6 data of $\text{Na}_2\text{RbC}_{60}$	208
6.2	Multiphonon Correction Parameters used with the FITDEN5 program for $\text{Na}_2\text{RbC}_{60}$	209
6.3	Structural parameters for two-phase Rietveld refinement of the powder diffraction profiles of $\text{Na}_2\text{RbC}_{60}$ (D1B, 2.3 K), as described in the text.	213

6.4	Profile parameters for single phase refinement of $\text{Na}_2\text{RbC}_{60}$ (D1B 285 K).	219
6.5	The Le Bail refinement parameters for the image plate data collected on $\text{Na}_2\text{Rb}_{0.5}\text{Cs}_{0.5}\text{C}_{60}$ at 295 K.	229
6.6	INX Correction Parameters for $\text{Li}_2\text{CsC}_{60}$ data collected at 4.12 Å on IN6.	239
6.7	Multiphonon Correction Parameters used with FITDEN5 for $\text{Li}_2\text{CsC}_{60}$.	239
6.8	Parameters extracted from fitting of the scattering law for $\text{Li}_2\text{CsC}_{60}$. The Lorentzians represent librational features, in both up- and down-scattering of neutrons. A Gaussian quasielastic component is necessary at 350 K.	243
6.9	INX Correction Parameters for $\text{Li}_{2-x}\text{CsC}_{60}$.	248
6.10	Multiphonon Correction Parameters used with the FITDEN5 program for $\text{Li}_{2-x}\text{CsC}_{60}$.	249
6.11	Parameters extracted from fitting of the scattering law for $\text{Li}_{2-x}\text{CsC}_{60}$. The peaks refer to the neutron energy gain side of the spectra.	251
6.12	The INX correction parameters used for the analysis of INS data collected on CsC_{60} under different cooling protocols.	265
6.13	Results of the fits to the measured scattering law, $S(Q, \omega)$, across the polymer→fcc transition.	268
6.14	Results of the fits to the measured scattering law, $S(Q, \omega)$, for CsC_{60} quenched to 77 K.	270
6.15	Results of the fits to the measured scattering law, $S(Q, \omega)$, for CsC_{60} quenched to 200 K.	274

List of Figures

1.1	Molecular C_{60} and the corresponding orbital energy levels[1].	2
1.2	The primitive cubic structure of solid C_{60} below 260 K (space group $Pa\bar{3}$).	4
1.3	C_{60} nearest neighbour orientational contacts in the orientationally ordered phase: $\phi \sim 98^\circ$ (left), $\phi \sim 38^\circ$ (right)[14]	6
1.4	Evolution of the cubic lattice constant for C_{60} as a function of temperature[17]. A first order phase transition occurs at 260 K that is accompanied by a discontinuous jump in the lattice parameter. A cusp is discernible at 90 K, as highlighted in the inset.	7
1.5	Molar heat capacity of C_{60} as a function of temperature. The inset highlights the region around the glass transition[21].	8
1.6	Variation of superconducting transition temperature with cubic lattice parameter for the alkali-metal fullerenes[28]. Coloured markers refer to the face centred cubic structures, while black ones refer to those fullerenes possessing a primitive cubic form. The dotted line is the T_c - a relationship expected from the BCS theory using $N(\epsilon_f)$ values obtained by LDA calculations, while the straight lines are guides to the eye.	10
1.7	Polymer chain of C_{60} showing the two single bonds connecting neigh- bouring fullerene units in AC_{60}	15
2.1	Van der Waals energy as a function of interatomic distance (\AA). . . .	20

2.2	a) Hexagonal close-packing. b) Cubic-close packing.	21
2.3	The 14 Bravais lattices. The general coordinate system is defined for the trigonal case.	23
2.4	Bragg's law, reflection by lattice planes.	25
2.5	The Ewald construction in reciprocal space, as the condition for diffraction from plane P.	27
2.6	Cones of diffracted rays for rotation about a direct axis. The green spots are successive reciprocal lattice points coming into contact with the Ewald sphere.	28
2.7	Electron density $\rho(\mathbf{r})$ scattering radiation.	29
2.8	Illustration of pion decay into a μ^+ and ν_μ viewed in the rest frame of the pion. The green and red block arrows represent the spin polarisation of the muon and neutrino respectively, while the black arrows show momenta.	40
2.9	The two-circle diffractometer on BM16 equipped with a horizontal cryostat. The beam enters from the right.	44
2.10	Schematic view of IN6.	50
2.11	Schematic view of IN5.	51
2.12	Horizontal cross-section of the GPS instrument at PSI[100].	54
2.13	Detector arrangements for experiments in; (left) transverse applied field and (right) zero- and longitudinal applied field[129].	76
2.14	Muon spin rotation in an applied transverse field for a none depolarising sample (top) and with a gaussian depolarisation function (bottom)[130].	80
2.15	Muon spin depolarisation in zero field. The rate of fluctuation of internal fields, ν starts from the static case ($\nu=0$).	82
2.16	Muon spin depolarisation as derived for static random fields. The Kubo-Toyabe function is plotted for the zero field case and a series of longitudinal applied fields.	83

3.1	Pressure variation of the X-ray diffraction patterns of solid $(\text{C}_{59}\text{N})_2$ at ambient temperature from 0.8 to 21.8 GPa ($\lambda = 0.5739 \text{ \AA}$). The observed reflections consistent with the hexagonal space group $P6_3/mmc$ are labelled (red) for the 0.8 GPa profile with the ticks below marking their positions. The bottom panel shows the calculated X-ray scattering form factor for a spherical molecule of radius $R = 3.55 \text{ \AA}$. The blue broken vertical lines mark the positions of the zero in the form factor for radii between 3.50 and 3.55 \AA	88
3.2	Le Bail pattern decomposition of one dimensional powder patterns of $(\text{C}_{59}\text{N})_2$ at 0.8 and 18.5 GPa. Black dots represent observed data points, with the red line showing the best fit. A difference curve (observed - calculated) and green tick marks, giving reflection positions within space group $P6_3/mmc$, are shown below.	89
3.3	Pressure variation of (top, red) the hexagonal lattice constants a and c and (bottom, blue) the (c/a) ratio. The broken line marks the ideal (c/a) ratio for a hexagonal-close-packed structure.	93
3.4	Pressure dependence of the hexagonal unit cell volume normalised to ambient pressure. The solid line is a fit to the semi-empirical second order Murnaghan equation of states.	94
3.5	Measured synchrotron X-ray powder diffraction pattern (black points) of $(\text{C}_{59}\text{N})_2$ in the range $2\text{-}20^\circ$ at 278 K ($\lambda = 0.8717 \text{ \AA}$). Le Bail pattern decomposition in space group $Bmmm$ gives the solid red line with the difference curve beneath. Vertical green marks indicate the positions of Bragg reflections for the orthorhombic cell, with the main peaks being labelled.	97
3.6	Relationship between the orthorhombic and monoclinic cells described in the text. The tiny green arrows indicate displacement directions of the C_{59}N units. White spheres are displaced by half a unit from the zero plane of the unit cell.	99

3.7	Minimisation of the goodness-of-fit factor R_{wp} for a Rietveld model of spherical $C_{59}N$ units. The top panel refers to the initial movement of the spheres along the monoclinic c axis with a minimum at 0.242. Further minimisation was performed by subsequently allowing movement along the a axis (lower panel).	101
3.8	Extracted reflection intensities normalised to the superlattice peak for rotations about the dimeric principal axis of $(C_{59}N)_2$. The best match of the ratio of intensities to those of the Le Bail extracted peaks is found at an angle of 90° (dotted line) from the starting position. This essentially places the 6:6 N-C(bridging) bond in the ac plane.	103
3.9	Unit cell basal plane projection of the structure of $(C_{59}N)_2$ down the b monoclinic axis. Nitrogen atoms are blue while the red dimer units are located at half a lattice translation into the unit cell. Only one of the two orientations, related by a 180° rotation about the c axis is shown.	105
3.10	X-ray powder diffraction pattern (black points) of $(C_{59}N)_2$. The profile calculated using a monoclinic cell with symmetry $C2/m$ and employing two merohedral images of the $(C_{59}N)_2$ dimers rotated by 1.5° about the c axis of the unit cell is also shown and displaced downwards for clarity (red line). Vertical green marks indicate the positions of Bragg reflections for the $C2/m$ monoclinic cell.	106
4.1	Perspective view of the body-centred cubic unit cell of Ba_6C_{60} . Fulleride cages are represented with orange cylinders, while the barium ions are blue. The unit cell is given by a dashed blue line.	111
4.2	Perspective view of the unit cell of Ba_3C_{60} . Barium ions are blue. The orange fulleride cages form a primitive cubic structure with the body centred anion rotated 90° about its z axis with relation to that at the origin.	113

4.3	Variation of χ^2 and R_{wp} as a function of rotation angle of the fulleride cage, where the origin is defined as having a 6:6 bond aligned with the a axis. Rotations about x are shown by green triangles, y by red circles and z by black diamonds. Blue double triangles show the result for rotations about the z axis in space group $Pnnm$	117
4.4	Rietveld refinement of the diffraction profile of Ba_4C_{60} at 295 K between 3° and 60° in 2θ . The observed points are shown as blue crosses and the calculated fit as a solid red line. The intensity has been multiplied by a factor of 2 above 17° in order to facilitate observation of weaker reflections. The difference curve is shown as the green line in the base of the figure with ticks marking the positions of the Bragg reflections from Ba_4C_{60} (majority phase: 86.1%, lower most), Ba_6C_{60} (minority phase: 11.8%) and Ba_3C_{60} (minority phase: 2.1% upper most). Peaks due to barium oxide are excluded, except for the region at 9.5° which is abnormally sharp in this pattern and is treated as an unknown impurity.	121
4.5	Perspective view of the refined orthorhombic body-centred unit cell of Ba_4C_{60} . The orientation is such that the ab plane is in the plane of the page with the b axis vertical. Fulleride cages are represented by pink carbon spheres and red covalent bonds, while the two sets of crystallographically distinct barium ions are dark (Ba(1)) and light (Ba(2)) blue.	122
4.6	A view of the coordination environment of Ba(1) (dark blue sphere) and Ba(2) (light blue sphere) to two hexagon and two pentagon nearest neighbours. Solid green lines highlight Ba-C contacts of less than 3.3 Å.	123

4.7	Ba ₄ C ₆₀ Rietveld refinement in space group <i>Pnnm</i> . Red crosses are data points and the solid blue line is a fit using the histogram parameters from the best fit <i>Immm</i> data. The top, middle and bottom panel show 2θ regions from 4° to 25° , 25° to 50° and 50° to 70° , respectively. Note the changes in scale for each panel. Black, red and green tick marks show reflections arising from Ba ₄ C ₆₀ , Ba ₆ C ₆₀ and Ba ₃ C ₆₀ , respectively. Even though this fit is statistically as good as for <i>Immm</i> , the refinement is unstable and immediately diverges.	126
4.8	Rietveld refinement of the synchrotron X-ray powder diffraction profile of Ba ₄ C ₆₀ in space group <i>Immm</i> at 10 K. Red crosses are data points and the solid blue line is a three phase fit. The top and bottom panel show 2θ regions from 5° to 25° and 25° to 50° , respectively. Note the changes in scale between panels. Black, red and blue tick marks show reflections arising from Ba ₄ C ₆₀ , Ba ₆ C ₆₀ and Ba ₃ C ₆₀ respectively. . . .	133
4.9	Rietveld refinement of the synchrotron X-ray powder diffraction profile of Ba ₄ C ₆₀ in space group <i>Immm</i> at 5 K. Red crosses are data points and the solid blue line is a three phase fit. The top and bottom panel show 2θ regions from 5° to 25° and 25° to 50° , respectively. Note the changes in scale between panels. Black, red and blue tick marks show reflections arising from Ba ₄ C ₆₀ , Ba ₆ C ₆₀ and Ba ₃ C ₆₀ , respectively. . . .	135
4.10	High resolution neutron diffraction profile of Ba ₄ C ₆₀ taken at 2.5 K on D2B.	139
4.11	(Top) Pressure dependence of the X-ray diffraction patterns of Ba ₆ C ₆₀ at selected pressures. (Bottom) Rietveld refinement of data taken at 0.01 GPa. Data are shown as black points while a three phase fit (described in the text) is shown as a solid blue line and the difference between measured and calculated profiles as a green line below. Ticks mark reflection positions of Ba ₄ C ₆₀ (upper), Ba ₆ C ₆₀ (middle) and Ba ₃ C ₆₀ (lower).	144

4.12	Left: evolution of the cubic lattice constants of Ba_6C_{60} and Ba_3C_{60} as a function of pressure, with error bars. The lines are fits to a second order Murnaghan equation of state with parameters given. Right: Normalised volume of the unit cell of Ba_6C_{60} as a function of pressure also fitted to the Murnaghan EOS.	147
4.13	Left: evolution of the orthorhombic lattice constants of Ba_4C_{60} as a function of pressure. Error bars are plotted. Lines for the a and b lattice constants are fits to a second order Murnaghan equation of state with parameters given next to each lattice. For the c lattice constant a linear equation is fitted to extract the compressibility. Right: Normalised volume of the unit cell as a function of pressure for Ba_4C_{60} , the line shows a fit to the Murnaghan EOS.	150
4.14	Section of a two dimensional image of Debye-Scherrer cones collected at 0.04 GPa for Ba_4C_{60}	151
4.15	Pressure dependence of selected diffraction profiles of Ba_4C_{60} . The dotted points are observed values, while the solid lines are Rietveld fits to the model given in the text. The lower panel also shows a green difference curve and tick marks for the three individual phases (top Ba_4C_{60} , middle Ba_3C_{60} and bottom Ba_6C_{60}) for the data at 0.04 GPa. Horizontal bars show excluded regions that are due to impurities of BaO.	154
4.16	Left: evolution of the orthorhombic lattice constants of Ba_4C_{60} as a function of pressure (error bars are plotted). Lines for the a and b lattice constants are fits to a second order Murnaghan equation of state with parameters given next to each lattice. For the c lattice constant a linear equation is fitted to extract the compressibility. Right: Normalised volume of the unit cell as a function of pressure for Ba_4C_{60} , the line shows a fit to the Murnaghan EOS.	156
4.17	Evolution of x fractional coordinate of the Ba(2) ion as a function of pressure in Ba_4C_{60} (error bars are plotted).	157

4.18	Left: evolution of the cubic lattice constants of Ba_6C_{60} and Ba_3C_{60} as a function of pressure (error bars are plotted). The lines are fits to a second order Murnaghan equation of state with parameters given. Right: Normalised volume of the unit cell of Ba_6C_{60} as a function of pressure also fitted to the Murnaghan EOS.	160
5.1	Proposed orthorhombic unit cell for $(\text{NH}_3)\text{K}_3\text{C}_{60}$ seen along the $\langle 110 \rangle$ direction[60]. Blue spheres represent ammonia coordination to disordered green potassium ions.	167
5.2	$(\text{ND}_3)\text{K}_3\text{C}_{60}$ Le Bail pattern decomposition of powder neutron diffraction at 100 K (top) in space group $I4/mmm$ and (bottom) in space group $Fmmm$. As a preliminary measure, we have ignored the superlattice peaks arising from cell doubling, as proposed by Ishii <i>et al.</i> [176]	169
5.3	Temperature dependence of the D20 diffraction patterns of $(\text{ND}_3)\text{K}_3\text{C}_{60}$ as a function of temperature. The arrowed superlattice reflections decrease in intensity until 150 K after which they are no longer visible .	170
5.4	Representative ZF- μ^+ SR spectra at various temperatures. The solid line through the 44 K data is a fit to a Gaussian function reflecting the presence of weak static nuclear dipole moments; below 40 K, the data are fitted with the two-component function of Eqn.5.1, representing the sum of a slowly relaxing and a rapidly relaxing Gaussian component.	173
5.5	High statistics ZF- μ^+ SR data for $(\text{NH}_3)\text{K}_3\text{C}_{60}$ at 7.2 K. The solid line is a fit to Eqn.5.2.	175
5.6	ZF and LF (100 G) μ^+ SR spectra of $(\text{NH}_3)\text{K}_3\text{C}_{60}$ at 3.9 K The application of the longitudinal field leads to a recovery of the asymmetry at long times indicating the static origins of the magnetic moments. . . .	176

5.7	(Lower) The temperature evolution of the relaxation rates, σ_1 (solid squares) and σ_2 (solid circles), of the two Gaussian components present in the TF μ SR spectra. The inset shows the temperature dependence of the asymmetries A_1 (solid squares) and A_2 (solid circles) of the two components. (Upper) Variation of muon frequency with temperature scales well with χ_s (inset) showing a transition around 40 K.	177
5.8	Neutron diffraction pattern of $(\text{ND}_3)\text{K}_3\text{C}_{60}$ at 100 K from a summation of IN6 time-of-flight data.	182
5.9	Neutron energy gain spectra of $(\text{NH}_3)\text{K}_3\text{C}_{60}$ at 1.5, 20 and 50 K. Scattering due to tunnelling is observable at 270 μeV at 1.5 K (red circles). The tunnelling transition is immediately suppressed with temperature as evidenced at 20 K (green squares) where the peak is now unresolved and lies within the elastic line. The intensities on energy gain and loss side of the elastic line are now comparable in accord with temperature and Boltzmann statistics. By 50 K the tunnelling feature is replaced by a quasielastic component that is indicative of diffusive motion (blue triangles).	184
5.10	Rotational energy level dependence for a threefold potential for NH_3 groups. As the potential barrier is increased, wavefunction overlap is reduced resulting in an almost exponential dependence of the tunnelling transition on barrier height. In the classical limit of infinite barrier, the wavefunctions are discrete and librational transitions occur.	187
5.11	(Left) Multiphonon corrected generalised phonon density of states for $(\text{NH}_3)\text{K}_3\text{C}_{60}$ above 100 K showing the full energy transfer range. (Right) Low energy region between 0 and 20 meV showing the growth of a librational peak below 150 K.	190

5.12	(Left) Multiphonon corrected generalised phonon density of states for $(\text{ND}_3)\text{K}_3\text{C}_{60}$ above 50 K showing the energy transfer range up to 70 meV. (Right) Low energy region between 0 and 20 meV, showing the detailed peak structure.	193
5.13	Temperature dependence of the normalised scattering law for $(\text{NH}_3)\text{K}_3\text{C}_{60}$. The observed points are plotted as open circles with a solid red line giving the calculated function. Each gaussian peak is convoluted with the resolution function, taken from the lowest temperature data, then summed to give the total plus a background.	197
6.1	The unit cell of the polymeric phase of $\text{Na}_2\text{RbC}_{60}$	205
6.2	Selected region powder neutron diffraction patterns obtained on D1b. The intensity scale is logarithmic to highlight the phase transitions. Reflections corresponding to those of the polymer transform abruptly at ~ 280 K to those of the primitive cubic structure (labelled on the right hand side of the figure). A further change is apparent around 300 K where the cubic reflections jump to larger d -spacings and increase in intensity, as expected for the $\text{pc} \rightarrow \text{fcc}$ transition.	210
6.3	Rietveld refinement of D1B data at 2.3 K using a two-phase polymer/pc model as described in the text. Structural parameters can be found in Table 6.3.	212
6.4	Temperature evolution of the lattice constant of cubic $\text{Na}_2\text{RbC}_{60}$ as extracted from the powder neutron diffraction data upon heating the sample to 350 K (upper panel): open black circles and grey squares refer to the pc and fcc phases, respectively. The monoclinic lattice parameters of polymeric $\text{Na}_2\text{RbC}_{60}$, normalised to the values 2.3 K, are shown in the lower panel with the key: a circles, b squares, c crossed-circles and angle β crossed-squares.	214

6.5	Temperature evolution of the lattice constant of cubic $\text{Na}_2\text{RbC}_{60}$ (upper panel) and the monoclinic lattice parameters a , b , c and angle β (lower panel) of polymeric $\text{Na}_2\text{RbC}_{60}$, as extracted from the powder neutron diffraction data upon cooling the sample to 155 K.	215
6.6	Volume fraction of the primitive cubic phase of $\text{Na}_2\text{RbC}_{60}$, as obtained from Rietveld analysis of the powder neutron diffraction profiles during the cooling (squares and full arrows) and heating (circles and dashed arrows) cycles. There are four different compositional regions as indicated: single phase fcc between 317 and 350 K, a phase coexistence region of pc and fcc phases between 296 and 317 K, single phase pc (278- 296 K), and the polymer and pc phase coexistence region. . . .	217
6.7	Rietveld refinement of D1B data at 285 K using a single <i>pc</i> phase. Structural parameters can be found in Table 6.4.	218
6.8	Near inelastic neutron scattering spectra ($Q_{av} = 1.42 \text{ \AA}$) of $\text{Na}_2\text{RbC}_{60}$ at 100, 200 and 320 K; the energy transfer shown is with respect to the sample. Data at 200 and 320 K have been scaled by the Bose factor so they are directly comparable to the 100 K spectrum. Each panel shows the normalised scattering law, $S(Q, \omega)_n$, as open circles with error bars. The data at 100 and 200 K were fitted by the convolution of a delta function at the elastic line, two broad Gaussians (one in neutron energy loss) and a weak Gaussian with the resolution function. The presence of quasielastic scattering is evident in the spectrum of the disordered fcc phase at 320 K and is modelled by a broad Lorentzian of width 2.8(1) meV.	223

6.9	Above: low energy part of the generalised phonon density-of-states for $\text{Na}_2\text{RbC}_{60}$ at 320 K (squares - fcc phase) and at 200 K (circles - co-existing polymer and primitive cubic phases). Below: difference curve of the GDOS at 200 and 320 K, highlighting the additional phonon modes in the energy range 8- 25 meV that arise from the bridging C-C bonds in the polymer.	226
6.10	The synchrotron X-ray diffraction pattern of $\text{Na}_2\text{Rb}_{0.5}\text{Cs}_{0.5}\text{C}_{60}$. The measured data points are shown as black points, while the red line is a fit using the Le Bail pattern decomposition technique with the cubic $Pa\bar{3}$ space group. The green bars indicate the positions of the reflections and the solid pink line below the pattern, the difference between measured and calculated data.	228
6.11	Temperature dependence of the <i>ac</i> magnetic susceptibility, χ of quenched $\text{Na}_2\text{Rb}_{0.5}\text{Cs}_{0.5}\text{C}_{60}$ at the indicated pressures. The inset shows an expanded view of the experimental data in the vicinity of T_c	230
6.12	Pressure dependence of the superconducting transition temperature, T_c (top panel) and of the fraction of the cubic phase, ϕ (bottom panel) for quenched $\text{Na}_2\text{Rb}_{0.5}\text{Cs}_{0.5}\text{C}_{60}$. The lines are guides to the eye. . . .	232
6.13	Temperature evolution of the <i>ac</i> susceptibility of $\text{Na}_2\text{Rb}_{0.5}\text{Cs}_{0.5}\text{C}_{60}$ at an applied pressure of 1 kbar. The two datasets shown correspond to equilibration times at room temperature before quenching of 0 and 2 hours as indicated. The inset displays the dependence of the superconducting fraction, ϕ , normalised to the value at 1 kbar with equilibration time.	233

6.14	Relationship between the superconducting transition temperature, T_c , and the cubic lattice constants, a of fulleride salts over a wide range of values for a . Data indicated by coloured symbols are experimental measurements on fulleride salts with the $Fm\bar{3}m$ structure at both ambient and elevated pressures. Data indicated by black symbols are experimental measurements on fulleride salts with the $Pa\bar{3}$ structure at ambient (circles) and elevated (squares for $\text{Na}_2\text{CsC}_{60}$ and hexagons for $\text{Na}_2\text{Rb}_{0.5}\text{Cs}_{0.5}\text{C}_{60}$) pressures. The dotted line is the T_c - a relationship expected from the BCS theory using $N(\epsilon_f)$ values obtained by LDA calculations, while the straight lines are guides to the eye.	236
6.15	Energy transfer integrated time-of-flight data of $\text{Li}_2\text{CsC}_{60}$ at 200 and 350 K. The diffraction patterns clearly show a change on heating. . .	240
6.16	Development of the near inelastic spectrum of $\text{Li}_2\text{CsC}_{60}$ with temperature at an average Q of 1.23 \AA^{-1} . Blue circles are observed points while the red line is a best fit of two Lorentzian peaks mirrored on either side of the elastic line convoluted with the resolution function. By 350 K the librational peaks have softened and we observe a weak quasielastic component. The data have been scaled by the appropriate Bose factor to allow direct comparison of the spectra.	242
6.17	Temperature evolution of the librational energy (upper) and width of the librational peak for the cubic salts: $\text{Li}_2\text{CsC}_{60}$ (red circles), K_3C_{60} (green squares), $\text{Na}_2\text{RbC}_{60}$ (blue triangles) and C_{60} (pink diamonds). Adapted from Ref[27]: note that the markers used for K_3C_{60} , $\text{Na}_2\text{RbC}_{60}$ and C_{60} are used to distinguish the curves and are not data points.	244
6.18	Temperature evolution of the generalised phonon density-of-states of $\text{Li}_2\text{CsC}_{60}$. Peaks at ~ 35 , ~ 47 and ~ 70 meV are due to intramolecular vibrations of the fulleride units.	247

6.19	The integrated data of $\text{Li}_{2-x}\text{CsC}_{60}$ at 200 and 250K. On heating, the diffraction patterns show the positions of the Bragg reflections moving to lower 2θ values, consistent with the expanding unit cell.	250
6.20	Temperature evolution of the scattering law at an average Q of 1.42 \AA^{-1} for $\text{Li}_{2-x}\text{CsC}_{60}$. A broad librational component broadens and softens with increasing temperature, collapsing into a quasielastic peak at 315 K. The sharp feature evident at 200 K disappears by 315 K. A peak at $4.12(9) \text{ meV}$ softens and increases in intensity, yet retains its width up to the highest temperature.	252
6.21	Generalised density-of-states for $\text{Li}_{2-x}\text{CsC}_{60}$ between 200 and 520 K. The spectra extend up to 120 meV with scattering above 30 meV arising from intramolecular C_{60} vibrations.	254
6.22	Low frequency part of the generalised density-of-states for $\text{Li}_{2-x}\text{CsC}_{60}$. The spectra are displaced from each other to facilitate viewing. No temperature dependence of the lowest energy C_{60} vibration is observed with limited softening in the group of peaks at 4 meV. Scattering density that lies in the gap region is seen to reduce in intensity with increasing temperature.	257
6.23	Polymeric chains formed in CsC_{60} . Spheres represent caesium ions that zig-zag in and out of the plane of the page along the chain directions.	259
6.24	Differential thermal analysis of the (upper) deeply quenched (to 77 K) and slowly cooled (lower curve) CsC_{60} [66]. Results are obtained on heating.	262
6.25	Temperature evolution of the normalised scattering law for the polymer \rightarrow fcc transition in CsC_{60} . At each temperature, the observed data are shown as open circles, while the red line is the best fit. Dashed blue lines and dotted green lines are Gaussian and Lorentzian components, respectively.	267

6.26	Temperature scaled scattering law for deeply quenched CsC_{60} . Observed data is shown by open circles with a fit as a solid red line. Contributions from Gaussian peaks are shown as dashed blue lines while Lorentzians are dotted green lines.	269
6.27	Q dependence of the scattering law for deeply quenched CsC_{60} at 200 K. The spectra are displaced relative to one another.	272
6.28	The scattering law for CsC_{60} after quenching in an acetone/ CO_2 mixture. Hydrogenous material is present as a time dependent quasielastic component.	275
6.29	Temperature evolution of the librational energy (upper) and width of the librational peak for the alkali fulleride salts: $\text{Li}_2\text{CsC}_{60}$ (red circles), K_3C_{60} (green squares), $\text{Na}_2\text{RbC}_{60}$ (blue triangles), C_{60} (pink diamonds), CsC_{60} quenched to 77 K (black circles) and CsC_{60} quenched to 200 K (open circles). Adapted from Ref[27]	277

Acknowledgements

Glad it is finished!!!!

There are people I want to thank both at Sussex, the I.L.L. and from around the world. Starting from university my gratitude goes to Kosmas for giving me this horizon expanding opportunity and the help and pushing he has given along the way. There has been additional influence and help from Jose Dianoux, Alexandros Lappas (damn good at what he does), Kostas Kordatos, Gigi Cristofolini, Kostas Vavekis, Iakavos Amigdalos (whatever he is doing now) and Serena Margadonna. Most of the experiments I have been involved in are due to people preparing samples, I would have a much shorter thesis without you; Kostas K., Alex, Hideo Shimoda, Katsumi Tanigaki, Balvinder Gogia and Mayumi Kosaka. Which brings me around to the experimental side. Thanks Andy Fitch, Phil Pattison, Kenneth Knudsen, Emma Suard (yep... you too!), la belle H  l  ne Casalta, Jose, Helmut Schober, Michael Hanfland, Martin Kunz, Daniel Hausermann, Don Kearley, Tadashi Takenobu, Hideo, Alex Amato, Paul Schleger and Andrew Wildes (who even read some of this!).

This is probably the only page of my thesis that anyone will actually read so I should keep up the exciting pace and move to the personal side of this life. Mum and Dad, wouldn't be here without the foresight and freedom I got from you. Don't know where things will go from here. To the people I've spent most time with, Ioanna, Trefor, Rob and Wimps, all in the same boat and had a good time along the way. Cheers, I enjoyed it. I have not left you out, Charlotte, along with Laurence, Wouter, Darius, Bob, Simon and Anibal. I think that I have had the misfortune of getting to know H  l  ne just before leaving, she kept me laughing while I was finishing. I want to say thanks to Ulrike, I'm sure she knows why. I know I have missed out loads of people but this is enough of a list as it is... believe me I have thought of you.

September 21, 1998

Craig Brown

Chapter 1

Introduction

Within this thesis, we are concerned with the structural, electronic and magnetic properties of compounds derived from the third allotrope of carbon: fullerene. To understand the properties of doped fullerenes, one must first understand those of the highly symmetric molecule and then consider the parent C_{60} solid.

1.1 Molecular and Solid C_{60}

The C_{60} molecule consists of sixty symmetry-equivalent carbon atoms with 12 isolated pentagons and 20 hexagons making the familiar football shape molecule (or a truncated icosahedron) with point group symmetry, I_h . Its electronic properties are determined by the 60 $p\pi$ C orbitals, which are filled by 60 electrons. Fig.1.1 illustrates the molecular structure with the corresponding energy scheme of the Hückel molecular orbitals[1].

Crystallisation results in the formation of a crystal structure that is face centred cubic (fcc) above 260 K. It is possible to describe experimental X-ray powder data using a model consisting of a uniform shell of electron density (radius= 3.55 Å) in place of the C_{60} units[2] within space group $Fm\bar{3}m$ (a = 14.1569(5) Å at 290 K).

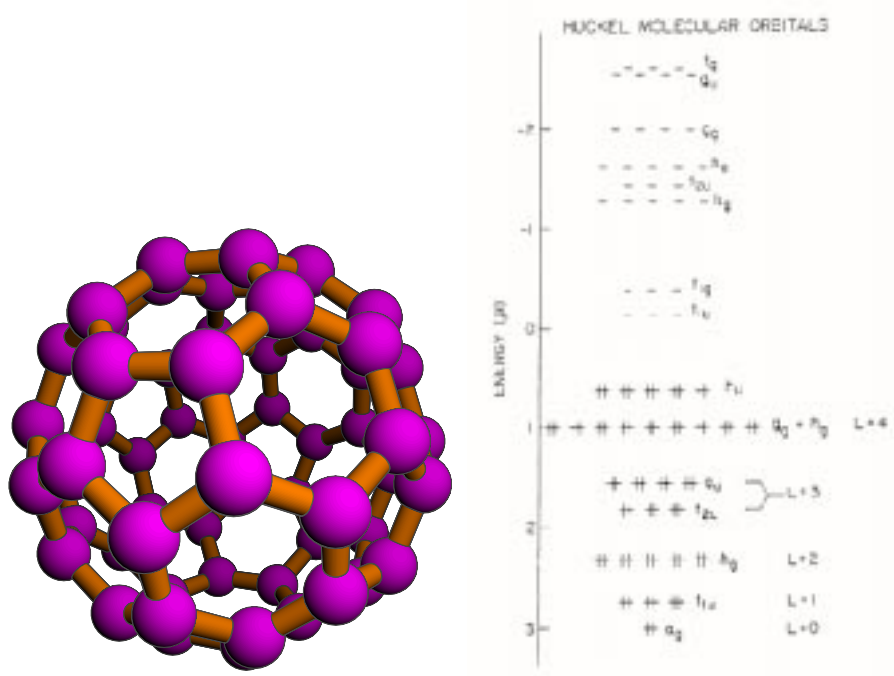


Figure 1.1: Molecular C_{60} and the corresponding orbital energy levels[1].

This corresponds to a picture where the fulleride units are disordered uniformly over all orientations. Other experimental techniques such as NMR[3, 4, 5], μ^+ SR[6] and inelastic neutron scattering[7] have confirmed that the C_{60} molecules are isotropically randomly rotating, with a rotational correlation time, τ of the order of 9-12 ps at room temperature, only three to four times slower than that in the gas phase. The translational symmetry and orientational disorder arising from rapid reorientation of the fullerene units has earned this molecule the label of a prototypical plastic crystal, with a large entropy of orientational disordering of 27.3 J/(K mol)[8].

X-ray diffraction work on C_{60} single crystals has, however, found deviations from this simple model. Instead, the electronic charge distribution of the C_{60} molecules is better modelled by symmetry adapted spherical harmonic (SASH) functions. In such

a case, the orientational scattering density is modified to

$$\rho(r) = \sum_l \sum_v C_{lv} K_{lv}(\theta, \phi) \delta(r - R) / 4\pi R^2 \quad (1.1)$$

where C_{lv} are refineable coefficients and the SASH functions, $K_{lv}(\theta, \phi)$, are derived from linear combinations of spherical harmonic functions, $Y_{lm}(\theta, \phi)$. The delta function ensures that the electron density is confined to a shell of radius, R . The rotational form factor, $F^{rot}(Q)$, becomes[9]:

$$F^{rot}(Q) = (4\pi)^{\frac{1}{2}} f_c(Q) \sum_l \sum_v i^l j_l(QR) C_{lv} K_{lv}(\theta, \phi) \quad (1.2)$$

with $f_c(Q)$ the carbon scattering factor and $j_l(QR)$ the l -th order spherical Bessel function. Only the coefficients which transform as the totally symmetric representation, A_{1g} of the point group of the the site symmetry of the shell of atoms are non-zero. v labels the particular representation within A_{1g} for a given value of l . In the fcc lattice, the shells occupy the $4a$ sites of $m\bar{3}m$ (O_h) symmetry, necessitating only the SASH functions with values for $l=0, 6, 10$ and 12 [10]. This analysis results in an excess charge density of 10% along the $\langle 100 \rangle$ and a deficiency of 16% along the $\langle 111 \rangle$ directions. This behaviour was attributed as arising from the effective potential experienced by a single C_{60} molecule, from the crystal field of its neighbouring molecules[11].



Figure 1.2: The primitive cubic structure of solid C_{60} below 260 K (space group $Pa\bar{3}$).

On cooling through 260 K, a first order structural phase transition occurs, with the reorientational motion of the C_{60} molecules in the crystal becoming slower and now best described as a librational motion. The phase transition is accompanied by a sudden contraction of 0.344(8)% in the cubic lattice constant[12]. Reflections not compatible with fcc symmetry are now present in the powder diffraction patterns[13, 14], reflecting a long range orientational ordering of the fulleride units and a primitive

cubic, $Pa\bar{3}$, space group[15](Fig.1.2). The orientation of the four molecules occupying the positions $(0,0,0)$, $(\frac{1}{2},0,\frac{1}{2})$, $(\frac{1}{2},\frac{1}{2},0)$ and $(0,\frac{1}{2},\frac{1}{2})$ in the new unit cell can be described starting from the standard fullerene orientations, in which the $[100]$ molecular axes align with three, twofold molecular symmetry axes (perpendicular to hexagon-hexagon fusions) and the $[111]$ axes pass through the centre of hexagonal faces. Each of the molecules is then rotated anticlockwise by an angle ϕ about the $[111]$, $[\bar{1}\bar{1}1]$, $[1\bar{1}\bar{1}]$ and $[\bar{1}1\bar{1}]$ axes, respectively[16].

Rietveld refinement of neutron powder diffraction data identified two types of C-C bonds related to short 'double bonds' (1.40 Å) and long 'single bonds' at 1.45 Å[14]. The double bonds fuse two hexagons together and are also known as 6:6 bonds, while the long hexagon:pentagon fusions are denoted as 6:5 bonds. The experimentally determined structure comprises of a majority fraction of molecules rotated by $\phi \sim 98^\circ$, for which optimisation of intermolecular interactions occurs with electron rich double bonds lying over electron deficient pentagonal faces of neighbouring molecules. A co-existing minority orientation is only slightly less energetically favourable (by ~ 11 meV[17]) and is characterised by the alignment of the 6:6 bonds parallel to hexagonal faces of neighbours for a rotation angle of $\phi \sim 38^\circ$ (Fig.1.3).

INS measurements have identified librational peaks at 2.5 meV at 100 K[7], while motional narrowing of lines in ^{13}C NMR spectra[3, 4, 5] was also observed. The dynamics in the primitive cubic phase were initially attributed to a jumping motion between the almost degenerate orientations, via 60° hops about the $\langle 111 \rangle$ axes[17]. This however gives rise to a uniaxial reorientation where only three of the 60 equivalent orientations are allowed. Alternatively the reorientation can be thought of as occurring via $\sim 36^\circ$ rotations about the $\langle 110 \rangle$ axes[17]. Two successive hops about the same



Figure 1.3: C_{60} nearest neighbour orientational contacts in the orientationally ordered phase: $\phi \sim 98^\circ$ (left), $\phi \sim 38^\circ$ (right)[14]

axis are unfavourable as this would place a pentagon perpendicular to the $[111]$ direction. The resultant pseudo-random sequence of uniaxial reorientations has a quasi-isotropic nature and all 60 equivalent orientations can be accessed. On the assumption that this is the dominant reorientational mechanism, then a cosine potential can be used to approximate the uniaxial rotational potential, which involves an activation barrier of ~ 250 meV separating the two C_{60} orientations[18]. Agreement with this value is found experimentally also using the NMR[4] and μ^+ SR[6, 19] techniques.

As the temperature is decreased below 90 K, the fraction of molecules in the 98° orientation reaches a plateau of 83.5%, with the molecules now having insufficient energy to overcome the potential barrier separating the two orientations. A cusp in the rate of change of lattice constant with temperature[17] is observable at

the same temperature, as shown in Fig.1.4. The dynamics of the C_{60} molecules are extremely limited performing only small amplitude librational motion[20]. Heat capacity measurements[21] have identified this as a subtle transition in comparison to the high temperature first-order transition (Fig.1.5). The onset of orientational glass behaviour is attributed to molecular orientational disorder which is frozen in, as a consequence of the long relaxation time of the molecular reorientation.

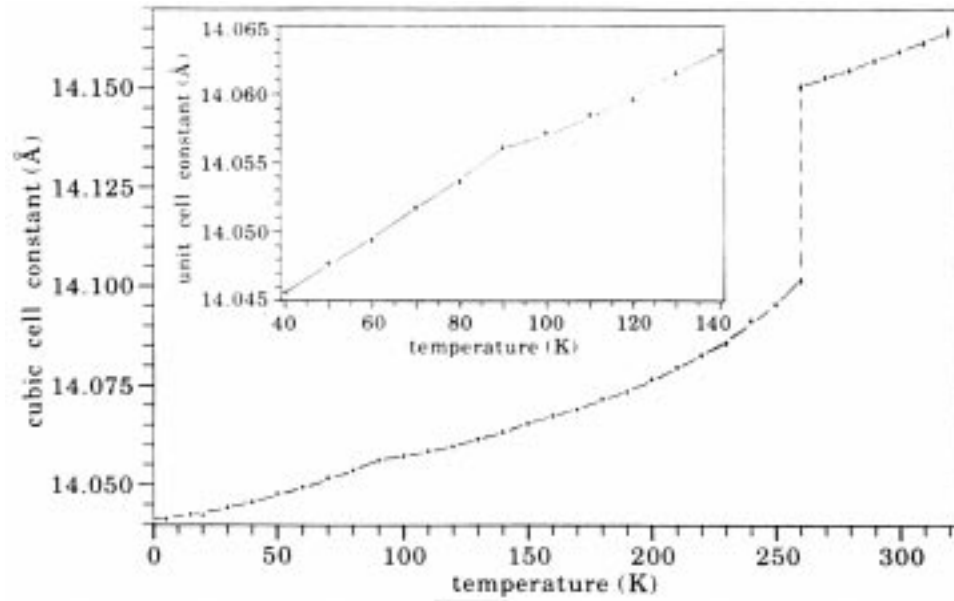


Figure 1.4: Evolution of the cubic lattice constant for C_{60} as a function of temperature[17]. A first order phase transition occurs at 260 K that is accompanied by a discontinuous jump in the lattice parameter. A cusp is discernible at 90 K, as highlighted in the inset.

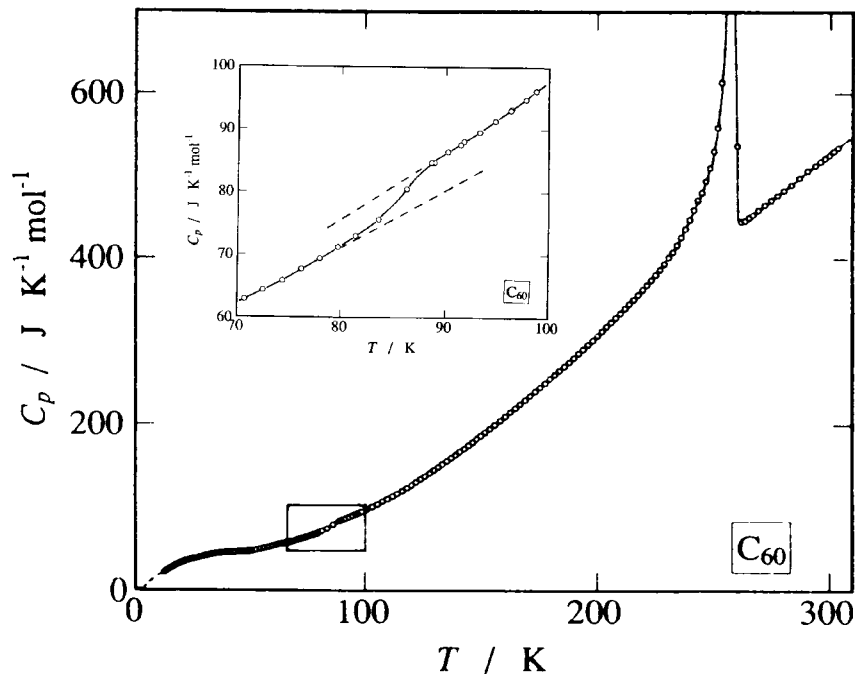


Figure 1.5: Molar heat capacity of C_{60} as a function of temperature. The inset highlights the region around the glass transition[21].

1.2 Fullerides

The high electronegativity of C_{60} and the weak intermolecular van der Waals forces between the molecules in the crystal, make it a potential host for reductive intercalation chemistry. Simple sphere packing arguments for the fcc structure of C_{60} , allow the sizes of the tetrahedral and octahedral intersitices to be estimated as 1.12 Å and 2.06 Å, respectively. This makes the octahedral site large enough to accommodate any alkali ion, while the tetrahedral site can only fit Li^+ and Na^+ without the need for expansion. The number and nature of the intercalate determines the structure and modify the properties of the resulting solid. The most extensively studied family

of intercalation compounds is that of the alkali metal fullerenes, though more recent work is expanding the area of alkaline earth and rare earth fullerenes as well.

Of interest in this thesis are the cubic fullerenes with stoichiometry $A_2A'C_{60}$ ($A, A' = \text{Li, Na, K, Rb, Cs}$). These leave the fullerene lattice intact with both the octahedral and two tetrahedral interstices per C_{60} occupied. At this doping level, half filling of the t_{1u} states occurs and metallicity is observed experimentally[22] along with superconductivity[23] as high as 33 K[24] at ambient pressure. The orientational behaviour of the fullerene molecules is now modified due to the inclusion of the alkali ions. For alkali ions larger than the size of the tetrahedral interstice (Cs^+, Rb^+ and K^+), the fulleride ions are forced to rotate and minimise the repulsive cation- C_{60}^{3-} interactions. Thus, a situation is encountered where the largest surface area of the fulleride cage is presented to the cations occupying the tetrahedral interstices: namely, the hexagonal faces of the C_{60}^{3-} ions. Experimentally[25], the space group that best describes these structures is $Fm\bar{3}m$. Since C_{60} has no fourfold molecular symmetry axis, disorder of the fulleride orientation must be present to allow raising of the symmetry in the solid. This is achieved by a merohedral disorder of two equally populated standard orientations that are related by 90° rotations about $\langle 100 \rangle$ axes. The unit cell sizes are larger than that of C_{60} : e.g. $a = 14.24 \text{ \AA}$ for K_3C_{60} ; and no phase transitions are seen as a function of temperature for these systems. The dynamics are typified by small amplitude librational motion[26] at energy transfers around twice the magnitude of those found for pristine C_{60} . The librational energy scales with the ratio of the radius of the alkali metal to the size of the tetrahedral interstice[27].

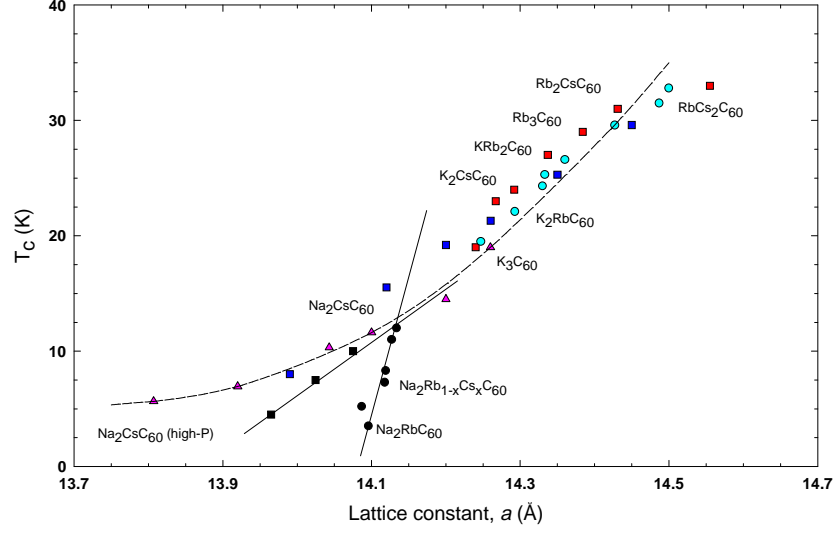


Figure 1.6: Variation of superconducting transition temperature with cubic lattice parameter for the alkali-metal fullerides[28]. Coloured markers refer to the face centred cubic structures, while black ones refer to those fullerides possessing a primitive cubic form. The dotted line is the T_c - a relationship expected from the BCS theory using $N(\epsilon_f)$ values obtained by LDA calculations, while the straight lines are guides to the eye.

An empirical correlation between the superconducting transition temperature, T_c , and the fcc lattice constant, a [24, 28, 29, 30], has been interpreted as resulting from a direct relationship between T_c and the density-of-states at the Fermi level, $N(\epsilon_F)$ [31]. Within the Bardeen-Cooper-Schreiffer (BCS) framework, $T_c \propto (\hbar\omega) \exp(-\frac{1}{N(\epsilon_F)V})$. This relationship is independent of the alkali atoms in the compound as they do not affect the magnitude of the coupling, V , of the electron-pair to the phonons of frequency ω . As such, if pressure is applied to Rb_3C_{60} to give the same lattice constant as

for K_3C_{60} at ambient pressure, the corresponding T_c s are almost equal[30](Fig.1.6). This fact and the absence of any alkali metal isotope effect place the emphasis on the fulleride network to explain the superconducting mechanism. In more recent work, this scenario is not so clear cut with a somewhat different compressibility found for Rb_3C_{60} than that reported in the earlier work and hence, a different T_c - a relationship is established[32]. Physical and chemical pressure seem to be slightly inequivalent.

It is widely accepted that fullerene superconductivity is driven by electron-phonon interaction, though a purely electronic mechanism[33] cannot be ruled out. Within the BCS framework, the larger the lattice constant, the narrower the conduction band, and hence a larger $N(\varepsilon_F)$ can give rise to a higher T_c . More explicitly an estimate of T_c can be obtained from the McMillan formula[34]

$$T_c = \frac{\omega_{ln}}{1.2} \exp\left[\frac{1.04(1 + \lambda)}{\lambda - \mu^*(1 + 0.62\lambda)}\right] \quad (1.3)$$

where ω_{ln} is the logarithmic average phonon frequency, λ is the electron-phonon coupling and μ^* is the Coulomb pseudopotential that describes repulsive interactions.

The two components for testing the BCS theory lie in the isotope effect and the influence of electron-phonon coupling on spectroscopic linewidths, i.e. phonons are involved, along with the dominance of $N(\varepsilon_F)$ on determining T_c . The former effect has been probed by neutron scattering[35] and Raman[36, 37] spectroscopy, whence the expected strong coupling of the t_{1u} electrons to H_g modes is evidenced. A carbon isotope effect[38] is observed, but this can also be explained via electronic coupling mechanism only. Scaling of T_c with $N(\varepsilon_F)$ seemed to confirm the simple relation expected from BCS theory, though this too is explainable by a purely electronic mechanism of superconductivity. It is experimentally observed that superconductivity is a sharply peaked function of anion charge, maximising at a doping level of 3 with

a steep fall off on either side[39]. Even though this observation is for a series of non-isostructural materials, it is not a facet explainable by electron-electron mediating mechanisms.

Production of ternary alkali fullerides, in which smaller ions (Na and Li) occupy the tetrahedral sites has a profound effect on the T_c evolution with lattice constant. This is now much steeper[40] than that in the larger fullerides, though $\text{Na}_2\text{CsC}_{60}$ is consistent with the fcc trend. Within the sodium systems, the structural behaviour is similar to that shown by pristine C_{60} . At high temperatures, the anions are free to rotate[27, 41]. Below about 300 K, a transition to orientationally ordered phases[42, 43] occurs. These are isostructural with that of C_{60} and adopt lattice constants with sizes smaller than 14.17 Å. INS has shown that these systems have a much softer intermolecular potential[27, 41] compared to that of K_3C_{60} and Rb_3C_{60} .

An initial explanation of the differing T_c - a dependence relied on the modified crystal structures and different orientational states of the fulleride ions. More recently, EPR[44, 45, 46] and NMR[47] measurements have found little difference between the lattice constant dependence of $N(\varepsilon_F)$ for $\text{Na}_2\text{CsC}_{60}$ and the fcc salts, K_3C_{60} and Rb_3C_{60} , to justify this, but still $N(\varepsilon_F)$ values for $\text{Na}_2\text{RbC}_{60}$ and $\text{Na}_2\text{KC}_{60}$ are strongly suppressed[48]. At the same time, magnetic susceptibility measurements at high pressure on $\text{Na}_2\text{CsC}_{60}$ [49] have led to the conclusion that the effects of physical[49] and chemical[40](see also §6.3) pressure on the superconducting properties of the $P\bar{a}\bar{3}$ phases are not identical, with chemical pressure suppressing T_c much faster than physical pressure.

High pressure X-ray diffraction studies on $\text{Na}_2\text{RbC}_{60}$ and $\text{Na}_2\text{CsC}_{60}$ revealed that

above 3 kbar a phase transition occurs to an orthorhombic phase[50] with small interball separation. Further work[51, 52, 53], at ambient pressure, has shown that a non-superconducting polymeric ground-state is in competition with the superconducting cubic phase, which may exert additional detrimental influence on superconductivity. The structure of this polymer is distinctly different from that of the doubly bonded AC_{60} salts, as a short interfullerene distance of 9.38 Å implies a single C-C bridging bond[53]. While $\text{Na}_2\text{CsC}_{60}$ is strictly cubic at all temperatures, a transformation to an isostructural polymer phase has been observed upon application of pressure[54]. Further observation that the quaternary $\text{Na}_2\text{Rb}_{1-x}\text{Cs}_x\text{C}_{60}$ ($0 < x < 1$) series undergoes this structural transformation at ambient pressure[55], begs the question ‘What critical interfulleride separation is needed for polymerisation to occur in these systems?’.

Different behaviour is evident within the $\text{Li}_2\text{AC}_{60}$ ($\text{A} = \text{Cs}, \text{Rb}$) family of fullerides which adopt a fcc structure showing an excess carbon density along the $\langle 111 \rangle$ directions and deficiency along the $\langle 100 \rangle$ directions, indicating an enhanced interaction between the carbon atoms and Li^+ [9]. No superconductivity is observed for these systems, despite apparent correct band filling. Recently, it has been shown that to assume complete charge transfer from the alkali metals is incorrect. Raman spectroscopy allows the frequency of the $A_g(2)$ fulleride vibration to be observed; this shows a monotonic shift of -6 cm^{-1} per unit charge accumulated on the fulleride unit. Studies on $\text{Li}_x\text{CsC}_{60}$ ($x=2, 3, 4$)[56] reveal reduced charge transfers from those expected on assumption of complete ionisation of the alkali metals. It is found experimentally that superconductivity at 10.5 K occurs for a composition of $\text{Li}_3\text{CsC}_{60}$, where C_{60}^{3-} units are now observed.

On the large lattice constant side of the alkali metal fullerenes lies Cs_3C_{60} , that is in fact a mixture of a body-centred cubic and a body-centred tetragonal phase. This system becomes superconducting under pressure with T_c reaching a value of 40 K at 15 kbar[57].

Ammoniation has been used to drive T_c in the fullerenes to higher values too, as it leads to an expansion of the cubic lattice and a concomitant increase in the density of states at the Fermi level. Upon ammoniation, the T_c of $\text{Na}_2\text{CsC}_{60}$ increases significantly from 10.5 to 29.6 K[58], while ammoniation only partially worked in the case of $(\text{NH}_3)_x\text{NaA}_2\text{C}_{60}$ ($0.5 < x < 1$, $A = \text{K}$ and Rb). The $\text{NaA}_2\text{C}_{60}$ systems themselves have not been isolated due to an unfavourable intercalation of both small and large radii alkali ion intercalation in the tetrahedral interstices. These ammoniated salts have cubic structures, with the ammonia preferentially coordinating to the small sodium ion so that this complex resides in the large octahedral interstice. However, T_c s in these systems were dramatically lower than the empirical relation would suggest. Even more surprising is that T_c decreases with *increasing* lattice parameter[59]. Ammoniation of K_3C_{60} led to a structural distortion, the adoption of an orthorhombic phase and no evidence of superconductivity[60]. The material however is magnetic and displays a magnetic instability at 40 K[61, 62] which should be the driving force for the accompanying metal-insulator transition. However when pressure in excess of 1 GPa is applied[63], superconductivity is recovered at a value in line with the empirical observation, implying that this salt is in the vicinity of the superconductor-nonsuperconductor boundary, while the $(\text{NH}_3)_x\text{NaA}_2\text{C}_{60}$ salts are just on the superconducting side.

Reducing the amount of alkali metal content can result in compounds of stoichiometry AC_{60} ($A = K, Rb, Cs$). While at high temperatures these salts crystallise in a face-centered cubic structure, below ~ 370 K a phase transition to an orthorhombic phase occurs in which the centres of neighbouring fulleride ions are separated by a distance of ~ 9.12 Å. The close contacts, much closer than the 10 Å found in the cubic phase, arise from polymerisation, where the fullerene units are connected by two C-C single bonds[64] as shown in Fig.1.7. The AC_{60} polymers are metallic and undergo a transition to magnetic insulating phases below 50 K[65].

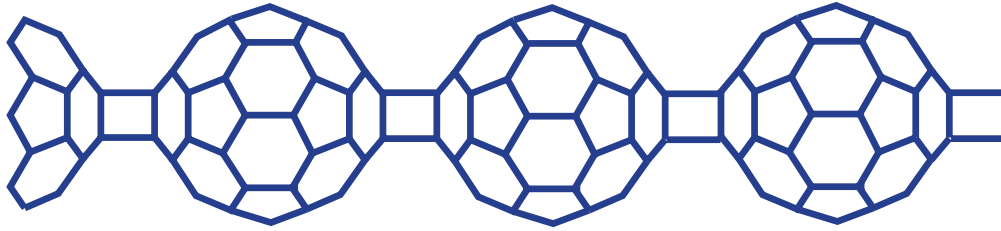


Figure 1.7: Polymer chain of C_{60} showing the two single bonds connecting neighbouring fulleride units in AC_{60} .

Rapid quenching can also lead to the isolation of two additional metastable forms[66]: a metallic cubic phase, comprising of C_{60}^- monomers[67] and a nonmetallic monoclinic phase, comprising of $(C_{60})_2^{2-}$ dimers[68, 69, 70].

Addition of a larger number of alkali metal ions than the number of available interstices in the C_{60} fcc lattice can result in less dense sphere packing structures. Compositions with alkali metal content as high as $Na_{11}C_{60}$ have been observed to retain the fcc structure via formation of sodium clusters in the octahedral interstices[71]. Intercalation of the larger alkali metals to saturation results in body centred cubic (bcc) structures (space group $Im\bar{3}$), in which there are two symmetry equivalent C_{60}^{6-} ions per

unit cell. An insulating phase with stoichiometry A_6C_{60} is achieved with the cations occupying the $(0,0.5,z; z\sim 0.25)$ positions[72, 73]. Synthesis of Na_4C_{60} extends the polymer systems into the C_{60}^{4-} systems and it also shows metallic conductivity[74]. Again, there is a difference with the larger alkali metals, as the line phases $(K,Rb)_4C_{60}$ adopt a body centred tetragonal structure (space group $I4/mmm$) where two-thirds of the distorted tetrahedral sites are occupied in an ordered manner[75] with a merohedral disorder of the fulleride orientations[76]. Increasing the cation size still further to Cs^+ suppresses the disorder and induces an orthorhombic distortion to $Immm$ symmetry[77].

1.3 Purposes of the Thesis

The aim of this thesis is to investigate the structural and dynamical properties of fullerene based materials. The experimental techniques of X-ray diffraction, neutron scattering and μ^+ SR spectroscopy, as well as the theoretical and practical aspects used for the analysis of the data collected, are discussed in detail in Chapter 2. Chapter 3 deals with the structural properties of a variant of C_{60} where a nitrogen atom replaces a carbon atom of the cage. The variety of bonding within the azafullerene solid is probed under high pressures, with an account of detailed structural work on a very limited X-ray diffraction pattern following.

Chapter 4 presents a structural determination of the superconducting alkaline earth fulleride, Ba_4C_{60} . Evolution of the unit cell and characteristic bonding distances are followed as functions of temperature and pressure. Chapter 5 deals with the use of the μ^+ SR technique to investigate the metal \rightarrow insulator transition of $(NH_3)K_3C_{60}$ fulleride at low temperature. The addition of ammonia and deuterated ammonia

to the fullerides allows us to probe the molecular potential in these systems using tunnelling spectroscopy and inelastic neutron scattering, from which we can comment on the size and symmetry of the torsional barrier at the ammonia site.

In Chapter 6, the structural and dynamical properties of the alkali metal fullerides are discussed in detail. Neutron diffraction was employed to describe the structure of $\text{Na}_2\text{RbC}_{60}$ over the whole temperature range that includes polymer, primitive cubic and face-centred cubic forms. Evidence for the polymeric structure is also given by inelastic neutron scattering with the observation of characteristic polymer vibrational modes. Susceptibility measurement on $\text{Na}_2\text{Rb}_{0.5}\text{Cs}_{0.5}\text{C}_{60}$ under pressure have given a deeper insight into the different factors affecting T_c in the primitive cubic fullerides. Finally, the dynamical behaviour of lithium containing fullerides has also been examined using inelastic neutron scattering with attempts to reconcile the data to the novel structural characteristics of this solid. Experiments were also attempted to characterise the changing dynamics within the polymer, dimer and cubic forms of CsC_{60} using INS. Finally, Chapter 6 gives a brief overview of the work presented here.

Chapter 2

Experimental and Practical Aspects

2.1 Introduction

A range of techniques has been employed to study the solid state properties of fullerenes of interest in this thesis. Extensive use has been made of elastic scattering of neutrons and X-rays to probe structural features as functions of temperature and pressures, allowing determination of parts of the structural phase diagram. The dynamics apparent within these same compounds can be probed by a range of techniques depending on the required energy resolution, momentum transfer resolution and time-scale window for the motions. Inelastic neutron scattering (INS) probes dynamical properties and also gives valuable information on the vibrational densities of states. As an example of the unique nature of INS one can compare selection rules with those of infrared and Raman spectroscopies. For C_{60} , there are 4 ir active vibrations of t_{1u} symmetry and 10 Raman active A_g and H_g modes, while all 46 modes are present in the INS spectra. In addition to the lack of selection rules, neutron scattering also is not confined to probing the Brillouin zone centre, as is a limitation

of light scattering techniques. Muons are ideal probes of magnetism and have been used successfully to characterise magnetism of a weak, disordered nature.

In this chapter, a brief overview of basic theory and a description of the above techniques is presented, together with more specific information about instrumentation and analytical techniques.

2.2 Basics

2.2.1 Crystal Packing

To see why atoms form solids, we can consider a simple model where two atoms are *placed* together and calculate their energy using only the London attraction and Born repulsion term¹ from the Lennard-Jones type expression:

$$V(r) = D[(\sigma/r)^{12} - 2(\sigma/r)^6] \quad (2.1)$$

where r is the distance between atoms and D and σ are parameterisations found experimentally from, say, neutron inelastic scattering measurements on polymeric RbC₆₀[78] giving values 1.3 meV and 4.42 Å respectively, for a carbon-rubidium interaction. This equation is graphically shown in Fig.2.1, where we see that the forces are attractive to 5 Å reaching an energy minimum at a distance of 4.5 Å and rapidly becoming repulsive below 4.4 Å. The energy minimum is associated with the equilibrium interatomic distance and is reduced in the actual solid due to attractive interactions with neighbouring atoms.

¹Both kinetic energy and Coulombic interaction terms are ignored.

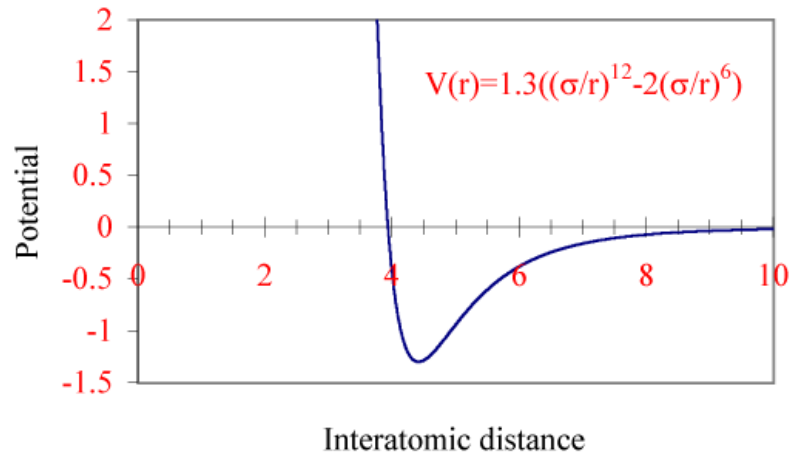


Figure 2.1: Van der Waals energy as a function of interatomic distance (\AA).

Extending this 1D picture to two dimensions, we can find the lowest energy where each atom has as many neighbours as possible. A close packed plane results where each atom is 'touching' 6 others. To extend this to 3D, we must place one close-packed plane on top of another so that the spheres of one layer fit into the triangular voids of the other layer. As each sphere has 6 vacancies around it but only 3 of them are filled with the addition of the extra layer, we have two possibilities of where to place the third layer. If it is placed in such a way that it coincides with the atoms in the first layer (i.e. an ABA structure), we have a hexagonal close-packed system (Fig.2.2a) where there are channels through the layers. However, if we place the third layer so that these channels are blocked (ABC stacking), we arrive at cubic close packing structural motif (Fig.2.2b).

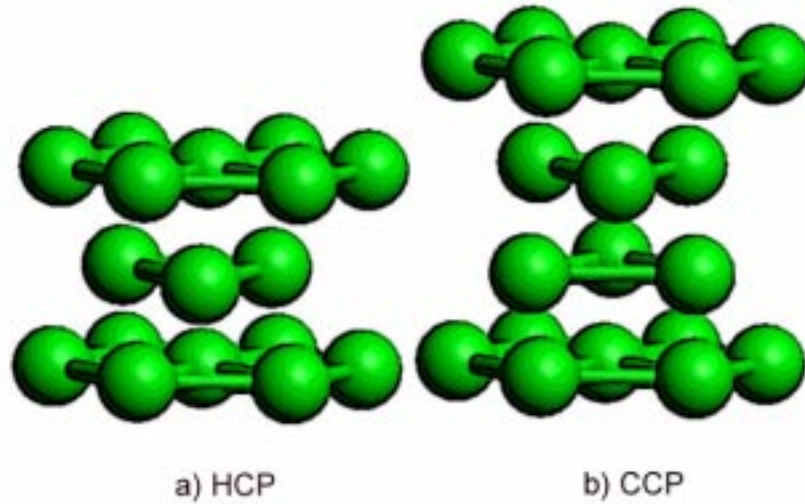


Figure 2.2: a) Hexagonal close-packing. b) Cubic-close packing.

The crystal structures of fullerenes and intercalated fullerenes can be mostly thought of in terms of packing of hard spheres, due to the predominantly ionic nature of the separate units, with the cations residing in octahedral (1 per C_{60}) and tetrahedral (2 per C_{60}) interstices[79]. There are, of course, additional factors which can lead to the final geometries adopted by these systems, but simple energetic arguments have been quite successful in rationalising these[75, 80].

2.2.2 The Lattice and Unit Cell

A crystal is defined as the infinite 3D translational repetition of a basis consisting of a unit cell and its motif (the atomic contents of the cell). This coordinate system is generally defined by three non-orthogonal basis vectors \mathbf{a} , \mathbf{b} , \mathbf{c} of different lengths (a, b, c) and angles α , β , γ with α defined as being the angle between the vectors \mathbf{b} and \mathbf{c} (Fig.2.3, defined for the trigonal case.). There are seven three-dimensional

coordinate systems that are useful in describing crystals and are the basis for their classification: cubic, hexagonal, trigonal, tetragonal, orthorhombic, monoclinic and triclinic. These systems are dependent upon the internal symmetry of the system: a combination of rotations about an axis ($1, 2, 3, 4$ and 6)² and reflections (mirror planes). A primitive unit cell is one with only one lattice point per unit cell. Bravais discovered that some cells are more complex but still conformed to the symmetry of one of the seven crystal systems. These non-primitive systems contain two or more lattice points per unit cell and can be simply viewed as a combination of a primitive lattice with one or more identical copies of itself but offset. A, B, C, I and F lattices can be constructed in this way. In total, there are 14 Bravais lattices[81] (shown in Fig.2.3), 7 of them being primitive lattices.

For any array of lattice points it is always possible to choose a primitive triclinic cell, but to do so is to lose the simplification of using the natural symmetry. The unit cell is chosen in such a way that it conforms to the symmetry actually present. Following this, there are sometimes other factors that can lead to different lattice designation. Convention comes to the aid here: for example, a monoclinic C-centred cell can be equivalently described as a monoclinic I-centred cell, though the C cell is usually chosen. A further difficulty is apparent as it is possible to define unit cells by alternative ways resulting in quite different shapes: an hexagonal cell can be described as an orthorhombic C-centred cell.

²5 fold rotations are not compatible with translational symmetry.

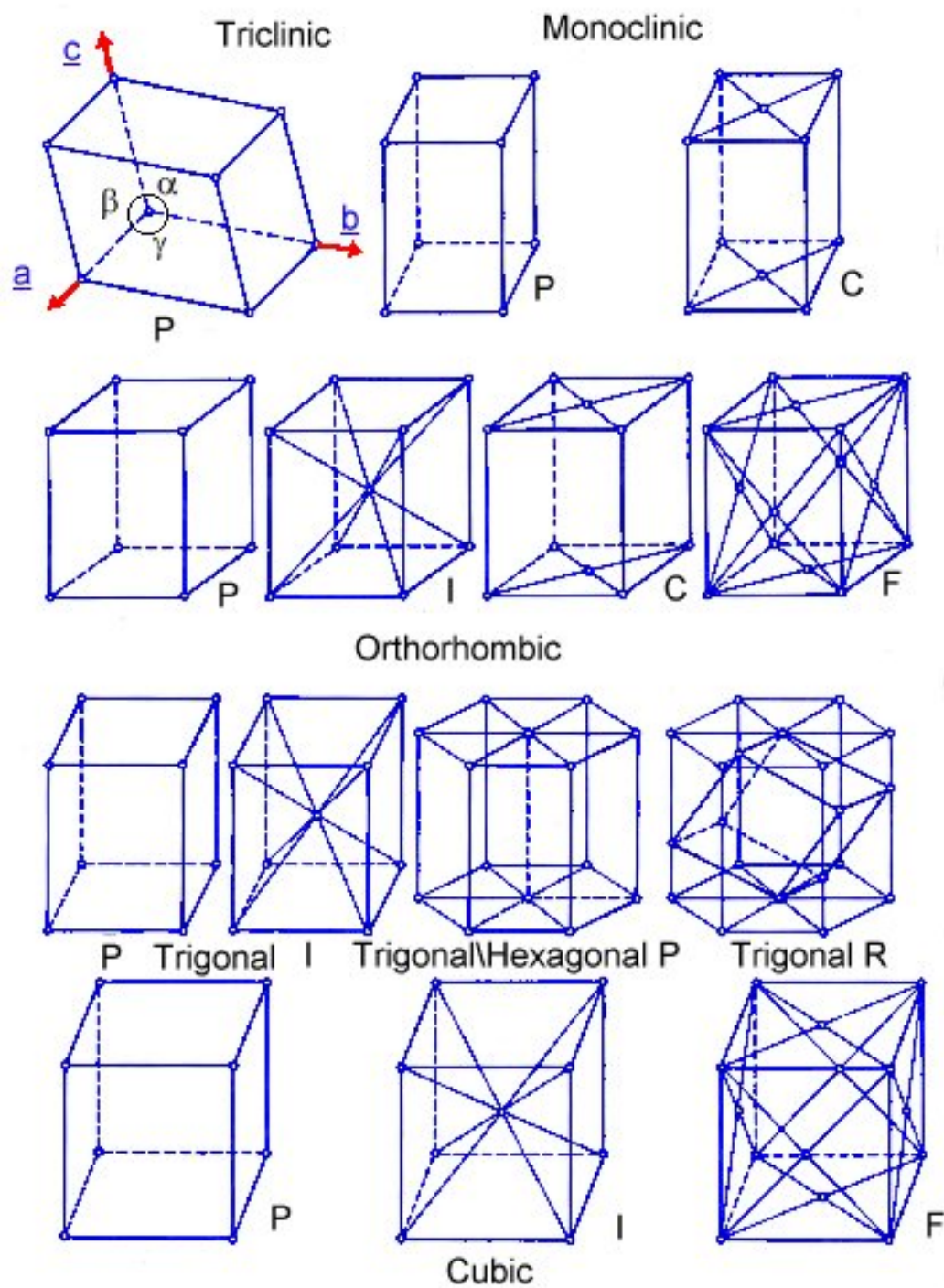


Figure 2.3: The 14 Bravais lattices. The general coordinate system is defined for the trigonal case.

It is important to understand the difference between a point group and a space group. A point group describes the symmetry of objects with finite dimensions (i.e. there are no translational operations), and applies equally to crystal morphology or molecular structures (e.g. the point group for planar benzene is $6/mmm$). There are 32 point groups distributed amongst the seven crystal systems, 11 of which are centrosymmetric (also called the *Laue class* of the system³). A space group describes the symmetry of 3D periodic structures. The total number of crystallographic space groups is 230. They can all be derived by combining the 32 point groups with the 14 Bravais lattices and further replacing symmetry axes by screw axes of the same order and mirror planes by glide planes. The *International Tables for Crystallography*[82] contain all the necessary space group information that is useful in solving crystal structures from diffraction data.

A full text on symmetry and how to use the international tables is found in ref[83].

2.2.3 Crystal Planes, Reciprocal Lattice and Diffraction

Real Space

Since many crystals are anisotropic it is necessary to distinguish the different directions present. A general point is characterised by the coordinates u, v, w or equivalently by the vector $\mathbf{r} = u\mathbf{a} + v\mathbf{b} + w\mathbf{c}$. Three non-collinear lattice points define a lattice plane, the equation of which $hu + kv + lw = n$ cuts the unit cell into h, k and l parts (or intercepts the axes at distances of $a/h, b/k, c/l$). The Miller indices, (hkl) ,

³Physical experiments do not normally reveal the true symmetry of the crystal but show the symmetry one would obtain by adding an inversion centre to the symmetry elements already present.

represent a family of planes extending from the origin throughout the crystal.

Bragg's Law

Diffraction is a wave property of electromagnetic radiation that causes the radiation to bend as it passes by an edge or through an aperture. Diffraction effects increase as the physical dimension of the aperture approaches the wavelength of the radiation. The resulting interference effects are useful for determining dimensions in solid materials, and therefore crystal structures. Since the distances between atoms or ions is on the order of 1 \AA , diffraction methods require radiation in the X-ray region of the electromagnetic spectrum, or beams of electrons or neutrons with a similar wavelength. Electrons and neutrons are commonly thought of as particles, but they have wave properties with the wavelength depending on the energy of the particles as described by the de Broglie equation. In addition, the radiations interact differently with matter; for instance, X-rays interact only with electrons, while neutrons are influenced by atomic nuclei and unpaired electrons.

Equivalently, we can think of diffraction as arising from the *reflection* of radiation from successive planes of spacing d , as shown in Fig.2.4.

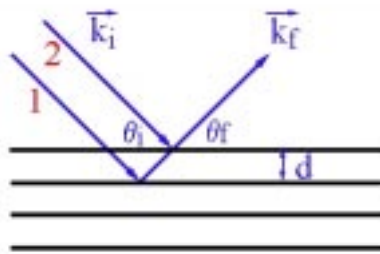


Figure 2.4: Bragg's law, reflection by lattice planes.

For constructive interference to be observed, the path difference between the reflected rays 1 and 2 must equal an integer number of wavelengths which leads to Bragg's law:

$$n\lambda = 2d\sin\theta \quad (2.2)$$

This fundamental law shows coherent diffraction effects can only be observed for monochromatic radiation at certain angles to the planes (hkl) and hence that the distribution of reflections in a diffraction pattern is a direct measure of the symmetry of the system.

Reciprocal Space

Bragg's Law gives an inverse relationship between $\sin\theta$ and d , so crystals with large lattices display compressed diffraction patterns. It is sometimes advantageous to have a linear relationship between these quantities, while still keeping the beneficial properties of the direct lattice: we use the reciprocal lattice construction. The definition of the reciprocal lattice revolves around a coordinate system \mathbf{a}^* , \mathbf{b}^* , \mathbf{c}^* where

$$\mathbf{a}^*.\mathbf{a} = \mathbf{b}^*.\mathbf{b} = \mathbf{c}^*.\mathbf{c} = 1; \mathbf{a}^*.\mathbf{b} = \mathbf{a}^*.\mathbf{c} = \mathbf{b}^*.\mathbf{a} = \mathbf{b}^*.\mathbf{c} = \mathbf{c}^*.\mathbf{a} = \mathbf{c}^*.\mathbf{b} = 0 \quad (2.3)$$

and the norms \mathbf{a}^* , \mathbf{b}^* , \mathbf{c}^* have dimensions of (meters)⁻¹ if \mathbf{a} , \mathbf{b} , \mathbf{c} are in meters. Another set of useful representations are the Brillouin zones which are extensively referred to within phonon dispersion circles. The first Brillouin zone is generated by taking the bisecting points of the nearest neighbour vectors and joining the points formed into a 3D surface.

After generating the reciprocal lattice, Bragg's law and the conditions for coherent elastic scattering are embedded in the Ewald construction: imagine that a beam of

monochromatic X-ray radiation impinges on a crystal, draw a line XO in the direction of the beam, passing through the reciprocal lattice origin O. Finally, describe a circle of radius $1/\lambda$ with its centre C on XO and located so that O falls on its circumference (Fig.2.5).

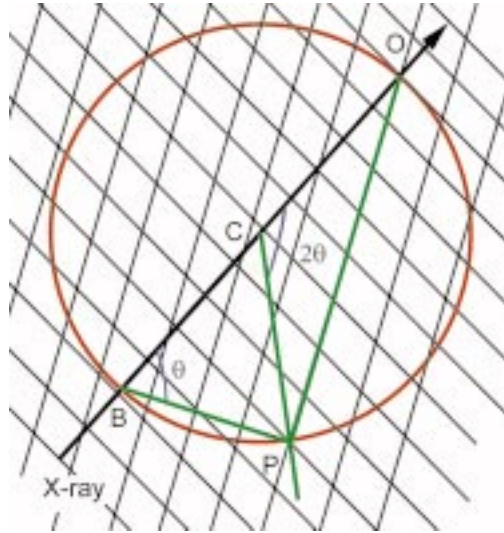


Figure 2.5: The Ewald construction in reciprocal space, as the condition for diffraction from plane P.

Considering point P, the length OP is by definition equal to $1/d_{hkl}$ and Bragg's law is obvious from here. This does imply that the diffracted beam is parallel to CP and this will only occur for a crystal orientation where a reciprocal lattice point coincides with the circle. In three dimensions, the Ewald sphere describes a 'sphere of reflection' that can be brought into contact with successive reciprocal lattice points by rotating the crystal in real space, so providing the basis of single crystal diffraction.

If a direct lattice is taken to be vertical and the radiation beam is assumed to be perpendicular to it (Fig.2.6), because levels of reciprocal lattice points are normal to the direct axis, a rotation about the axis will cause each level of points to intersect

the sphere in a circle. The diffracted rays pass through these circles from the centre of the sphere, forming cones. This is an important concept for powder diffraction.

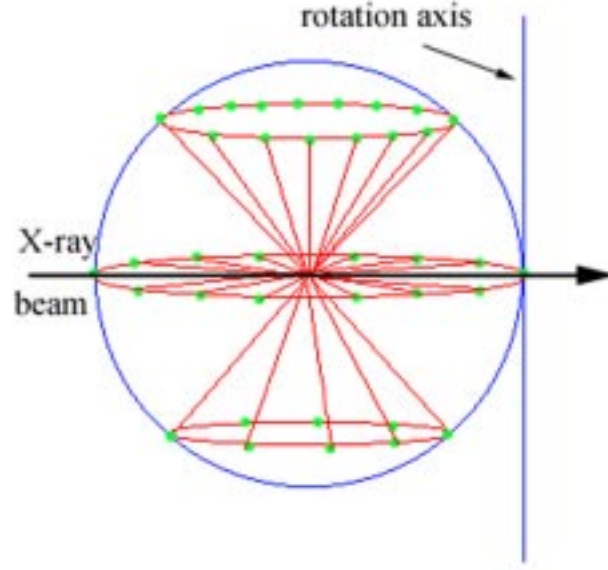


Figure 2.6: Cones of diffracted rays for rotation about a direct axis. The green spots are successive reciprocal lattice points coming into contact with the Ewald sphere.

Scattered Amplitude

The distribution of electrons in matter is described by the electron density function, $\rho(\mathbf{r})$, so the number of electrons per volume element $d^3\mathbf{r}$ is $\rho(\mathbf{r})d^3\mathbf{r}$. Taking an incident beam of wavevector, \mathbf{k}_0 that interacts with the volume elements at the origin and at vector \mathbf{r} , as in Fig.2.7, produces the scattered waves A and B, respectively. The path difference, $\Delta = \lambda\mathbf{r} \cdot (\mathbf{k} - \mathbf{k}_0)$, so the wave B can be expressed as

$$\psi = \rho(\mathbf{r})e^{2\pi i \cdot \mathbf{r}(\mathbf{k} - \mathbf{k}_0)} d^3\mathbf{r} \quad (2.4)$$

with $\mathbf{k} - \mathbf{k}_0 = 2\sin\theta/\lambda = 1/d$. The total scattering is given by the integral over the sample volume; the scattered amplitude is proportional to the Fourier transform of the electronic density. The formalism for neutrons is exactly the same, but the electron density is replaced by the Fermi pseudo-potential

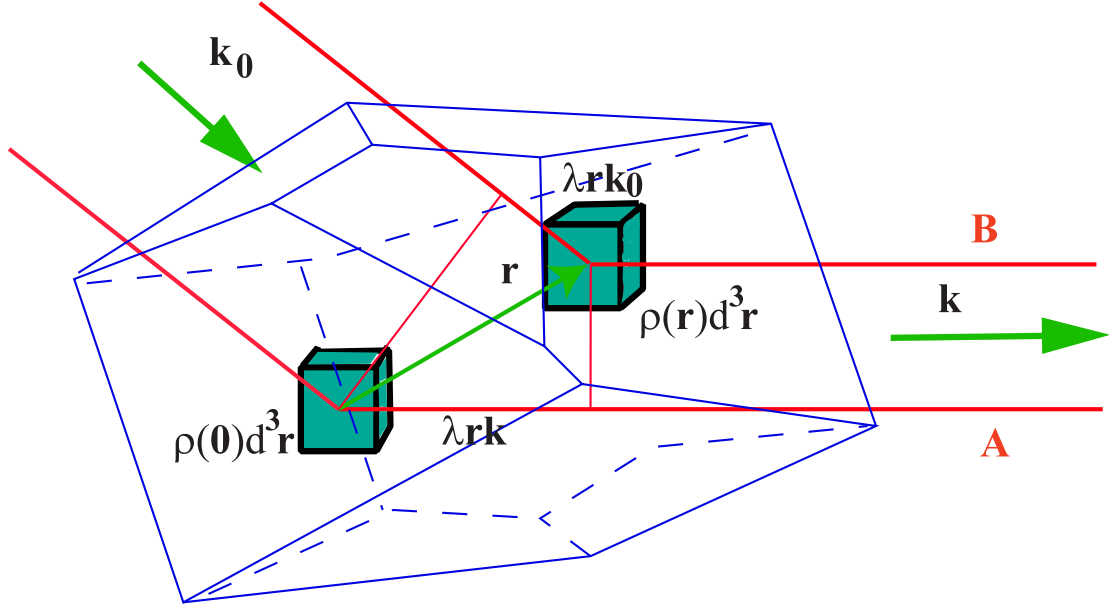


Figure 2.7: Electron density $\rho(\mathbf{r})$ scattering radiation.

$$V(\mathbf{r}) = \frac{2\pi\hbar^2}{m} b\delta(\mathbf{r} - \mathbf{R}_i) \quad (2.5)$$

where b is the scattering length.

For a crystal, the scattered density has a three-dimensional periodic distribution. We define the position of an atom, as $\mathbf{R}_i = \mathbf{R}_l + \mathbf{r}_i$, where \mathbf{R}_l is a vector of the direct lattice and \mathbf{r}_i is the atom position in the unit cell. The scattered amplitude can then

be written

$$A_{\mathbf{k}} \propto \sum_i f_i(\mathbf{k}) e^{2\pi i \cdot (\mathbf{k} \cdot (\mathbf{R}_l + \mathbf{r}_i))} \equiv \sum_i f_i(\mathbf{k}) e^{2\pi i \cdot \mathbf{k} \cdot \mathbf{r}_i} \sum_l e^{2\pi i \cdot \mathbf{k} \cdot \mathbf{R}_l} = F(\mathbf{k}) \cdot L(\mathbf{k}) \quad (2.6)$$

The two exponential terms are the *structure factor*, $F(\mathbf{k})$ and *lattice factor*, $L(\mathbf{k})$, depending on the basis of the unit cell and the lattice, respectively. $f_i(\mathbf{k})$ has replaced the integral over electronic density

$$f_i(\mathbf{k}) = \int_{atom\ i} \rho_i(\mathbf{r}) e^{2\pi i \cdot \mathbf{k} \cdot \mathbf{r}_i} d^3\mathbf{r} \quad (2.7)$$

Neglecting the effect of chemical bonding we assume that the electronic distribution is spherical. After integration in spherical coordinates

$$f_i(k) = \int_0^\infty 4\pi R^2 \rho_i(R) \frac{\sin 2\pi Rk}{2\pi Rk} dR \quad (2.8)$$

the obtained result is the *atomic form factor* which is the Fourier transform of the atomic electron density distribution. This factor describes the scattering power of an atom, the equivalent in neutron scattering being the scattering length, b . Taking into account anomalous dispersion (§2.2.4 *P, Polarisation Correction*) the form factor becomes: $f_{tot} = f + \Delta f' + i\Delta f''$. The atomic form factor is a function of $\sin \theta / \lambda$, the forward scattering having a value equal to the number of electrons in the atom/ion. The fall off of scattering with increasing angle is determined by the diffuseness of the electron distribution.

An added contribution to the atomic form factor comes from thermal effects that cause atoms to oscillate about their mean positions. An instantaneous structure on a timescale of less than 10^{-14} sec will not have translational symmetry. The time averaged structure characterised by the average electron density, $\langle \rho \rangle_t$, is periodic and allows the observation of diffraction patterns. Assuming that the fluctuation of the

electron density about its average is negligible and the total distribution is spherical, we obtain the *Debye-Waller factor*

$$T(\sin \theta / \lambda) = e^{-2\omega} = e^{-8\pi^2 U_{iso} (\sin \theta / \lambda)^2} \quad (2.9)$$

with U_{iso} in units of \AA^2 and having a typical value of 0.10 \AA^2 . The temperature factor can also be expressed as $B_{iso} = U_{iso}/8\pi^2$. In anisotropic solids, the thermal ellipsoids are described using a 3x3 tensor of the form

$$e^{B_{11}h^2a^{*2} + B_{22}k^2b^{*2} + B_{33}l^2c^{*2} + 2B_{12}hka^*b^* + 2B_{13}hla^*c^* + 2B_{23}klb^*c^*} \quad (2.10)$$

What can be obtained from a diffraction experiment is the intensity of the scattered beam, I_{obs} , which is given by the square of the total diffracted amplitude. This is essentially the phase problem of crystallography: if we could measure the phases as well as the magnitude of the amplitudes, structure solution would 'just' involve an inverse fourier transform of the data.

We shall look at the structure factor in section §.2.5.1 and shall delay discussing the meaning of this function until then.

The lattice factor gives rise to the Laue condition. The function

$$\sum_{m,n,p} e^{2\pi i \cdot \mathbf{k} \cdot (m\mathbf{a} + n\mathbf{b} + p\mathbf{c})} \quad (2.11)$$

has a maximum when the scalar products $\mathbf{k} \cdot \mathbf{a}$, $\mathbf{k} \cdot \mathbf{b}$ and $\mathbf{k} \cdot \mathbf{c}$ are integers, i.e. \mathbf{k} is a vector of the reciprocal lattice. The contribution to the diffracted intensity from the lattice is then

$$|L(\mathbf{k})|^2 = \left(\frac{\sin \pi M a k}{\sin \pi a k} \cdot \frac{\sin \pi N b k}{\sin \pi b k} \cdot \frac{\sin \pi P c k}{\sin \pi c k} \right)^2 \quad (2.12)$$

with M, N and P representing the number of lattice points along the three directions of the direct lattice.

For an infinite lattice, $|L(\mathbf{k})|^2$ can be described as a succession of Dirac peaks corresponding to the nodes in the reciprocal lattice. When the crystal has finite size, the peaks broaden and have definite 'sine wiggles' in their tails. The lattice factor defines the directions of the diffracted beams and is equivalent to the Bragg equation.

Neutron Cross-sections

The basic quantity measured in neutron scattering experiments is the partial differential cross-section, $d^2\sigma/d\Omega dE'$, which gives the fraction of neutrons of incident energy E scattered into an element of solid angle $d\Omega$ with an energy between E' and $E' + dE'$. After some manipulation and the use of Fermi's Golden Rule for the probability of transitions between states λ_0 to λ_f of the wavevectors \mathbf{k}_i (initial) and \mathbf{k}_f (final), where a weight is attributed to the state $|\lambda\rangle$ by p_λ ⁴ we arrive at

$$\frac{d^2\sigma}{d\Omega dE'} = \frac{k_f}{k_0} \sum_{\lambda_0 \lambda_f} p_\lambda |\langle \mathbf{k} - \mathbf{k}_f | V | \mathbf{k}_0 \lambda_0 \rangle|^2 \delta(\hbar\omega + E_{\lambda_0} - E_{\lambda_f}) \quad (2.13)$$

where the horizontal bar represents relevant averages over isotopes, nuclear spin orientations and positions of nuclei.

The scattering length, b , is a complex quantity where the imaginary part represents absorption⁵. Scattering from bound, independent nuclei is calculated via the Fermi pseudo-potential (Eqn.2.5), hence the differential cross-section is

$$\frac{d\sigma}{d\Omega} = |b|^2 \quad (2.14)$$

and the total cross-section is

$$\sigma = 4\pi \overline{|b|^2} \quad (2.15)$$

⁴Physically this represents degeneracy and thermodynamic Boltzmann factors and is normalised in such a way that the sum of all weights is equal to 1.

⁵Absorption being proportional to wavelength.

Extending this analysis to that of a rigid array of N nuclei for a scattering process where there is only a momentum transfer to the sample and otherwise no other change, the scattering is elastic and

$$\frac{d\sigma}{d\Omega} = \sum_{ii'} e^{i\mathbf{Q} \cdot (\mathbf{R}_i - \mathbf{R}_{i'})} \overline{b_{i'}^* b_i} \quad (2.16)$$

again the average being over isotope and nuclear spin states. In general, b_i depends on which isotope is at site \mathbf{R}_i and therefore can be generalised to $|\bar{b}|^2 + \delta_{i,i'} (|\bar{b}|^2 - |\bar{b}|^2)$, allowing a factorisation of (Eqn.2.16) into the sum:

$$\frac{d\sigma}{d\Omega} = \frac{d\sigma}{d\Omega_{coh}} + \frac{d\sigma}{d\Omega_{incoh}} \quad (2.17)$$

The coherent cross-section is defined by

$$\frac{d\sigma}{d\Omega_{coh}} = |\bar{b}|^2 \left| \sum_i e^{i\mathbf{Q} \cdot \mathbf{R}_i} \right|^2 \quad (2.18)$$

while the incoherent cross-section is

$$\frac{d\sigma}{d\Omega_{incoh}} = N \overline{|b - \bar{b}|^2} \quad (2.19)$$

The coherent cross-section gives rise to a term much the same as obtained for X-ray scattering and has the same lattice dependencies. For incoherent scattering there is no interference at all and the cross-section is completely isotropic (for a stationary lattice). The difference between these two scattering processes can be viewed as interference effects occurring only for the average potential that the neutron sees (proportional to \bar{b}). Deviations from the average potential are randomly distributed and give rise to the incoherent part (proportional to the mean-square deviation). The scattering lengths are dependent on isotope concentration and also on spin state of the sample. For a fuller treatment see volume 1 of Lovesey[84].

2.3 Production and Characteristics of Radiation

For the purposes of this section, it is sufficient to understand the properties of the three types of radiation used in structural studies, that obtained from a standard laboratory diffractometer, from a synchrotron source and neutrons. Finally, we shall look at the production of a muon beam.

The properties of neutrons are well documented though there is still on going research to improve the absolute values of the neutron lifetime and dipole-moment. The usefulness of neutrons stems from the de Broglie relationship between finite mass particles and wavelength. Wavelengths of the order of interatomic spacings and energies on the same scale as thermal excitations can be achieved by using thermally moderated neutrons.

The main advantages of neutrons over X-rays in structural work are apparent with scattering from light atoms, isotopes and neighbours in the periodic table, as the neutron scattering length varies randomly from atom to atom about an almost constant value, and is constant with increasing $\sin(\theta)/\lambda$, unlike with X-rays. The intrinsic magnetic moment associated with neutrons can be also put to good use as magnetic scattering can be of the same order of magnitude as nuclear scattering, though with a fall off for increasing $\sin(\theta)/\lambda$ similar to X-rays, due to the finite extent of the spatial distribution of electrons. However, new instrumental methods are becoming available with the use of third generation synchrotron sources where magnetic and inelastic scattering experiments are available.

There are a few other considerations to be taken into account before choosing which radiation to use for a particular sample. The penetration of neutrons into the sample is much greater than X-rays, enabling larger samples to be used: in

fact, larger samples are required because of the low flux of neutrons. For neutrons, incoherent scattering causes a background that in the case of hydrogenous material can dominate the diffraction pattern, necessitating the use of deuterated samples. In both diffraction scenarios, there is absorption to consider. While some isotopes have large absorption cross-sections for neutrons (lithium, boron, cadmium etc.), it is usually the heavier elements which absorb X-rays (lead, for example) though here consideration must also be given to absorption edges from elements within the sample.

Overall, the results from diffraction of neutrons and X-rays are complimentary.

2.3.1 Neutrons

Neutrons are produced by two methods: steady-state nuclear reaction or spallation. The I.L.L. will be used as the example for a steady-state source. It has the highest flux in the world and operates at a thermal power of 58 MW. Neutrons are produced in the reactor core by fission of enriched uranium. The core sits inside a heavy water moderator and cooler that partially reflects the neutrons back towards the core and shifts the high energy neutrons towards a longer wavelength⁶ with a Maxwellian distribution (peak 1.2 Å). Further moderation is done using heated graphite or liquid deuterium in the horizontal and vertical (less flux). Instruments are situated either in the reactor area or externally, where the neutrons are channelled via guide tubes of various cross-sections from the different moderators. The characteristics of the neutrons arriving at the instrument are a function of which moderator source and the characteristics of the guide tubes[85]. The intensity of neutron sources are weak however, the brilliance being an order of magnitude lower than that obtained

⁶The maximum in wavelength is proportional to the reciprocal of the effective temperature.

from an X-ray tube and up to 10^{12} lower than that from the E.S.R.F.[86].

Due to the continuous distribution of neutron wavelengths, monochromatisation of the beam is necessary. This is performed by a silicon or germanium single crystal that has a high mosaic spread[87] to increase the neutron flux at the sample. From Bragg's law, the diffracted wavelength can be chosen by altering the diffraction angle, the so-called take-off angle, θ_m . Since *Si* and *Ge* both have the diamond structure any reflections from planes whose Miller indices are all even are systematically absent. Hence, when (111), (311) or (331) reflecting planes are used there is no $\lambda/2$ contamination of the monochromated beam. The beam is not suitable for use in a diffraction experiment yet, and must be further made parallel by the use of collimators[88] coated with cadmium to absorb diverging neutrons. These can be placed before and after the monochromator and before the detectors to provide a high resolution that is dependant upon the horizontal divergence of each collimator⁷. Vertical divergence is responsible for asymmetry in the peak shapes of the Bragg reflections by broadening the low angle sides and is also a function of 2θ . An interesting point here is that the resolution across the entire diffraction pattern varies with 2θ and is dependent not only on the collimation but also on the monochromator mosaic spread and take-off angle[89], so that the best resolution occurs when 2θ equals $2\theta_m$, the parallel focussing condition. The combination of these parameters has been optimised to produce the highest resolution, essentially limited by particle size, and high intensity for the D2b diffractometer at the I.L.L.[90]

An example of a spallation source is ISIS (Rutherford Appleton Laboratory, Oxford), also the brightest source of neutrons in its field. Here neutrons are produced

⁷Defined as the ratio of width to length of the collimator channel.

via bombarding a heavy metal target such as tantalum, with highly energetic protons (~ 800 MeV) from an accelerator. The protons then knock nuclear fragments out of the target producing ~ 20 neutrons per incident proton. Since the spallation target is much smaller than a nuclear reactor, a higher flux is found, but also it is pulsed at a frequency of 50 Hz leading to a peak flux that is equivalent to that of a high flux steady state reactor. Moderation is achieved using hydrogenous material around the target that ensures the white beam structure is still sharp. In general, instruments at spallation sources are optimally designed where the geometry is fixed and energy resolution is achieved by the time-of-flight technique. This gives an essentially constant resolution over a larger Q -range than that for the angle-dispersive case. Incidentally, muons and other fundamental particles can also be produced by the same method but using a lighter, intermediate graphitic target.

As Dr. R. Scherm would say "To count a neutron it has to be killed". A typical reaction is to use a highly absorbing isotope such as ${}^3\text{He} + n^0 \rightarrow {}^3\text{He} + {}^1\text{He} + 0.77\text{MeV}$ and the gas ionised by these particles is detected by as a charge pulse. The pulse is proportional to the initial ionisation and hence to the number of incoming neutrons.

2.3.2 X-ray tubes

A laboratory X-ray generator consists of an electron gun and a metal anode in a high-vacuum chamber. The resulting emission spectrum consists of a continuous background of white radiation (which is independent of the anode) superposed with intense lines characteristic of the metal anode. The characteristic lines are due to ionisation of core electrons of the anode which are replaced by electrons from a higher level. Copper is the most widely used anode, showing L \rightarrow K and M \rightarrow K transitions

known as $K\alpha$ and $K\beta$ lines⁸. Further fine structure is apparent within the radiation corresponding to a transition from a $P_{1/2}$ or a $P_{3/2}$ and are further labelled $K_{\alpha 1}$ and $K_{\alpha 2}$ lines. An approximate monochromatisation can be achieved by isolating the most intense $K_{\alpha 1}/K_{\alpha 2}$ doublet. In practice this wavelength twinning is very troubling for high resolution studies coupled with the low intensity and high beam divergence of X-ray tube radiation. There are approximate corrections that strip the diffraction pattern [91] but, depending on the needs, it is better to remove the problem at source with a focusing monochromator in either the incident or diffracted beam. This method will decrease the intensity of the beam but does away with the need to use Söller slits[92] and a β filter.

2.3.3 Synchrotron

Synchrotron radiation is generated by relativistic particles being deviated from their direction of travel. External magnets around a storage ring keep the electrons circulating, accelerating inwards, also providing a focusing effect that keeps the bunches of electrons together. The E.S.R.F. works with electrons with an energy of 6 GeV, circulating around a ring of 844 meters circumference providing a maximum current of 200mA for a beam lifetime of ~ 50 h. White radiation is produced tangentially to the curved path of electrons steered by bending magnets. The radiation produced in this way is extremely brilliant⁹, coherent, polarised and of small divergence. Additional insertion devices can replace bending magnets: wigglers cause sharper bends in the electrons path so as to shift the wavelength distribution to higher energies

⁸i.e. the quantum number n having values of 1 to n are labelled alphabetically from K onwards

⁹The brilliance of an X-ray source is defined as the number of photons emitted per second, per unit source size, per unit space angle and for a bandwidth of $1/1000$ of the photon energy.

and increase intensity. Undulators create a series of small deviations such that the emissions produced at each turn are subject to interference from all other turns[86]. The result is a radiation distribution that has an intense characteristic wavelength plus harmonic related frequencies, while also reducing the horizontal divergence of the beam. There are many methods¹⁰ using monochromators to select the desired wavelength while also tweaking the properties of the beam and possibly focusing the beam on the sample so increasing the effective flux and reducing divergence[93].

2.3.4 Muons

The μ^+ SR technique in all its variants has been used extensively in the characterisation of the physical and dynamical properties of fullerenes and intercalated fullerides[19, 94]. The positive muon itself has a mass approximately $1/9^{th}$ of that of a proton and as such, can capture an electron forming the muonium atom, Mu, viewed in a chemical sense as a light isotope of hydrogen. The magnetic moment of the muon is 3.18 times that of a proton making it an extremely sensitive probe of magnetism within a sample. A summary of the properties of the muon is given in Table.2.1.

¹⁰Double crystal monochromators, multi-layer monochromators and bent mirrors for sagittal focussing.

Table 2.1: Selected properties of the muon

Mass	$0.113 \text{ amu} = 207 m_e = 0.1126 m_p$
Spin	$\frac{1}{2}$
Charge	$+e$
Lifetime	$2.1971 \mu s$
Magnetic moment	$4.84197 \times 10^{-3} \mu_B$
Gyromagnetic ratio	$(2\pi) \times 13.5544 \text{ kHzG}^{-1}$

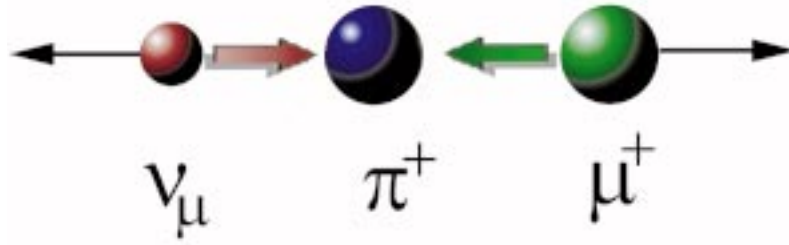


Figure 2.8: Illustration of pion decay into a μ^+ and ν_μ viewed in the rest frame of the pion. The green and red block arrows represent the spin polarisation of the muon and neutrino respectively, while the black arrows show momenta.

Experiments with muons in this thesis were performed using the π M3 beamline at PSI. The muons originate from the decay of pions produced by the interaction of the 1.5 mA, 590 MeV proton beam with the nuclei of the five millimeter thick graphite target. After a very short time the lowest energy positive pions come to rest at the surface of the target. The stationary pion then decays with a total lifetime of 26 ns into a muon and a neutrino. Muons produced in this way have energies of 4.1 MeV and are 100% spin polarised. Schematically Fig. 2.8 shows the collinear decay of the

pion from its rest frame. The spin polarisation arises from the fact that the pion has no spin and a neutrino is always produced with a negative helicity, hence from the conservation of angular momentum the muon also is produced with its spin being antiparallel to its momentum. The muons emitted in a particular direction are then collected and guided to the sample via a series of magnets within a beamline. A spin rotator magnet can be used to rotate the muon polarisation into a transverse direction, the rotation angle being roughly 70° . In fact after this rotator the muon beam can be divided between the GPS¹¹ and LTF¹² facilities which are used simultaneously.

2.4 Instrumentation and Experiments

Sample preparation for most fullerenes follows the same pattern: the sample is sealed in a container in an inert and dry atmosphere. Similarly, after an experiment the sample is recovered and sealed under vacuum. Sample quality is checked via laboratory X-ray diffraction prior to - and post - experiment. Sample environments are pretty varied across techniques depending on factors such as money, available space, user demand and technical challenge. In this section, I shall give a description of relevant instruments used in this thesis.

2.4.1 Powder Diffraction

Invariably, X-ray powder diffraction is performed upon a few tenths of a milligram of sample sealed in glass capillaries: diameters of 0.5 mm have been common for our purposes. The use of a 0.7 mm capillary will afford a gain in intensity (but when

¹¹General Purpose Surface-Muon Instrument.

¹²Low Temperature Facility (base temperature 10 mK).

using the image plate system of the SNBL, this is accompanied by a worsening of the resolution). High pressure measurements involve a more difficult procedure for sample loading in diamond anvil cells[95] (DAC).

SNBL, ESRF

The experimental hutch close to the storage ring is called 'station B' and takes part of the radiation from the beamline's bending magnet. Monochromatisation is achieved with a water-cooled, flat-crystal Si monochromator resulting in a nominally $35 \times 3 \text{ mm}^2$ unfocused beam. Station A's radiation is first vertically collimated by a primary mirror, before hitting a double Si monochromator crystal. The first crystal of the monochromator is water cooled, while the second crystal is sagittally bent for horizontal focusing. Finally a secondary mirror, identical to the first mirror, provides vertical focusing at the sample. Along the way are anti-scatter slits and beam collimators.

There are two possible diffractometers on the Swiss-Norway beamline. One is a conventional high resolution 2θ diffractometer (station B) that achieves slightly better resolution than BM16, even without the germanium analysers (four of these are planned for the end of 1998), but with much reduced intensity. Alternatively, on station A, a MAR image-plate area detector can be used for fast collection of entire rings of Debye-Scherrer cones over short exposure times. The scattered photons are trapped in f -centres until they are excited by a laser (or light!). The intensity of the light emitted is photomultiplied and recorded. 2D detectors are characterised by low, smooth backgrounds and extremely high statistics. Compared with a 2θ arm whose solid angle covered is small and stepwise along a radial direction to the diffraction

cones, it is no surprise that this is a more efficient method of counting even though the resolution is reduced.

The image plate systems is accompanied by an Oxford Cryosystems nitrogen blower (>100 K) that directs a jet of nitrogen towards the capillary. Care has to be taken that the flow is smooth, and there is no place for turbulence of the stream to occur so frosting is prevented. An acetylene heater could be used with the MAR. So far the diffractometer on station B has a 4 K, closed loop helium cryostat.

BM16, ESRF

BM16 is designed to achieve very high angular and energy resolution with fast data acquisition times. X-rays emitted from a bending magnet provide a source size of $0.3 \times 0.3 \text{ mm}^2$, the high resolution being achieved via the use of a vertically collimating mirror before a double-crystal Si(111) monochromator. The first crystal is flat and water-cooled. The second crystal can be bent to focus sagittally the horizontal fan onto the sample. After the monochromator, a second mirror provides the option to focus the X-rays vertically onto the sample, gaining intensity at the expense of resolution.



Figure 2.9: The two-circle diffractometer on BM16 equipped with a horizontal cryostat. The beam enters from the right.

A nine-crystal analyser stage (with nine Ge(111) crystals separated by 2 intervals) and Debye-Scherrer slits are mounted on a 2-circle diffractometer. This analyser geometry means that high resolution and low backgrounds are extended to very high scattering angles. Data are collected in a continuous scanning mode. This eliminates the dead time of a conventional step scan. Following data collection, the counts from the nine detectors are rebinned and normalised, to give the equivalent normalised step scan, which is suitable for analysis by standard programs. The capillary samples are rotated to achieve a better spatial average and reduce preferred orientation.

The constraints on space here are much less severe than on SNBL, so it is possible to have an acetylene heater (<1000 K), a nitrogen blower (>100 K) or a helium flow cryostat (>4 K). The diffractometer and cryostat are shown in Fig.2.9.

High Pressure

Diamond anvil cells are prepared after electrochemically drilling a hole of the order of $100\text{ }\mu\text{m}$ into pre-indented stainless steel gaskets. To access pressures up to 20

GPa, diamond faces of 600 μm diameter and a preindented gasket thickness of 70-80 μm are used. Such high pressures are available due to the ratio of the diaphragm membrane area (10cm^2) compared to the diamond face area. Two crystal ruby chips for pressure calibration are placed just off-centre of one diamond face and the gasket replaced (can be held in place by 'blu-tac'). A gentle pressurisation (15 bar) of the cell, using the normal membrane/helium gas system, will ensure that the gasket is firmly in place without contracting the hole. The difficulties start when filling the hole with air sensitive samples, while in the glovebox. We have found that cactus needles are excellent tools for working on such a small scale as this. One technique of introducing the sample is to drop sample from a broken capillary straight onto the hole. Another possibility is to push the sample inside the hole from the edges, though there is a greater risk of some sample sticking to the cactus needle and removing the rubies from the hole. At this point we have used two types of pressure transmitting media. One is cryogenic liquid gas (nitrogen or argon). While these produce low backgrounds, they also solidify at pressures approaching 2 GPa[96] into a complicated series of phases whose Bragg peaks are usually much more intense than those from the average fulleride. The other method is to use degassed silicone oil (or fluorinert 77, which is somewhat inferior) which is added while in the glovebox. The best way we have found is to make small tracks of oil from a drop placed on the outer rim of the gasket, towards the hole. If the sample is just swimming with oil then we usually stop adding more. After sealing the cell with the diaphragm, the sample should fill the entire hole. Outside of the glovebox an applied diaphragm pressure of 10 bar seals the cell. It is wise at this point to try and find one of the rubies by using the ruby resonance laser systems that have a microscope and camera attached for ease of

use.

A blue laser is used to monitor the wavelength/pressure dependence of the R_1 luminescent line. Pressure is calibrated from the observed λ , according to the formula[97]

$$P = \frac{B_0}{B'} \left(\left(\frac{\lambda}{\lambda_0} \right)^{B'} - 1 \right) \quad (2.20)$$

with $B_0 = 1904$ GPa and $B' = 7.665$. λ_0 is a function of the ruby quality and is calibrated at the start of each experiment (usually ~ 694 nm)

Due to the minute amounts of sample within the diamond cells, both the ID9 and ID30 beamlines take their hard X-rays from intense undulator devices with focussing of the beam down to 20×20 and 10×10 μm , respectively. Monochromatisation is achieved by Si(111) crystals. Two-dimensional images of Debye-Scherrer cones are recorded on phosphor Molecular Dynamics image plates. The FIT2D[98] program is used to correct the scanned image plate data for spatial distortions, fit the centre of the 2D pattern (via fitting circles to a chosen number of rings after defining the distance of the plate away from the sample, the tilt axis and angle and wavelength), mask unwanted features and integrate around the rings to obtain the more familiar 1D pattern. A standard silicon calibration is done to refine the wavelength, sample to detector distance and tilts of the image plate. The same process is used at the SNBL with a standard LaB_6 sample.

We have also performed 'test' experiments with DAC and a He cryostat. Difficulties arose however, as it was necessary to rock the DAC during data collection, and hence a solution was to rotate the entire cryostat. This produces undesirable misalignments of the entire table system if the cryostat is too heavy, and so far it has been. A DAC heater jacket is available that reaches temperatures on the order of 500 K.

D1B, ILL

This instrument is dedicated to diffraction experiments requiring a high intensity neutron flux (at the expense of resolution) and as such is excellent for time resolved experiments where patterns can be recorded on a time-scale of minutes. Studies of phase transformations and kinetics are routine. One of its main other uses is to search for magnetic reflections at small angles. An array of three pyrolytic graphite (002) monochromators focus onto the sample position at a wavelength of 2.52 Å. The high flux is partly a consequence of this focusing and having essentially no collimation of the beam. A $^3\text{He}/\text{Xe}$ position-sensitive detector spans a range of 80° , with the option to move the detector bank and increase this to 160° . The detector size limits the effective step size of a pattern to 0.2° . Detector efficiencies are taken into account via a vanadium calibration.

A typical ILL cryostat with low background (1.7 to 300 K) and a furnace (~ 1000 K) are available. The sample is press sealed in vanadium¹³ cylindrical cells. The resolution is governed by the sample cell and detector diameters being small compared to the distance between them[99].

D2B, ILL

D2B was conceived by A. Hewat[99] of the ILL to increase resolution until the limitations imposed by powder particle size. Slices of germanium crystal of high mosaic spread are used to increase intensities at high take-off angles (135°) and focus the beam onto 50 mm at the sample position. Collimation before the monochromator ($5'$ to $35'$) and after the sample ($5'$) is essentially what defines the resolution, while the

¹³Incoherent scatterer gives a weak, broad background but no Bragg reflection.

mosaic spread does not affect the focussed peak width. $64\ ^3\text{He}$ detector tubes, with a vertical divergence that approximately matches that from the monochromator, are placed at 2.5° to cover 160° in 2θ . 100 step scans of 0.025° are needed to cover the full 2θ range. Detector calibration is done using a vanadium sample.

An ILL cryostat (1.5 to 300 K), cryofurnace (1.5 to 525 K) and a furnace (200 to 1000 K) are available. Again the sample is sealed in a vanadium cylindrical can¹⁴.

2.4.2 Inelastic Neutron Scattering

Depending upon the amount of sample and sample absorption factors, there are three sample cans for INS. High absorbers and liquids are used with thin annular aluminium cans so as to effectively minimise the absorption of the beam or contain the liquid. A more usual case (and easier to make corrections to the data!) is a flat plate geometry that is placed at an angle of 135° to the incoming beam. Both these cells require that there is plenty of sample available, so that aluminium scattering is weak in comparison to that of the sample. We also developed flat plates that are extremely thin around the sample and yet have a groove around the window to allow an indium seal. This proved to be unsatisfactory as the length of the seal was of the order of 10 cm so allowing a high risk of a poor sealing and possible degradation of the sample. More important for the actual measurement is that there could be a settling of the low density powder within the container with time. This makes the scattering geometry extremely difficult to account for. It was also seen that the aluminium scattering was still of the same order as that from the sample even with gadolinium used to cover all but the sample window.

¹⁴Due to constraints of the cryostats, the sealing heads have a different diameter on the diffraction instruments.

In the case of weakly scattering fullerenes which are also only available on the order of 1g, the use of a thin walled aluminium cylinder would cut down the amount of aluminium within the beam and could also be made thinner due to the stronger geometry of a cylinder. The diameter was chosen so that around 1.5 g (optimistically) of sample would be completely within the height of the beam (5 cm) and an aperture used so that the beam is reduced to the size of the sample within the cell. The cell is press sealed using 1 mm indium or lead wire. Cadmium is used to cover all non-sample parts of the cell¹⁵. Spare cans were made to the same specifications to use as background and vanadium (a roll of foil¹⁶ that has the same geometry as the sample) runs. The best results, in terms of statistics and aluminium removal, have been achieved by using this method.

IN6

This time focussing time-of-flight spectrometer (Fig.2.10) is designed to give high flux and excellent resolution at energy transfers less than 50 meV. A series of three vertically focussing pyrolytic graphite monochromator crystals (a beryllium filter removes second order reflections) are set at different angles relative to the guide and different distances from the sample. Discrete wavelengths between 4.12 and 5.9 Å are available with a resolution at the elastic line that is Q dependent between 0.14 and 0.17 meV for a wavelength of 4.12 Å. To achieve time-focussing a Fermi chopper (possible frame overlap being ruled out by a suppressor chopper) is rotated at speeds of 2000 to 10000 rpm, so as to give slower neutrons (those reflected at high 2θ from the

¹⁵This means making a new mask for every sample as the depth of sample in the cell is different for each experiment.

¹⁶When using INX, the effective radius of a solid rod of the same mass as the amount of vanadium in the beam should be used.

monochromators) a head start. All neutrons that have transferred the same amount of energy to the sample will then arrive at the same time at the detectors. 337 ^3He elliptical detectors make up the detector bank and are in a helium filled box to reduce background.

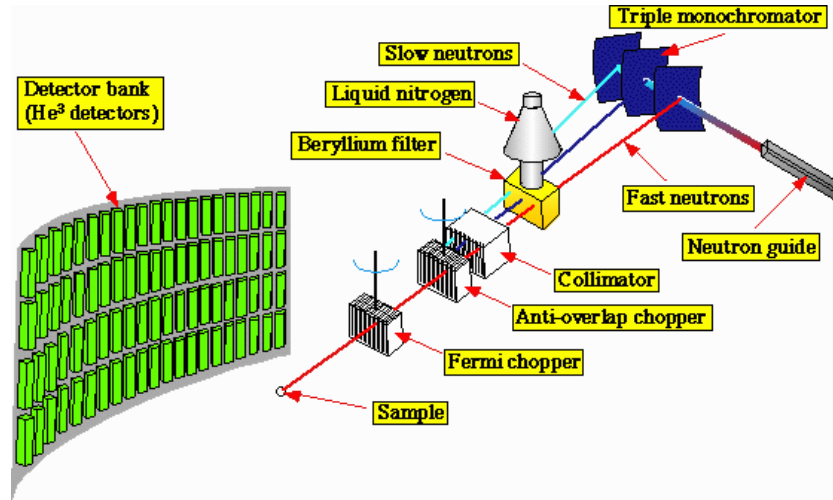


Figure 2.10: Schematic view of IN6.

Standard cryostat (1.5 to 310 K), furnace (320 to 1200 K, high background) and cryo-furnace (2.5 to 600 K, slower temperature regulation) are available. As well as the above, sample environments for flat plate geometry include a heating and cooling loop (100 to 620 K) that reduces cryostat contamination to the spectra.

IN5

IN5 (Fig.2.11) uses a double set of choppers to select a monochromatic neutron beam. Two other choppers are used to eliminate harmonics of the desired neutron velocity and to cut out frame overlap (neutrons from a 'subsequent' pulse arrive at the detectors before the slowest neutrons from the 'current' pulse). This use of choppers

and their speed selection offers total flexibility of wavelength selection leaving a resolution function that is essentially triangular. The resolution, ΔE , is related to the wavelength by:

$$\Delta E = \frac{1.3668}{\lambda^3} \quad (2.21)$$

with the wavelength in units of Å, the resolution is in μeV (e.g. for $\lambda = 6$ Å, $\Delta E = 63 \mu\text{eV}$). A 4 m long argon filled secondary flight-path reduces extra scattering and absorption. Further reduction of background has been achieved by adding an evacuated tube in the forward scattering direction and using collimating blades to absorb background neutrons. 1000 ^3He detectors cover an angular range of 11 to 130° with an angular resolution varying from 20 to 70 mrad. A multidetector is available in the forward scattering tube.

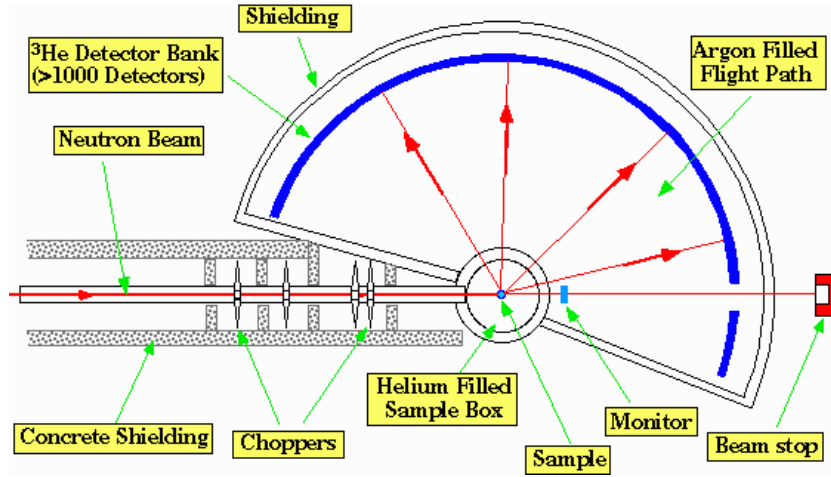


Figure 2.11: Schematic view of IN5.

The only relevant sample environment is the ILL 'orange' cryostat with a workable temperature range of 1.2 to 300 K.

2.4.3 μ^+ SR

In a muon spin rotation/relaxation experiment, a muon enters the sample after it passes through a detector that initiates a clock counter. When the muon is implanted in the sample, it thermalises almost instantly. Its spin will start precessing in the presence of internal and external magnetic fields, and it will finally decay anisotropically emitting a positron and two neutrinos. The emitted positron is detected by positron detectors, in a coincidence arrangement¹⁷, that surround the sample which immediately stops the clock counter. The time between the implantation of the muon in the sample and the emission of the positron is counted with respect to the position of the counters. This process is repeated until approximately 10^7 *individual* events have been collected. A low intensity, continuous beam is used, with a very small probability that a second muon can appear in the lifetime of the first muon. Events such as muons not stopping in the sample, no positron detection in the corresponding time limit, or more than one incoming muon appearing are vetoed and not counted.

GPS

In a typical μ^+ SR experiment, the sampleholder is usually made of silver (because of its small relaxation) with a thin mylar foil window that is press-sealed with vanadium. The sampleholder is screwed on to a cryostat stick which has a suitable length, so that the sample lies in the muon beam when inserted into the cryostat. Detectors are located around the sample environment in the forward, backward, up, down and right positions, with respect to the muon beam direction. The cryostat occupies the 'left' side as shown in the horizontal cross-section of the GPS instrument in Fig.2.12.

¹⁷To reduce background noise in the signal.

A pair of Helmholtz coils are used to provide a strong magnetic field (< 6 kG) along the beam direction. The field at the sample can be accurately measured using a NMR probe. A much smaller field (~ 100 G) can be also generated perpendicular to the muon beam. A further series of magnets can be used to compensate for the earth's magnetic field. To be able to perform transverse field (TF) measurement using the strong magnetic field, a spin rotator can be used to rotate the muon polarisation by roughly 70° towards the vertical.

Currently an Oxford Cryosystems helium cryostat is available on GPS with a two temperature ranges, 1.2 to 20 K and 20 to 300 K, that are accessible via different He flow and heater settings. The LTF has a $^3\text{He}/^4\text{He}$ dilution fridge that allows temperatures as low as 100 milli-Kelvin.

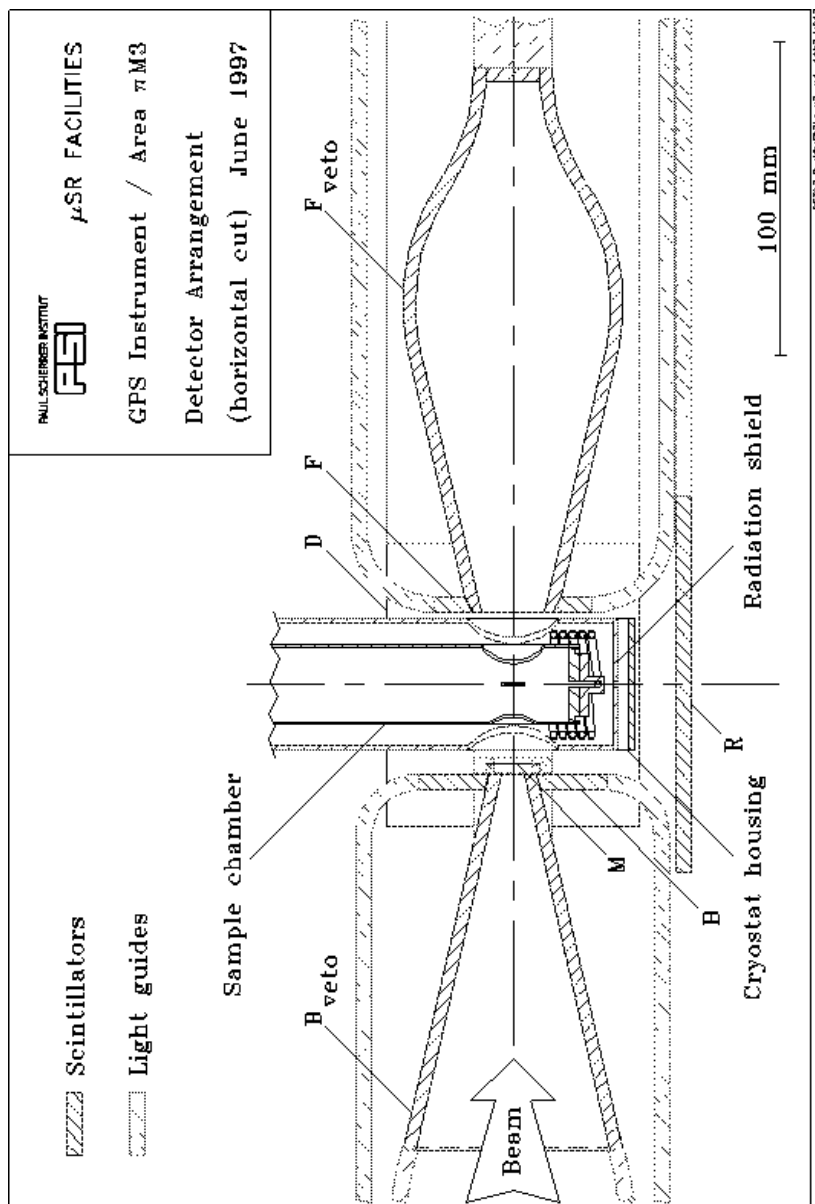


Figure 2.12: Horizontal cross-section of the GPS instrument at PSI[100].

2.5 Data Treatment and Analysis

2.5.1 Powder Diffraction

Bragg's law is only valid if the initial and final wavevectors have the same magnitude, with their directions being constrained from the Ewald construction. This is the case for elastic scattering, namely there is no energy transfer between the sample and the radiation. When one performs a 'diffraction' experiment, there are many characteristics of the sample under scrutiny: crystal structure, particle size, texture, disorder effects, purity, stress and strain. Within this thesis, I am concerned primarily with crystal structure determination, refinement and characterisation of powder samples as a function of temperature and pressure.

A 'powder' sample is composed of a large number of randomly oriented microcrystals with sizes of the order of $10\text{ }\mu\text{m}$. For each lattice plane, the sample contains some microcrystals in reflecting positions. From the Ewald sphere construction (Fig.2.5), this means that the sum of all the reciprocal lattices of all the single crystals form concentric spheres around the point O, that was taken as the reciprocal lattice origin. The intersection of these spheres with the Ewald sphere results in diffracted cones of intensity about the X-ray beam direction. It is this resulting intensity and its 2θ position that we wish to measure with as great an accuracy as possible in both values. The basic method was first reported by Debye and Scherrer[101] using a camera and photographic film with monochromatic X-rays. Other parafocusing methods have been developed, such as the Guinnier method where a divergent beam bathes a sample film that is (ideally) curved to match the curvature of the detector circle[83].

Such methods increase the resolution of powder lines but can increase the complexity of the resulting line shape[102]. The constant wavelength method is not alone in the world of powder diffraction with neutron time-of-flight instruments competing strongly in resolution and being especially appropriate for time resolved experiments (e.g. HRPD and POLARIS at ISIS).

One-dimensional diffraction peak positions allow us to search for a basis and hence label the peaks according to the three-dimensional reciprocal lattice. We have to solve an equation of the form

$$\left(\frac{1}{d_{hkl}}\right)^2 = \left(\frac{2 \sin \theta}{\lambda}\right)^2 = h^2 a^{*2} + k^2 b^{*2} + l^2 c^{*2} + 2hk \mathbf{a}^* \cdot \mathbf{b}^* + 2hl \mathbf{a}^* \cdot \mathbf{c}^* + 2kl \mathbf{b}^* \cdot \mathbf{c}^* \quad (2.22)$$

For further analysis the powder pattern is split into i equal steps in 2θ each of intensity I_{obs} . The calculated intensity, I_{calc} , at each point is described by the sum of a background intensity, I_b , and a summation over all contributing phases that includes the scale factor, S_p , and contribution from the h^{th} reflection of the p^{th} phase

$$I_{calc} = I_b + \sum_p S_p Y_{ph} \quad (2.23)$$

The contribution to the intensity, Y_{ph} , from a Bragg peak is dependent on numerous factors

$$Y_{ph} = M.L.P.E.A.O.V. |F_{hkl}|^2 \quad (2.24)$$

each dealt with separately below. There is also a 'zero-point error' correction applied to the calculated contributions to shift the spectrum by a constant angular offset.

M, Multiplicity

The multiplicity is the number of reflections that gives rise to the scattered intensity at a particular d -spacing. It is entirely crystal system dependent.

L, Lorentz Correction

Trigonometric factors are obviously machine dependent, but the source of the correction is in principle the same. The Lorentz factor is made up of three parts. (i) The first part reflects the fact that for a particular plane scattering at some Bragg angle, θ_B , there will be some crystallites that have a small deviation from this angle that can also diffract. This is very much in analogy to single crystal rocking curves. The maximum intensity of the Bragg peak is proportional to $1/\sin\theta_B$, being larger at small angles. The width of the peak varies in the opposite sense, being larger at higher angles and varying as $1/\cos\theta_B$. The integrated intensity of the peak is therefore proportional to $1/\sin 2\theta_B$. (ii) The second factor is dependent on the number of crystallites reflecting at a particular Bragg angle. Even though the crystallites are distributed randomly, and the normals to the planes are evenly distributed over an imaginary sphere around the sample (at an angle $(90^\circ - \theta_B)$), the *fraction* of the total normals is not. The number of crystallites favourably oriented is proportional to $\cos\theta_B$. (iii) The third effect comes from the fact that in Debye-Scherrer mode we are not sampling the full cone of diffracted intensity and as such the intensity in the forward and backwards directions is greater than that from $2\theta = 90^\circ$. We thus have to scale the intensities by $1/\sin\theta_B$. In combination, these factors give an overall

correction

$$L = \frac{1}{4 \sin^2 \theta \cos \theta} \quad (2.25)$$

P, Polarisation Correction

When an X-ray beam is diffracted, the reflected beam is polarised. This arises because the X-ray beam is a form of electro-magnetic radiation of high frequency which forces electrons also to oscillate in the plane perpendicular to the beam direction. When $2\theta=90^\circ$, the polarisation is complete. Generally the polarisation correction is of the form

$$P = \cos^2 \mu + \sin^2 \mu \cdot \cos^2 2\theta \quad (2.26)$$

where the angle μ is the angle of polarisation in the diffracted beam measured away from the initial polarisation direction. For a non-polarised beam, μ is uniformly distributed so the expectation values of $\cos^2 \mu$ and $\sin^2 \mu$ are $\langle \cos^2 \mu \rangle = \langle \sin^2 \mu \rangle = 1/2$.

For electrons of light elements or in the outer shells of heavier elements, the interaction energy with the nucleus is low and the natural resonance frequency of these electrons is lower than the radiation frequency. This is not necessarily the case for interior shell atoms of heavy elements where the binding energy is close to, or larger than that of the radiation. The resulting complex modification of the scattering is known as *anomalous dispersion* (see §2.2.3 *Scattered Amplitude*).

E, Extinction

Extinction results in a decrease of observed scattered intensity and arises for perfect crystals. It is separated into *primary* and *secondary* forms.

Primary extinction is caused by diffracted waves which are Bragg reflected back into the crystal from exactly the same family of planes that caused the diffraction. The GSAS[103] and FULLPROF[104] programs are both equipped to analyse this phenomenon though it has not been used in this thesis. A correction[105] based on spherical grains of diameter D , is given by a multiplication of the peak intensity by $(1 + x)^{-1/2}$, where

$$x = (3/4)^2 (NF\lambda D)^2 \quad (2.27)$$

N is the number of unit cells in the crystal and F the structure factor per unit cell. This has been extended to include Bragg and Laue components[106].

Secondary extinction is from strongly diffracted waves reducing the intensity of incoming radiation, so not all parts of the sample receive the full incident intensity. Generally this effect decreases with the volume of the crystal, and is seldom used for powders.

A, Absorption

Again, this correction is dependent upon the scattering geometry and sample shape, though it can be excluded from calculations of flat plate geometries due to equal but opposing effects[107]. It results from absorption of the initial beam within the sample itself so that a capillary in Debye-Scherrer mode has less intensity at low scattering angles. The difference in absorption between high angle and low angle reflections decreases with the linear absorption coefficient, μ . The absorption factor, $A(\theta)$, for a cylinder is the integral over the cross-section of $\exp(-\mu x)$, where x is all path lengths within the sample. An empirical solution for weak absorbers with neutrons or X-rays

in Debye-Scherrer geometry is given by

$$A(\theta) = e^{(-T_1\mu\lambda - T_2\mu\lambda^2)} \quad (2.28)$$

with T_1 and T_2 are functions of $\sin\theta$ [108, 109].

O, Preferred Orientation

Most crystallites do not exhibit a spherical habit but tend to have a definite shape, dependent upon cleavage or growth mechanisms. When powders are compacted into a holder or laid upon a surface, the crystallites tend to orientate with a preferred crystallographic direction. In extreme cases, the habits can be platelets or needles and a diffraction pattern can have low or even no intensity for specific families of planes. For capillaries, this effect can be reduced by spinning the sample about its axis during acquisition. The effect is also less evident with neutrons where larger sample volumes are used and the tendency for crystallites to align is reduced. Rietveld initialised a correction function of the form[110]

$$O_h = e^{-G\alpha_h^2} \quad (2.29)$$

where α is the acute angle between the scattering vector and the normal to the crystallites. G is a refinable parameter, and is a measure of the halfwidth of the assumed Gaussian distribution of the normals around the preferred orientation direction.

Both GSAS[103] and FULLPROF[104] use a formulation based on that of Dollase[111] and March[112] which covers both Debye-Scherrer or Bragg-Bretano geometries *and* platey or needle habits.

$$O_h = (G^2 \cos^2 \alpha_h + \sin^2 \alpha_h / G)^{-1.5} \quad (2.30)$$

with the correction only applied to the fraction of the sample that is textured.

V, Peak Shape

For constant wavelength neutrons and X-rays an excellent and widely used function is the pseudo-Voigt[113], whereas TOF diffraction patterns can be fitted by Gaussians convoluted with exponentials to characterise asymmetric tails[114]. The pseudo-Voigt function, V , is a simple addition of 2θ dependent Gaussian and Lorentzian peaks

$$V = \eta.L(2\theta, \Gamma) + (1 - \eta).G(2\theta, \Gamma) \quad (2.31)$$

where the Lorentzian component is given by

$$L(2\theta, \Gamma) = \frac{\Gamma}{2\pi} \left(\frac{1}{(\Gamma/2)^2 + (2\theta - 2\theta_h)^2} \right) \quad (2.32)$$

and the Gaussian one by

$$G(2\theta, \Gamma) = \frac{1}{\sqrt{2\pi}\sigma^2} e^{-\frac{(\theta - 2\theta_h)^2}{2\sigma^2}} \quad (2.33)$$

Γ is the total FWHM:

$$\Gamma = \sqrt{5}\Gamma_g^5 + 2.69269\Gamma_g^4\gamma + 2.42843\Gamma_g^3\gamma^2 + 4.47164\Gamma_g^2\gamma^3 + 0.07842\Gamma_g\gamma^4\gamma^5 \quad (2.34)$$

and η depends[102] upon Γ and the Lorentzian coefficient (γ) through

$$\eta = 1.36603(\gamma/\Gamma) - 0.47719(\gamma/\Gamma)^2 + 0.11116(\gamma/\Gamma)^3 \quad (2.35)$$

The Gaussian FWHM:

$$\Gamma_g = \sqrt{8\sigma^2 \ln 2} \quad (2.36)$$

with σ and γ given by

$$\sigma^2 = U.\tan^2\theta + V\tan\theta + W + P/\cos^2\theta \quad (2.37)$$

$$\gamma = X/\cos\theta + Y\tan\theta \quad (2.38)$$

This neatly avoids the need for a convolution of the two components in a true Voigt function and provides an excellent description of most data.

Improvements in this basic pseudo-Voigt model are needed in cases where the peak shape is not symmetrical due to axial divergence, as exemplified by the low-angle tails observed in the data from the BM16 diffractometer at the ESRF. Such a function has been incorporated into both GSAS[103] and FULLPROF[104] where the only extra parameters are related to the sample height, detector size and sample-to-detector distance[115], which are essentially known and should be considered constants for most diffractometers with only slight divergence. Asymmetry for neutron diffractometers has been expressed as a sum of Gaussians[116] and in certain cases¹⁸ the use of the axial divergence function[115] above is recommended.

Whatever function is chosen to represent the data, there is always a truncation of the peak range. For a Gaussian peak, a cutoff of $3\times\text{FWHM}$ includes more than 99% of the profile area. For Lorentzians, the equivalent value is 63%, due to the longer tails. GSAS[103] works in a slightly different way here, and cuts the peaks at a percentage of the maximum peak intensity, typically 0.05%.

F_{hkl} , Structure Factor

The structure factor brings the contents of the unit cell into the equation

$$F_{hkl} = \sum_{i \text{ atoms}}^{unit \text{ cell}} f_i e^{2\pi i \mathbf{h} \cdot \mathbf{x}_i} e^{-2\omega} \quad (2.39)$$

where the sum over all atoms, i , takes into account the fractional occupancies and the Debye-Waller temperature factor (§2.2.3 *Scattered Amplitude*) for each atom with

¹⁸e.g. for the D2b diffractometer at the ILL.

fractional coordinates \mathbf{x}_i , contributing to reflection \mathbf{h} . The basis and Bravais lattice can result in the structure factor having zero magnitude for certain reflections and results in systematic absent reflections.

2.5.2 Structure Refinement

Structural refinements from powder diffraction data are divided into two parts: (i) one attempts to find the crystal system and (ii) to find the contents of the unit cell and determine the correct space group. Thanks to the aid of various computer programs¹⁹ the derivation of a symmetry system and initial unit cell parameters, via Eqn.2.13, is usually a matter²⁰ of accurately measuring the d -spacing of Bragg reflections and choosing the crystal class that is the best fit to the data. If one is lucky, as it is often the case in the high symmetry structures adopted by fullerenes, then immediate indexing can be performed by comparison to other known structures. At this point, a comparison of predicted peaks²¹ with the observed data or a Le Bail refinement within a specific space group can give clear indications that one is indeed in the correct 'ball park'. Systematically absent reflections give information about the appropriate space group and can limit the choice to one space group or its sub-groups.

Structural refinements can be easy, difficult or impossible. If similar fullerides exist, one could start by trying their space groups and the corresponding fulleride orientations/disorder as starting models. If not, a wise placement of spherical shells²² (to replace the C_{60} s) within the cell and any other ions on high symmetry sites so the correct stoichiometry is kept, can give excellent starting ideas. The final structure

¹⁹TREOR (Werner *et. al.* 1985), DICVOL Louer and Vargas 1982), ITO(Visser 1986)

²⁰Unless there are severe overlapping reflections and/or other impurity phases present.

²¹DRAGON[117]

²²see programs PROFIL[118] and FULLPROF[104]

must have the correct orientational order of the C_{60} units. This can be achieved by hand, with step-by-step rotations of C_{60} about a high-symmetry axis (note: this will probably reduce the symmetry of the system) so as to cover all symmetry related orientations possible. Care must be also taken that the correct space group is indeed used; for instance, it could be difficult to distinguish Ba_4C_{60} in the space groups $Immm$ or $Pnmm$ as the difference is just a 90° rotation of the body-centred fulleride unit that is a weak scatterer in comparison to barium. Finally, a decomposition of the powder diffraction pattern into integrated intensities can lead to a solution by *ab initio* methods.

2.5.3 Rietveld Refinement

The basis of the Rietveld method is to minimise, by least-squares methods, the difference between observed, $y_i(obs)$, diffraction pattern intensity and a calculated, $y_i(calc)$, pattern intensity for all i steps. The calculated pattern consists of the summation of the intensities of neighbouring Bragg reflections for point i and of a background function²³. The Bragg intensity is calculated (to a given cut-off limit) from an initial structural model that is to be refined²⁴, machine dependent parameters and finally all factors affecting the peak shape functions. The first use of this method was by Rietveld himself for the case of neutron powder data[110] with minimisation of

$$S_i = \sum_i w_i (y_i(obs) - y_i(calc))^2 \quad (2.40)$$

²³The background can be taken by hand, Fourier filtered or fitted by such functions as polynomials.

²⁴The structure must have the correct space group, and approximately correct structural parameters as the Rietveld method does not allocate observed intensity to particular Bragg reflections or resolve overlapping peaks in advance.

where the residual, S_i , is the quantity minimised and $w_i = 1/y_i(obs)$. This process adjusts refinable parameters until the residual is minimised achieving a best fit. The best fit is dependent on the adequacy of the starting model and may be affected by correlations of parameters. Care must be taken to avoid falling in a local minimum. Various reliability R -factors have been defined to help judge the goodness-of-fit. These are, however, faceless numbers and must be considered in a visual context of the actual fit and with the aid of a difference plot between observed and calculated profiles.

One of the mathematically more meaningful R -factors that best reflects how well the refinement is proceeding is the *weighted profile* one: this reflects how well the structural refinement accounts for both large and small Bragg peaks across the pattern

$$R_{wp} = \left(\frac{\sum_i w_i |y_i(obs) - y_i(calc)|^2}{\sum_i w_i y_i^2(obs)} \right)^{\frac{1}{2}} \quad (2.41)$$

An additional reliability R -factor can be defined when the profile is not weighted:

$$R_p = \frac{\sum_i |y_i(obs) - y_i(calc)|}{\sum_i y_i(obs)} \quad (2.42)$$

The *Bragg/Integrated Intensity* R -factor is closest to those used in single crystal work, though it is biased towards the model relating the quality of fit on structural parameters. It is defined as

$$R_I = \frac{\sum_k |I_k(obs) - I_k(calc)|}{\sum_k I_k(obs)} \quad (2.43)$$

with the intensity assigned to the k^{th} Bragg reflection after the refinement.

The *expected* R -factor measures the statistical quality of the data and takes into account the number of variables used. It is defined as

$$R_{exp} = \left(\frac{N - P + C}{\sum_i w_i y_i^2(obs)} \right)^{\frac{1}{2}} \quad (2.44)$$

with N = number of observations, P = number of refinable parameters and C = number of constraints used. The fit can be monitored by the agreement χ^2 factor which approaches unity when the agreement between observed and calculated profiles is satisfactory.

$$\chi^2 = \left(\frac{R_{wp}}{R_{exp}} \right)^2 = \frac{\sum_i |y_i(obs) - y_i(calc)|^2}{N - P + C} \quad (2.45)$$

A value of χ^2 of less than 'one' is an indication that there are more parameters in the model than justified by the quality of the data. Low counting times or low R_{wp} ²⁵ factors can also reduce the χ^2 value.

A simple fitting routine is the Pawley[119] method. This is an intensity matching method that requires no structural information but a starting space group, lattice parameters and peak shape function. The resulting refinement is performed in much the same way as for the Rietveld refinement. Problems occur in low and high symmetry structures where there may be unavoidable overlap of non-equivalent reflections. The Le Bail[120] method is an improvement on the Pawley extraction technique and has been incorporated into Rietveld refinement programs which initially use an arbitrary set of structure factors and only those parameters of the non-structural model refined. The integrated intensities are extracted in the same manner as the original Rietveld program, though equipartition of the overall intensity for overlapping peaks is done. This is an excellent way to start a structure refinement as it gives initial lattice constants and peak shape parameters.

²⁵Achievable via the *fitting* of an intense background by a simple function.

2.5.4 Inelastic Scattering

During a neutron scattering experiment, an incident neutron beam impinges on a sample with an initial wavevector \mathbf{k}_0 and energy $\frac{1}{2}mv_0^2$. After being scattered from the sample the final wavevector is \mathbf{k}_f with a corresponding energy, $\frac{1}{2}mv_f^2$, that makes an angle of 2θ to the initial wavevector. The scattering vector \mathbf{Q} is the difference between the final and initial wavevectors, $\mathbf{Q} = \mathbf{k}_f - \mathbf{k}_0$.

The parameters of interest relate to the energy and momentum transfered between the neutron and sample. Momentum transfer for the neutron is given by $\hbar\mathbf{Q} = \hbar(\mathbf{k}_f - \mathbf{k}_0)$, but since we will only be concerned with polycrystalline samples, the measured quantity is the magnitude of \mathbf{Q} , given by the equation $Q^2 = k_f^2 + k_0^2 - 2k_f.k_0 \cos 2\theta$. The sizeable momentum transfer in the scattering process is a consequence of the fact that the neutron wavelength is of the order of interatomic spacing. The energy transfer is given by $\hbar\omega = \frac{\hbar^2}{2m}(k_f^2 - k_0^2)$.

General

The partial differential cross-section of an array of N scatterers is given by the double differential cross-section[84]

$$\frac{d^2\sigma}{d\Omega dE'} = \frac{N\sigma}{4\pi} \frac{k_f}{k_0} S(\mathbf{Q}, \omega) \quad (2.46)$$

with a factorisation into the scattering cross-section σ , which describes the neutron-atom interaction, and the scattering function $S(\mathbf{Q}, \omega)$ which depends on the solid state properties of the sample (though strictly only for a monatomic sample). This factorisation can be carried further into a separation of elastic and inelastic scattering, each with coherent and incoherent parts (if isotope and/or spin inhomogeneities are

present).

$$\frac{d^2\sigma}{d\Omega dE'} = \frac{N\sigma}{4\pi} \frac{k_f}{k_0} \left[b_{coh}^2 S_{coh}(\mathbf{Q}, \omega) + [b_{inc}^2 S_{inc}(\mathbf{Q}, \omega)] \right] \quad (2.47)$$

In the case of coherent scattering the waves of scattered neutrons may interfere constructively. Neutrons that are scattered elastically and coherently can produce a diffraction pattern of the crystal structure of the material. In the case of inelastically scattered neutrons, the coherent part of the scattering observes collective excitations which involve many atoms or molecules in the system, such as phonons.

To derive a complete expression for the coherent one-phonon interaction cross-section, certain assumptions are made[84]. These include the harmonic behaviour of the time dependent atomic motion of an array of N atoms that gives rise to a phonon branch of frequency, ω_s , and wavevector q . For cases that have several atoms for the basis of the unit cell (volume v_0), one obtains:

$$\left(\frac{d^2\sigma}{d\Omega dE'} \right)_{coh}^{+1phon} = \frac{N\sigma}{4\pi} \frac{k_f(2\pi)^3}{k_0} \sum_{s\mathbf{G}} \frac{F^2(\mathbf{Q}, \mathbf{q})}{2\omega_s} \times \left[\langle n(\omega_s) \rangle + \frac{1}{2} + \left(-\frac{1}{2}\right) \delta(\omega \pm \omega_s) \delta(\mathbf{Q} \pm \mathbf{q} - \mathbf{G}) \right] \quad (2.48)$$

with the summation taken over all phonon modes and all phonon wavevectors, s , and all reciprocal lattice vectors, \mathbf{G} . The first term in square brackets is the Bose occupation factor for up $(e^{\frac{-\hbar\omega}{k_B T}} - 1)^{-1}$ or down $(e^{\frac{-\hbar\omega}{k_B T}} + 1)^{-1}$ scattering of the neutron, while the delta functions ensure conservation of energy and momentum. $F(\mathbf{Q}, \mathbf{q})$ is called the dynamic structure factor:

$$F(\mathbf{Q}, \mathbf{q}) = \left| \sum_d \frac{b_d}{\sqrt{M_d}} e^{i\mathbf{k} \cdot \mathbf{r}_d} [\mathbf{Q} \cdot \boldsymbol{\varepsilon}(\mathbf{q})] e^{-W_d(\mathbf{q})} \right| \quad (2.49)$$

that contains the sum over all basis atoms at positions \mathbf{r}_d in the unit cell. b_d is the scattering length and M_d is the mass of the d^{th} particle. The Debye-Waller attenuation

factor is given by e^{-2W} . The polarisation term $[\mathbf{Q} \cdot \boldsymbol{\varepsilon}(\mathbf{q})]$ is the only selection rule. It allows the possibility of using an oriented single crystal sample and collecting data with the Q -vector aligned parallel or perpendicular to the displacement vectors of the vibrational modes under study. In this way, one can separate longitudinal and transverse phonon modes in a neutron scattering experiment. For polycrystalline samples the cross-section must be averaged over all orientations of Q . For a cubic lattice, the polarisation term averages to $1/3(Q^2)$.

In summary, for a given phonon of frequency, ω_s and wavevector \mathbf{q} , the scattering function contains two delta functions in ω - and \mathbf{q} -space for phonon creation and phonon annihilation processes. The cross-section is proportional to $1/\omega_s$, and hence so is the measured intensity in an inelastic neutron scattering experiment. Further attenuation to the signal comes from the Debye-Waller factor.

The neutrons are not confined to interacting only with phonons. At low enough temperatures fullerene units perform librational motion about well defined axes within quasi-equilibrium orientations which give rise to librational peaks observed a few meV away from the elastic peak. As the temperature is increased, a structural phase change is often witnessed, to orientationally disordered structures, where the C_{60} units undergo rapid rotational diffusion (isotropic to a good approximation). This diffusion causes a broadening of the elastic peak and the appearance of a quasi-elastic component, with a FWHM dependent on the diffusion constant of the rotational motion. In the case of uncorrelated rotational diffusion of the fullerene molecules about their fixed centres, the powder-averaged rotational component of the scattering

function can then be expressed as a sum of Lorentzians[20]

$$S_r(q, \omega) = \sum_{l=1}^{\infty} a_l (2l+1) j_l^2(QR) \frac{1}{\pi} \frac{\tau_l}{1 + \omega^2 \tau_l^2} \quad (2.50)$$

where

$$\tau_l = \frac{1}{l(l+1)D_r}, \quad (2.51)$$

j_l is a spherical Bessel function, R is the radius of the C_{60} molecule and D_r is the rotational diffusion constant. The coefficients a_l are linear combinations of Legendre polynomials. Just as with symmetry-adapted spherical-harmonics (§1.1), only those terms with values of $l=6, 10, 12, 16, 18$ and 20 , for which a_l takes the values $6.3, 224, 31, 123, 496$ and 90 , contribute to the scattering.

For incoherent scattering, the one-phonon double differential cross-section is approximately equal to the phonon density of states albeit weighted by scattering power, σ/m^{26} . The fullerene compounds are dominated by the scattering due to the 60 carbon atoms per fullerene unit and as such the scattering is almost completely coherent. Luckily in powders the orientational disorder present causes the smearing of the sharp coherent peaks, and on average the coherent cross-section is equivalent to the the incoherent cross-section[121].

$$\int_{Q_{min}}^{Q_{max}} \frac{d^2 \sigma_{coh}}{d\Omega dE'} dQ = \int_{Q_{min}}^{Q_{max}} \frac{d^2 \sigma_{incoh}}{d\Omega dE'} dQ \quad (2.52)$$

Hence we need to average over all orientations and \mathbf{Q} values in the Brillouin zone. This is easily achieved with the large unit cell fullerene systems as $2\pi/a \approx 0.5 \text{ \AA}^{-1}$ and the Q -range sampled with the IN6 instrument is 0 to 2.5 \AA^{-1} (at 4.12 \AA). The

²⁶See Lovesey[84] vol.1, p.123, Eqn.4.92

larger the $|\mathbf{Q}|$ chosen, the better will be the orientational and Brillouin zone average at the expense of an increase of multiphonon contributions²⁷.

The spectral distribution function $P(\bar{\alpha}, \beta)$ [122] is given by

$$P(\bar{\alpha}, \beta) = 2\beta \sinh\left(\frac{\beta}{2}\right) \left(\frac{S(Q, \omega)}{\bar{\alpha}}\right) \quad (2.53)$$

where $S(Q, \omega)$ is the uncorrected symmetrised scattering law and the dimensionless variables α and β are related to momentum and energy transfer through

$$\bar{\alpha} = \frac{\hbar^2 Q^2}{2MkT}, \quad \beta = \frac{\hbar\omega}{kT} \quad (2.54)$$

where M is an average atomic mass. The spectral distribution function can be corrected for multiphonon contributions[123] (see the next section). This results in a corrected one-phonon spectral distribution $P_1(\bar{\alpha}, \beta)$ from which the generalised or 'neutron-weighted' phonon DOS is obtained:

$$G(\omega) = \exp(2W)P_1(\bar{\alpha}, \beta) \quad (2.55)$$

where $\exp(-2W)$ is the Debye-Waller attenuation factor. In the general case for a polyatomic system with n atoms of species i , concentration c_i , in the unit cell the *neutron-weighted* density of states is defined as

$$G(\omega) = \frac{\bar{M}}{\bar{\sigma}} \sum_{i=1}^n c_i \frac{\sigma_i}{m_i} g_i(\omega) \quad (2.56)$$

where \bar{M} is the average atomic mass and $\bar{\sigma}$ is the average atomic cross-section.

Bragg reflections can also be obtained from an integration of the scattering law over all energy transfers, $S(\mathbf{Q}) = \int S(\mathbf{Q}, \omega) d\omega$ and is the time averaged view as in elastic diffraction. Note, this gives the *total* scattering that includes incoherent scattering, giving a background to the low resolution diffraction data.

²⁷The one phonon scattering process increases in intensity with momentum transfer as Q^2 , but the two phonon interaction goes as Q^4 .

Data Reduction

In the course of an experiment, the number of neutrons detected within a time channel of width Δt , by a detector covering a solid angle $\Delta\Omega$, during a period T , with a sample illuminated by a beam of Φ_0 incident neutrons per second (energy E_0) can be expressed as

$$\Delta n_s = \Phi_0 T \Delta\Omega \cdot F(E) \cdot A(E) \cdot \left(\frac{\delta^2 \sigma}{\delta\Omega \delta t} \right) \Delta t \quad (2.57)$$

$F(E)$ is the detector efficiency and $A(E)$ is the energy dependent self-attenuation factor. For vanadium, an integration over all energies results in the same formula, but the scattering law is assumed to reduce to the standard Debye-Waller factor as vanadium is a completely incoherent scatterer and scatters equally over all Q . After normalisation and correction for energy dependent factors, as described in the next section, the output is

$$y(E) = \frac{N_s \sigma_s}{N_v \sigma_v} S(\mathbf{Q}, \omega) \quad (2.58)$$

with the number of atoms, N , in the neutron beam. Subscripts, s and v , label the sample and vanadium, respectively.

An empty can is collected and a transmission factor is used to crudely subtract a background ²⁸ from all runs to be further used in the data reduction. The transmission is equivalent to assuming the relative amounts of the beam scattered before and after the sample. Numerically this is equivalent to removing a fraction of the empty can from the spectrum. The geometrical shape of both the vanadium and sample has a correction for self attenuation in the form of a slab at an angle to the incoming beam or as a cylinder. In principle the correction should be made at all angles and for all

²⁸Hence all data analysis programs also come with a background subtraction option.

final neutron energies, though in general the energy dependence of the correction is smooth and the number of parameters can be reduced.

Vanadium is used as a calibrant for the relative efficiencies of detectors with respect to each other. Two corrections are made to the vanadium spectra: (i) a Debye-Waller factor correction taken to be proportional to temperature and (ii) a self attenuation correction. The correction for detector efficiencies depends on the detectors used and the energies of the incoming neutrons. Both IN6 and IN5 use ^3He detectors and involve a combination of absorption of the detector walls ($\mu \propto \lambda$ for $\lambda > 4\text{\AA}$) and by the ^3He itself.

At the I.L.L., there is a data reduction program (INX) available [124] that is used to perform these corrections and determine the elastic peak position to define zero energy transfer. The data can be grouped in terms of channels (normal 'binning') or constant energy widths. Q dependence of the scattering can be monitored by grouping angles. For GDOS determination, all angles²⁹ are used whereas for librational and quasi-elastic spectra, all elastic peaks are excluded.

Analysis

In fitting $S(Q, \omega)$ data to various combinations of Gaussian and Lorentzian shape functions one can use most scientific spreadsheet packages nowadays, but I have consistently used PROFIT[125] in this thesis. For this program, a resolution file is needed and this can be either a vanadium run or any sample run that represents the resolution of the instrument (e.g. 0.14- 0.17 meV at the elastic line on IN6). The input parameters are the elastic position and intensity, the inelastic peak positions,

²⁹Excluding bad detectors.

their intensity and half-width at half maximum, flat and sloping backgrounds and the temperature. The fitting is weighted so as to include the detailed balance correction, $S(-Q, \omega) = \exp(-\hbar\omega/k_B T)S(Q, \omega)$. To view the spectra at different temperatures, on the same scale, the Bose factor must be removed. The scattering law is related to the imaginary part of the dynamic susceptibility, χ'' via;

$$S(Q, \omega) = \frac{1}{\pi} \frac{1}{e^{\frac{\hbar\omega}{k_B T}} - 1} \chi'' \quad (2.59)$$

for neutron energy gain. In the limit of $T \gg \hbar\omega$, $e^{-x} - 1 = -x$, enabling a scaling to an arbitrary temperature T_0 by multiplying each spectrum at temperature T , by a factor $\frac{T_0}{T}$. In this way, the spectra retain their relative error bars. Alternatively, the direct Bose factors can be used to scale the spectra and will give absolutely correctly scaled results.

For the transformation of the spectral distribution function to the one-phonon counter part, a corrections for multi-phonon contributions has to be applied to eliminate distortions in the measured distribution function that increase with temperature and Q . Multiphonon events arise from sample-neutron interactions where two or more excitations are created/destroyed. Mathematically, when identifying the inelastic, incoherent partial differential cross-section with the phonon density of states³⁰, exponential terms are neglected if they are greater than first order (i.e. equivalent to $P_1(\bar{\alpha}, \beta)$). It is the consideration of higher order exponential terms that constitutes our multiphonon correction.

To obtain the experimental $G(\omega)$ for mainly coherent scatterers the use of the following iterative procedure: given a user defined number of vibrational modes,

³⁰Equation 4.80 of Lovesey[84], p. 121

characterised by 5 parameters each, i. e., the scatterer mass contributing to the vibrational peak, the peak maximum frequency, the peak intensity, the cutoff frequency (after which the peak contributes nothing to the spectrum) and the shape of the peak in the spectrum, the theoretical density of states is calculated. From this, both the Debye-Waller factor and the multiphonon contribution to the spectrum are estimated and used to evaluate a model $P(\bar{\alpha}, \beta)$ which is fitted to the experimental one. After varying the initial parameters until a satisfactory fit is achieved, the process is inverted and $G(\omega)^{31}$ is obtained after subtraction of the multiphonon contribution and a background. A version of the FITDEN5[126, 127] program was adapted for UNIX use with a graphics option for the purposes of this thesis.

2.5.5 μ^+ SR

After implantation of the muon into the sample, it thermalises at an interstitial site and in the presence of local fields, B , it will precess³² at the Larmor frequency, ω_μ , where ω_μ is

$$\omega_\mu = \gamma_\mu B \quad (2.60)$$

and the muon gyromagnetic ratio, γ_μ , is 85.1648 kHz G⁻¹. The muon decays with a lifetime of 2.2 μ s into a positron, neutrino and an antineutrino. The decay is characterised by the positron being emitted preferentially along the polarisation direction of the μ^+ spin. The probability that a positron of energy within $d\varepsilon$ of ε is emitted

³¹Normalised so that the integral is equal to unity. To compare different spectra with different maximum frequencies, a common limit to the spectra must be used so they have the same normalisation factors.

³²Diffusion of the muon is negligible at low temperatures and it is assumed that any local deformation of the lattice where the muon comes to rest will not seriously alter the sample properties over the length scales of interest.

within $d\theta$ of θ , the angle with respect to the μ^+ spin at the time of decay, is

$$dW = \tau_\mu^{-1} \left[1 + \frac{2\varepsilon - 1}{2 - 2\varepsilon} \cos \theta \right] \varepsilon^2 (3 - 2\varepsilon) d\varepsilon d \cos \theta, \quad (2.61)$$

where ε is the positron energy relative to the maximum positron energy of 52.3 MeV[128]. Typically no energy discrimination of the emitted positrons is performed, resulting in a theoretical maximum for the asymmetry parameter, $A = \frac{2\varepsilon-1}{2-2\varepsilon}$, of $\frac{1}{3}$. In practice the maximum asymmetry is dependent on thickness, geometry and material for both target and detectors and is usually calibrated using a silver sample.

The arrangement of positron detectors can be seen in Fig.2.13 with the detectors labelled U (up), D (down), L (left), R (right), F (forward) and B (backward) according to the convention of looking along the beam. For longitudinal- or zero field measurement the unrotated beam polarisation points toward the B counter, while for transverse field measurements, in the spin-rotated mode, the polarisation points towards the U counter.

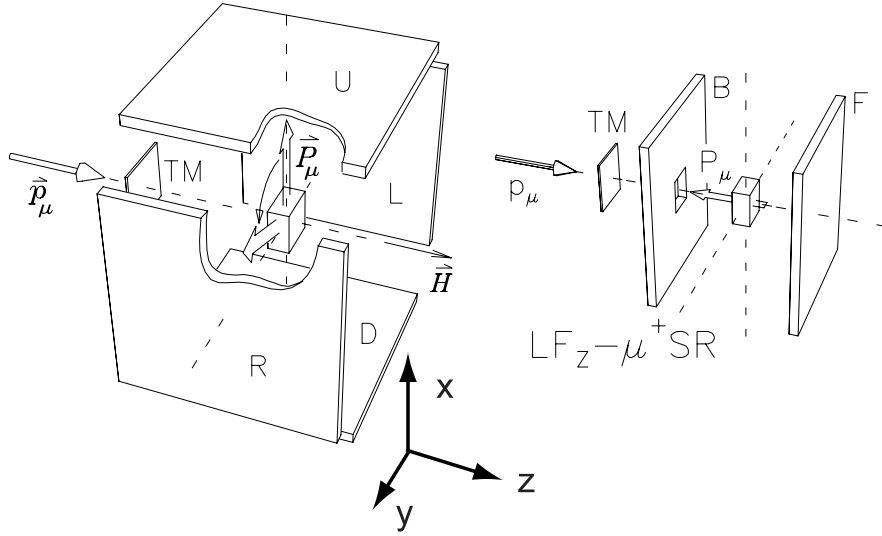


Figure 2.13: Detector arrangements for experiments in; (left) transverse applied field and (right) zero- and longitudinal applied field[129].

Histogramming of the time differences between muon implantation into the sample and the detection of the decay positron in a counter is given by:

$$N(t) = N_0 e^{-t/\tau_\mu} [1 + A \mathbf{P}_\mu(t)] + b_0 \quad (2.62)$$

where N_0 is an overall normalisation, b_0 is a time-independent background and A is the experimental initial asymmetry. $\mathbf{P}_\mu(t)$ is the time dependent muon polarisation function that is also known as the asymmetry. The time evolution of the polarisation vector is given by[128]

$$\mathbf{P}_\mu(t) = [P_x(0) \cos(\omega_\mu t + \phi), P_y(0) \sin(\omega_\mu t + \phi), P_z(0)] \quad (2.63)$$

with ϕ the angle between the initial muon spin direction and the direction of the detectors, with the initial muon spin polarisation given by $[P_x(0), P_y(0), P_z(0)] = [P(0) \cos \phi, P(0) \sin \phi, P(0)]$. The coordinate system x, y, z is defined in Fig.2.13.

In a typical μ^+ SR experiment, three configurations are used.

(i) Transverse field (TF). In this configuration a magnetic field is applied normal to the muon spin polarisation. The detectors U , D and R (on the GPS instrument at PSI) are used to record the Larmor precession signal as a function with time. For the case that $P(0) = P_x(0)$ and $P_y(0) = P_z(0) = 0$, Eqn.2.62 becomes:

$$N_T(t) = N_0 e^{-t/\tau_\mu} [1 + A P_x(0) \cos(\omega_\mu t + \phi)] + b_0 \quad (2.64)$$

this is analogous to a free-induction decay after a $\pi/2$ radio frequency pulse is applied to nuclear spins with the NMR technique.

(ii) Zero field (ZF). No external field is applied in this configuration. The time dependence of polarisation, $P(0) = P_z(0)$, is monitored in the F and B counters.

(iii) Longitudinal field (LF). In this configuration an external field is applied parallel

to the initial muon spin polarisation direction, hence $P(0) = P_z(0)$ and $P_x(0) = P_y(0) = 0$. F and B counters are used to detect the decay positrons. Here, Eqn.2.62 becomes:

$$N_L(t) = N_0 e^{-t/\tau_\mu} [1 + AP_z(0) \cos \phi] + b_0 \quad (2.65)$$

Both $P_z(0)$ and $P_x(0)$ in the previous two equations may also have a time dependence if depolarisation processes take place within the target sample. Dephasing can occur due to interaction of the muon spin with local static fields, whereas relaxation of the muon spins occurs by interactions with fluctuating fields. The introduction of a relaxation function, $G(t)$, into Eqn.2.64 and Eqn.2.65 describes the time dependence of the depolarisation. Hence, for a transverse field configuration we have

$$N_T(t) = N_0 e^{-t/\tau_\mu} [1 + AP_x(0)G_x(t) \cos(\omega_\mu t + \phi)] + B, \quad (2.66)$$

and for a longitudinal configuration we have

$$N_L(t) = N_0 e^{-t/\tau_\mu} [1 + AP_z(0)G_z(t) \cos \phi] + B \quad (2.67)$$

It is this depolarisation function that holds the key to the physics of the interaction of the muon with the system. In a sample with a coexistence of phases with differing magnetic properties, $G(t)$ is the sum of all the depolarisation functions weighted by their corresponding volume fractions. One typically extracts the asymmetry and fits the time dependence to an appropriate model. A number of functions are available that correspond to particular models and experimental configurations. We shall now examine some of these functions.

Depolarisation in a Transverse Field

With the application of an external field, the muon will precess due to a vector sum of the external and internal fields (Fig.2.14). Depolarisation may occur if there is a distribution of fields at the muon sites and hence a distribution of Larmor precession frequencies causing a loss of coherence amongst the precessing muons, in analogy to T_2 relaxation in NMR. The depolarisation function is derived from the experimental signal by taking the real part of the Fourier transform of the frequency distribution, $F(\omega_\mu)$

$$G_T(t) = \frac{2}{\pi} \int_0^\infty F(\omega_\mu) \cos(\omega_\mu t) d\omega_\mu \quad (2.68)$$

In practice it is often assumed that $F(\omega_\mu)$ is approximately a Gaussian distribution.

$$F(\omega_\mu) = \frac{1}{\sigma\sqrt{2\pi}} e^{-\frac{(\omega_\mu - \omega_0)^2}{2\sigma^2}} \quad (2.69)$$

with σ^2 the variance (width) of the frequency spectrum and ω_0 the average Larmor precession frequency. The depolarisation function is then a Gaussian (Fig.2.14) of the form:

$$G_T(t) = e^{-\frac{\sigma^2 t^2}{2}} \quad (2.70)$$

It can be further shown[131] that the variance can be related to the spread of the z -component of the nuclear dipole moments, ΔB_z through:

$$\langle \Delta B_z^2 \rangle = \frac{\sigma^2}{\gamma_\mu^2} \quad (2.71)$$

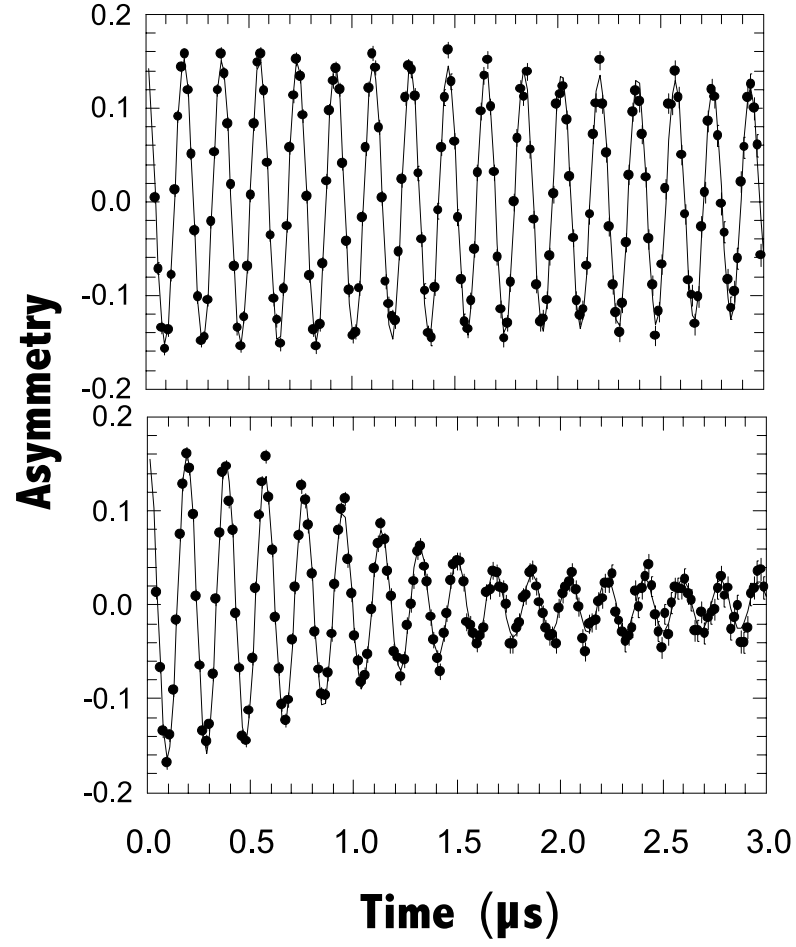


Figure 2.14: Muon spin rotation in an applied transverse field for a none depolarising sample (top) and with a gaussian depolarisation function (bottom)[130].

It can be further shown[131] that the variance can be related to the spread of the z -component of the nuclear dipole moments, ΔB_z through:

$$\langle \Delta B_z^2 \rangle = \frac{\sigma^2}{\gamma_\mu^2} \quad (2.72)$$

Depolarisation in Zero Field

With no external field, the depolarisation function of the muon spin occurs due to the internal local fields of the sample, whether they be static or dynamic in their origins. The time evolution of the depolarisation function is extracted from the ratio $\frac{N_F(t)-N_B(t)}{N_F(t)+N_B(t)}$, for the forward and backward detectors.

In the case of a Gaussian distribution of randomly oriented static internal fields, H_i of width, Δ , the field distribution is described by:

$$f(H_i) = \frac{1}{\sqrt{2\pi}} \frac{\gamma_\mu}{\Delta} e^{-\frac{\gamma_\mu^2 H_i^2}{2\Delta^2}} \quad (2.73)$$

along the cartesian i directions. The ensemble average of the polarization in the z direction leads to the Kubo-Toyabe relaxation function[132]

$$G(t) = \frac{1}{3} + \frac{2}{3}(1 - \Delta^2 t^2)e^{-\frac{1}{2}\Delta^2 t^2} \quad (2.74)$$

The Kubo-Toyabe function is characterised by an initial Gaussain-like damping, at short times, followed by a recovery of the asymmetry to a value approaching $\frac{1}{3}$ at longer times (see Fig.2.16). The $\frac{1}{3}$ component represents the average number of muons that have stopped where the local field is parallel to the initial muon direction. After long times only those muons with their local fields in this configuration will remain polarised.

For a case where the local field at the muon site is the result of fluctuating moments, the depolarisation is described by the *dynamic* Kubo-Toyabe function[131, 128]. This function is calculated from a model where (i) the local field at the muon site changes abruptly, while retaining the Gaussian distribution of fields, with no correlation of the local field before and after the event and (ii) the rate of moment fluctuations is ν . In effect this function can be described as a static Kubo-Toyabe

function until a change of field at the muon site takes place. At this instant the time evolution of the depolarisation restarts with a reduced amplitude as not all muons feel a change of their local field at the same time. The total dynamic function is a summation of contributions from the muons which still retain their original local field up to a certain time, and those which have undergone one or more changes in their local field. There is no general analytical expression for the dynamic Kubo-Toyabe and it is tabulated as a function of the fluctuation rate of internal fields. The function is illustrated in Fig.2.15.

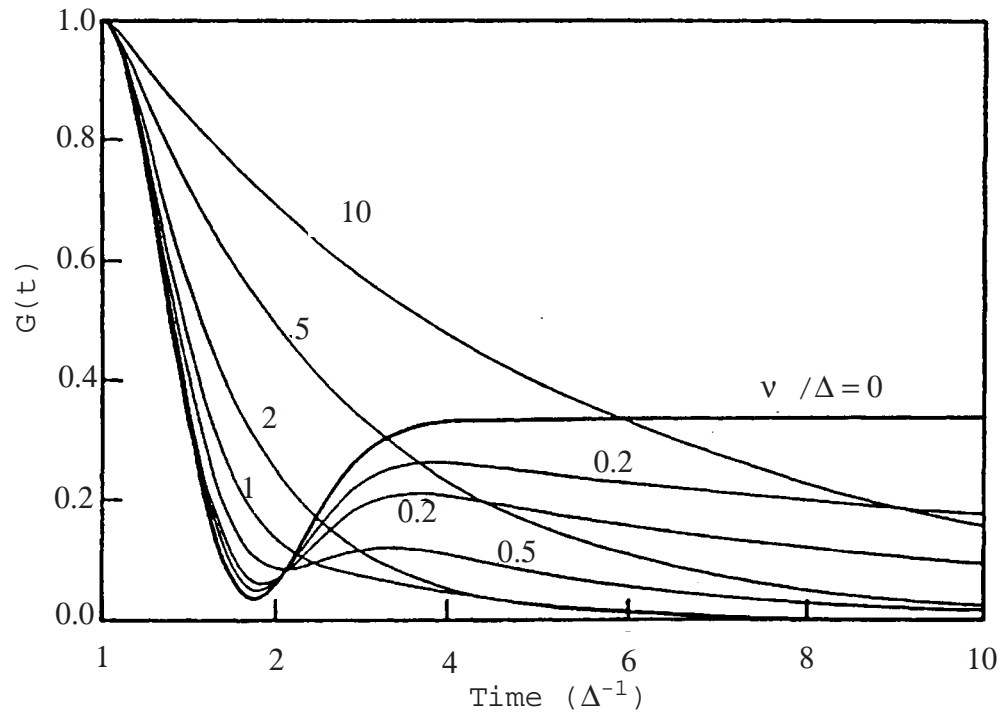


Figure 2.15: Muon spin depolarisation in zero field. The rate of fluctuation of internal fields, ν starts from the static case ($\nu = 0$).

Depolarisation in a Longitudinal Field

Depolarisation in zero field is due to the muon spin interacting with internal fields of both static and dynamic origin. The two sources of relaxation/dephasing are not distinguishable by a ZF measurement. However, application of a strong longitudinal field parallel to the initial μ^+ spin polarisation will decouple the μ^+ spin from the static internal fields (Fig.2.16). Any remaining depolarisation must then be due entirely to fluctuating moments within the sample. This is a convenient method of separating the static and dynamic components of the local magnetic field experienced by the muons. The relaxation processes that occur at high applied longitudinal fields are of the T_1 type.

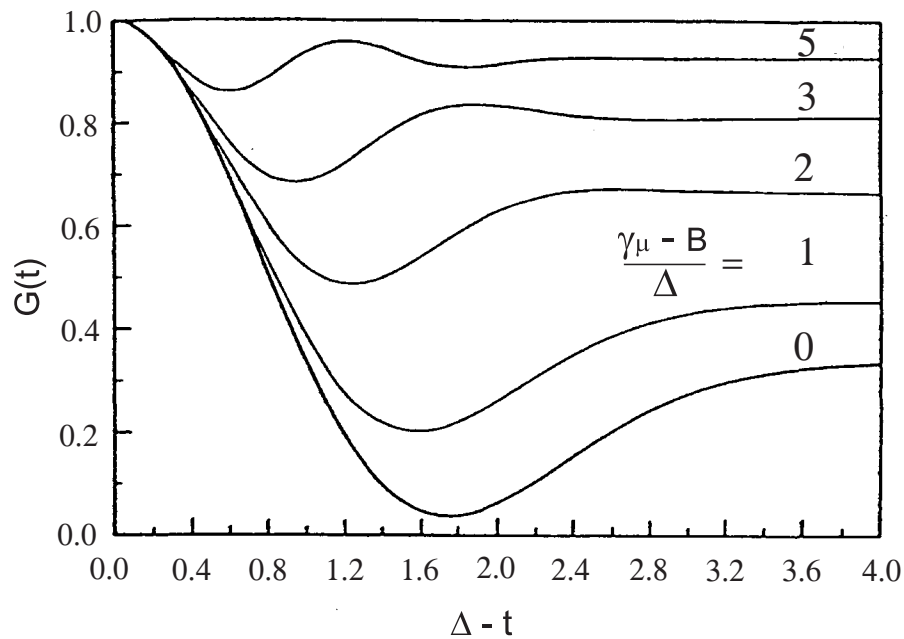


Figure 2.16: Muon spin depolarisation as derived for static random fields. The Kubo-Toyabe function is plotted for the zero field case and a series of longitudinal applied fields.

Chapter 3

Azafullerene

3.1 Introduction

Doping fullerenes can be done in several ways. One can envisage adding species to the interstitial sites, or even inside the fullerene cages themselves. Alternatively the molecular potential can be modified by removing a carbon atom from the cage and replacing it with an element like boron or nitrogen. Synthesis and isolation in bulk quantities of the nitrogen substituted fullerene solid[133] has afforded us the opportunity to characterise this heterofullerene and commence the search for C_{60} variants that are expected to have interesting solid state properties. As a result of exchanging a carbon for a trivalent nitrogen, the $C_{59}N^{\cdot}$ radical is found to rapidly dimerise yielding the $(C_{59}N)_2$ dimer or abstract a hydrogen atom to produce the 'stable'[134] monomeric hydroazafullerene, $C_{59}HN$ [135]. As-isolated $(C_{59}N)_2$ is insulating and diamagnetic with only a weak electron spin resonance signal, indicating the presence of one unpaired electron for roughly every 250 molecules[136]. The as-prepared $(C_{59}N)_2$ solid, before the recrystallisation stage, consists principally of a poorly crystalline

phase with only a minor crystalline component[136]. Electron diffraction reveals hollow particles on the lengthscale of 1 to 10 μm that are hierarchically organised as the paper title eloquently expressed 'Spheres of Spheres of Azafullerene in the Solid State'. The crystalline part gave an indexable X-ray diffraction pattern (space group $P6_3/\text{mmc}$ or one of its subgroups) with the c/a ratio close to the ideal close packing ratio ($\sqrt{8/3}$) with a close interball spacing of ~ 9.8 Å.

Recrystallisation from CS_2 leads to a well crystalline material ¹ with hexagonal lattice constants, $a = 9.97$ Å and $c = 16.18$ Å at ambient temperature. No evidence for a phase transition was found between 60 and 500 K using synchrotron X-ray diffraction. Rietveld refinements on this data were not able to decide on the correct orientation of the dimer within the unit cell, but refined quite well using spherical shells as a first approximation for the individual cages[137] with incorporation of ~ 0.5 CS_2 solvent molecules per formula unit (also detectable in solid state ^{13}C NMR measurements). Further, sublimation of the recrystallised solid affords pristine $(\text{C}_{59}\text{N})_2$; crystallography and direct evidence for dimerisation will be discussed in this chapter.

Redox potentials via cyclic voltammetry imply both $(\text{C}_{59}\text{N})_2$ and C_{59}HN should be more easily reduced than C_{60} [135]. The facile synthesis of $\text{K}_6\text{C}_{59}\text{N}$ [138] lead to the observation that the conductivity of $\text{K}_6\text{C}_{59}\text{N}$ is larger than that shown by both the wide gap insulators, A_6C_{60} , and pristine $(\text{C}_{59}\text{N})_2$. Band structure calculations suggest the likelihood of metallicity, though $\text{K}_6\text{C}_{59}\text{N}$ exhibits a Curie-like magnetic behaviour consistent with the presence of unpaired spins.

Further doping as a function of alkali metal radius has been performed by K. Kordatos[139]. $\text{K}_6\text{C}_{59}\text{N}$ and $\text{Rb}_6\text{C}_{59}\text{N}$ adopt body centred cubic structures (space

¹It also tends to stick to surfaces making it difficult to work with.

group $Im\bar{3}$) that are essentially isostructural with the corresponding salts of C_{60} , K_6C_{60} and Rb_6C_{60} . However, $Na_6C_{59}N$ adopts a hexagonal close packed structure that is essentially identical to that of the hexagonal form of azafullerene, except that the c/a ratio has now reached the ideal value of 1.633, as expected for the presence of monomeric azafulleride ions. The interball separation expands considerably upon intercalation (from 9.97 Å to 10.26 Å) consistent with the presence of Na clusters in the octahedral interstices. The observed structural behaviour is reminiscent of the situation encountered for the Na_6C_{60} salt[71] which is not body centred like K_6C_{60} and Rb_6C_{60} ; instead it adopts a face centred cubic structure like C_{60} .

3.2 High Pressure Experiments

High pressure powder synchrotron X-ray diffraction on a crystalline solid azafullerene sample was used to probe the diversity of bonding interactions present in this material with pressure tuning of the intermolecular distances.

The azafullerene sample[133] used in the present study was prepared from a "holey bucky"[140] with purification by HPLC on a Cosmosil "Buckyprep" column using toluene as eluent. Solid $(C_{59}N)_2$ was obtained from a solution in *o*-dichlorobenzene (ODBC) which was evaporated rapidly to dryness in a rotary evaporator. Recrystallisation from a CS_2 solution led to a highly crystalline material which was subsequently degassed under dynamic vacuum ($\sim 10^{-6}$ Torr) at 140 °C for 12 hours. The sample was loaded into a DAC equipped with 600 μm diamond faces and a gasket preindented to 80 μm thickness with a 200 μm diameter hole. Cryogenic nitrogen loaded in the DAC at 77 K was used as pressure medium. A pressure of ~ 0.5 GPa was applied in order to seal the gasket hole. The image plate system of beamline ID9 at the ESRF

was used to monitor the diffraction patterns as a function of isothermal pressure up to 21.8 GPa. Pressure was monitored by the ruby fluorescence method (§2.4.1). A monochromatic beam was produced by a Si(111) monochromator in Bragg geometry with vertical focussing with a Pt coated Si mirror to a beamsize of $70 \times 30 \mu\text{m}^2$. A silicon standard was employed for wavelength calibration, whence the wavelength refined to 0.5739 Å. Masking of ruby spots and integration of the two-dimensional images were performed with the FIT2D² program.

Fig.3.1 illustrates the pressure evolution of the powder diffraction profiles of solid $(\text{C}_{59}\text{N})_2$ between 0.8 and 21.8 GPa at room temperature[141]. At low pressures, ten sharp reflections are clearly resolved and indexed on a hexagonal cell. The observed extinction conditions ($hh2\bar{h}l : l = 2n$ only) are consistent with space group $P6_3/mmc$ or one of its subgroups. Accurate lattice parameters may be extracted from these clean, high symmetry diffraction data by employing the model independent Le Bail pattern decomposition technique. Two typical refinements are shown in Fig.3.2 at 0.8 and 18.5 GPa with the derived PROFIL[118] parameters given in Table.3.1. The only parameters that are variable, besides a manually chosen smooth background function, are the lattice constants, zero point error, profile peak shape parameters and an intensity scale factor. Due to the high symmetry of the crystal and to the fact that most peaks are resolved, the fits are excellent, with agreement factors $R_{wp} \sim 10\%$ and $R_{exp} \sim 0.4$. The high statistics for each data point makes their corresponding errors extremely small and any deviations of the calculated profile from the observed data are severely punished in terms of statistics and the error-weighting. The result is a

²The beam centre was refined using a Gaussian fit of the residual beam image after brief exposure at the beginning of the experient, with tilt plane and angle being refined from the 'circular' powder rings.

χ^2 of the order of 10^3 .

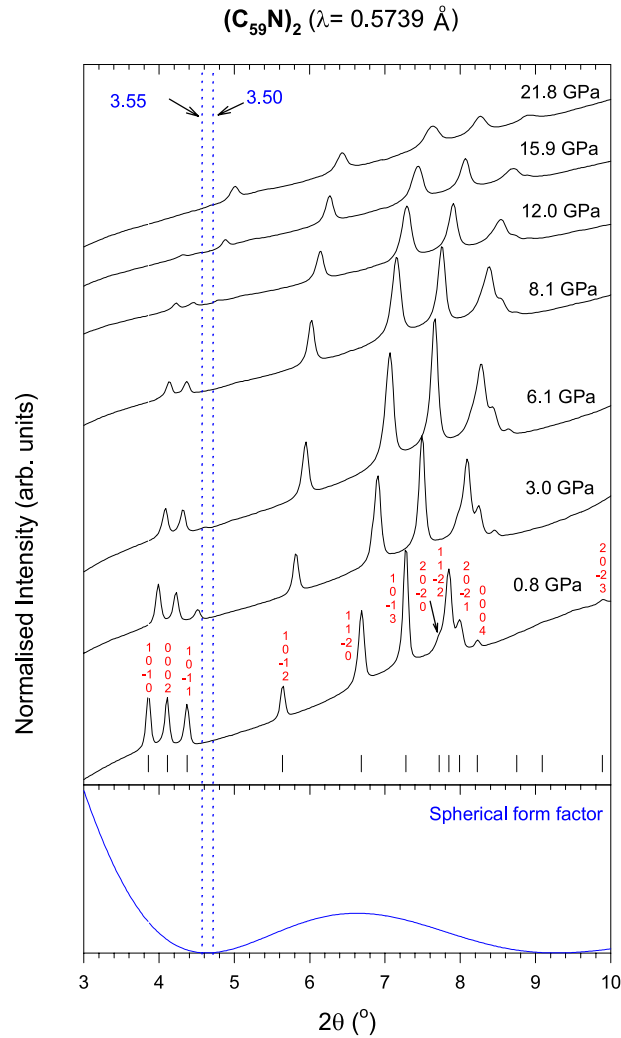


Figure 3.1: Pressure variation of the X-ray diffraction patterns of solid $(\text{C}_{59}\text{N})_2$ at ambient temperature from 0.8 to 21.8 GPa ($\lambda = 0.5739 \text{ \AA}$). The observed reflections consistent with the hexagonal space group $P6_3/mmc$ are labelled (red) for the 0.8 GPa profile with the ticks below marking their positions. The bottom panel shows the calculated X-ray scattering form factor for a spherical molecule of radius $R = 3.55 \text{ \AA}$. The blue broken vertical lines mark the positions of the zero in the form factor for radii between 3.50 and 3.55 \AA .

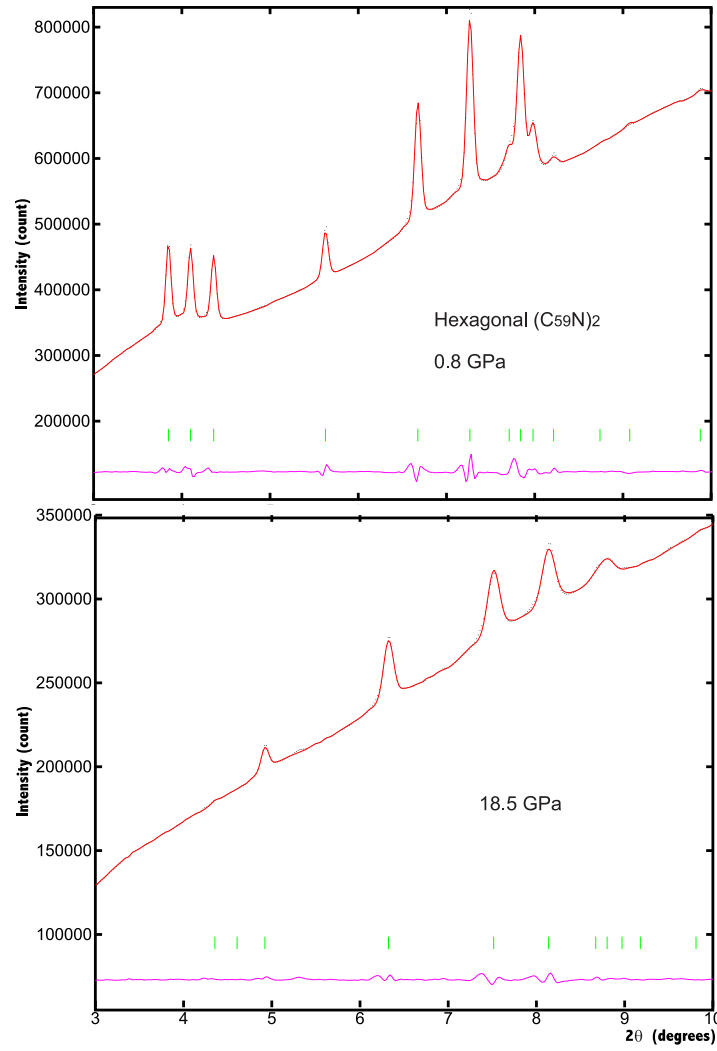


Figure 3.2: Le Bail pattern decomposition of one dimensional powder patterns of $(C_{59}N)_2$ at 0.8 and 18.5 GPa. Black dots represent observed data points, with the red line showing the best fit. A difference curve (observed - calculated) and green tick marks, giving reflection positions within space group $P6_3/mmc$, are shown below.

Table 3.1: Le Bail refinement parameters for $(\text{C}_{59}\text{N})_2$ at 0.8 and 18.5 GPa

Value	0.8 GPa	18.5 GPa
$a / \text{\AA}$	9.9156(6)	8.8095(30)
$c / \text{\AA}$	16.122(3)	14.416(15)
R_{wp}	9.55	11.02
R_{exp}	0.2	0.6
$\lambda / \text{\AA}$	0.5739	0.5739
$\Delta_{2\theta} / ^\circ$	-0.012(1)	0.044(7)
W	0.0293(5)	9.7×10^{-5}
V	-0.016(2)	-0.0241(3)
U	1.36(2)	6.16
η	0.085	0.036

As the applied pressure increases, the reflections exhibit a monotonic shift towards high angles, accompanied by a gradual increase in peak line width. Outside of the 2θ range shown in the above figures, there is also a contribution to the powder pattern from solidified nitrogen crystals at about ~ 12 GPa. Even though the solidification induces non-hydrostatic components in the stress tensor, it is still a very soft solid and uniaxial compression is minimal up to 20 GPa. Evidence for this is seen in the gradual collapsing together of the two distinct R_1 and R_2 ruby resonance lines, as the pressure is increased towards 20 GPa.

The most striking feature of the data in Fig.3.1 is the behaviour of the low-angle peak triplet which indexes as $(10\bar{1}0)$, (0002) and $(10\bar{1}1)$ in the hexagonal cell. As we were taking this data, it appeared that a phase transition to another structure was occurring in the vicinity of 3 GPa, as the intensity of the $(10\bar{1}1)$ reflection gradually vanishes with increasing pressure. However, as the pressure increases still further and the peaks continue to shift to high 2θ , the intensities of the (0002) and $(10\bar{1}0)$

reflections also successively diminish, while the $(10\bar{1}1)$ peak re-emerges with a non-zero intensity. This effect was first seen early in the history of C_{60} under pressure[142]. The (200) reflection for the fcc C_{60} solid has zero intensity at low pressures as result of its accidental coincidence at the same d -spacing with a node in the X-ray scattering form factor of the hollow spherical molecules. The intensity changes in the low-angle region of solid $(C_{59}N)_2$ can be interpreted along the same lines.

Assuming the $C_{59}N$ units can be modelled, to a first approximation, as hollow spherical shells of uniform charge density ρ and radius R , the molecular form factor, $f(\theta)$ is given by

$$f(\theta) = \rho \frac{\sin(2\pi R/d)}{2\pi R/d} \quad (3.1)$$

where d is the lattice spacing. The lower panel of Fig.3.1 shows the 2θ dependence of the X-ray scattering form factor, $[f(\theta)/\rho]^2$, which is zero at $\sim 4.6^\circ$ for a $C_{59}N$ molecule of $\approx 3.55 \text{ \AA}$ radius. Generally the 'nth' node in the function $[f(\theta)/\rho]^2$ occurs when $2R = nd$. Even though the $C_{59}N$ units should display a non-uniform charge density distribution on their shell[133, 143, 134], orientational disorder effects are expected to smooth out such deviations. The observed behaviour of the low angle peaks can then be understood, as they successively pass through the zero in the form factor and re-emerge on it high angle side. Such an interpretation is consistent with a compressibility of the molecule significantly lower than that of the bulk solid.

The top panel of Fig.3.3 shows the pressure evolution of the hexagonal lattice constants a and c . A similar monotonic dependence is exhibited by both, revealing absence of substantial anisotropy in the compressibility along a and c . A measure of the anisotropy can be arrived at from considering the pressure dependence of the (c/a) ratio (lower panel Fig.3.3). A somewhat less compressible $(C_{59}N)_2$ structure

along the c axis is revealed, as (c/a) smoothly increases from an initial value of 1.623 at ambient pressure towards 1.634(1) at 6.74 GPa and then remains essentially unchanged to the highest pressure of the present experiment. These observations can be rationalised if the bridging C-C bonds of the $(\text{C}_{59}\text{N})_2$ dimers are exactly inclined with neither the basal plane nor the unique axis of the hexagonal cell. The smaller observed compressibility along the c axis is consistent with the C-C bonds inclined to it at a smaller angle than that formed with the basal plane.

Efforts to incorporate this view into Rietveld refinements of high resolution synchrotron powder data have used a model, consistent with this interpretation, where the dimer bonds are aligned parallel to the $(\frac{1}{3}, \frac{2}{3}, \frac{1}{2})$ direction. The inclination of the dimer bond is 56.3° out of the ab plane, with a corresponding projection of the dimer centre-to-centre distance on to the c axis of 8.093 Å, at ambient pressure. The limiting value for the (c/a) ratio reached at ~ 6.5 GPa is close to the ideal ratio of 1.633, expected for a hexagonal close packed structure, that would imply little difference between intradimer and interdimer distances. This is exactly in the pressure range that the interdimer centre-to-centre distances are compressed to values of 9.332(8) Å (at 6.12 GPa), essentially identical to those found for bonded pairs in the Rietveld analysis of the sublimed material §3.3 and by density-functional-based calculations[134].

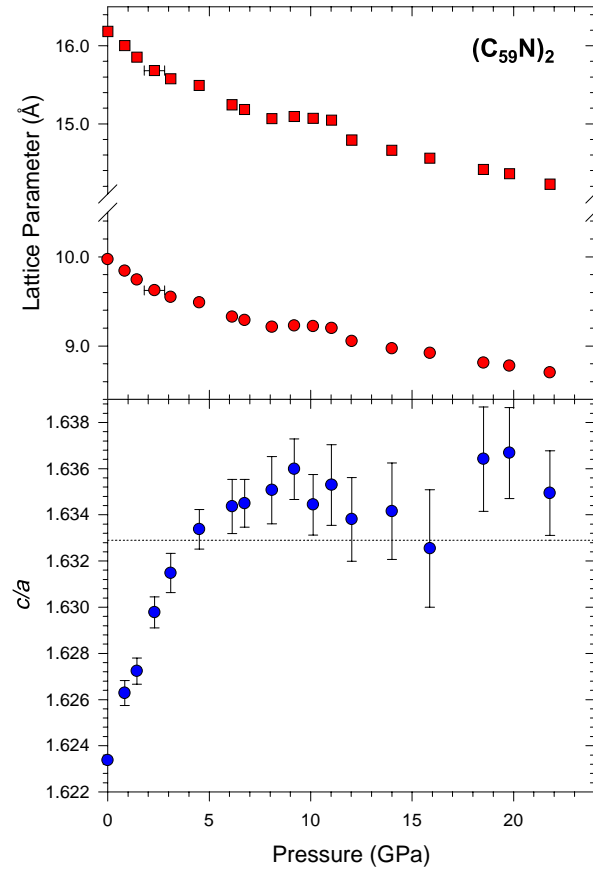


Figure 3.3: Pressure variation of (top, red) the hexagonal lattice constants a and c and (bottom, blue) the (c/a) ratio. The broken line marks the ideal (c/a) ratio for a hexagonal-close-packed structure.

Raman scattering of the strongest $H_g(7)$, $A_g(2)$ and $H_g(8)$ intramolecular phonon

modes of $(C_{59}N)_2$ under pressure also observes a modification of their pressure coefficient of frequency through the 6.5 GPa region[144]. These modes have large components of their eigenvector directed along the dimer bridge and reflect the fact that above this pressure the compression is no longer being dominated by the van der Waals component of the solid.

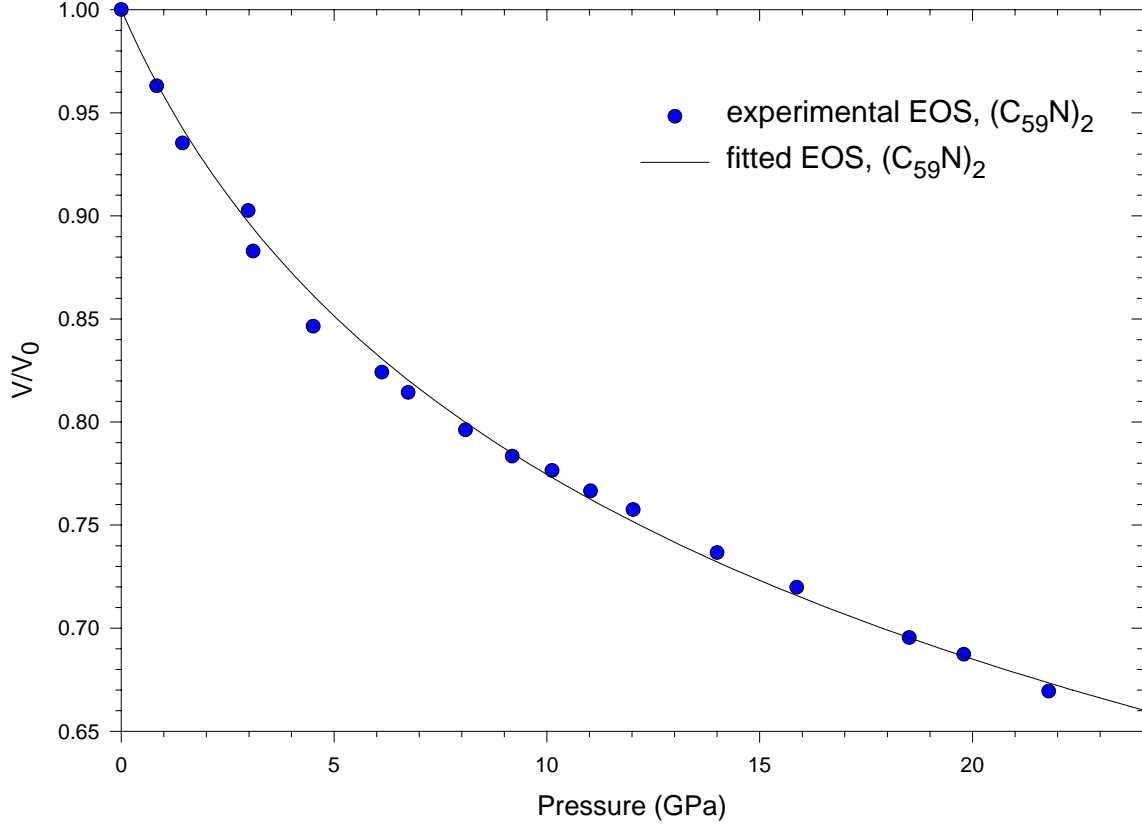


Figure 3.4: Pressure dependence of the hexagonal unit cell volume normalised to ambient pressure. The solid line is a fit to the semi-empirical second order Murnaghan equation of states.

The ambient pressure equation of state for solid $(C_{59}N)_2$ is shown in Fig.3.4 along

with a least-squares fit to the semi-empirical second order Murnaghan equation of states[145, 146].

$$P = \frac{3}{2}K_0 \left[\left(\frac{V_0}{V} \right)^{\frac{7}{5}} - \left(\frac{V_0}{V} \right)^{\frac{5}{3}} \right] \left[1 - \frac{4}{3} \left(4 - \frac{dK_0}{dP} \right) \left(\left(\frac{V_0}{V} \right)^{\frac{5}{3}} - 1 \right) \right] \quad (3.2)$$

The latter results in an atmospheric-pressure isothermal bulk modulus of $K_0 = 21.5(8)$ GPa (compressibility, $\kappa = 4.6(2) \times 10^{-2} \text{ GPa}^{-1}$) and a pressure derivative of $dK_0/dP = 4.2(1)$. The bulk modulus of azafullerene is only marginally larger than that measured for solid C_{60} [142] ($K_0 = 18.1(1.8)$ GPa) and implies a somewhat tighter crystal packing: the volume of the azafullerene unit cell is $\sim 98\%$ that of C_{60} at ambient pressure, increasing to $\sim 99\%$ at 20 GPa, implying stiffer nearest-neighbour bonds. The azafullerene units survive intact and their molecular bonding character is retained to pressures as high as 22 GPa.

3.3 Pure Azafullerene

Knowing that residual solvent helps stabilise the hexagonal form of C_{60} , it became increasingly important as the mass of partially solvated $(\text{C}_{59}\text{N})_2$ became manageable to try and remove that solvent. Sublimation of the sample was performed under dynamic vacuum ($\sim 10^{-6}$ Torr) at 500 °C for 12 hours. High resolution X-ray diffraction measurements on this sample, sealed in a thin-walled glass capillary 0.5 mm in diameter were performed at 278 and 500 K at the SRS Station 9.1, Daresbury Laboratory, U.K. Data were collected at a silicon refined wavelength of 0.8717 Å in the 2θ angular range 2 to 40°. Images of the Debye-Scherrer rings from the same sample were also recorded at 295 K on the Mar Research circular image plate system (diameter = 300 mm) on line A of the Swiss-Norwegian beamline at the E.S.R.F. One-dimensional

images were obtained after fitting the circular diffraction rings to calculate the image centre and tilts[98]. Images of a LaB_6 standard (space group $Pm\bar{3}m$, $a = 4.15695 \text{ \AA}$ at 295 K) were treated in the same fashion and later used to refine the wavelength to a value of $0.8736(3)$ with a zero point error of $-0.004(5)^\circ$. Data analysis was performed with the PROFIL suite of Rietveld programs, incorporating form factors for spherically disordered molecules and the Le Bail pattern decomposition technique.

The observed X-ray pattern at 278 K (shown as dots in Fig.3.5) reveals essentially no Bragg peaks above $2\theta_{max} \approx 20^\circ$ ($Q_{max} \approx 2.5 \text{ \AA}^{-1}$) at all temperatures. Most of the intensity is concentrated within clusters of peaks at $2\theta \sim 6^\circ, 10^\circ$ and 12° . These regions are precisely where one would expect the dominant peaks of a pseudo-cubic solid with lattice dimensions of the same order as C_{60} to be. These peaks are broad yet the instrumental resolution is sufficient to allow splittings to be observed, signifying a reduced crystal symmetry. An unusual feature is the observation of a significant peak on the leading edge of the $(111)_{cubic}$ reflection at $\sim 6^\circ$; we ascribe this to the presence of hexagonal stacking faults in the fcc parent structure, an interpretation that is confirmed by selected area electron diffraction patterns. This explanation has also accounted for a similar feature in the diffraction patterns of the higher fullerenes C_{70} [147] and C_{84} [148]. More important for this pattern is the occurrence of a superlattice peak at $\sim 3^\circ$ that indexes as $(\frac{1}{2}, \frac{1}{2}, \frac{1}{2})_{cubic}$ in the fundamental psuedo-cubic cell with lattice dimensions $a_0 \approx 13.9 \text{ \AA}$. This necessitates the existence of an enlarged unit cell along all three dimensions $(2a_0, 2a_0, 2a_0)$ or equivalently, a body-centred orthorhombic cell with dimensions $(\sqrt{2}a_0, 1/\sqrt{2}a_0, 2a_0)$, whence the superlattice peak indexes as $(101)_{orthorhombic}$. Unit cell parameters for the orthorhombic cell were extracted with the Le Bail pattern decomposition technique, employing space group $Bmmm$,

giving $a = 19.444(9) \text{ \AA}$, $b = 9.962(3) \text{ \AA}$, $c = 28.491(15) \text{ \AA}$. The resulting fit is shown in Fig.3.5 with a final $R_{wp} = 18.5\%$ and $R_{exp} = 4.6\%$. Peak parameters are $U = 0.19(5)$, $V = -0.12(2)$, $W = 0.026$ and $\eta = 0.42$.

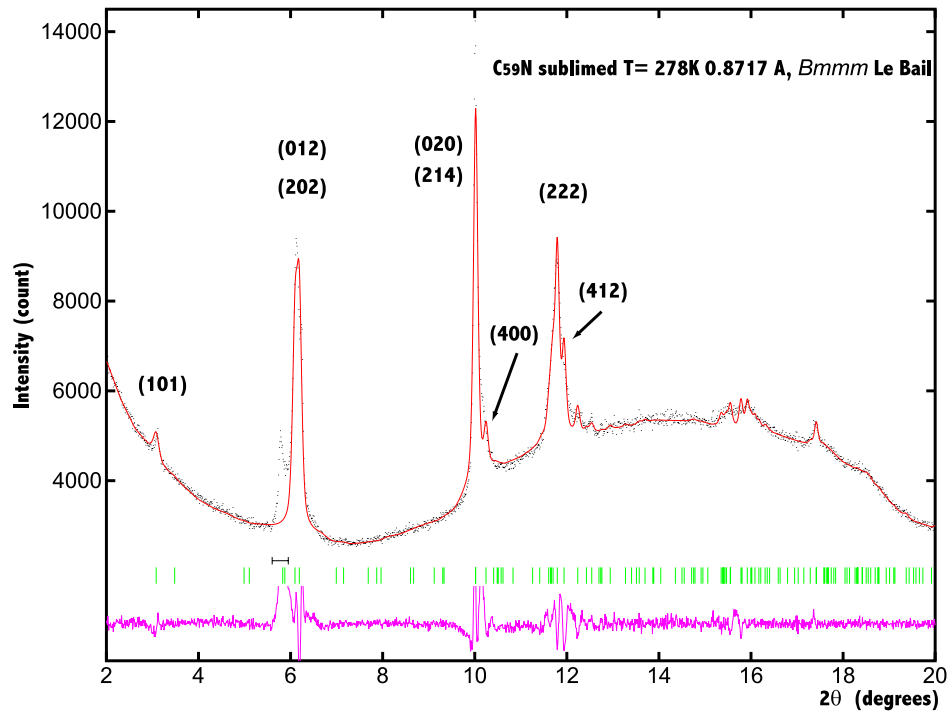


Figure 3.5: Measured synchrotron X-ray powder diffraction pattern (black points) of $(C_{59}N)_2$ in the range $2-20^\circ$ at 278 K ($\lambda = 0.8717 \text{ \AA}$). Le Bail pattern decomposition in space group $Bmmm$ gives the solid red line with the difference curve beneath. Vertical green marks indicate the positions of Bragg reflections for the orthorhombic cell, with the main peaks being labelled.

A strict constraint imposed by the observation of finite intensity for the $(101)_{orthorhombic}$ superlattice peak is that the $C_{59}N$ molecular units can no longer occupy the high symmetry ideal positions in the unit cell, thus precluding an undistorted monomeric

structure as this will result in negligible intensity at the $(101)_{orthorhombic}$ position. We therefore considered the possibility of relaxing the molecular positions by allowing adjacent molecules, considered in the first instance as quasi-spherical units of radius 3.55 Å, to move towards each other. Under these circumstances, however, orthorhombic crystal symmetry is not possible and, in the case of orientationally disordered C₅₉N units, it reduces to monoclinic. To help understand this transformation, Fig.3.6 shows the relationship between the orthorhombic and monoclinic unit cells. The orthorhombic a axis becomes the monoclinic c axis, while retaining an identity operation between the orthorhombic b axis and the monoclinic unique axis.

Trigonometry allows the calculation of the equivalent monoclinic lattice constants from those derived with the orthorhombic Le Bail refinement:

$$a_{monoclinic}^2 = \left(\frac{a_{orthorhombic}}{2} \right)^2 + \left(\frac{c_{orthorhombic}}{2} \right)^2 \quad (3.3)$$

$$\beta = \pi + \tan^{-1} \left(\frac{a_{orthorhombic}}{c_{orthorhombic}} \right) \quad (3.4)$$

Hence, $a_{monoclinic}$ = 17.25 Å, $b_{monoclinic}$ = 9.96 Å, $c_{monoclinic}$ = 19.44 Å and β = 124.31° at 278 K.

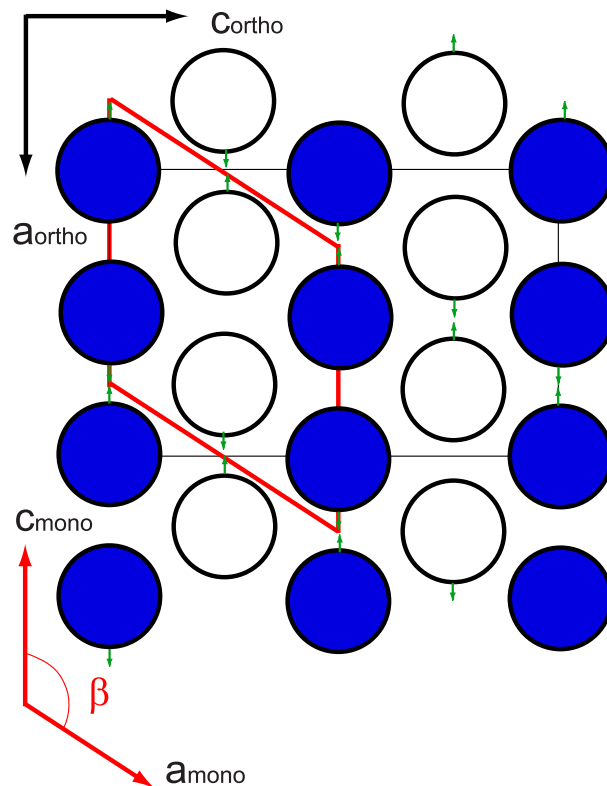


Figure 3.6: Relationship between the orthorhombic and monoclinic cells described in the text. The tiny green arrows indicate displacement directions of the C_{59}N units. White spheres are displaced by half a unit from the zero plane of the unit cell.

In this case allowing the spherical units to move along the c axis only, their optimal positions can be judged as a function of the goodness-of-fit factor, R_{wp} . Throughout this exercise peak profile parameters were fixed at the Le Bail values so as not to induce artificial changes in the profile fits apart from the effects of moving the molecular units in steps of 0.1 \AA . The best match is found to be for the spherical shell located at fractional coordinates $(0,0,0.242)$ as seen in Fig.3.7. These positions are consistent with a short intradimer centre-to-centre separation of 9.41 \AA along the

c axis. The other 11 nearest neighbour distances range between 9.81 and 10.11 Å, resulting in an average of 9.97 Å, only marginally smaller than the 10.02 Å distances in orientationally disorder fcc C_{60} . We have no *a priori* reason to just confine the displacements to the c axis and so we extended our search of the R_{wp} minimum to take into account a possible movement along the a axis. A slight improvement is obtained in the fit for a displacement of ~ 0.3 Å along a that translates into a larger centre-to-centre distance of 9.44 Å accompanied with a tilt about the c axis of 3.6° .

As we relaxed the azafullerene sphere from the $(0,0,\frac{1}{4})$ symmetry position, it became increasingly apparent that even though we were reducing R_{wp} significantly, we were fitting far too much of the powder pattern with the emphasis being to fit the more intense peaks and so not taking into account the real significance of the superlattice peak. An alternative approach was to reproduce the the intensity of the $(101)_{orthorhombic}$ peak normalised to the intensities of the peaks at $\sim 10^\circ$ and $\sim 12^\circ$. We used the PROFIL output from the above analysis for displacement along the c axis and found a best match of these peak intensities corresponding to a centre-to-centre distance of 9.41(1) Å, in good agreement with our R_{wp} minimisation. Table.3.2 collects the lattice constant information from the analysis of the diffraction data at the temperatures studied. No significant anisotropy in the thermal expansivity is observed.

Table 3.2: Structural data for solid $(C_{59}N)_2$ at different temperatures (space group $C2/m$)

T (K)	diffractometer	a (Å)	b (Å)	c (Å)	β ($^\circ$)
500	9.1(SRS)	17.312(6)	9.998(2)	19.524(8)	124.33(2)
295	SNBL(ESRF)	17.258(5)	9.968(3)	19.459(4)	124.32(2)
278	9.1(SRS)	17.250(7)	9.959(3)	19.445(8)	124.31(2)

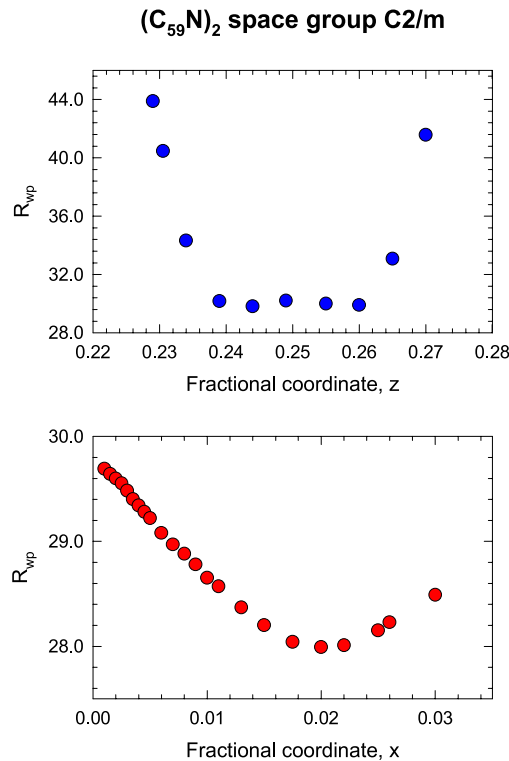


Figure 3.7: Minimisation of the goodness-of-fit factor R_{wp} for a Rietveld model of spherical C₅₉N units. The top panel refers to the initial movement of the spheres along the monoclinic c axis with a minimum at 0.242. Further minimisation was performed by subsequently allowing movement along the a axis (lower panel).

While this does not constitute a thorough modelling of the data, the observation of only a single superlattice peak and the lack of significant intensity in the diffraction profile at high Q severely hinder more detailed analysis. We note that there exists good agreement between the intradimer separation derived in the present

analysis using the spherical approximation for each monomer and that obtained from optimisation of the molecular structure of $(\text{C}_{59}\text{N})_2$ (9.31 Å) by density-functional calculations[134]. These reveal a gain in energy of ~ 18 kcal/mol upon dimerisation and sizeable changes in the vicinity of the bridges. The dimer comprises of two units linked by one long C-C bond (1.61 Å) with the nitrogen atoms in a *trans* configuration.

Hence, we proceeded by replacing the quasi-spherical units employed so far in the refinements by the optimised molecular structure, with the principal molecular axis, defined by the centres of the two monomers aligning with the c axis. In the general case, the appropriate monoclinic space group is $P2_1/a$. We first explored the effects of orientational order by allowing the dimer to rotate about its principal axis. This affects the calculated intensity of the superlattice peak very little with changes evident only at higher Bragg angles. We employed the extraction of intensity from individual reflections technique described above, to find the best orientation that reproduced the relative intensities of peaks compared to the $(001)_{\text{monoclinic}}$. Fig.3.8 shows the normalised intensities for the overlapping $(\bar{3}12)$ and (112) at $\sim 10^\circ$ and $(\bar{2}22)$ and (022) at $\sim 12^\circ$ as a function of the rotation angle about the principal axis of the dimer. The starting orientation is defined from the optimised structure with the bridging carbon lying on the z axis with the 6:6 bond that connects the bridging carbon to the nitrogen lying in the bc plane³. Blue diamonds show normalised intensities for the equivalent peaks extracted by the Le Bail method (which performs an equipartition of intensities over the pairs of reflection). The best agreement with the rotated data is at 90° that essentially places a hexagon-hexagon (6:6) fusion perpendicular to the

³This places the nitrogen outside of the traditional unit cell in the $-b$ direction.

b -axis (Fig.3.9) for the two orientational images of the dimer; in this special case, the appropriate monoclinic space group is $C2/m$. Superimposing these two merohedral images is again consistent with $C2/m$, but in the absence of well-resolved data at higher Q , we cannot exclude additional orientational fluctuations.

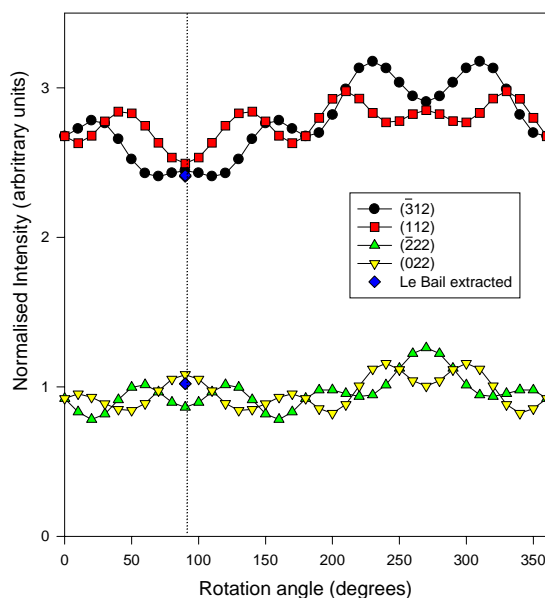


Figure 3.8: Extracted reflection intensities normalised to the superlattice peak for rotations about the dimeric principal axis of $(C_{59}N)_2$. The best match of the ratio of intensities to those of the Le Bail extracted peaks is found at an angle of 90° (dotted line) from the starting position. This essentially places the 6:6 N-C(bridging) bond in the ac plane.

Finally the dimers were allowed to rotate about the b axis. Even small tilts are now found to drastically alter the calculated intensity of the superlattice peak as witnessed by direct manipulation of the dimer and online monitoring of the calculated diffraction pattern within the CERIUS[149] modelling package. The best agreement is achieved for an anticlockwise rotation of $\sim 1.5^\circ$. Refinements performed with a 1.5° and 2° rotation only degrade the fit by $\delta R_{wp} = 0.4\%$ but the decrease in R_i is more significant at 1.1%. The (101) basal plane projection of the resulting structure is shown in Fig.3.9. with the Rietveld refinement of the 278 K data in Fig.3.10 and the corresponding structural parameters in Table.3.3.

In this configuration the principal molecular axis lies on the ac -plane and is inclined at an angle of $\sim 1.5^\circ$ with the c axis; the bridging C-C bond also lies on the ac plane and is inclined at an angle of $\sim 3.8^\circ$ from the c axis. It is also noteworthy that, consistent with the more compact, less compressible structure of azafullerene, the adopted interdimer contacts lead to a shortest C-C intermolecular distance of 3.02 Å, somewhat shorter than the equivalent one in the orientationally ordered form (space group $Pa\bar{3}$) of C_{60} (3.12 Å)[14].

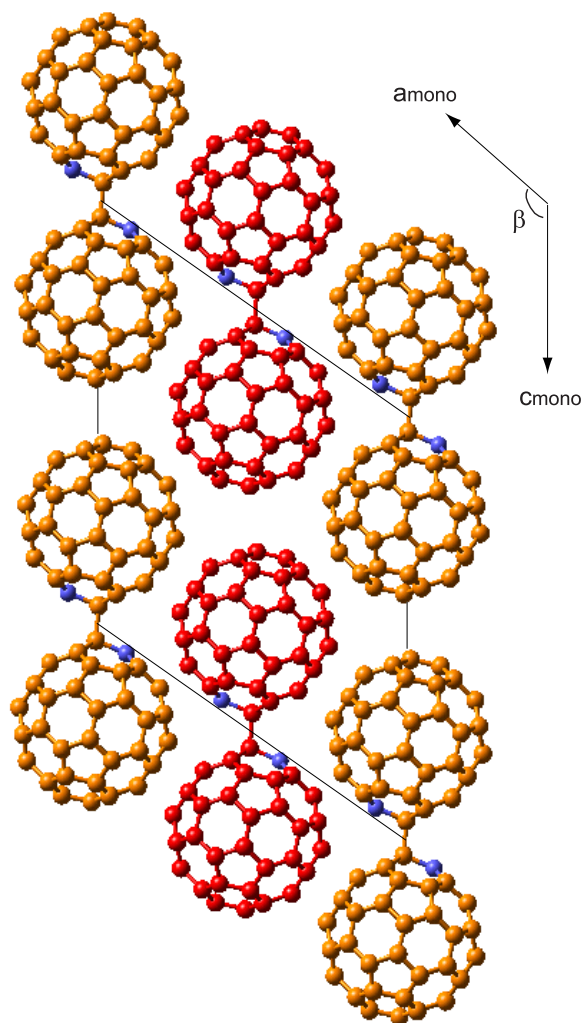


Figure 3.9: Unit cell basal plane projection of the structure of $(C_{59}N)_2$ down the b monoclinic axis. Nitrogen atoms are blue while the red dimer units are located at half a lattice translation into the unit cell. Only one of the two orientations, related by a 180° rotation about the c axis is shown.

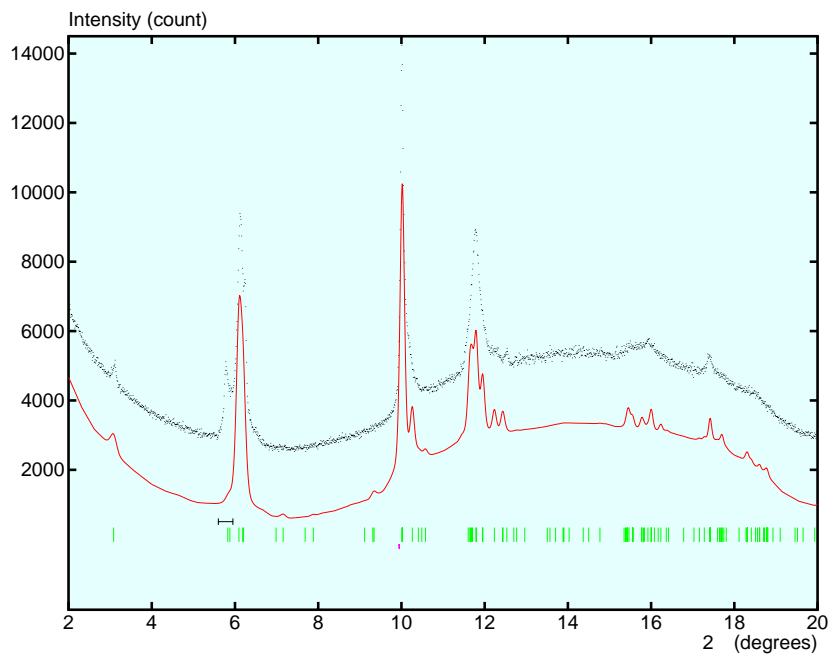


Figure 3.10: X-ray powder diffraction pattern (black points) of $(C_{59}N)_2$. The profile calculated using a monoclinic cell with symmetry $C2/m$ and employing two merohedral images of the $(C_{59}N)_2$ dimers rotated by 1.5° about the c axis of the unit cell is also shown and displaced downwards for clarity (red line). Vertical green marks indicate the positions of Bragg reflections for the $C2/m$ monoclinic cell.

Table 3.3: Refinement data for $(C_{59}N)_2$ at 278 K. Atomic coordinates are for the optimised dimer structure.

Space group	$C2/m$			R_{wp}, R_i	22.3, 23.9		
Wavelength	0.8717 Å			$\Delta 2\theta$	-0.026°		
U	1.06			V	-0.38		
W	0.04			η	0.506		
Atom	x	y	z	Atom	x	y	z
C(1)	0.10822	0.00000	0.46122	C(2)	0.15142	-0.11839	0.45221
C(3)	0.22163	-0.07322	0.43799	C(4)	0.22163	0.07322	0.43799
C(5)	0.15142	0.11839	0.45221	C(6)	0.01194	0.00000	0.42814
C(7)	-0.04481	0.11837	0.38524	C(8)	-0.04481	-0.11837	0.38524
C(9)	-0.13666	0.07329	0.31579	C(10)	-0.13666	-0.07329	0.31579
C(11)	0.09681	-0.23230	0.41063	C(12)	-0.00337	-0.23228	0.37639
C(13)	0.11003	-0.30491	0.35312	C(14)	-0.05194	-0.30556	0.29804
C(15)	0.01804	-0.34968	0.28325	C(16)	0.23476	-0.14362	0.38283
C(17)	0.17793	-0.26210	0.33962	C(18)	0.24795	-0.07027	0.32533
C(19)	0.15620	-0.26160	0.25568	C(20)	0.19888	-0.14365	0.24663
C(21)	0.23476	0.14362	0.38283	C(22)	0.24795	0.07027	0.32533
C(23)	0.17793	0.26210	0.33962	C(24)	0.19888	0.14365	0.24663
C(25)	0.15620	0.26160	0.25568	C(26)	0.09681	0.23230	0.41063
C(27)	0.11003	0.30491	0.35312	C(28)	-0.00337	0.23228	0.37639
C(29)	0.01804	0.34968	0.28325	C(30)	-0.05194	0.30556	0.29804
C(31)	-0.20341	-0.07221	0.05114	C(32)	-0.13259	-0.11498	0.03835
C(33)	-0.13259	0.11498	0.03835	C(34)	-0.20341	0.07221	0.05114
C(35)	-0.21846	-0.14437	0.10480	C(36)	-0.23229	-0.07048	0.16182
C(37)	-0.16263	-0.26249	0.14688	C(38)	-0.18363	-0.14387	0.24034
C(39)	-0.14035	-0.26238	0.23105	C(40)	-0.08120	-0.23177	0.07523
C(41)	-0.09483	-0.30399	0.13237	C(42)	0.01985	-0.23043	0.11039
C(43)	-0.00274	-0.34867	0.20240	C(44)	0.06750	-0.30384	0.18843
C(45)	0.00376	0.00000	0.04316	C(46)	0.06120	-0.11938	0.10090
C(47)	0.06120	0.11938	0.10090	C(48)	0.15061	-0.07299	0.17091
C(49)	0.15061	0.07299	0.17091	C(50)	-0.08120	0.23177	0.07523
C(51)	0.01985	0.23043	0.11039	C(52)	-0.09483	0.30399	0.13237
C(53)	0.06750	0.30384	0.18843	C(54)	-0.00274	0.34867	0.20240
C(55)	-0.21846	0.14437	0.10480	C(56)	-0.16263	0.26249	0.14688
C(57)	-0.23229	0.07048	0.16182	C(58)	-0.14035	0.26238	0.23105
C(59)	-0.18363	0.14387	0.24034	N(60)	-0.09501	0.00000	0.02333

All isotropic temperature factors refined to 0.34 Å².

The $C_{59}N$ monomer is isoelectronic with the singly charged C_{60}^- ion due to the replacement of a carbon by a trivalent nitrogen. Study of the electronic structure by electron energy-loss and photoemission spectroscopy[150, 151] reveals little mixing between the N- and C- electronic states with strong localisation of the excess electron at the nitrogen. Unlike $(C_{59}N)_2$, C_{60}^- exists as a monomeric moiety in a range of charge transfer salts. In the case of alkali metal salts AC_{60} ($A = K, Rb, Cs$) the most stable form is a conducting orthorhombic phase consisting of linear chains of C_{60}^- ions formed by $[2+2]$ cycloaddition reactions[64]. However, rapid quenching can also lead to the isolation of two additional metastable forms: a metallic cubic one (space group $Pa\bar{3}$), comprising of C_{60}^- monomers[67] and a non-metallic monoclinic one (space group $C2/m$) comprising of $(C_{60})_2^{2-}$ dimers[68]. The latter is essentially isostructural with $(C_{59}N)_2$ with very similar lattice constants and a comparable centre-to-centre separation of 9.34 Å. While there is similarity in the structural behaviour and bonding of the two dimers, calculations find that $(C_{60})_2^{2-}$ is not bound and needs the presence of cations to be stabilised[134].

In conclusion, X-ray diffraction measurements were performed on the hexagonal form of $(C_{59}N)_2$ upto 22 GPa at room temperature, revealing a somewhat less compressible solid than pristine C_{60} . We were able to probe the diverse bonding interactions present in the solid, ranging from those in individual quasispherical $C_{59}N$ monomer units to the intradimer C-C bridging bonds and the weak interdimer van der Waals interactions. The lack of strong anisotropy is rationalised in terms of nonalignment of the C-C bridging bonds of the dimer with the unit cell axes. As the pressure increases, however, the interdimer distances compress faster than the intradimer ones, and at ~ 6.5 GPa, they are both of comparable magnitude, leading

to a novel high pressure solid structure which appears to be characterised by almost isotropic bonding. Synchrotron powder diffraction measurements indicate that the sublimed solid adopts a monoclinic structure between 278 and 500 K with strong evidence for molecular dimerisation. This is consistent with the observed diamagnetic and insulating properties of the solid and with density functional theory-based calculations which confirm the stability of the dimer.

Chapter 4

Crystallography of Barium Fullerides

4.1 Introduction

Over the past 8 years since the bulk production of fullerenes via the carbon arc discharge method[152], progress has been made in all dependent fields of study. The discovery of superconductivity within the alkali metal fullerides[23] provided the impetus to especially characterise these solids and attempt to increase the superconducting transition temperature, T_c . Due to particular difficulties in production and purity control of non-alkali metal intercalates, such as the alkaline earth (AE) fullerides, the characterisation of other systems has lagged behind. Initially superconductivity was reported at 8.4 K in Ca_5C_{60} [153] where a retention of the parent C_{60} fcc packing was observed with a lattice constant that was consistent with the universal T_c - a curve, despite electrons now populating the (LUMO+1)-derived C_{60} states. Subsequently a photoemission study on magnesium, strontium and barium doped C_{60} films[154] showed semiconducting behaviour in Mg_xC_{60} , while Sr_xC_{60} and Ba_xC_{60} were both

metallic with hybridisation of alkaline-earth s and d states and C_{60} π states. Superconductivity was then reported by Kortan *et al.*[155] at 7 K in Ba_6C_{60} . They found a 12% superconducting volume fraction and no evidence of a secondary phase from room temperature lab X-ray diffraction. The crystal structure of Ba_6C_{60} was bcc (space group $Im\bar{3}$, $a=11.171$ Å. Fig.4.1).

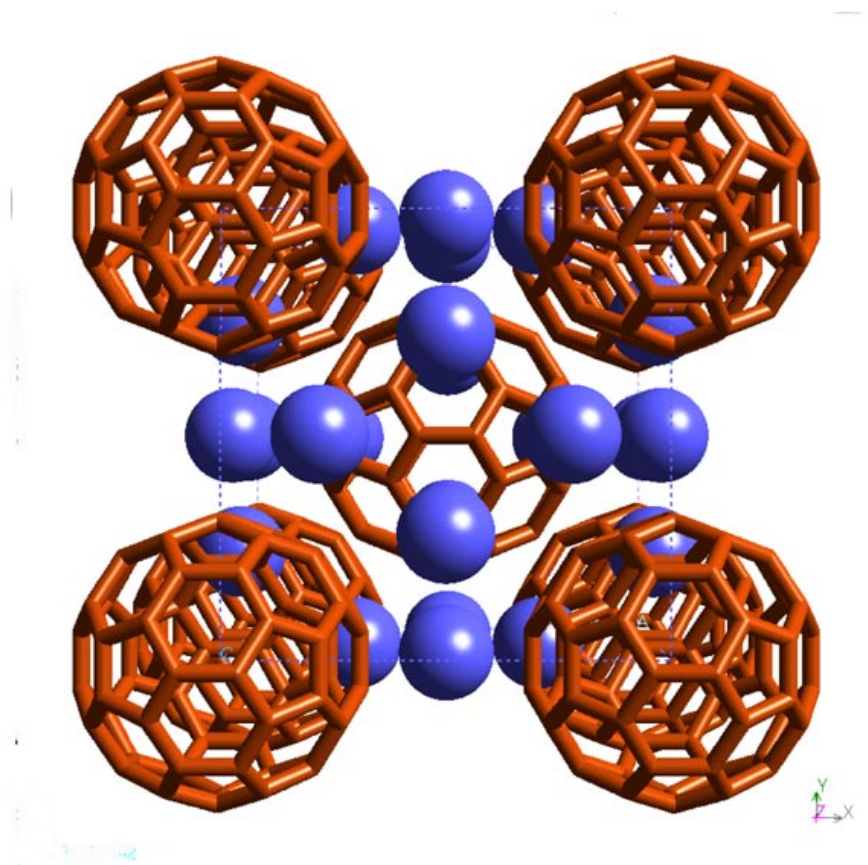


Figure 4.1: Perspective view of the body-centred cubic unit cell of Ba_6C_{60} . Fulleride cages are represented with orange cylinders, while the barium ions are blue. The unit cell is given by a dashed blue line.

Sr_6C_{60} was also reported to be superconducting with a T_c of 4 K[156] with the same body centred structure as the barium analogue ($a=10.975\text{ \AA}$), the best quality sample having 6% diamagnetic shielding fraction. LDA calculations by Saito *et al.*[157] showed Ba_6C_{60} and Sr_6C_{60} both to be semimetals, while Erwin *et al.*[158] reported insulating behaviour. Both articles emphasise that hybridisation between Sr $4d$ /Ba $5d$ and C $2p$ states leads to covalent bonding and close C-AE distances (3.1 \AA). Metallic behaviour has more recently been confirmed[159], though Sr_6C_{60} with the smaller lattice constant has a *larger* density of states at the Fermi level than that of Ba_6C_{60} , in agreement with theory[157]. This is the opposite trend from that found both experimentally and theoretically for the $\text{A}_2\text{A}'\text{C}_{60}$ fullerides.

Another stable phase, Ba_3C_{60} , was observed to have the A15 structure[80] (space group $Pm\bar{3}n$, $a=11.343\text{ \AA}$, Fig.4.2) with the two-fold axis of the body centred fulleride unit rotated by 90° compared to the origin. This salt is insulating, consistent with a doubly positive charge of the barium ions which results in the t_{1u} derived band being fully occupied in a rigid band model.

Further systematic synthesis of Ba_xC_{60} salts[160, 161] showed a new minority phase via lab X-ray diffraction, that was attributed to an orthorhombic Ba_4C_{60} composition ($a=11.25\text{ \AA}$, $b=11.69\text{ \AA}$, $c=10.90\text{ \AA}$) which also coincided with the phase exhibiting the largest superconducting fraction in their series. The superconducting transition temperature was observed to be uniquely 6.8 K, shedding doubts upon the presence of two distinct superconducting phases. The superconducting stoichiometry was however still ambiguous with a following photoemission report indicating semiconducting behaviour for stoichiometries with less than 4.5 barium ions[162] and metallic behaviour occurring for $x > 6.1$.

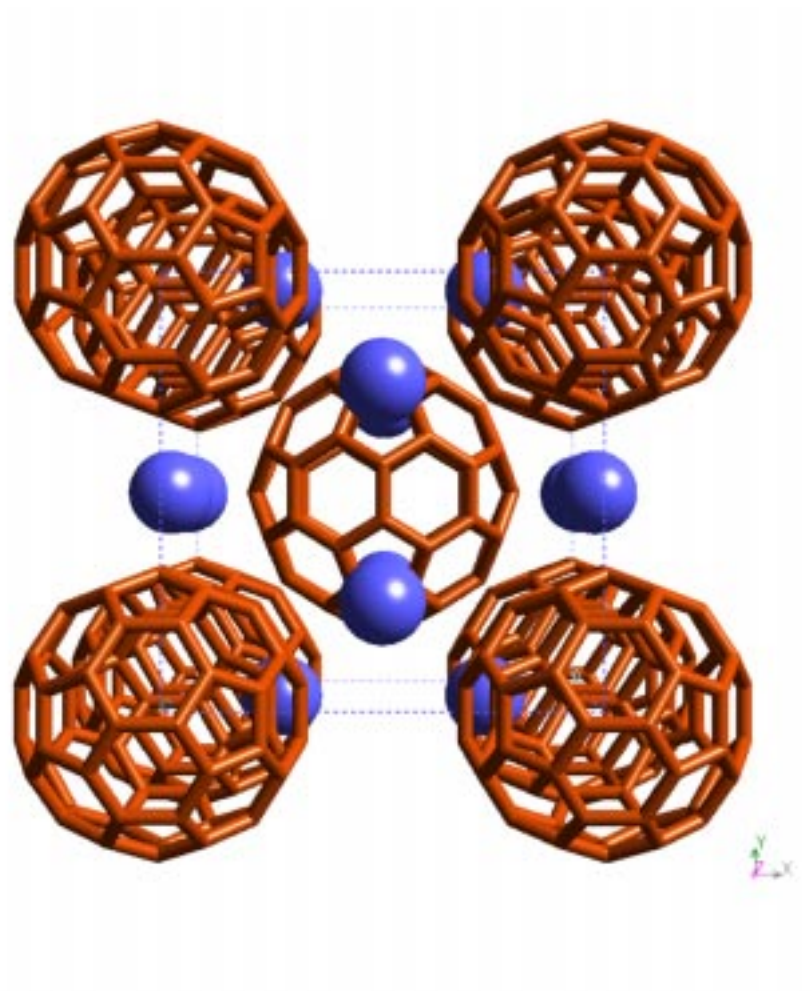


Figure 4.2: Perspective view of the unit cell of Ba₃C₆₀. Barium ions are blue. The orange fulleride cages form a primitive cubic structure with the body centred anion rotated 90° about its z axis with relation to that at the origin.

Measurement of T_c as a function of pressure for Ba₄C₆₀[163] found a value for the pressure coefficient, dT_c/dP of -1.9 K GPa^{-1} , four times smaller than that in K₃C₆₀ (-7.8 K GPa^{-1}) and Rb₃C₆₀ (-9.7 K GPa^{-1})[164]. Lacking compressibility data, an approximation for the coefficient Γ , $d\ln(T_c)/d\ln(V)$, was derived using compressibility

data for K_3C_{60} . A Γ value of 16.6 was derived for Ba_4C_{60} , more than twice as large as for the alkali metal fullerenes where $\Gamma \sim 7$. Again, controversy arises as a separate study of Ca_5C_{60} showed that T_c *increases* with pressure[165].

Diligent work by K. Kordatos and the subsequent efforts at the NEC Fundamental Laboratory (Tsukuba) and JAIST (Hokuriku) has recently come to fruition and synthesis of phase pure Ba_3C_{60} , Ba_4C_{60} and Ba_6C_{60} systems has been achieved. This allowed the unambiguous identification of Ba_4C_{60} as the superconducting phase and the start of a systematic study of its structural, conducting and electronic properties. In order to determine the unknown crystal structure of these novel AE_4C_{60} systems, we collected high resolution powder diffraction data on the BM16 beamline at the ESRF. Structural studies have been extended to low temperatures and high pressure in an attempt to better characterise the physics in these solids.

4.2 Ba_4C_{60} : X-ray Diffraction

High resolution diffraction data was collected for a high-quality Ba_4C_{60} sample (JAIST) at ambient temperature. The sample was loaded in a 0.5 mm diameter glass capillary and mounted on a goniometer head that was spun about the capillary axis at a frequency of around 1 Hz to reduce preferred orientation effects. The beam was characterised by a wavelength of 0.84884 Å and a size of 1 mm vertically and 7 mm horizontally. All Rietveld analysis was performed using the GSAS[103] program.

Le Bail analysis of this exceptional data set using a single orthorhombic Ba_4C_{60} phase (space group $Immm$), as described previously[160], failed to account for numerous reflections. The possibility of the presence of impurities from either of the more stable Ba_3C_{60} and Ba_6C_{60} phases was investigated. The best solution was reached

by using all three phases with lattice constants that refined towards those published earlier with the major contribution to the diffraction profile arising from the Ba_4C_{60} phase. A few anomalously sharp reflections were unaccounted for within this model, but can be traced to the formation of barium oxide in the preparation stage, as noted previously[160].

In comparison to the tetragonal A_4C_{60} systems, there is a loss of the fourfold rotation axis along the z direction via the inequivalence of the a and b axes. This is reflected by the removal of the disorder present in the fulleride anion orientations in K_4C_{60} and Rb_4C_{60} [166, 76] by aligning 6:6 bonds along either the a or b axes. Our Rietveld model starting point is hence defined as having a 6:6 bond aligned perpendicular to c , and lying along the long a axis. Carbon positions were generated by assuming that the difference between bond lengths for the 'single' and 'double' character bonds is reduced to zero as a function of increasing electron transfer[167] and each bond is 1.44 Å. *Immm* symmetry results in two inequivalent, distorted tetrahedral barium sites, where the cations are confined to mirror planes.

Initially, refinements were unsatisfactory at high 2θ . Scattering at high angles is sensitive to anion orientations and ordering, and this situation could not be improved by allowing radial dilation of the fulleride units. Since the orientation of the cages was initially somewhat arbitrary, a sequential series of refinements was undertaken where the C_{60} was rotated in steps of 5° about each of the principal axes. However, this reduces the symmetry of the crystal. Consultation of the *International Tables for Crystallography*[82] shows that the possible subgroups are *I222*, *I2/m*, *Imm2*, *Im2m* or *I2mm*. A special cell choice of the *C2/m* space group with the required 90° α, β and γ angles gives the space group *I112/m* for rotations about all axes and

was used in this search. In practice the C_{60} can be generated within CERIUS²[149] to ensure that the correct symmetry and minimum carbon atoms are defined. Note that due to the symmetry of C_{60} , 90° rotations around any of the cartesian axes will result in the same fulleride orientation in the crystal, and we checked all three axes due to the orthorhombicity of the system, so as to include possibilities of differential orientational interactions with near neighbour ions.

R_{wp} and χ^2 factors were monitored simply as a function of the fulleride orientation. All other factors were fixed at the Le Bail derived values besides the scale factor, zero-point, phase fractions, lattice constants and Ba_4C_{60} cation position. Fig.4.3 shows the goodness-of-fit factors after rotating about the x, y and z axes. As it can be seen for the original orientation, typical values of $R_{wp} = 10\%$ and $\chi^2 = 23$ are achieved. Both factors are sensitively dependent upon the fulleride orientation, increasing significantly to a maximum at around 30° , then entering a shallow minimum at $\sim 45^\circ$ for rotations about all axes. Further rotation leads to a pronounced minimum in both fit factors at 90° . There is also another, blue, curve depicted in the same figure that results from the same rotation about the z axis, but performed in space group $Pnnm$. This covers the possibility that the body centred anion is 90° out of phase with that at the origin, as it is the case with the A15 structure of Ba_3C_{60} . This curve mirrors exactly, in this crude part of the analysis, the progression of the previously described series finally arriving at the same deep minimum with coincident fit factors. We can hence conclude that our initial orientation of C_{60} is in fact wrong, and should be rotated by $\pi/2$ about the z axis, but the correct space group will be decided by a careful Rietveld analysis, using the two possible space groups $Immm$ and $Pnnm$.

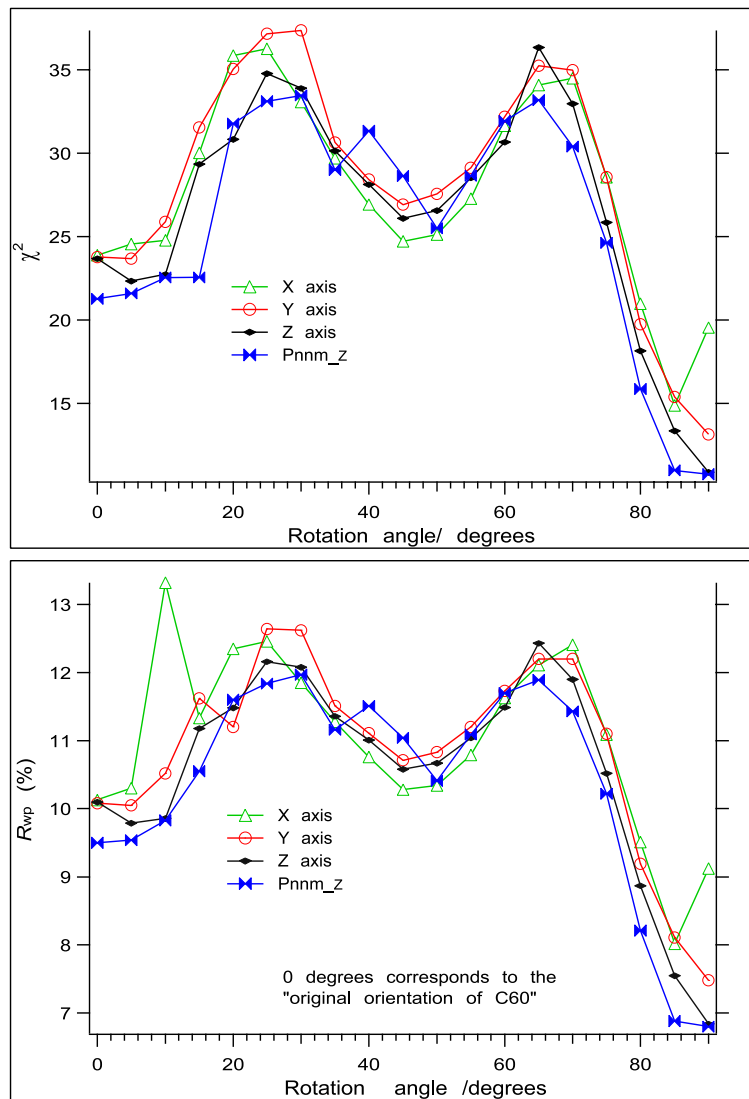


Figure 4.3: Variation of χ^2 and R_{wp} as a function of rotation angle of the fulleride cage, where the origin is defined as having a 6:6 bond aligned with the a axis. Rotations about x are shown by green triangles, y by red circles and z by black diamonds. Blue double triangles show the result for rotations about the z axis in space group $Pnnm$.

4.2.1 *Immm* Space Group

Full Rietveld analysis was performed with Ba_4C_{60} in the space group *Immm* and the published structures of Ba_6C_{60} and Ba_3C_{60} with atomic coordinates scaled to the current lattice constants. Twenty background points were fixed through the entire range of 2θ , and a six coefficients cosine Fourier series was used to fit the background. The peak shape was well described by the asymmetry function of Finger *et al.*[115] using only four parameters that were constrained to be equal for all phases¹. The histogram parameters are listed in Table 4.1 along with the agreement factors for the final fit.

Table 4.1: Histogram details for the BM16 data of Ba_4C_{60} collected at 295 K.

HISTOGRAM	
R_{wp}, R_p /%	5.29, 3.96
χ^2	4.27
$\lambda/\text{\AA}$	0.848836(3)
$\Delta_{2\theta}$ /°	0.0095(4)
2θ range /°	4 - 70
step size /°	0.005
Peak cutoff	1%
W	0
Lx	0.65(7)
Ly	35.5(4)
S/L	$8.2(3) \times 10^{-3}$
H/L	$8.9(3) \times 10^{-3}$
Background	$3.00(1) \times 10^4$
coefficients	$-5.25(2) \times 10^4$
	$3.45(2) \times 10^4$
	$-1.65(1) \times 10^4$
	$5.16(8) \times 10^3$
	$-7.8(2) \times 10^2$

The final Rietveld refinement ($R_{wp} = 5.29\%$) is shown in Fig.4.4 (note the scale

¹Available within the PC version of GSAS.

is multiplied by two above 17°) with all parameters listed in Table 4.2. Ba_4C_{60} and Ba_6C_{60} fulleride units were allowed to dilate radially, so as to preserve the high symmetry and maintain all bond angles and equal bond lengths. For Ba_4C_{60} , refinement gives $120.06(9)^\circ$ and $108.000(8)^\circ$ for the bond angles and $1.436(4)$ Å for the bond lengths. This was not allowed for Ba_3C_{60} due to the extremely low percentage contribution to the total pattern. A global carbon isotropic temperature factor was assigned to a sensible value of 0.01 Å² for Ba_6C_{60} and Ba_3C_{60} , while the values for the carbon atoms in Ba_4C_{60} refined to $0.002(1)$ Å². Positional parameters for the inequivalent barium ions in Ba_4C_{60} were refined. An improvement in the refinement was evident with the use of independent anisotropic temperature factors giving values that represent a motion mainly in the *ab* plane. Cation fractional coordinates were only varied for Ba_6C_{60} , while the isotropic temperature factors of both minority phases were constrained to refine together leading to a reasonable $1.8(1)$ Å². In later stages of refinement, no improvement was obtained by allowing fractional occupancies of cations in Ba_4C_{60} to refine: the result was always full occupancy within the calculated error.

A perspective view down the *c* axis of the orientationally ordered orthorhombic cell of Ba_4C_{60} is shown in Fig.4.5. The crystallographically distinct barium ions, dark and light blue in colour, occupy *m2m* and *2mm* sites. Compared to the isotropic $Im\bar{3}$ structure of Ba_6C_{60} , we have a vacancy ordering in Ba_4C_{60} that aids the contraction of the lattice preferentially along the *c* axis. This can be understood if one simply considers that the (001) planes remain full with (010) and (100) planes containing half as many bariums. The closest distance between barium ions in the *ab* plane is $4.428(15)$ Å, while it is $4.57(18)$ Å in the *bc* plane, both values being quite similar

to the interatomic distance of 4.35 Å found in metallic barium. Distances from C₆₀ centres to barium ions vary from 6.17 Å to 6.36 Å for all coordination environments.

Table 4.2: Structural Information for the Rietveld refinement of Ba₄C₆₀ in space group *Immm*. The data were collected at 295 K on the BM16 diffractometer.

PHASE 1: Ba₄C₆₀

Space group	<i>Immm</i>				
Weight Fraction /%	86.1				
<i>a</i> / Å	11.6101(2)	<i>b</i> / Å	11.2349(2)	<i>c</i> / Å	10.8830(2)
Atom	<i>x/a</i>	<i>y/b</i>	<i>z/c</i>	100×(<i>U</i> ₁₁ , <i>U</i> ₂₂ , <i>U</i> ₃₃)	Fraction
Ba(1)	0.5	0.2034(2)	0.0	2.4(1), 3.7(2), 1.2(1)	1
Ba(2)	0.2488(1)	0.5	0.0	2.7(1), 3.7(2), 0.6(1)	1
C(11)	0.3005(2)	0.0	0.0652(1)	0.2(1)	1
C(12)	0.0	-0.06388(4)	0.3206(2)	0.2(1)	1
C(13)	0.10014(6)	-0.12786(7)	0.2798(2)	0.2(1)	1
C(21)	0.2003(1)	-0.06388(4)	0.2389(1)	0.2(1)	1
C(22)	0.12373(7)	-0.2710(2)	0.10682(6)	0.2(1)	1
C(23)	0.06187(4)	-0.3105(2)	0	0.2(1)	1
C(31)	0.2240(2)	-0.2070(1)	0.06600(3)	0.2(1)	1
C(32)	0.06187(4)	-0.2314(1)	0.2137(1)	0.2(1)	1
C(33)	0.2622(2)	-0.10345(6)	0.13199(8)	0.2(1)	1

PHASE 2: Ba₆C₆₀

Space group	<i>Im</i> $\bar{3}$				
Weight Fraction /%	11.8(1)				
<i>a</i> / Å	11.1959(2)				
Atom	<i>x/a</i>	<i>y/b</i>	<i>z/c</i>	100× <i>U</i> _{iso}	Fraction
Ba	0.2824(4)	0.0	0.5	1.8(1)	1
C(1)	0.0000	0.3139(7)	0.0647(2)	1.0	1
C(2)	0.2733(6)	0.1292(3)	0.1047(2)	1.0	1
C(3)	0.2098(5)	0.2339(5)	0.0647(2)	1.0	1

PHASE 3: Ba₃C₆₀

Space group	<i>Pm</i> $\bar{3}n$				
Weight Fraction /%	2.1(1)				
<i>a</i> / Å	11.338(1)				
Atom	<i>x/a</i>	<i>y/b</i>	<i>z/c</i>	100× <i>U</i> _{iso}	Fraction
Ba	0.25	0.0	0.5	1.8(1)	1
C(1)	0.0000	0.3021	0.0622	1.0	1
C(2)	0.1244	0.1007	0.2636	1.0	1
C(3)	0.0622	0.2013	0.2351	1.0	1

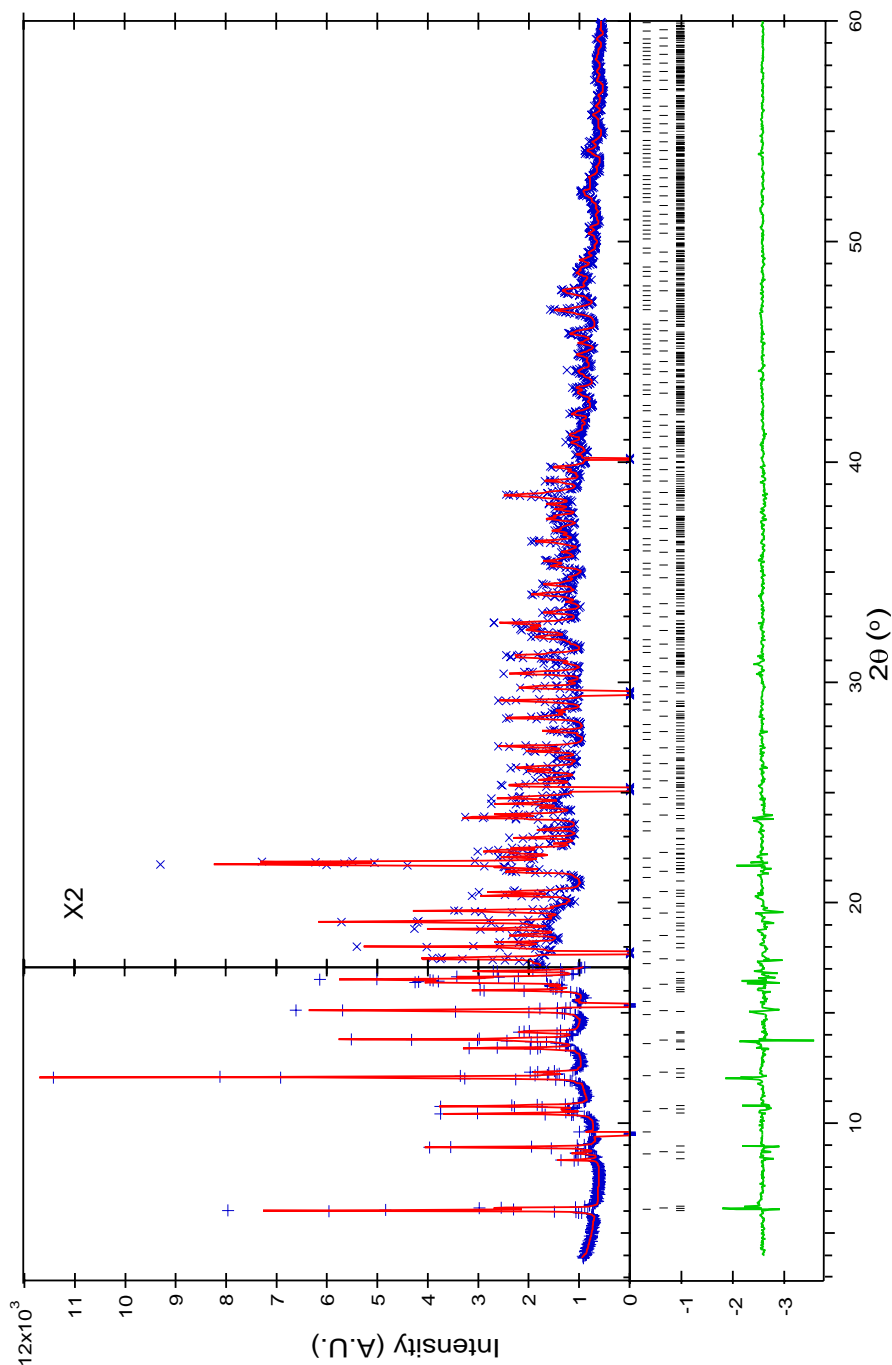
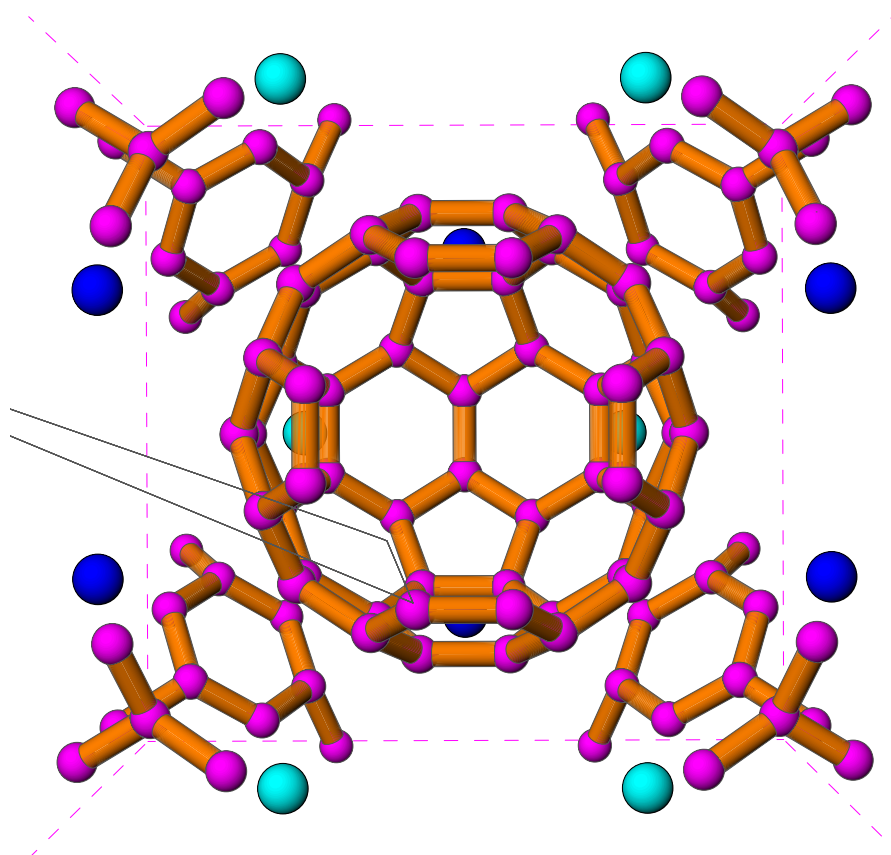


Figure 4.4: Rietveld refinement of the diffraction profile of Ba_4C_{60} at 295 K between 3° and 60° in 2θ . The observed points are shown as blue crosses and the calculated fit as a solid red line. The intensity has been multiplied by a factor of 2 above 17° in order to facilitate observation of weaker reflections. The difference curve is shown as the green line in the base of the figure with ticks marking the positions of the Bragg reflections from Ba_4C_{60} (majority phase: 86.1%, lower most), Ba_6C_{60} (minority phase: 11.8%) and Ba_3C_{60} (minority phase: 2.1% upper most). Peaks due to barium oxide are excluded, except for the region at 9.5° which is abnormally sharp in this pattern and is treated as an unknown impurity.

This implies that all contacts are optimised and the short c axis is hence a necessity. One can imagine a situation where we add two more barium ions (per unit cell) to the bc plane without expanding the lattice. Resulting barium contacts as short as 3.5 Å will result leading to mutual Coulombic repulsion and an expansion of the c axis towards the size of 11.2 Å found for the b axis and the cubic lattice constant of Ba_6C_{60} .



The local environments of the two barium sites are quite similar on average with a mean barium-carbon distance of around 3.28 Å for both barium ions and ring coordinations (Table 4.3). To compare to other fullerides, the closest distances are 3.20 Å for K_3C_{60} for which the ionic radius of K^+ (1.33 Å) is the closest to the ionic radius of Ba^{2+} (1.35 Å)². In the present case, we observe a very short distance of 3.00 Å (Ba(2)-C(21)), comparable to what is also seen in Ba_6C_{60} . Barium 5*d* states exhibit a maximum at a radius of approximately 1.5-1.6 Å with appreciable tails out as far as 2.8 Å[158]. Hence, this close contact can be taken as resulting from overlap of barium 5*d* states and C 2*p* states, giving rise to a 'covalent' bond.

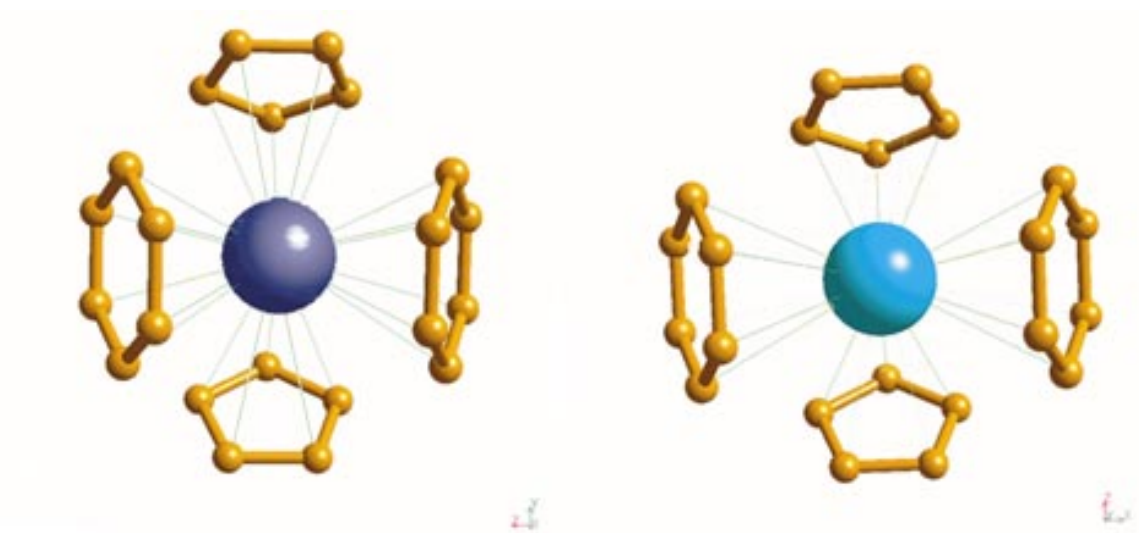


Figure 4.6: A view of the coordination environment of Ba(1) (dark blue sphere) and Ba(2) (light blue sphere) to two hexagon and two pentagon nearest neighbours. Solid green lines highlight Ba-C contacts of less than 3.3 Å.

While the sites are similar on average, the Ba(1) site is more regular, being only

²The actual radius is expected to be somewhat larger due to possible incomplete charge transfer, as postulated in Ba_6C_{60} [157, 158].

slightly displaced from the ring centroids (Fig.4.6), while the Ba(2) site is displaced towards the C(21)-C(21)' bond of the hexagon ring and the C(23) atom of the coordinating pentagons. The magnitude of this displacement is quantified by the tilt angle away from the ring centres and also the standard deviation of the Ba-C contacts that are listed in Table 4.3.

Table 4.3: A description of closest contacts of barium in Ba₄C₆₀ for the two distinct sites at 295 K. All distances are in Å. The numbers in brackets refer to the standard deviation of the measurement, giving a quantification of the distribution of bond lengths.

shortest contact Ba(1)-C distance for pentagon	3.26316(4)
mean Ba(1)-C distance for pentagon	3.27(1)
Ba(1)-centroid of pentagon distance	3.04
tilt from ring normal toward C(12)	1.1°
shortest contact Ba(1)-C distance for hexagon	3.28467(5)
mean Ba(1)-C distance for hexagon	3.31(2)
Ba(1)-centroid of hexagon distance	2.98
tilt from ring normal toward C(13)-C(13)'	1.1°
shortest contact Ba(2)-C distance for pentagon	3.03983(4)
mean Ba(2)-C distance for pentagon	3.23(10)
Ba(2)-centroid of pentagon distance	2.99
tilt from ring normal toward C(23)	9.5°
shortest contact Ba(2)-C distance for hexagon	2.98969(4)
mean Ba(2)-C distance for hexagon	3.29(24)
Ba(2)-centroid of hexagon distance	2.97
tilt from ring normal toward C(21)-C(21)'	15.3°

4.2.2 $Pnnm$ Space Group

Having achieved an excellent fit with the $Immm$ model, we also attempted a similar Rietveld study with the $Pnnm$ space group. The Rietveld refinement is shown in Fig.4.7. While this fit is visibly no different from that of $Immm$, the refinement is extremely unstable and no parameters could be varied at any time. The atomic positions for Ba_4C_{60} are shown in Table 4.4 along with the fit factors. Because of this instability and marginal improvements in fit factors, we assume this to be an incorrect choice of space group. The remarkable thing is that it is so difficult to tell the Rietveld refinements of both space groups apart even though there is excellent data to high angles where even slight differences in model should give rise to visible changes in peak intensities.

Table 4.4: Structural Information for the Rietveld refinement of Ba_4C_{60} (295 K) in space group $Pnnm$

PHASE 1: Ba_4C_{60}			
Space group	$Pnnm$		
R_{wp}, R_p	5.29%, 3.96%		
χ^2	4.26		
Atom	x/a	y/b	z/c
Ba(1)	0.5	0.2034	0
Ba(2)	0.2488	0.5	0
C(11)	0.3005	0	0.0652
C(12)	0.0000	-0.0639	0.3206
C(13)	0.1001	-0.1279	0.2798
C(21)	0.2003	-0.0639	0.2389
C(22)	0.1237	-0.2710	0.1068
C(23)	0.0619	-0.3105	0
C(31)	0.2240	-0.2070	0.0660
C(32)	0.0619	-0.2314	0.2137
C(33)	0.2622	-0.1034	0.1320
C(41)	0.2622	0.1034	0.1320
C(42)	0.0619	0.2314	0.2137
C(43)	0.2240	0.2070	0.0660
C(44)	0.0619	0.3105	0.0000
C(45)	0.1237	0.2710	0.1068
C(46)	0.2003	0.0639	0.2389
C(47)	0.1001	0.1279	0.2798

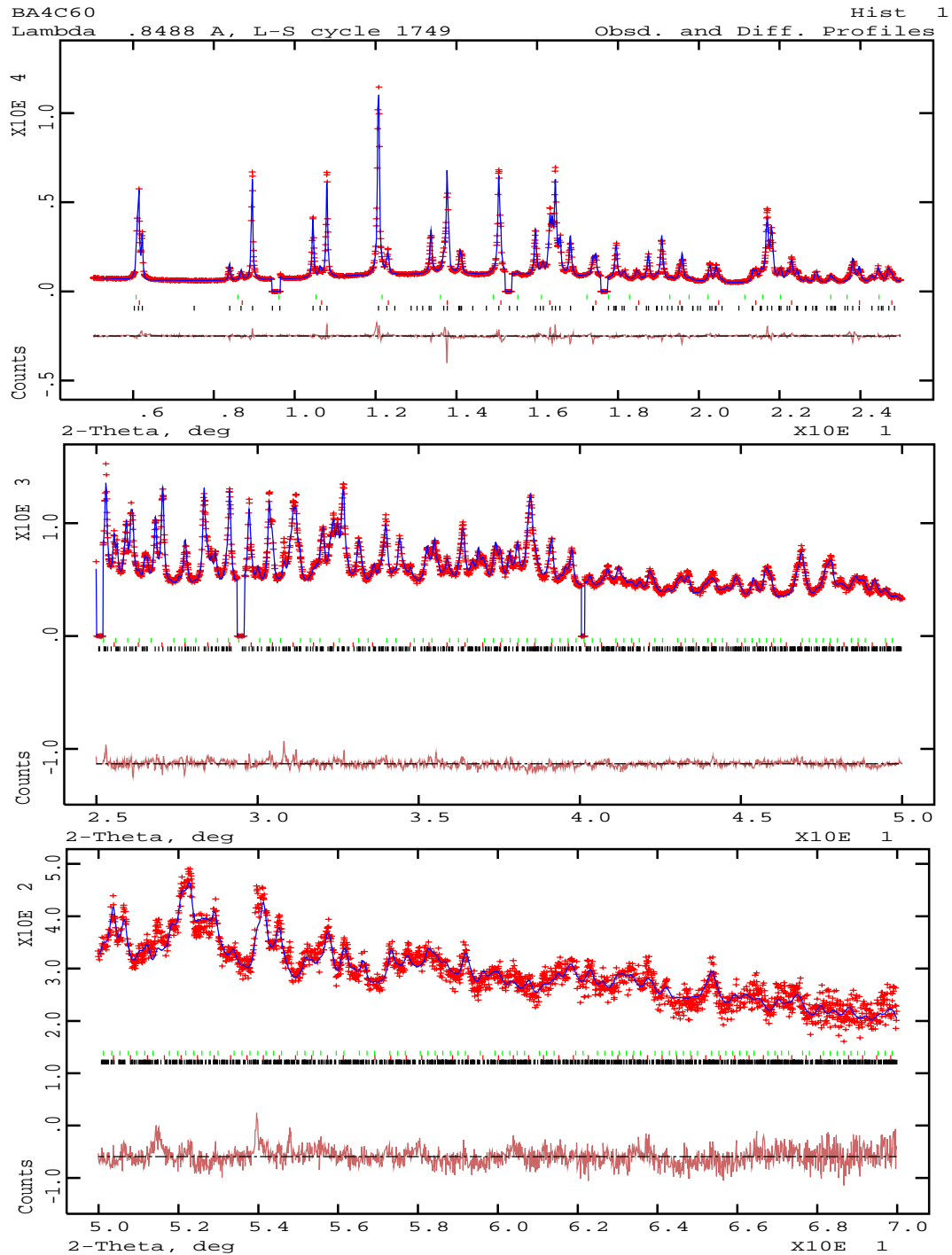


Figure 4.7: Ba_4C_{60} Rietveld refinement in space group $Pnnm$. Red crosses are data points and the solid blue line is a fit using the histogram parameters from the best fit $Immm$ data. The top, middle and bottom panel show 2θ regions from 4° to 25° , 25° to 50° and 50° to 70° , respectively. Note the changes in scale for each panel. Black, red and green tick marks show reflections arising from Ba_4C_{60} , Ba_6C_{60} and Ba_3C_{60} , respectively. Even though this fit is statistically as good as for $Immm$, the refinement is unstable and immediately diverges.

Disorder

An alternative model using merohedral disorder of the C_{60} units about the z -axis (space group $Immm$) was also explored. Refinement of the background, the peak shape, the lattice constants and the temperature factors of the Ba^{2+} ions in the Ba_4C_{60} phase were allowed. The resulting values of the parameters are the same within error to those from the orientationally ordered model in space group $Immm$. There is however a degradation in the fit with the agreement factors, $R_{wp}=6.43\%$ and $\chi^2=6.29$. This is manifested throughout the diffraction pattern as the occasional excess allocation of intensity to some peaks, while the majority of the pattern remains well accounted for.

Remarks

We have confirmed the crystal structure of Ba_4C_{60} which beyond reasonable doubt belongs to the space group $Immm$. This is the *first* confirmation of the orthorhombic structure of a fulleride superconductor (at ambient pressure) and unlike the alkali metal fullerenes, cubic symmetry is evidently not a prerequisite for superconductivity³. The crystal is characterised by orientational order of C_{60} ions in an orthorhombic cell with two distinct barium sites, one of which is more regularly coordinated to its neighbouring fullerenes than the other. Close Ba-C contacts are prevalent reflecting what could be interpreted as 'bonding' with the fullerene cages. This postulate will be further examined by observation of the crystal structure as a function of temperature and pressure. Also, that lattice constant for Ba_6C_{60} at $a=11.1959(2)$ Å is ~ 0.18 Å shorter than the essentially isostructural K_6C_{60} salt. The difference reflects the

³Orthorhombic $(NH_3)K_3C_{60}$ [63] and metastable bcc/bct Cs_3C_{60} [57] show superconductivity at elevated pressures.

tighter crystal packing in Ba_6C_{60} due to increased charge transfer to the fulleride ions.

Independently, Dahlke *et al.* found the same *Immm* structure for semiconducting Cs_4C_{60} [77], in which there is a similar Cs environment to the present case albeit with a larger lattice and longer Cs-C contacts⁴. Their analysis of the local caesium coordination agrees exceptionally well with our own, even with the direction and magnitudes of the displacements from the ring centroids.

4.2.3 Low Temperature

The same Ba_4C_{60} sample as above was used to record low temperature diffraction patterns with the diffractometer on the BM1(SNBL) beamline at the ESRF. Our intention was to look for possible signatures of a modified crystal structure and/or fulleride orientation when cooling through the superconducting transition temperature. Powder patterns were taken at 10 K and 5 K in a continuous flow helium cryostat with a rotating sample stick. Both patterns were recorded over 11.5 hours with a step size of 0.01° . The counting time per point was varied through the data collection with 5 sec/point between 4.8° - 22.4° , 8 sec/point between 22.5° - 37.6° and 15 sec/point between 37.6° - 51° . Calibration of the monochromatised beam with a silicon standard resulted in a wavelength of $0.79930(1)$ Å. Data were fitted according to the same *Immm* model, as found for the BM16 data with the fulleride cages for all phases now scaled to the low temperature lattice constants which were determined by preliminary Le Bail refinements. For both histograms, a six coefficient cosine Fourier series was refined for the background with 21 fixed background points. The peak

⁴reflecting the increased ionic radius of Cs^+ at 1.7Å.

shape was fitted once more by the asymmetric function of Finger[115], with the three phases constrained together.

The histogram data for both temperatures are presented in Table 4.5 The data are of a worse quality than that obtained on BM16 for a number of reasons. Firstly, the alignment of the capillary in the holder is never perfect, hence when the stick is rotated during data collection, there can be a precession of the sample in and out of the beam. Secondly, the non-horizontal rotation can lead to a movement of the crystalline sample within the capillary so reducing, over time, the actual amount in the beam. Thirdly, the use of a cryostat adds a rather large background from the kapton windows. Considering the actual diffractometer itself and its lack of analyser crystals, we have around a five fold reduction in intensity⁵ compared to BM16, hence longer counting times for similar statistics are needed to obtain comparable data.

Table 4.5: Histogram details for the SNBL data of Ba_4C_{60} collected at 10 and 5 K.

Value	10K	5K
R_{wp}, R_p /%	9.66, 7.57	8.17, 6.48
χ^2	1.85	1.99
$\lambda/\text{\AA}$	0.7993	0.7993
$\Delta_{2\theta}$ /°	-0.005(2)	-0.0026(5)
Peak cutoff	1%	1%
W	5.259×10^{-3}	5.259×10^{-3}
Lx	1.58(4)	1.54(9)
Ly	28(1)	27.8(9)
S/L	$5(1) \times 10^{-4}$	$5(1) \times 10^{-4}$
H/L	$5(1) \times 10^{-4}$	$5(1) \times 10^{-4}$
Background	$-1.77(3) \times 10^3$	$-1.38(5) \times 10^3$
coefficients	3.736×10^2	3.021×10^2
	5.181×10^3	5.2166×10^3
	$-7.0(2) \times 10^3$	$-8.7(3) \times 10^3$
	$4.6(3) \times 10^3$	$7.5(5) \times 10^3$
	$-1.6(2) \times 10^3$	$-3.7(3) \times 10^3$

⁵Even though there are nine analysers on BM16, only a five-fold gain is seen due to their angle selectivity and other beam related factors.

Rietveld refinement of the data at both temperatures was performed with more restrictions placed on both Ba_6C_{60} and Ba_3C_{60} phases that reflect the poorer quality of the data when compared to that obtained on BM16. After scaling, only the phase fraction and lattice constants of the minority Ba_3C_{60} and Ba_6C_{60} phases were allowed to change together with the isotropic temperature factor and the x fractional coordinate of Ba in Ba_6C_{60} . In contrast the scale factor, lattice constants, alkaline earth fractional positions, isotropic temperature factors, dilation of C_{60}^{x-} and an overall carbon isotropic Debye-Waller factor for Ba_4C_{60} were all allowed to vary. The resulting fits are shown in Fig.4.8 and Fig.4.9 at 10 K and 5 K, respectively with the corresponding atomic parameters listed in Tables 4.6 and 4.7.

The results of the Rietveld analysis are very similar at both temperatures, although a better series of R -factors are achieved for the 5 K data set. Examination of the lattice constants for all phases reveals a logical reduction in magnitude when compared to the room temperature data, except in the case of the c axis of Ba_4C_{60} where a slight expansion seems to have occurred. At 5 K, the intramolecular C-C bond lengths are 1.44 Å, essentially the same as those at room temperature. However, this is not the case for the 10 K refinement, where the bond lengths have expanded to 1.45 Å. The refinements have been repeated for both data sets after slight perturbations of the lattice size and zero point errors. The 5 K refinement shows no dependence on the starting configuration. For the 10 K data, another minimum in the refinement process ($R_{wp}=9.39\%$, $R_p=7.45\%$ and $\chi^2=1.755$) can be found with a positive zero point error ($\Delta_{2\theta}=0.0044(2)$). This minimum reduces the C-C bondlengths in Ba_4C_{60} to 1.44 Å, but a concomitant decrease of the lattice constants to values *smaller*

than those at 5 K are observed⁶. The uncertainty in the refinement of the 10 K data is also reflected in the profile R -factors, which are much smaller for the 5 K refinement. Deciding which refinement is correct is difficult as both of the 10 K results described here have have unwelcome characteristics. Since we collected the data at both temperatures in succession and on the same diffractometer, it should be expected that the lattice constants and zero point errors are similar for both powder diffraction patterns. Hence, we shall continue the analysis with the initial 10 K refinement. Bearing in mind the large standard deviation of the zero point and atomic positional parameters in this measurement, most emphasis will be on the 5 K refinement.

Fitting linear values for expansivities along each axis between 5 and 295 K, we can see how anisotropic the system is. For Ba_4C_{60} , $d\ln(a)/dT$ values are $2.4(4) \times 10^{-6} \text{ K}^{-1}$, $1.565(8) \times 10^{-5} \text{ K}^{-1}$ and $-1(1) \times 10^{-7} \text{ K}^{-1}$ for the a , b and c axes, respectively. Amazingly there is negligible, even slightly negative, expansivity along the c axis that is reminiscent of the situation encountered for polymeric fulleride systems which exhibit *bonding* between fulleride units, and a strong tendency not to expand along the chain axis[54, 168, 169]. Comparison to C_{60} ($\alpha = 6.1 \times 10^{-5} \text{ K}^{-1}$)[2, 170] with its weaker intermolecular potential than K_3C_{60} ($\alpha = 2.8 \times 10^{-5} \text{ K}^{-1}$) and Rb_3C_{60} ($\alpha = 2.9 \times 10^{-5} \text{ K}^{-1}$)[171] show how extremely low the current expansivities are. The b axis of Ba_4C_{60} has the largest expansivity for this solid yet it is still half the magnitude found in the cubic A_3C_{60} salts. The current data also give us values of $\alpha = 3.9(4) \times 10^{-6} \text{ K}^{-1}$ for Ba_6C_{60} and $\alpha = 2.4(8) \times 10^{-6} \text{ K}^{-1}$ for Ba_3C_{60} . These values are again much reduced from the pristine C_{60} solid or the alkali metal intercalated salts. Care must be used when interpreting these data as it is based on 3 points on a non-linear curve

⁶For reference, the lattice constants of Ba_4C_{60} become: $a = 11.5997(5) \text{ \AA}$, $b = 11.1827(5) \text{ \AA}$ and $c = 10.8828(4) \text{ \AA}$.

that has been approximated to linear. The most that can definitely be concluded here is that Ba_4C_{60} has a remarkably low expansivity along the c axis. It will be intriguing to see if the expansivities of all the other alkaline earth fullerides follow suit as indicated by the generally low thermal expansion coefficients of the barium fullerides.

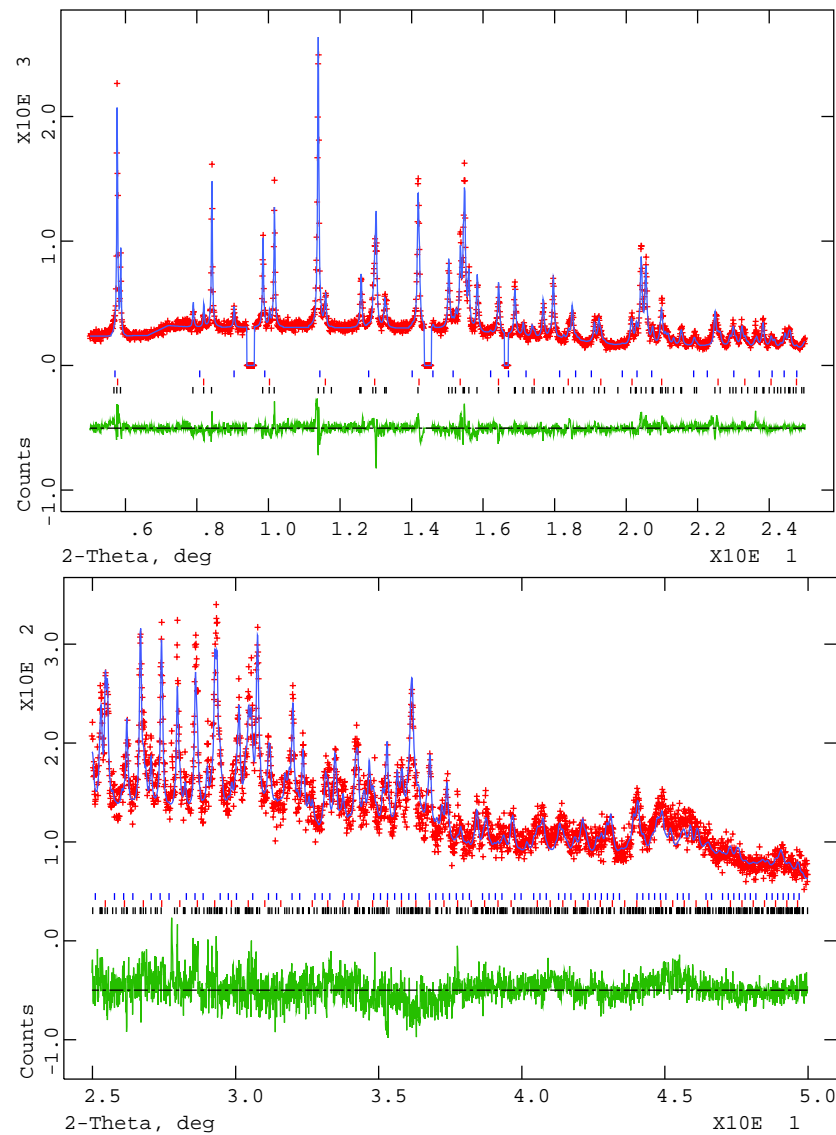


Figure 4.8: Rietveld refinement of the synchrotron X-ray powder diffraction profile of Ba_4C_{60} in space group $Immm$ at 10 K. Red crosses are data points and the solid blue line is a three phase fit. The top and bottom panel show 2θ regions from 5° to 25° and 25° to 50° , respectively. Note the changes in scale between panels. Black, red and blue tick marks show reflections arising from Ba_4C_{60} , Ba_6C_{60} and Ba_3C_{60} respectively.

Table 4.6: Structural Information for the Rietveld refinement of Ba_4C_{60} (space group $Immm$) at 10 K.

PHASE 1: Ba_4C_{60}

Space group	$Immm$				
Weight Fraction /%	85.1				
$a/\text{\AA}$	11.6032(4)	$b/\text{\AA}$	11.1847(4)	$c/\text{\AA}$	10.8865(3)
Atom	x/a	y/b	z/c	$100 \times U_{iso}$	Fraction
Ba(1)	0.5	0.2030(4)	0	0.7(2)	1
Ba(2)	0.2516(4)	0.5	0	1.1(2)	1
C(11)	0.3044(4)	0	0.06599(8)	0.74(4)	1
C(12)	0	-0.06493(8)	0.3242(4)	0.74(4)	1
C(13)	0.1014(1)	-0.1300(2)	0.2830(3)	0.74(4)	1
C(21)	0.2029(3)	-0.06493(8)	0.2417(3)	0.74(4)	1
C(22)	0.1253(2)	-0.2754(4)	0.1080(1)	0.74(4)	1
C(23)	0.06267(8)	-0.3156(4)	0	0.74(4)	1
C(31)	0.2269(3)	-0.2104(3)	0.06675(8)	0.74(4)	1
C(32)	0.06269(7)	-0.2352(3)	0.2161(3)	0.74(4)	1
C(33)	0.2657(3)	-0.1051(1)	0.1335(2)	0.74(4)	1

PHASE 2: Ba_6C_{60}

Space group	$Im\bar{3}$				
Weight Fraction /%	12.8(4)				
$a/\text{\AA}$	11.1847(4)				
Atom	x/a	y/b	z/c	$100 \times U_{iso}$	Fraction
Ba	0.286(1)	0	0.5	2.1(4)	1
C(1)	0.0000	0.3041	0.0626	1.0	1
C(2)	0.2647	0.1252	0.1014	1.0	1
C(3)	0.2028	0.2266	0.0626	1.0	1

PHASE 3: Ba_3C_{60}

Space group	$Pm\bar{3}n$				
Weight Fraction /%	2.1(2)				
$a/\text{\AA}$	11.335(3)				
Atom	x/a	y/b	z/c	$100 \times U_{iso}$	Fraction
Ba	0.25	0	0.5	2.1(4)	1
C(1)	0.0000	0.3141	0.0647	1.0	1
C(2)	0.1293	0.1047	0.2741	1.0	1
C(3)	0.0647	0.2093	0.2341	1.0	1

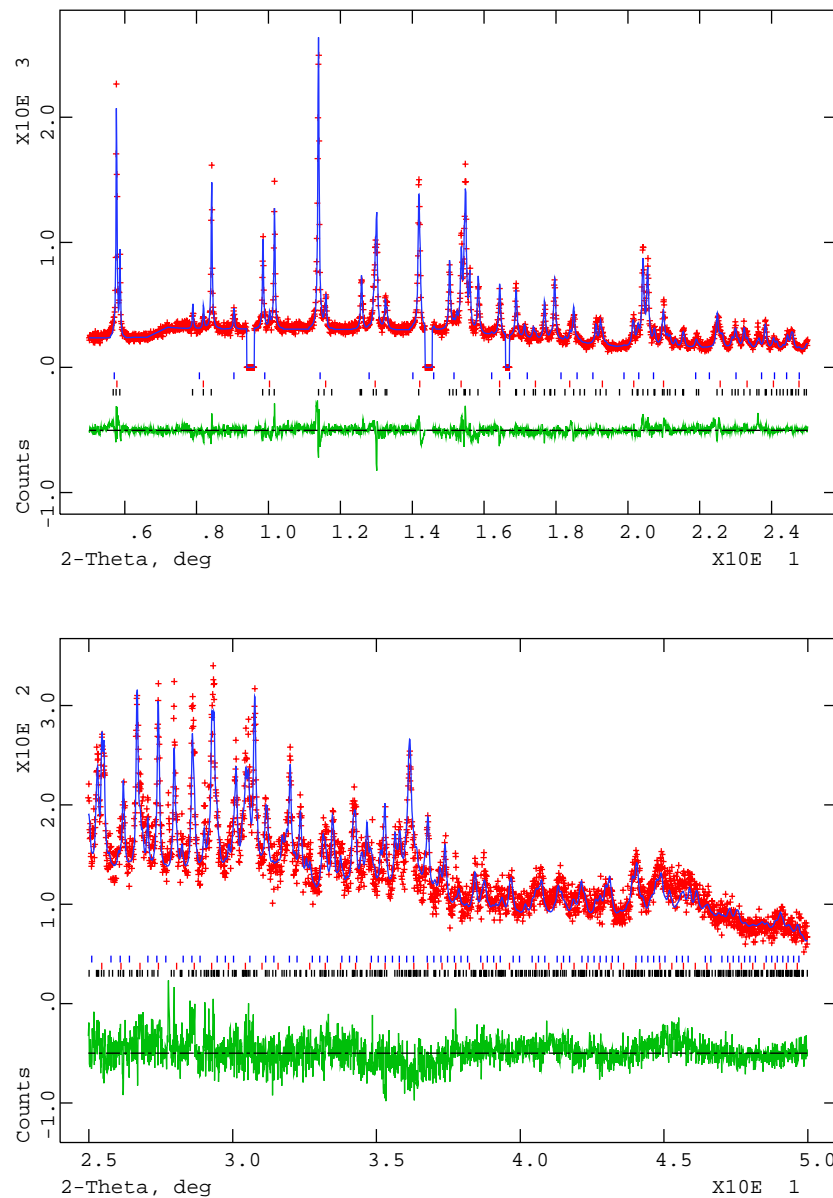


Figure 4.9: Rietveld refinement of the synchrotron X-ray powder diffraction profile of Ba_4C_{60} in space group $Immm$ at 5 K. Red crosses are data points and the solid blue line is a three phase fit. The top and bottom panel show 2θ regions from 5° to 25° and 25° to 50° , respectively. Note the changes in scale between panels. Black, red and blue tick marks show reflections arising from Ba_4C_{60} , Ba_6C_{60} and Ba_3C_{60} , respectively.

Table 4.7: Structural Information for the Rietveld refinement of Ba_4C_{60} (space group $Immm$) at 5 K.

PHASE 1: Ba_4C_{60}

Space group	$Immm$				
Weight Fraction /%	85.2				
$a/\text{\AA}$	11.6008(5)	$b/\text{\AA}$	11.1842(5)	$c/\text{\AA}$	10.8840(4)
Atom	x/a	y/b	z/c	$100 \times U_{iso}$	Fraction
Ba(1)	0.5	0.2030(4)	0	1.5(5)	1
Ba(2)	0.2513(4)	0.5	0	3.6(6)	1
C(11)	0.3019(4)	0	0.06548(8)	1.1(4)	1
C(12)	0	-0.06441(8)	0.3217(4)	1.1(4)	1
C(13)	0.1006(1)	-0.1289(2)	0.2808(3)	1.1(4)	1
C(21)	0.2012(3)	-0.06441(8)	0.2398(3)	1.1(4)	1
C(22)	0.1243(2)	-0.2732(3)	0.1072(1)	1.1(4)	1
C(23)	0.06215(8)	-0.3131(4)	0	1.1(4)	1
C(31)	0.2250(3)	-0.2087(3)	0.06623(8)	1.1(4)	1
C(32)	0.06215(8)	-0.2333(3)	0.2144(3)	1.1(4)	1
C(33)	0.2634(3)	-0.1043(1)	0.1325(2)	1.1(4)	1

PHASE 2: Ba_6C_{60}

Space group	$Im\bar{3}$				
Weight Fraction /%	12.7(4)				
$a/\text{\AA}$	11.1832(5)				
Atom	x/a	y/b	z/c	$100 \times U_{iso}$	Fraction
Ba	0.284(1)	0	0.5	1.7(4)	1
C(1)	0.0000	0.3041	0.0626	1.0	1
C(2)	0.2647	0.1252	0.1014	1.0	1
C(3)	0.2028	0.2266	0.0626	1.0	1

PHASE 3: Ba_3C_{60}

Space group	$Pm\bar{3}n$				
Weight Fraction /%	2.1(2)				
$a/\text{\AA}$	11.330(2)				
Atom	x/a	y/b	z/c	$100 \times U_{iso}$	Fraction
Ba	0.25	0	0.5	1.7(4)	1
C(1)	0.0000	0.3141	0.0647	1.0	1
C(2)	0.1293	0.1047	0.2741	1.0	1
C(3)	0.0647	0.2093	0.2341	1.0	1

The average coordination shell of the Ba^{x+} ions in Ba_4C_{60} , is again defined by the average distances and standard deviation, the closest contact, the distance to the ring centroids and the tilt from the ring centroid. These data are summarised in Table 4.8.

Table 4.8: A description of closest contacts of barium in Ba_4C_{60} for the two distinct sites at 10 and 5 K. All distances are in Å. The numbers in brackets refer to the standard deviation of the measurement, giving a quantification of the distribution of bond lengths.

	10 K	5 K
shortest contact Ba(1)-C distance for pentagon	3.225(4)	3.245(5)
mean Ba(1)-C distance for pentagon	3.24(1)	3.26(1)
Ba(1)-centroid of pentagon distance	2.99	3.02
tilt from ring normal toward C(12)	0.7 °	0.7 °
shortest contact Ba(1)-C distance for hexagon	3.253(3)	3.271(3)
mean Ba(1)-C distance for hexagon	3.27(2)	3.29(2)
Ba(1)-centroid of hexagon distance	2.93	2.96
tilt from ring normal toward C(31)-C(31))'	1.0 °	1.0 °
shortest contact Ba(2)-C distance for pentagon	3.010(6)	3.031(6)
mean Ba(2)-C distance for pentagon	3.19(13)	3.20(12)
Ba(2)-centroid of pentagon distance	2.94	2.97
tilt from ring normal toward C(23)	8.9 °	8.9 °
shortest contact Ba(2)-C distance for hexagon	2.953(3)	2.974(3)
mean Ba(2)-C distance for hexagon	3.25(24)	3.27(14)
Ba(2)-centroid of hexagon distance	2.91	2.94
tilt from ring normal toward C(21)-C(21))'	14.9 °	14.8 °

The data shown here are self consistent with only minor excursions between values at 10 and 5 K despite the longer C-C fulleride cage bond lengths in the case of the 10 K refinement. Comparison with the 295 K contact geometry data (Table.4.3) with

the current data at 5 K reveals that the local environment for symmetrically coordinated Ba(1) ion is basically unchanged. A slight decrease in the shortest Ba(1)-C distances for both pentagonal and hexagonal environments is observed, with a slight reduction in the mean distances between the barium carbon atoms. The anisotropy of the Ba(2) site is still evidenced with displacements towards the same carbon atoms as found previously in the room temperature analysis. The 'hexagonal' coordination still exhibits the shortest barium-carbon contact distance that is remarkably small at 2.974(3) Å. The 'off-centering' of the barium ion is reduced in magnitude somewhat, as described the reduced tilt angles from the ring normal and the reduction of the mean Ba(2)-C distance along with the associated standard deviation. These observation are also applicable to the 'pentagon' environment. With regard to the cation environments at 10 K, we immediately notice the reduced contact distances while retaining the contact geometry. This is unsurprising if we remember that the fulleride cage expanded somewhat in the Rietveld refinement.

To sum up, the already short c axis shows a negligible temperature coefficient of expansion while the a and b axes have much lower coefficients than the alkali metal fullerides. The low coefficients of expansion for the barium fullerides compared to the alkali fullerides is due to a tight crystal packing. These systems are characterised by large charge transfer levels from the barium ions to the fulleride cages that results in large ionic interactions. The symmetrically coordinated Ba(1) ion retains physically reasonable closest contacts to the fulleride cage of 3.245(5) Å at 5 K, a value comparable to that seen in K_3C_{60} . However, the Ba(2) ion has a reduced fulleride contact distance of 2.974(3) Å at 5 K. The short contact distances suggests that there is an overlap between the extended $5d$ wavefunctions of barium and the carbon $2p$.

4.3 Ba₄C₆₀: Neutrons

A high resolution diffraction pattern was recorded on the diffractometer D2B ($\lambda = 1.594$ Å) at 2.5 K. A Ba₄C₆₀ sample (Sussex sample code NT018) of mass 265 mg was indium press-sealed within a vanadium cylindrical sample holder ($\phi = 0.4$ mm) and cooled to 2.5 K in an "orange" helium cryostat. The highest flux was used to collect data over 23 hours.

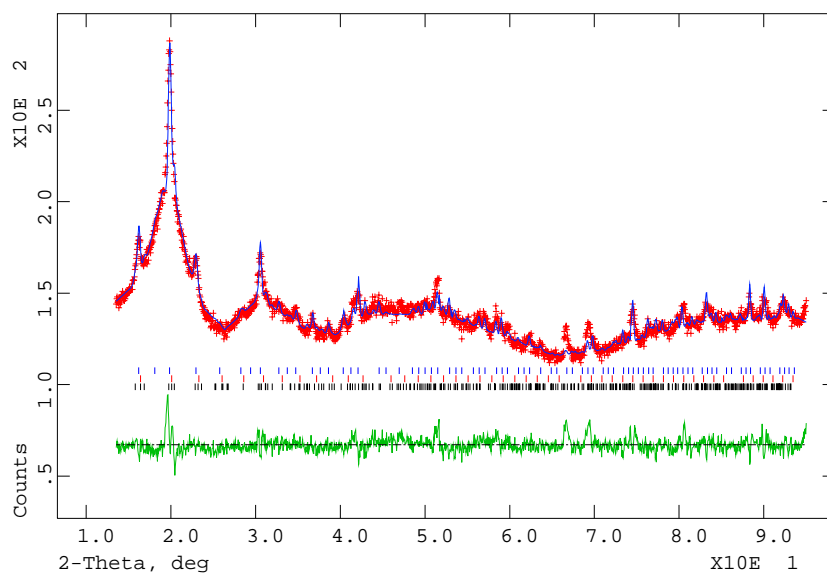


Figure 4.10: High resolution neutron diffraction profile of Ba₄C₆₀ taken at 2.5 K on D2B.

The poor quality of this data set can be put down to extreme disorder within this particular sample with contributions from bulk inhomogeneities of barium concentrations. I stress that due to time pressures the exact quality of this sample could not be confirmed by synchrotron X-ray diffraction prior to this experiment. However, the diffraction profile from a laboratory X-ray diffractometer shows almost phase pure Ba₄C₆₀. The data are none-the-less refined with the Rietveld technique using the

Immm model derived from the BM16 data above (§4.2). The lattice constants of the assumed three phases were refined along with the phase fractions and the histogram parameters (Table 4.9). The fit being shown in Fig.4.10. The extremely low χ^2 is an artifact of refining too many parameters with low statistics data. The Ba_4C_{60} *c*-lattice constant is too short by 0.02 Å compared to the 5 K X-ray data (a factor of 0.2%), reflecting the poor definition of the Bragg reflections within the data. We cannot safely extract any meaningful information out of this data set. With better prepared sample we may be able to come back and re-address the questions that stimulated this experiment. In principle, with a neutron data set, one should be able to extract information of the fulleride geometry not clearly visible in the X-ray data. This information might reflect a modification of the fulleride cage as a result of a large charge transfer or even be indicative of Ba-C bonding.

Table 4.9: Histogram and phase contributions for Ba₄C₆₀ neutron data collected at 2.5 K on D2B.

HISTOGRAM	
Rwp, Rp /%	2.7, 2.0
χ^2	0.14
U /($\times 10^2$) ^o	754
V /($\times 10^2$) ^o	-64
W /($\times 10^2$) ^o	10
PHASE 1: Ba₄C₆₀	
Space group	Immm
Weight Fraction /%	38.6
a/ Å	11.616(5)
b/ Å	11.268(6)
c/ Å	10.866(4)
PHASE 2: Ba₆C₆₀	
Space group	Im $\bar{3}$
Weight Fraction /%	26.5
a/ Å	11.314(5)
PHASE 3: Ba₃C₆₀	
Space group	Pm $\bar{3}$ n
Weight Fraction /%	34.9
a/ Å	11.3442(7)

4.4 Effects of Pressure

We have already seen evidence for extremely close contacts between barium and carbon in Ba₄C₆₀ and an interesting anisotropy of the Ba₄C₆₀ lattice on cooling. In an effort to further understand the bulk structural properties of Ba₄C₆₀, more forceful methods than changing temperature are needed; this is where we turn to high pressure experiments to better define phase changes and possible anisotropy in non-cubic systems. The evolution of lattice constants and the strongly scattering barium positions can be refined with appreciable accuracy up to 10 GPa when using the intense X-ray source of the ESRF. We will be then in a position to comment

upon the findings of Sparn *et al.*[163] that the volume dependence of T_c in Ba_4C_{60} deviates from the alkali metal norm by a factor of two. The main point here is that, in contrast to the alkali metal fullerides, there seems to be no universal scaling of T_c with interfulleride spacing for the alkaline earth superconductors.

Our first experiment using high pressure on these alkaline earth systems was on Ba_6C_{60} .

4.4.1 Ba_6C_{60}

The sample was loaded in a DAC cell (600 and 700 μm diameter faces) with a stainless steel gasket (200 μm thick) preindented to 75 μm with a 200 μm diameter electro-eroded hole. Prior to this loading in a glovebox, two small rubies were placed near the centre of one diamond face. The pressure transmitting medium was degassed silicone oil that was subsequently stored in the glovebox. After hand sealing the cell and removing it from the glovebox, a membrane pressure of 5 bar was applied to ensure it was sealed. A ruby sample (from the same batch of rubies as in the cell) was used to calibrate the ruby fluorescence at ambient pressure. The resonance occurred at $\lambda_0 = 6943.44 \text{ \AA}$ and was introduced into an on-line fitting program that uses Eqn.2.20 to calculate the pressure. At every pressure reading we note the actual resonance wavelength and the calculated pressure. The Ba_6C_{60} sample itself was prepared by K. Kordatos and the majority Ba_6C_{60} composition (Ba_4C_{60} and Ba_3C_{60} impurities) was determined by synchrotron diffraction using the MAR scanner at the SNBL.

Two dimensional images were collected using the 'traditional' image plate and Storm scanner setup on ID30 with typical exposure times of 20 minutes. The beam was Si(111) monochromised without the microfocusing option, the size being defined

by clean-up slits as $65 \times 65 \mu^2\text{m}$. Silicon calibration ($a = 5.43094 \text{ \AA}$ at 25°C) gave the wavelength as 0.63635 \AA and a sample to image plate distance, D , of 446.226 mm . Traditional one-dimensional images are produced using the FIT2D[98] program as described in §2.4.1 with careful masking of single crystal ruby peaks.

Pressure evolution of selected diffraction patterns in the range 0.46 to 9.39 GPa is shown in the upper panel of Fig.4.11. The low pressure patterns are extremely well resolved but above $\sim 2 \text{ GPa}$ the breadth of the peaks can be expected to reduce the accuracy of any extracted structural parameters.

Exploratory Le Bail refinements with the PROFIL refinement program[118] using Ba_6C_{60} , Ba_4C_{60} and Ba_3C_{60} phases were sufficient in describing the data. One unindexed peak remains at 11° that could not be attributed to a BaO phase. Due to overlap between this work and the structural elucidation of Ba_4C_{60} above, initial Rietveld refinements were performed using the published structures for each phase including the *old*, *Immm* structure of Ba_4C_{60} where the fulleride units are rotated 90° from their true orientation as we found in §4.2. After the structure of Ba_4C_{60} was solved a return to this data was appropriate and I shall show the results derived from an analysis based on the room temperature structure derived from the BM16 synchrotron X-ray diffraction data.

Initial lattice constants from the 'wrong Ba_4C_{60} orientation' refinement were used to scale the BM16 derived atomic coordinates of all three phases at each pressure. This can be justified by the observed incompressibility of the C_{60} cage[172]. Immediate reductions in R_{wp} of the order of 0.5% were observed, as compared to the original 'wrong' refinements, resulting in values of $R_{wp} \sim 11\%$.

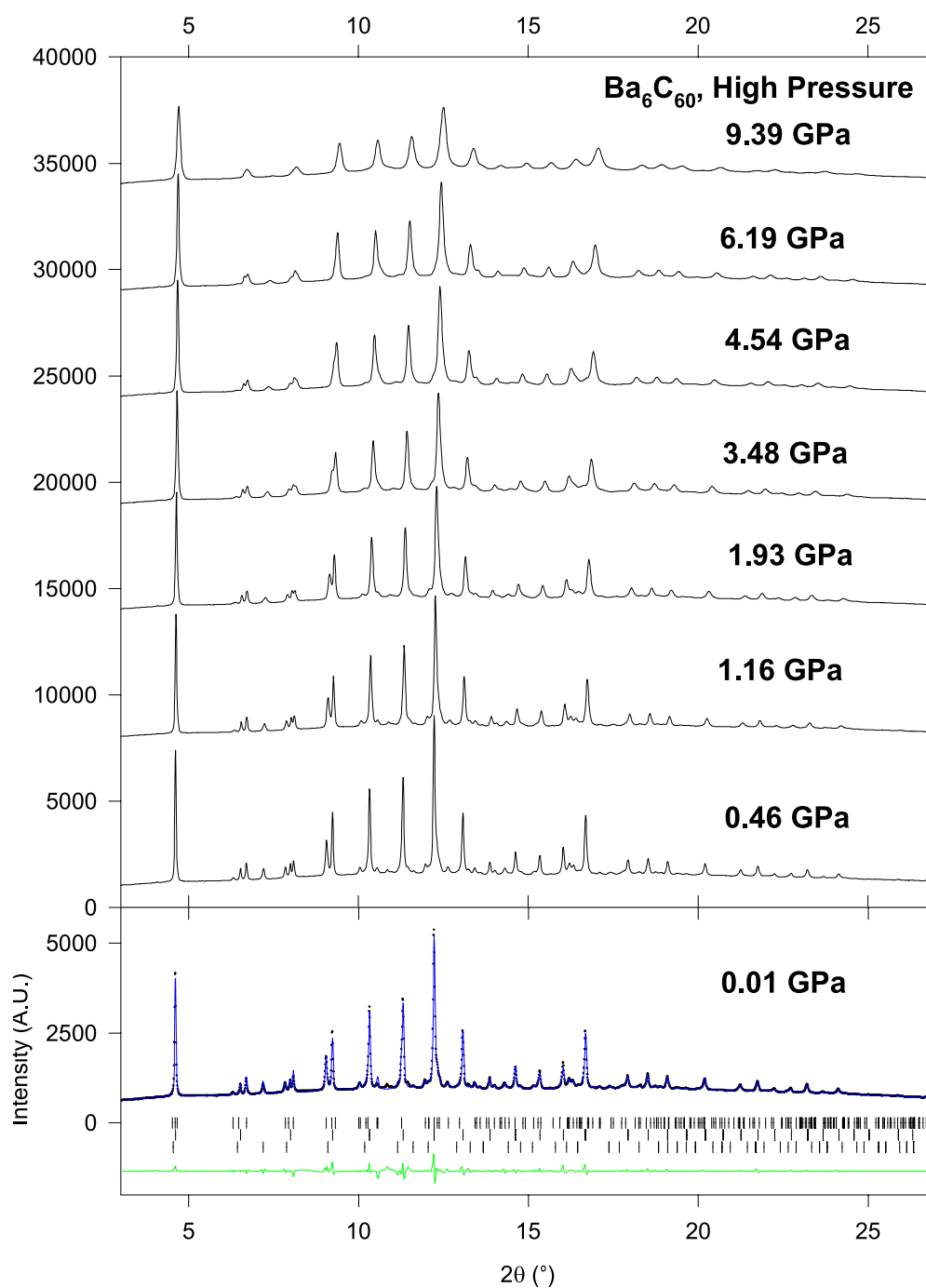


Figure 4.11: (Top) Pressure dependence of the X-ray diffraction patterns of Ba_6C_{60} at selected pressures. (Bottom) Rietveld refinement of data taken at 0.01 GPa. Data are shown as black points while a three phase fit (described in the text) is shown as a solid blue line and the difference between measured and calculated profiles as a green line below. Ticks mark reflection positions of Ba_4C_{60} (upper), Ba_6C_{60} (middle) and Ba_3C_{60} (lower).

Pseudo-Voigt peak shapes were constrained to be the same between phases, except above 4.54 GPa, where it became apparent that reflections arising from Ba_3C_{60} were not well fitted by this constraint and broadened faster than the other two phases. To overcome this without adding too many parameters to the fit of the rapidly broadening spectra, the W breadth parameter was made independent for each phase. Ba_6C_{60} maintained the sharper peaks, with Ba_4C_{60} having a W parameter about twice that value, while a 5-fold increase in the value for Ba_3C_{60} was observed. Values for η , the peak shape mixing parameter, varied smoothly from a value of 0.77(2) at 0.01 GPa to 0.46(2) at 7.23 GPa. This reflects the increased Gaussian like character of the profile arising from peak broadenings.

Analysis of the weights of each phase as a function of pressure revealed a pressure dependence that is probably linked to the reduced resolution of peaks at higher pressures. This was compensated for by taking the average compositional ratios 0.694:0.278 :0.029 for Ba_6C_{60} : Ba_4C_{60} : Ba_3C_{60} and adjusting the individual profile scale-factors accordingly to maintain this ratio. The scales were then fixed. Further improvement was obtained by allowing the 'rigid' fulleride cage of the majority Ba_6C_{60} phase to expand/contract radially, while still maintaining high symmetry. Typical R_{wp} values are now 7- 9%. Refined parameters for the data sets at applied pressures of 0.01, 1.45 and 6.19 GPa are shown in Table 4.10. The result of the refinement of the data at 0.01 GPa is shown graphically in the bottom panel of Fig.4.11.

Table 4.10: Summary of the refined parameters for the Rietveld analysis of the diffraction profiles of Ba₆C₆₀ at 0.01, 1.45 and 6.19 GPa.

Parameter	0.01 GPa	1.45 GPa	6.19 GPa
$R_{wp} / \%$	12.3	9.9	6.4
$R_{exp} / \%$	6.5	8.4	8.5
$\lambda / \text{\AA}$	0.63635	0.63635	0.63635
$\Delta_{2\theta} / ^\circ$	0.0041(6)	0.0063(6)	0.0023(5)
$U / ^\circ$	0.28(4)	0.7(1)	1.7(1)
$V / ^\circ$	-0.037(8)	-0.04(2)	-0.06(4)
$W / ^\circ$	0.0035(4)	0.0036(6)	Ba ₆ C ₆₀ : 0.0054(6)
	-	-	Ba ₄ C ₆₀ :0.012(3)
	-	-	Ba ₃ C ₆₀ :0.034(9)
η	0.77(2)	0.72(2)	0.59(1)

Ba₆C₆₀

$a / \text{\AA}$	11.2018(6)	11.1312(7)	10.9875(6)
Ba z	0.2813(5)	0.2807(4)	0.2819(3)
Ba $B_{iso} / \text{\AA}^2$	7.0(2)	6.0(2)	5.6(2)
C $B_{iso} / \text{\AA}^2$	2.7(5)	0.6(3)	0.8(2)

Ba₄C₆₀

$a / \text{\AA}$	11.601(2)	11.498(3)	11.295(5)
$b / \text{\AA}$	11.291(2)	11.135(3)	10.830(4)
$c / \text{\AA}$	10.897(2)	10.871(3)	10.812(4)
Ba(1) y	0.203(2)	0.199(2)	0.201(2)
Ba(2) x	0.244(2)	0.250(2)	0.266(2)
Ba $B_{iso} / \text{\AA}^2$	4.7(4)	5.0(3)	3.8(3)
C $B_{iso} / \text{\AA}^2$	2.2(5)	2.6(4)	2.0(2)

Ba₃C₆₀

$a / \text{\AA}$	11.363(4)	11.263(5)	11.01(2)
Ba $B_{iso} / \text{\AA}^2$	6	6	6
C $B_{iso} / \text{\AA}^2$	2.7(5)	0.6(3)	0.8(2)

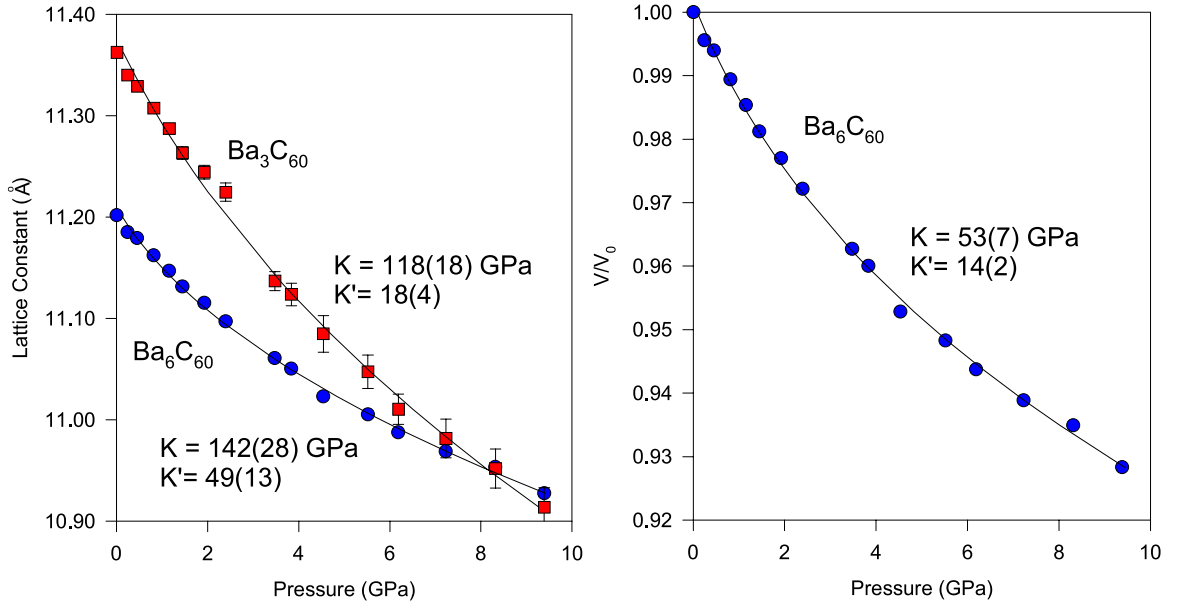


Figure 4.12: Left: evolution of the cubic lattice constants of Ba_6C_{60} and Ba_3C_{60} as a function of pressure, with error bars. The lines are fits to a second order Murnaghan equation of state with parameters given. Right: Normalised volume of the unit cell of Ba_6C_{60} as a function of pressure also fitted to the Murnaghan EOS.

Fig.4.12 details the pressure evolution of the extracted lattice constants for the cubic Ba_6C_{60} and Ba_3C_{60} phases (left) and the volume dependence for Ba_6C_{60} normalised to ambient pressure (right). A smooth decrease of all curves is apparent and even though error bars are plotted they are only visible for the 3% Ba_3C_{60} impurity. In relation to data taken at 295 K, the lattice constants for the lowest pressure data are longer by $\sim 0.004\text{--}0.009$ Å and are outside the scope of the calculated errors. This could be due to inaccuracies in the image plate integration method that results in an effective peak shift. The solid lines are fits to the semi-empirical second order

Murnaghan equation of states[145, 146] (EOS):

$$P = \frac{3}{2}K \left[\left(\frac{V_0}{V} \right)^{\frac{7}{5}} - \left(\frac{V_0}{V} \right)^{\frac{5}{3}} \right] \left[1 - \frac{4}{3} \left(4 - \frac{dK}{dP} \right) \left(\left(\frac{V_0}{V} \right)^{\frac{5}{3}} - 1 \right) \right] \quad (4.1)$$

This details the pressure dependence of normalised volume, $\frac{V}{V_0}$ as functions of the atmospheric-pressure isothermal bulk modulus and its derivative K' . Hence a larger value for K indicates a less compressible solid. The bulk modulus of Ba_6C_{60} is much greater at 53(7) GPa, than that of pristine C_{60} where $K = 18.1(1.8)$ GPa[142]. Even in comparison to the tightly packed polymeric phase of $\text{Na}_2\text{CsC}_{60}$ ($K = 28(1)$ GPa[173]) which exhibits a much reduced compressibility along the chain axis bonding direction compared to the other axes, Ba_6C_{60} is approximately half as compressible. Also, the lattice constant for the essentially isostructural K_6C_{60} is, at 11.38 Å[166], $\approx 1.6\%$ larger than that of Ba_6C_{60} at ambient pressure. We can interpret these results for Ba_6C_{60} in terms of it being much less compressible than C_{60} and the alkali metal fullerenes as a result of increased electrostatic interactions and a tighter crystal packing.

The same equation was fitted to the individual lattice constants for both phases to allow comparison between the curves. Ba_3C_{60} is more compressible than Ba_6C_{60} with a steeper derivative. This is understandable because of the tighter crystal packing in Ba_6C_{60} , which also has a smaller lattice constant at zero pressure, due to stronger ionic forces.

Equivalent plots for extracted values for the Ba_4C_{60} phase are shown in Fig.4.13. We can see that the Ba_4C_{60} cell is more compressible than Ba_6C_{60} , but much less so than the alkali fullerenes. More striking however is the extreme anisotropy in the behaviour of the individual lattice constants. Up until 6 GPa, the c axis remains the shortest but a combination of its incompressibility and the larger, more normal, compressibility of the b axis results in a crossover between these axes above ~ 6.5 GPa

after which b retains the shorter characteristic. The overall behaviour reflects that shown as a function of temperature, with a small compressibility, κ of $-9.8(8) \times 10^{-4}$ GPa $^{-1}$ along c .

The initial slope of the volume curve can be fitted to extract the volume compressibility, $d\ln(V)/dP$, so as to compare the dependence of superconducting transition temperature with pressure to those of the alkali metal fullerenes. We find $d\ln(V)/dP = -0.0138(5)$ GPa $^{-1}$ for Ba $_4$ C $_{60}$. This is quite similar to that obtained for Ba $_6$ C $_{60}$ at $-0.0109(4)$ GPa $^{-1}$, but over four times that obtained for K $_3$ C $_{60}$. Sparn *et al* gives a value for dT_c/dP for Ba $_4$ C $_{60}$ at 1.9 K-GPa $^{-1}$ [163]. Hence, we calculate $\Gamma = 20.25$, which is larger than the value derived by Sparn from assuming a compressibility of K $_3$ C $_{60}$. In absolute scales it is over twice as large as typical values for the alkali metal fullerenes K $_3$ C $_{60}$ and Rb $_3$ C $_{60}$.

The next section will focus on the high pressure results of a Ba $_4$ C $_{60}$ rich sample.

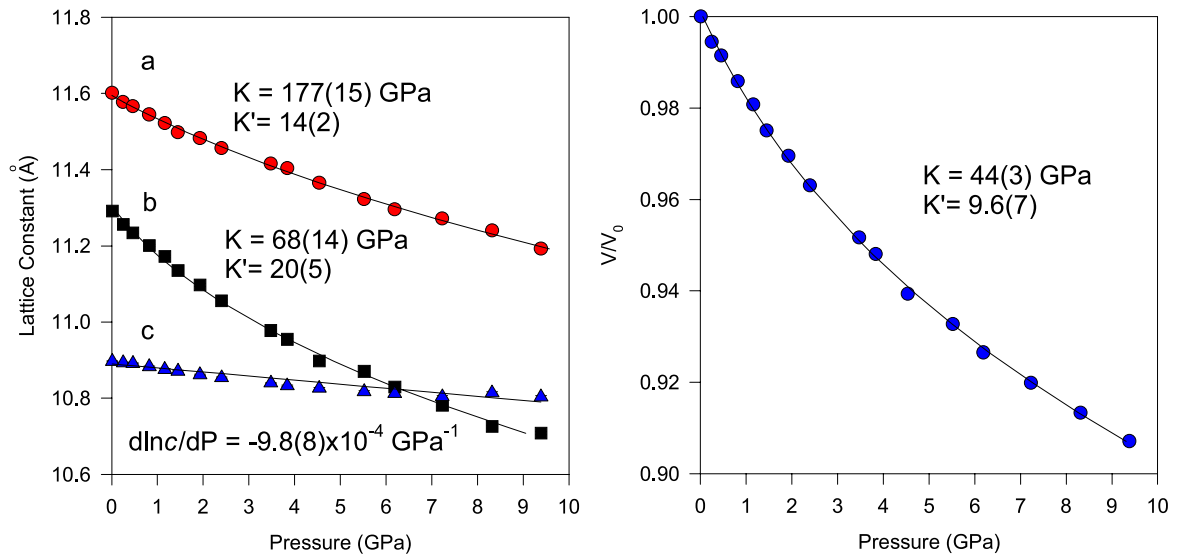


Figure 4.13: Left: evolution of the orthorhombic lattice constants of Ba_4C_{60} as a function of pressure. Error bars are plotted. Lines for the a and b lattice constants are fits to a second order Murnaghan equation of state with parameters given next to each lattice. For the c lattice constant a linear equation is fitted to extract the compressibility. Right: Normalised volume of the unit cell as a function of pressure for Ba_4C_{60} , the line shows a fit to the Murnaghan EOS.

4.4.2 Ba₄C₆₀

Our best Ba₄C₆₀ sample (JAIST) was loaded in a DAC cell (600 and 600 μm diameter faces) with a stainless steel gasket (200 μm thick) preindented to 70 μm with a 200 μm diameter electro-eroded hole. Prior to this loading in a glovebox, two small rubies were placed near the centre of one diamond face. The pressure transmitting medium was degassed silicone oil. After hand sealing the cell and removing it from the glovebox, a membrane pressure of 5 bar was applied to ensure it was sealed. Two dimensional images (Fig.4.14) were collected using the image plate and Storm scanner setup on ID9 with typical exposure times of 15 minutes and a beam current of ~ 70 mA. The beam was Si(111) monochromised and cut down to a size of $30 \times 40 \mu\text{m}^2$.

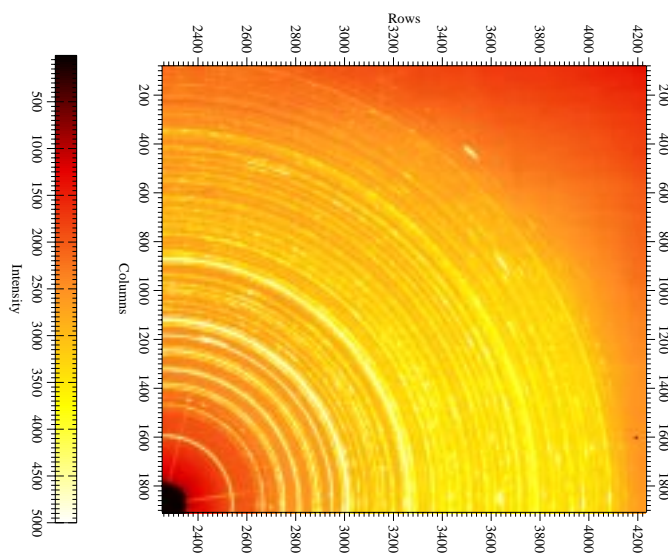


Figure 4.14: Section of a two dimensional image of Debye-Scherrer cones collected at 0.04 GPa for Ba₄C₆₀.

Silicon calibration ($a = 5.43094 \text{ \AA}$ at 25°C) gave the wavelength as 0.49953 \AA , and a sample to image plate distance, D , of 444.127 mm , a rotation of the 2D detector

plane of 0.441° about an axis 10.486° from the vertical. Traditional one-dimensional images are produced using the FIT2D program[98], as described in §2.4.1, following careful masking of single crystal ruby peaks. Due to a technical hitch (the scanner broke), we were limited to an upper pressure of 3.28 GPa for this series of experiments, up to which pressure the details in the powder pattern are amazingly well defined.

Again the data were Rietveld refined using scaled atomic coordinates from the BM16 refinement above. The background was defined by linear interpolation of selected points, while the peak shape function was chosen as pseudo-Voigt.

Profile parameters were constrained to be refined together for all phases up to 1.5 GPa where once again, Ba_3C_{60} displayed broader Bragg reflections. Ba_4C_{60} and Ba_6C_{60} profiles were still constrained, while those of Ba_3C_{60} were left free. Carbon isotropic temperature factors were fixed at 1 \AA^2 for all three phases, and those of barium in the minority phases were constrained to refine together. In later stages of refinement, the majority phase carbon cage was allowed to dilate radially, in a similar fashion as above. Bond lengths remained constant at $1.437(4) \text{ \AA}$ in excellent agreement with the room temperature, ambient pressure refinement of §4.2. Constraints on percentage contributions to the overall pattern were once again employed with 85.6% Ba_4C_{60} , 12.7% Ba_6C_{60} and 1.7% Ba_3C_{60} which was the average encountered through the free stages of refinement. These percentages are slightly different from those of the BM16 refinement though this is not too surprising considering the minute amounts of this three phase sample in the beam.

Table 4.11: Summary of refined parameters for the diffraction profiles of Ba_4C_{60} at 0.04, 1.49 and 2.64 GPa. For the peak shape values, the numbers in square brackets show the values for Ba_3C_{60} .

Parameter	0.04 GPa	1.49 GPa	2.64 GPa
R_{wp}	10.33	11.70	12.40
R_{exp}	6.75	7.11	8.35
$\lambda / \text{\AA}$	0.49953	0.49953	0.49953
$\Delta_{2\theta} / ^\circ$	0.0046(4)	0.0049(4)	0.0047(5)
$U / ^\circ$	0.06(3)	0.13(5) [0.7(2)]	0.34(7) [0.5(1)]
$V / ^\circ$	-0.009(4)	-0.024(6) [-0.10(5)]	-0.014(9) [-0.014(6)]
$W / ^\circ$	0.0015(2)	0.0011(2) [0.0054(6)]	0.0015(3) [0.012(1)]
η	0.56(2)	0.53(2)	0.51(2)

Ba_4C_{60}

$a / \text{\AA}$	11.6171(7)	11.5242(9)	11.476(1)
$b / \text{\AA}$	11.2440(6)	11.0811(9)	10.983(1)
$c / \text{\AA}$	10.8876(6)	10.8637(9)	10.850(1)
Ba(1) y	0.2000(4)	0.1979(5)	0.1965(5)
Ba(2) x	0.2479(4)	0.2539(5)	0.25775(5)
Ba(1) $B_{iso} / \text{\AA}^2$	2.2(2)	1.9(2)	2.0(2)
Ba(2) $B_{iso} / \text{\AA}^2$	2.0(1)	1.8(2)	1.9(2)

Ba_6C_{60}

$a / \text{\AA}$	11.2018(8)	11.133(1)	11.087(1)
Ba z	0.286(1)	0.286(1)	0.289(1)
Ba $B_{iso} / \text{\AA}^2$	3.4(3)	1.5(3)	0.7(2)

Ba_3C_{60}

$a / \text{\AA}$	11.341(5)	11.24(1)	11.16(2)
Ba $B_{iso} / \text{\AA}^2$	3.4(3)	1.5(3)	0.7(2)

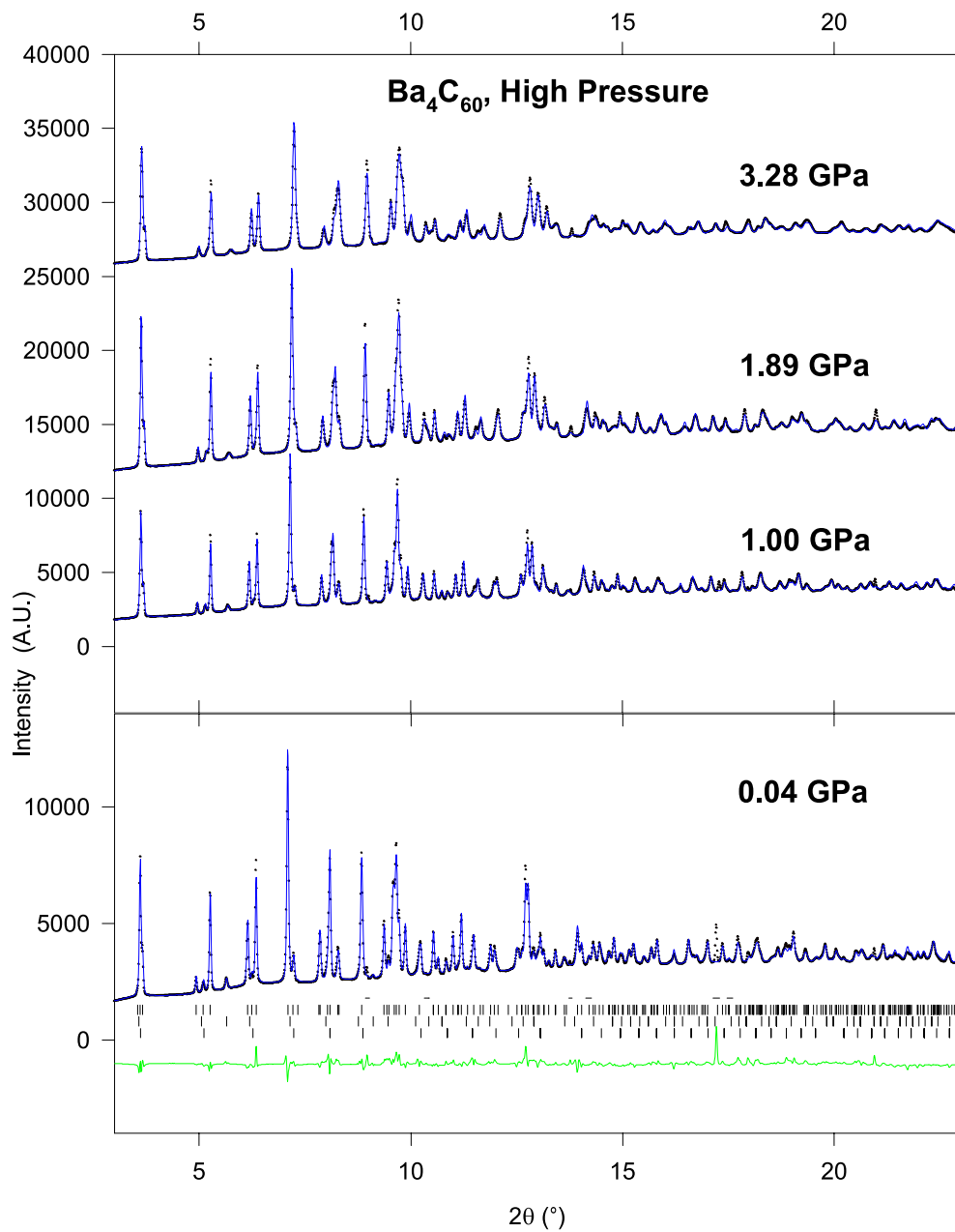


Figure 4.15: Pressure dependence of selected diffraction profiles of Ba_4C_{60} . The dotted points are observed values, while the solid lines are Rietveld fits to the model given in the text. The lower panel also shows a green difference curve and tick marks for the three individual phases (top Ba_4C_{60} , middle Ba_3C_{60} and bottom Ba_6C_{60}) for the data at 0.04 GPa. Horizontal bars show excluded regions that are due to impurities of BaO .

Fig.4.15 presents the base pressure Rietveld refined data and a difference curve with data at additional pressures (observed and calculated) in the upper panel. In general, excellent fits are observed with R_{wp} values between 10.3 and 12.5% and a typical R_{exp} of 6.5%. A summary of parameters is given in Table 4.11. Lattice constants (Fig.4.16) are around 0.005 Å longer than their 295 K data equivalent, and are in line with the data from the previous experiment. Along with a decrease in the fitted error bars of the bulk modulus of Ba_4C_{60} , there is a decrease in magnitude in comparison to the first experiment. This could be due to a more exact observation of peak positions due to these reflections contributing more to the overall pattern. Since these data are from a majority phase Ba_4C_{60} , it is more logical to trust these numbers more than those from the Ba_6C_{60} experiment with the previous data seen as a check on the magnitudes of these values.

Confirmation of the anisotropy within the crystal is evidenced with the compressibility of the c axis being extremely small at $\kappa = -1.16(4) \times 10^{-3} \text{ GPa}^{-1}$, a value that agrees within experimental error to the previous high pressure experiment on the majority Ba_6C_{60} phase sample. In contrast, the compressibility along the b axis is an order of magnitude larger, $\kappa = -1.4(3) \times 10^{-2} \text{ GPa}^{-1}$.

From the initial slope of the volume curve we find the volume compressibility to be $d \ln(V)/dP = -0.0149(4) \text{ GPa}^{-1}$. This is somewhat larger than the value we obtained from the Ba_6C_{60} experiment. Hence, $\Gamma = 18.75$, lying halfway between our previous value and the one calculated by Sparn[163]. The superconducting transition temperature in Ba_4C_{60} is more sensitive to changes in volume than K_3C_{60} and Rb_3C_{60} . We can be quite sure of this value now and confirm the conclusions of Sparn *et al.*[163]. The alkaline earth fullerides have no universal scaling of T_c with interfulleride spacing.

Ba_4C_{60} has a negative dependence of T_c with pressure ($dT_c/dP = -1.9 \text{ K/GPa}$)[163] whereas Ca_5C_{60} is positive at $dT_c/dP = +1.1 \text{ K/GPa}$ [174].

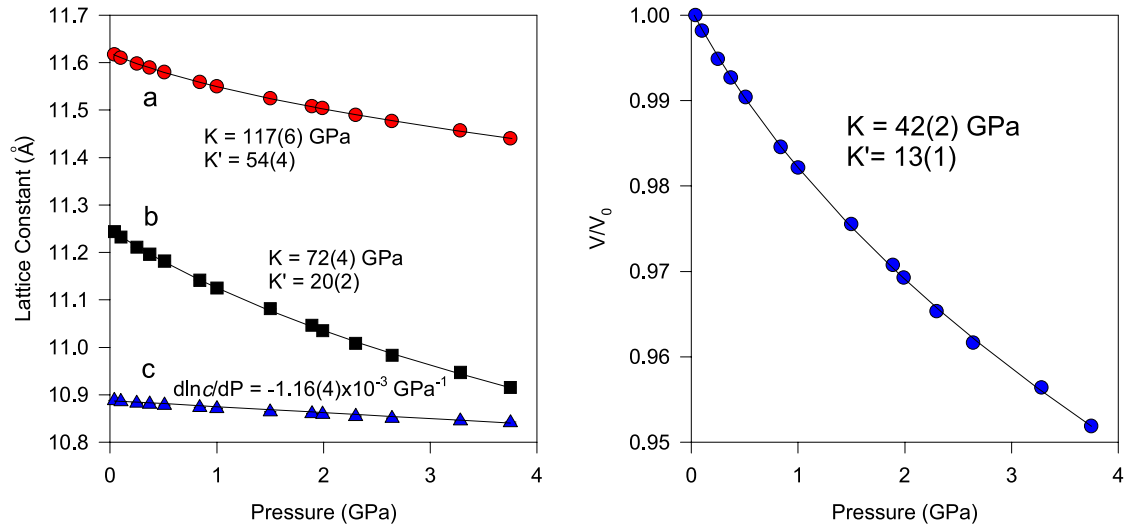


Figure 4.16: Left: evolution of the orthorhombic lattice constants of Ba_4C_{60} as a function of pressure (error bars are plotted). Lines for the a and b lattice constants are fits to a second order Murnaghan equation of state with parameters given next to each lattice. For the c lattice constant a linear equation is fitted to extract the compressibility. Right: Normalised volume of the unit cell as a function of pressure for Ba_4C_{60} , the line shows a fit to the Murnaghan EOS.

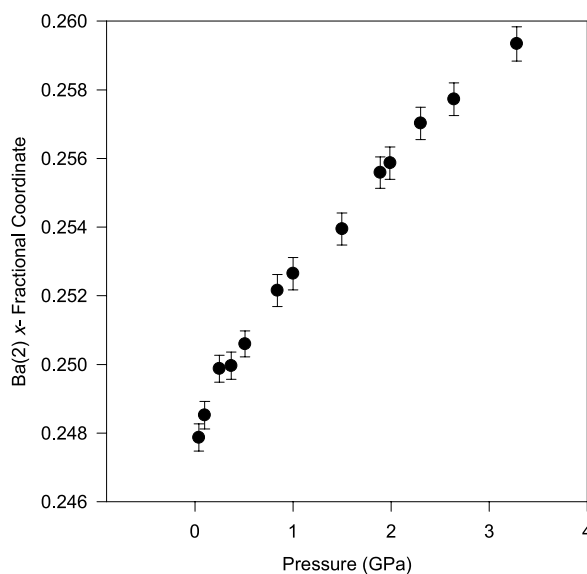


Figure 4.17: Evolution of x fractional coordinate of the Ba(2) ion as a function of pressure in Ba_4C_{60} (error bars are plotted).

Positional parameters for the independent barium sites are seen to vary smoothly over the range of pressures studied here. The Ba(1) ion seems to have no obvious correlation with pressure, while the fractional x coordinate of Ba(2) moves from 0.248 at ambient pressures through to 0.259 above 3 GPa (Fig.4.17) What this implies for the local coordination environments and close contacts of each barium ion can be described in terms already established for our ambient pressure data. Taking data at

pressures of 0.04 and 2.64 GPa as examples, we can characterise these structures by the parameters given in Table 4.12.

At 0.04 GPa, we have the same contact geometry at the two barium sites with parameters that are in excellent agreement with the ambient pressure data. Upon application of pressure, there is a shift of the Ba(1) ion position. The Ba(1) ion is now a little closer to the centroid of the pentagonal face, but the difference with the ambient pressure BM16 data is unremarkable. However, there is a larger change with respect to the hexagonal coordinating face of the fulleride unit. At 2.64 GPa both the closest Ba(1)-C(hexagon) contact and the mean Ba(1)-C distance have reduced by ~ 0.1 Å. This is accompanied by a slight shift towards the hexagonal face and a slight movement towards a more centred position. All contact distances are still longer than 3.20 Å. For the Ba(2) ion environment, the magnitude of the off-centering of the barium ion from the pentagonal face is reduced while it is now 0.08 Å closer to the centroid after application of pressure. The mean Ba-C distance has reduced markedly unlike for the pentagonal environment of the Ba(1) ion. For the hexagonal contact face, the mean Ba(2)-C distance has reduced to 3.12(19) Å, that is the result of a shift of 0.1 Å towards the ring centroid and a reduction of the tilt from the ring normal.

Table 4.12: A description of closest contacts of barium in Ba_4C_{60} for the two distinct sites at 0.04 and 2.64 GPa. All distances are in Å. The numbers in brackets refer to the standard deviation of the measurement, giving a quantification of the distribution of bond lengths.

	0.04 GPa	2.64 GPa
shortest contact Ba(1)-C distance for pentagon	3.29	3.25
mean Ba(1)-C distance for pentagon	3.29(1)	3.26(1)
Ba(1)-centroid of pentagon distance	3.07	3.02
tilt from ring normal toward C(12)	0.7 °	0.1 °
shortest contact Ba(1)-C distance for hexagon	3.29	3.20
mean Ba(1)-C distance for hexagon	3.31(1)	3.21(1)
Ba(1)-centroid of hexagon distance	2.95	2.87
tilt from ring normal toward C(31)-C(31))'	0.9 °	0.6 °
shortest contact Ba(2)-C distance for pentagon	3.04	3.00
mean Ba(2)-C distance for pentagon	3.23(14)	3.15(10)
Ba(2)-centroid of pentagon distance	2.99	2.91
tilt from ring normal toward C(23)	9.7 °	7.3 °
shortest contact Ba(2)-C distance for hexagon	2.99	2.95
mean Ba(2)-C distance for hexagon	3.30(25)	3.14(19)
Ba(2)-centroid of hexagon distance	2.98	2.88
tilt from ring normal toward C(21)-C(21))'	15.4 °	13.3 °

The dependence of the Ba_6C_{60} and Ba_3C_{60} lattice constants upon pressure are shown in Fig.4.18, with the normalised volume of Ba_6C_{60} fitted to the Murnaghan EOS. Overall good agreement between these results and those of the previous experiment is achieved, with the lower error bars obtained in the present case.

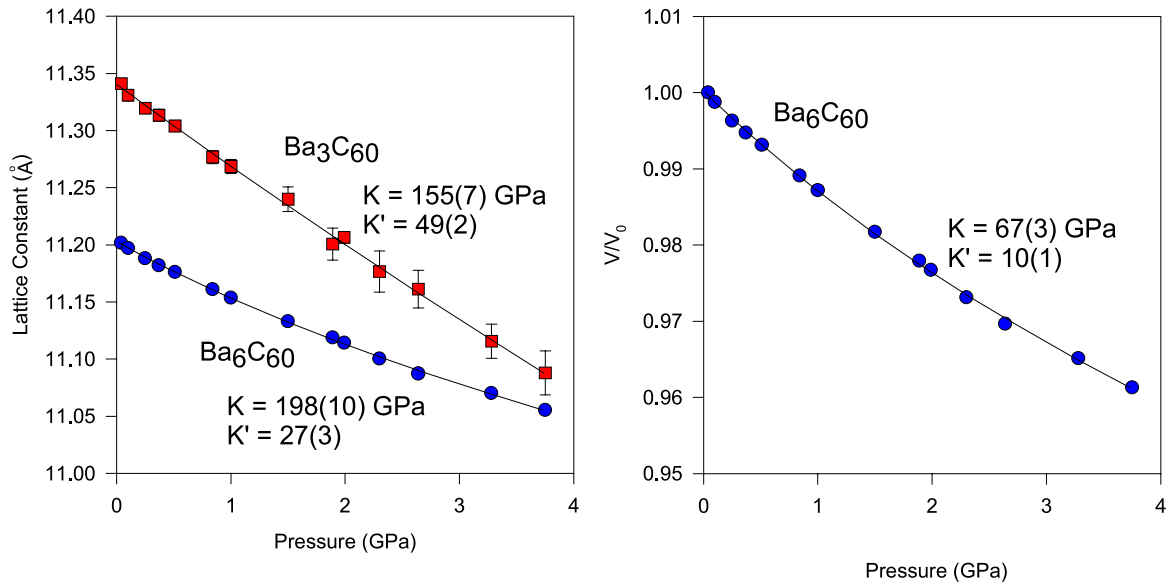


Figure 4.18: Left: evolution of the cubic lattice constants of Ba_6C_{60} and Ba_3C_{60} as a function of pressure (error bars are plotted). The lines are fits to a second order Murnaghan equation of state with parameters given. Right: Normalised volume of the unit cell of Ba_6C_{60} as a function of pressure also fitted to the Murnaghan EOS.

We have seen how incompressible Ba_4C_{60} is along the c axis, and that the cation $\text{Ba}(2)$ moves significantly closer to the fulleride cage upon the application of pressure while maintaining the shortest Ba-C distances. As with the low temperature data, the incompressible c axis is very intriguing and it is tempting to assign these observations as a result of Ba-C bonding.

4.5 Conclusion

On doping from the cubic Ba_3C_{60} to cubic Ba_6C_{60} , a structural change via orthorhombic Ba_4C_{60} is observed. No evidence of a Ba_5C_{60} phase has been shown. We have performed detailed Rietveld refinements of high resolution synchrotron powder diffraction data of Ba_4C_{60} collected at 295, 10 and 5 K. We find that the best description of this structure is within the orthorhombic space group *Immm*. The structure is characterised by orientationally ordered fulleride units with the barium ions occupying two distinct sites. The barium ions can be distinguished by their closest contacts distances to the fullerene cages and how regularly they coordinate to the exposed pentagonal and hexagonal fulleride faces. At 295 K, one barium site has a closest distance of 3.26316(4) Å while the other exhibits extremely close contacts of 2.98969(4) Å. No structural phase transition is apparent on cooling to 5 K. As such Ba_4C_{60} is the first non-cubic ambient pressure fulleride superconductor with a T_c of 6.8 K.

We have shown that the room temperature Ba_4C_{60} *Immm* model is scalable down to low temperatures. The closest barium-carbon interaction at 5 K now occurs at 2.974(3) Å, a distance that is very short in comparison to a K-C distance of 3.20 Å in K_6C_{60} and the average Cs-C distance of ~ 3.6 Å in the isostructural Cs_4C_{60} . We find a severe anisotropy in the expansivity of the lattice constants of Ba_4C_{60} between 5 and 295 K with the *c* axis showing negligible expansivity while the *b* axis shows the largest coefficient of expansion at $1.565(8) \times 10^{-5} \text{ K}^{-1}$. The values for the coefficients of expansion for cubic A_3C_{60} salts are approximately twice as large as that of the Ba_4C_{60} *b* axis. The local barium ion environments at 5 K are similar to those found at room temperature, while the magnitude of the displacement of the Ba(2) ion from the ring centroids is somewhat reduced. Even though there is an uncertainty in

the refinement at 10 K, we cannot attribute the slight modification of the Ba(2) ion environment to the occurrence of superconductivity. Additionally, tentative values for the coefficient of expansion for Ba_6C_{60} and Ba_3C_{60} are $3.9(4) \times 10^{-6} \text{ K}^{-1}$ and $2.4(8) \times 10^{-6} \text{ K}^{-1}$, respectively. These are of the same order of magnitude as that extracted for the Ba_4C_{60} a axis.

Further structural studies to pressures of 9.4 GPa have been performed on Ba_6C_{60} and Ba_4C_{60} . The barium fullerides have been characterised by their low compressibilities compared to alkali metal fullerides as a result of larger ionic interactions in the lattice. The pressure dependence of the volume of the unit cell of Ba_6C_{60} and Ba_4C_{60} were fitted to the second-order Murnaghan equation-of-state. Values for the isothermal bulk modulus and its derivative for Ba_6C_{60} and Ba_4C_{60} are $K = 53(7) \text{ GPa}$, $K' = 14(2)$ and $K = 42(2) \text{ GPa}$, $K' = 13(1)$, respectively. The tight crystal packing in the alkaline earth fullerides is reflected by the large values of the bulk modulus in comparison to pristine C_{60} and the alkali fullerides. As the pressure is increased, the local coordination environments of the distinct barium ions change very little though reduced Ba-C contacts are observed. The shortest Ba-C distance is 2.95 Å at 2.64 GPa.

In this chapter we have seen evidence of a short orthorhombic c axis for Ba_4C_{60} , with very close contacts between one of the symmetry inequivalent barium ions and mainly one carbon of the fulleride cage. From the very short nature of the Ba-C contact it is difficult to deny an overlap of the respective wavefunctions and hence the observation of a chemical 'bond'. From this conclusion more questions now arise, such as why is the bonding concentrated on one carbon atom? Does the other barium ion also bond with the fulleride cage? Is the short c axis a consequence of Ba-C bonding,

or is the close Ba-C distance the result of a balance between a Ba-C repulsion energy and an overall increase in the lattice energy by having a short c axis? Further work is needed to answer these questions.

Chapter 5

Ammoniated Fullerenes

5.1 Introduction

Since the report of superconductivity in K_3C_{60} [23], the electronic and structural properties of the superconducting $A_2A'C_{60}$ alkali-metal fullerenes have been studied in detail[175]. In particular, ammoniation of alkali fullerenes has led to diverse responses in their solid state properties. Upon ammoniation, the superconducting transition temperature, T_c of Na_2CsC_{60} increases significantly from 10.5 to 29.6 K, consistent with the observed expansion of the cubic unit cell[58] and the accompanying increase in the density of states at the Fermi level[75]. Ammonia is being used here as a neutral structural spacer that coordinates to an octahedral sodium ion in a disordered cubic fashion. The resulting composition is $(NH_3)_4Na_2CsC_{60}$. In contrast, ammoniation only partially worked in the case of $(NH_3)_xNaA_2C_{60}$ ($0.5 < x < 1$, $A = K$ and Rb). The NaA_2C_{60} systems themselves have not been isolated. These ammoniated salts have cubic structures, with the ammonia preferentially coordinating to the small sodium ion so that this complex resides in the large octahedral interstice. However, T_c s in these systems were dramatically lower than expected with T_c decreasing

with *increasing* lattice parameter[59]. The size of the cubic lattice parameter can be controlled by varying the ammonia content in the unit cell: the more ammonia intercalated, the larger the resulting lattice parameter. X-ray powder diffraction studies show that the amine complex at the octahedral site is displaced somewhat from the centre of the interstice (Na^+ lies ~ 0.1 - 0.2 \AA away from the centre) with the ammonia symmetry axis lying along the $\langle 111 \rangle$ directions to produce a disordered coordination 'cube'. The depression of superconductivity in these systems is attributed to the nature of the octahedral complex.

Further, ammoniation of K_3C_{60} leads to the formation of $(\text{NH}_3)\text{K}_3\text{C}_{60}$. Despite evidence of complete charge transfer and a C_{60}^{3-} oxidation state, the ammonia induces a structural distortion and suppression of superconductivity at ambient pressure[60]. A structural phase transition has also been identified below 150 K and attributed to the ordering of the orientations of K^+ - NH_3 pairs residing in the interstitial sites[176]. A metal-insulator transition has been identified at $\approx 40 \text{ K}$ [61, 62] with recovery of the metallic state and superconductivity ($T_c = 28 \text{ K}$) observed upon application of pressure ($> 10 \text{ kbar}$)[63]. ESR and ^{13}C NMR measurements have shown $(\text{NH}_3)\text{K}_3\text{C}_{60}$ to be a narrow-band metal. The exact nature of the insulating state could not be determined though a vanishingly small spin susceptibility is reported.

Following the availability of this sample in bulk quantities, we had interests in using a variety of solid state techniques to probe different aspects of this novel material. Muon spin relaxation/rotation ($\mu^+\text{SR}$) has been a highly successful technique for studying small moment magnetism, especially in instances where magnetic order is random, short range, spatially inhomogeneous or incommensurate in nature. This technique has been used to characterise the insulating ground state of $(\text{NH}_3)\text{K}_3\text{C}_{60}$,

providing the first confirmation of antiferromagnetism within the C_{60}^{3-} series. Inelastic neutron scattering, including high and low resolution neutron time-of flight measurements on $(NH_3)K_3C_{60}$ and its deuterated analogue has been used to observe rotational transitions within the ammonia group: the exact energy transfers being dependent on the potential at the ammonia site. The effects of this extra ammonia intercalation on the librational potential of the fulleride ions also comes under scrutiny. Isotopic substitution is necessary for neutron diffraction studies due to the large incoherent scattering of hydrogen while it is also beneficial for our INS studies. The increased moment of inertia of deuterated ammonia provides an especially sensitive probe when looking at inelastic scattering between low lying rotational levels and allows observation of weak scattering from carbon based vibrations.

5.2 Neutron Diffraction

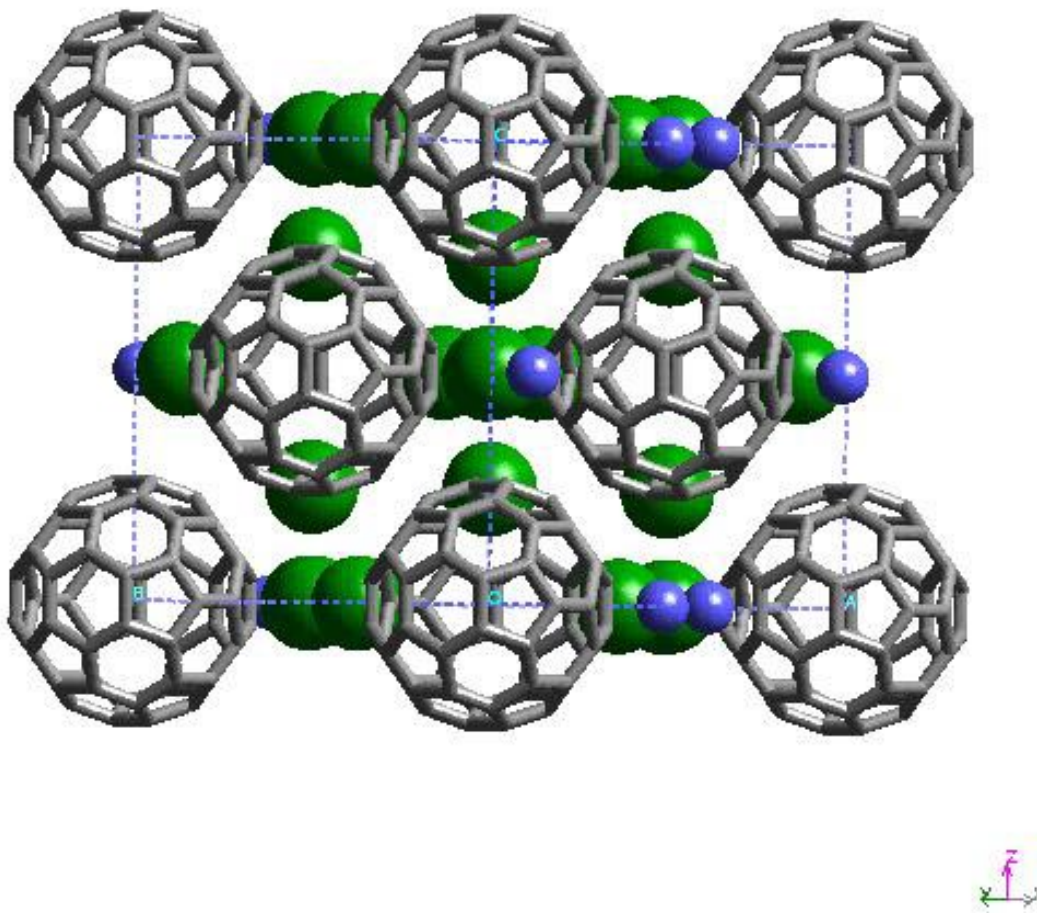


Figure 5.1: Proposed orthorhombic unit cell for $(\text{NH}_3)\text{K}_3\text{C}_{60}$ seen along the $\langle 110 \rangle$ direction[60]. Blue spheres represent ammonia coordination to disordered green potassium ions.

X-ray diffraction has proposed two statistically equivalent distortions of the high temperature cubic structure to (i) tetragonal (space group $I4/mmm$) with orientationally disordered and (ii) orthorhombic (space group $Fmmm$) with orientationally

ordered anions. The orthorhombic structure was chosen on the grounds of more chemically meaningful N-C contact distances. The proposed orthorhombic structure for $(\text{NH}_3)\text{K}_3\text{C}_{60}$ is shown in Fig.5.1. Within space group $Fmmm$, it is simply viewed as an orthorhombic distortion of the parent fcc structure with ordering of the fulleride ion orientations.

To be able to improve on this model an improved determination of the crystal structure is needed. We collected neutron diffraction data at 10 and 100 K on D2B with 910 mg of a $(\text{ND}_3)\text{K}_3\text{C}_{60}$ sample, sealed in a vanadium can ($\lambda = 1.594 \text{ \AA}$). A preliminary Le Bail analysis in both space groups indicate that an additional phase of unreacted K_3C_{60} is present at 100 K. Le Bail fits of the 100 K data are shown in Fig.5.2 for (a) $I4/mmm$ ($a = 10.5016(9) \text{ \AA}$, $c = 13.522(2) \text{ \AA}$, $R_{wp} = 5.7\%$ and $R_{exp} = 3.4 \%$) and (b) for $Fmmm$ ($a = 14.810(2) \text{ \AA}$, $b = 14.884(2) \text{ \AA}$, $c = 3.526(2) \text{ \AA}$, $R_{wp} = 5.6\%$ and $R_{exp} = 3.3 \%$). A slightly better fit is achieved with the orthorhombic space group and this highlights the slight orthorhombicity that can almost be modelled as a tetragonal cell.

Progressing on to Rietveld refinements of these data with atomic coordinates derived from X-ray profile refinements, it is apparent that the scattering up to 35° in 2θ is dominated by deuterium scattering. Efforts to define the high temperature structure with a highly disordered amine complex are progressing but it is still apparent that this model is inappropriate in the high Q range, where most influence comes from the orientational structure of the fulleride units. Further work needs to be performed in this area especially in combination with the low temperature structure and our INS results.

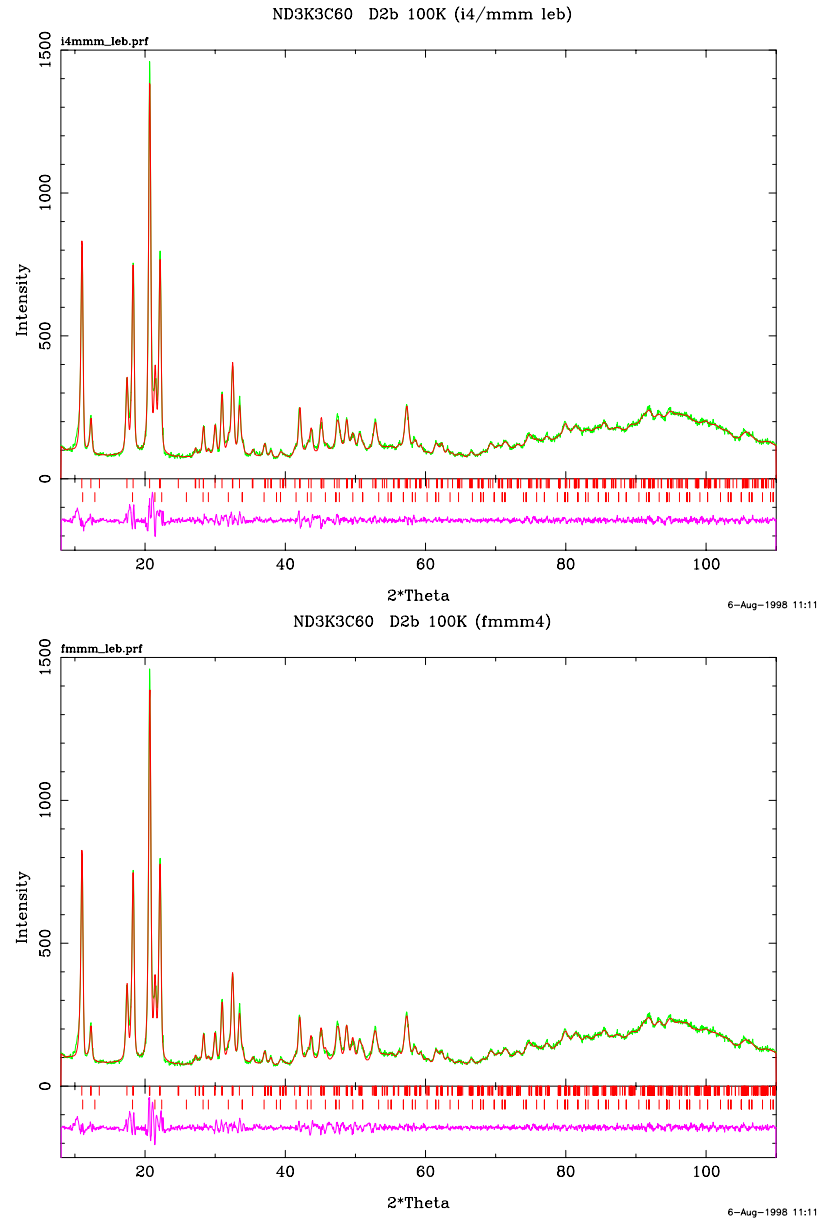


Figure 5.2: $(\text{ND}_3)_3\text{K}_3\text{C}_{60}$ Le Bail pattern decomposition of powder neutron diffraction at 100 K (top) in space group $I4/mmm$ and (bottom) in space group $Fmmm$. As a preliminary measure, we have ignored the superlattice peaks arising from cell doubling, as proposed by Ishii *et al.*[176]

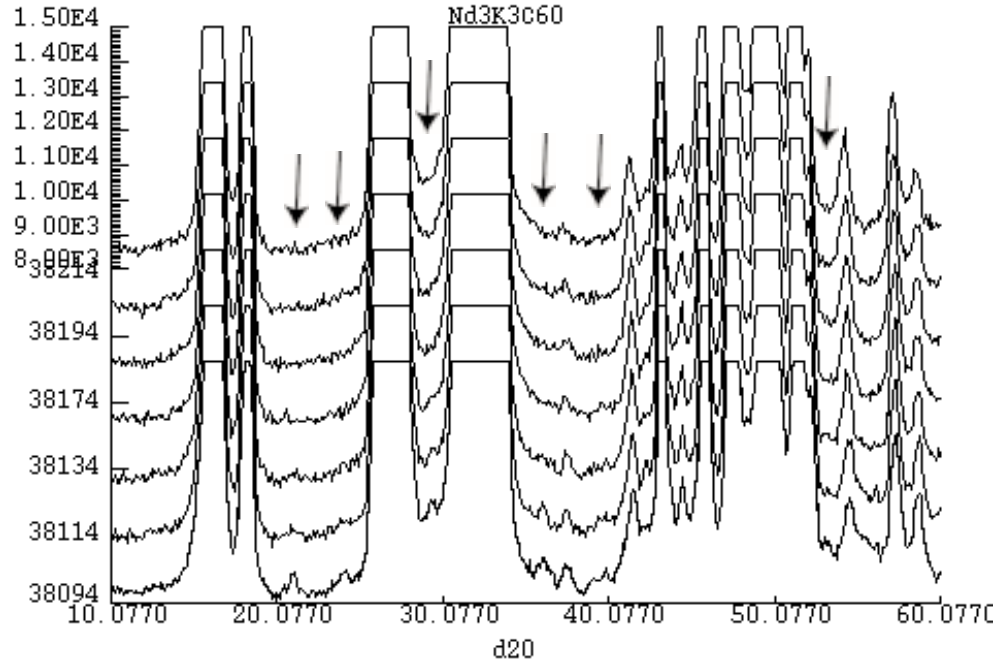


Figure 5.3: Temperature dependence of the D20 diffraction patterns of $(\text{ND}_3)\text{K}_3\text{C}_{60}$ as a function of temperature. The arrowed superlattice reflections decrease in intensity until 150 K after which they are no longer visible

We also took data between 2.5 and 250 K on the same $(\text{ND}_3)\text{K}_3\text{C}_{60}$ sample using the high flux D20 spectrometer at the I.L.L. The same sample as for the D2B experiment was sealed in a vanadium cylindrical can ($\phi = 0.4$ mm) and cooled to 2.5 K in an 'orange' cryostat. Diffraction patterns were recorded every 10 minutes on heating to 250 K with a wavelength of 2.400 Å. Fig.5.3 shows the temperature dependence of the diffraction patterns between 100 and 170 K. The weak peaks marked by arrows are not accounted for by the high temperature X-ray models and are consistent with the doubling of the unit cell along the b and c axes[176]. As the temperature is increased, the intensity of these reflections decreases until 150 K after which they are no longer visible. No change in the diffraction patterns is noticeable by eye, on heating through

the metal-insulator transition at 40 K. Again a full analysis is necessary here and will be performed in the future.

5.3 μ^+ SR studies of $(\text{NH}_3)\text{K}_3\text{C}_{60}$

Zero field (ZF- μ^+ SR) and transverse field (TF- μ^+ SR) variants of the μ^+ SR technique were used to characterise the low temperature insulating phase of $(\text{NH}_3)\text{K}_3\text{C}_{60}$. Experiments were performed in the 2-300 K temperature range in zero field (ZF) and 6 kG applied transverse field (TF) by implanting 100% spin-polarised μ^+ in 110 mg of sample¹, sealed under argon in an Ag sample holder equipped with indium seals and mylar windows.

In the presence of a local magnetic field, the muon spin will precess with a frequency given by Eqn.2.60. In ZF, the observation of a precession signal is a manifestation of magnetic ordering within the sample. Moreover, application of a longitudinal field parallel to the initial μ^+ spin polarisation will decouple the μ^+ spin from the static internal fields.

Fig.5.4 shows representative ZF time-dependent μ^+ SR spectra of $(\text{NH}_3)\text{K}_3\text{C}_{60}$ taken above and below the metal-insulator transition at 40 K, observed by ESR and NMR. At high temperatures, the depolarisation is characterised by a slow relaxation rate, $\sigma \approx 0.1 \mu\text{s}^{-1}$, implying the presence of weak nuclear dipole moments with a field width of ≈ 1.3 G at the μ^+ site (Eqn.2.72) that are essentially static in the μ^+ SR time window. At about 40 K, a second, rapidly relaxing component appears and grows as the temperature is lowered. This new component can be described as a Gaussian function at all temperatures, so necessitating the use of a phenomenological

¹Supplied by H. Shimoda and Y. Iwasa, JAIST

two-component fitting function of the form:

$$P_{\mu}(t) = A_1 \exp[-\frac{1}{2}(\sigma_1 t)^2] + A_2 \exp[-\frac{1}{2}(\sigma_2 t)^2] \quad (5.1)$$

where the depolarisation is characterised by two relaxation rates σ_1 and σ_2 with the asymmetries, A_1 and A_2 reflecting the respective amplitudes of the two components. The first component of the equation comes from the fact that for randomly distributed internal fields, some muons will not precess since the field they will experience will have a direction parallel to the initial spin direction of the muons. The second component describes the relaxation of the muons due to both static and dynamic inhomogeneities of the magnetic moments of the sample. Both the relaxation rate, σ_2 and the volume fraction, A_2 of the rapidly relaxing component increase smoothly as the temperature is lowered. The situation is reminiscent of that encountered in CsC_{60} fulleride which showed the appearance of static magnetic order of a random nature gradually below about 30 K with no clear evidence of long range order[177]². However, close inspection of the fitted spectra in $(\text{NH}_3)\text{K}_3\text{C}_{60}$ indicate that Eqn.5.1 fails in describing the data well in the 0.5-1.5 μs^{-1} range, thus raising the possibility of alternative, more appropriate fitting functions. To explore this option, we collected a high- statistics ZF dataset (≈ 35 million events) at 7.2 K. It is now clear that a good description of the data can be obtained if a strongly-damped oscillating component is included (Fig.5.5):

$$P_{\mu}(t) = A_1 \exp[-\frac{1}{2}(\sigma_1 t)^2] + A_2 \exp[-\frac{1}{2}(\sigma_2 t)^2] \cos(2\pi\nu_{\mu}t + \phi) \quad (5.2)$$

² CsC_{60} has recently been shown to be an antiferromagnet using the antiferromagnet resonance technique[178].

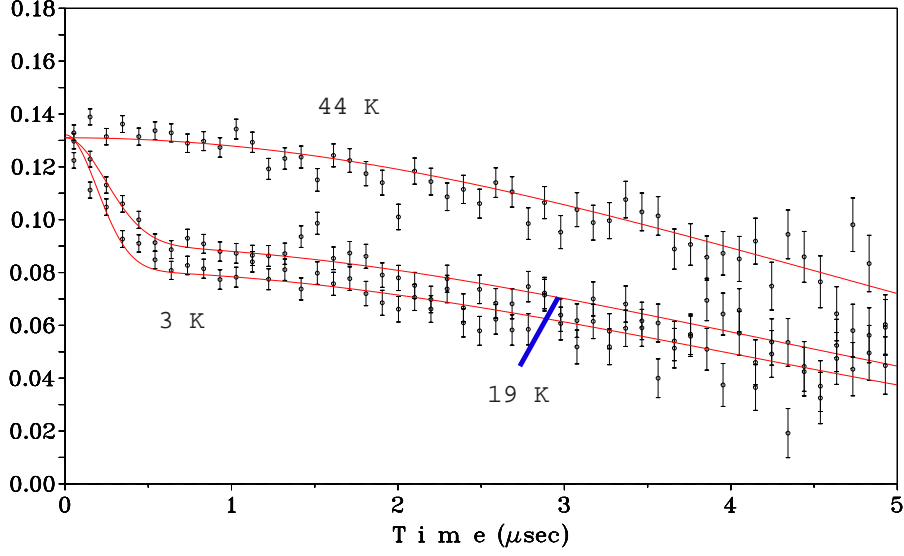


Figure 5.4: Representative ZF- μ^+ SR spectra at various temperatures. The solid line through the 44 K data is a fit to a Gaussian function reflecting the presence of weak static nuclear dipole moments; below 40 K, the data are fitted with the two-component function of Eqn.5.1, representing the sum of a slowly relaxing and a rapidly relaxing Gaussian component.

where $\nu_\mu = \omega_\mu/2\pi$ is the μ^+ Larmor precession frequency. The observation of ν_μ in zero external field indicates the onset of magnetic order, where the spontaneous magnetisation is proportional to ν_μ .

The observed frequency of 0.51(2) MHz corresponds to a static local field at the muon site of $\langle B_\mu \rangle \approx 40$ G. The highly-disordered nature of the antiferromagnetic state is evident by noting that the observed depolarisation rate, $\sigma_2 = 3.0(2) \mu\text{s}^{-1}$, implies a distribution of local fields with a width $\sqrt{\langle \Delta B^2 \rangle} \approx 25$ G, only smaller than $\langle B_\mu \rangle$ by a factor of 1.6. The muons thus experience a local field with large spatial inhomogeneities which may be due to a number of physical factors, including

orientational disorder effects or incommensurate order between the crystallographic and magnetic structures. The overall behaviour resembles the situation encountered in the other authenticated magnetic fullerene salt, (TDAE) C_{60} [179]. We can estimate the the magnetic moment per C_{60}^{3-} by comparison to (TDAE) C_{60} where a magnetic moment of $0.33 \mu_B$ gives rise to a Larmor frequency of $1.01(2)$ MHz[179, 180]. Due to the Larmor frequency being dependent on the unknown muon stopping site, we estimate the magnetic moment to be of the order of $0.1-0.2 \mu_B$.

Given the small magnitude of the local field experienced by the μ^+ , we also explored fits of the μ^+ polarisation by using the dynamic Kubo-Toyabe relaxation function, appropriate for a Gaussian distribution of fluctuating random fields of width, Δ whose fluctuation rate, ν , decreases with decreasing temperature. However, even though this function can describe the data well, it implies a fluctuation rate of $\approx 1.7 \mu s^{-1}$ at 7.2 K that is inconsistent with the evidence provided by complementary LF- μ^+ SR measurements. The effect of applied LFs is to allow the depolarisation due to dynamic or fluctuating moments to be decoupled from that due to static components. In the present case, LF fields greater than 100 G lead to complete recovery of the asymmetry with no evidence of any remaining dynamic fields.

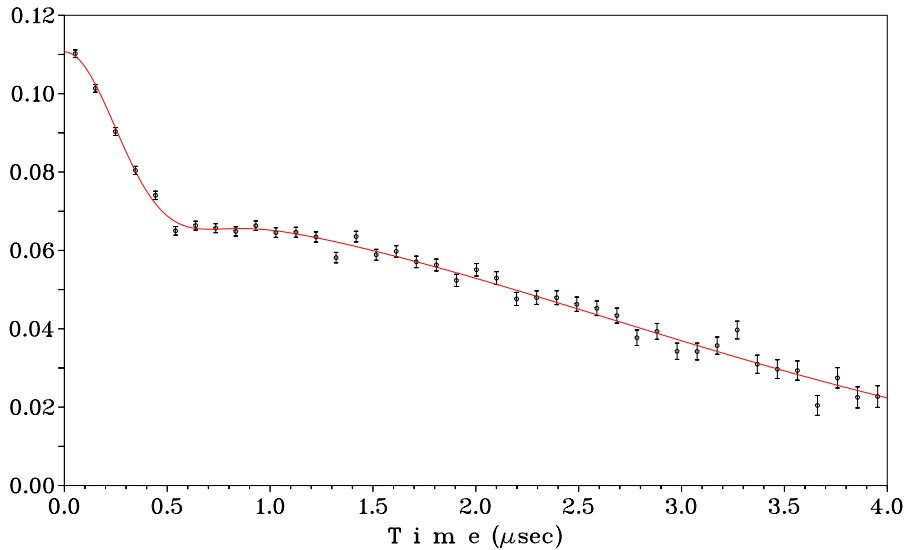


Figure 5.5: High statistics ZF- μ^+ SR data for $(\text{NH}_3)\text{K}_3\text{C}_{60}$ at 7.2 K. The solid line is a fit to Eqn.5.2.

Muon spin rotation data at an applied TF of 6 kG were also collected in the temperature range 2-300 K. The μ^+ polarisation was best fitted at high temperatures by a single oscillating component with an essentially temperature-independent Gaussian relaxation rate $\approx 0.1 \mu\text{s}^{-1}$, reflecting again the nuclear dipole field spread as in ZF. Below 40 K, a second rapidly relaxing component which was approximated in the fit by a Gaussian function becomes clearly evident. The total relaxation function is now given by:

$$P_\mu(t) = A_1 \cos(\omega_1 t + \phi_1) \exp\left[-\frac{1}{2}(\sigma_1 t)^2\right] + A_2 \cos(\omega_2 t + \phi_2) \exp\left[-\frac{1}{2}(\sigma_2 t)^2\right] \quad (5.3)$$

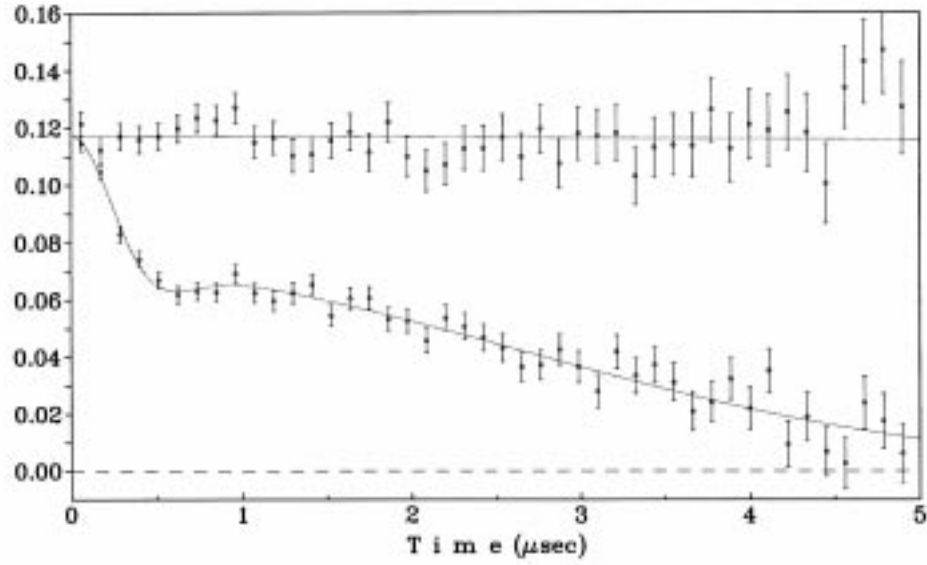


Figure 5.6: ZF and LF (100 G) μ^+ SR spectra of $(\text{NH}_3)\text{K}_3\text{C}_{60}$ at 3.9 K. The application of the longitudinal field leads to a recovery of the asymmetry at long times indicating the static origins of the magnetic moments.

Both the relative fraction and the relaxation rate of component #2 are smoothly increasing with decreasing temperature, mimicking the behaviour described earlier in ZF. Fig.5.7(lower panel) shows the temperature dependence of the relaxation rates for the two components with the corresponding asymmetries shown in the inset. Finally, the μ^+ precession frequency, ν_μ exhibits a shift in the same temperature range in agreement with the behaviour of the spin susceptibility, χ_s , measured by ESR (4); however, ν_μ does not scale with χ_s at higher temperatures Fig.5.6(upper panel).

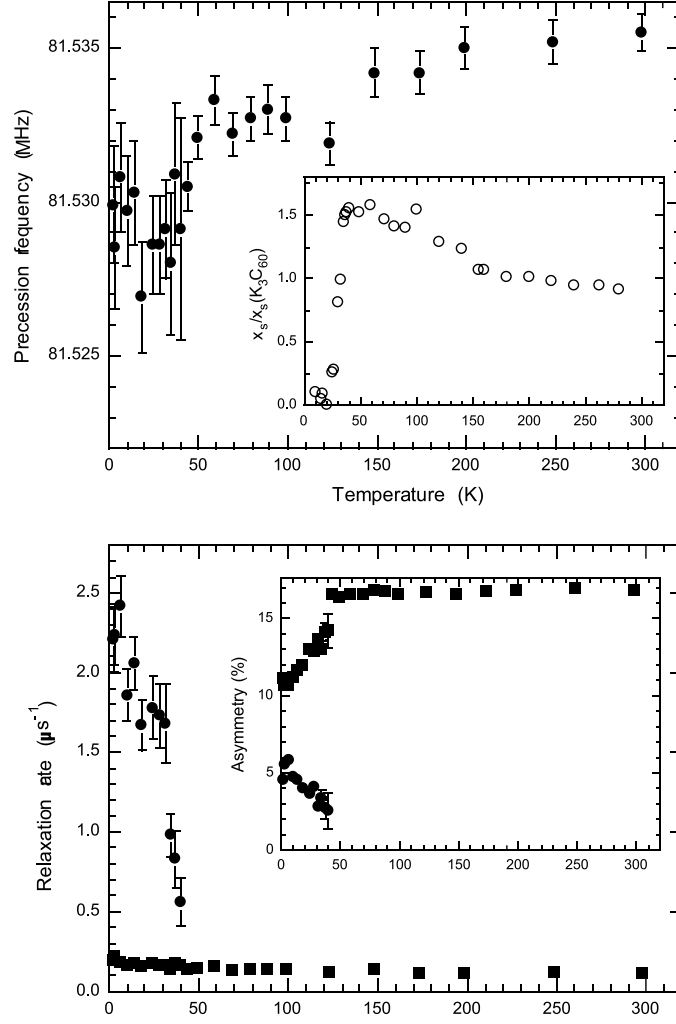


Figure 5.7: (Lower) The temperature evolution of the relaxation rates, σ_1 (solid squares) and σ_2 (solid circles), of the two Gaussian components present in the TF μ SR spectra. The inset shows the temperature dependence of the asymmetries A_1 (solid squares) and A_2 (solid circles) of the two components. (Upper) Variation of muon frequency with temperature scales well with χ_s (inset) showing a transition around 40 K.

5.4 Inelastic Neutron Scattering of $(\text{NH}_3)\text{K}_3\text{C}_{60}$ and $(\text{ND}_3)\text{K}_3\text{C}_{60}$

Tunnelling is a phenomenon that arises due to wavefunction penetration into classically forbidden regions lifting the degeneracy of symmetric potential wells. At low temperatures, the fluctuations of the rotational potential die out and these quantum aspects begin to appear. Transitions within ground-state multiplets ($A \rightarrow E$ or equivalently between the rotational levels labelled $J = 0 \rightarrow 1$) are usually accompanied by a change of the nuclear-spin function which can be produced by neutrons. Transitions from the lowest rotational level to $J > 2$ are described as librational motions of the molecule. Not every molecule will show rotational tunnelling as the rotational constant, B , is usually just too small³ for all except the linear H_2 , symmetric top CH_3 and NH_3 and the spherical CH_4 and NH_4^+ molecules. Backscattering techniques are pushing resolution limits to about $0.1 \mu\text{eV}$ enabling measurements on much larger molecules the size of CCl_4 . With the present compound, we have an unknown distortion of the ideal gaseous ammonia structure ($B = 0.7867 \text{ meV}$) that will manifest as a change in the rotational constant about the symmetry axis. Tunnelling work on graphitic intercalation compounds has assumed a value of B to be 0.885 meV [181], while others have used the value of around 0.65 meV for three dimensional materials[182, 183]. It seems sensible that when ammonia acts as a ligand to K^+ within our sample, it is donating part of the lone pair resting on the nitrogen. According to the simple valence shell electron repulsion model, the N-H bonds are now 'repelled' less and so their perpendicular distance to the symmetry axis increases⁴. Since an increase in moment of inertia

³The $J \rightarrow J+1$ unhindered transition frequency is $2(J+1)B$

⁴The interstices between fulleride ions are larger than the potassium amine complex.

will reduce the rotational constant, we use the B value employed by Kearley *et al.* and Press of 0.6475 meV. Combination of tunnelling and ammonia torsional frequencies is a sensitive test of site structure as well as the size and shape of the potential in which the ammonia moves. Probing site structure by this method has featured heavily in the physics and chemistry of ternary graphite intercalates[181, 184] and for free ammonia in matrices of transition metal halides. Notably, sixfold and threefold potentials have been distinguished within $\text{Ni}(\text{NH}_3)_6(\text{PF}_6)_2$ [183] and in $\text{Ni}(\text{NH}_3)_6\text{I}_2$ and $\text{Ni}(\text{ND}_3)_6\text{I}_2$ [185]. The temperature dependence of the tunnelling spectra from these compounds provides a sensitive measure of the distribution of local ammonia potentials.

5.4.1 Experimental and Data Reduction

Neutron inelastic scattering measurements on $(\text{NH}_3)\text{K}_3\text{C}_{60}$ (mass 500 mg) were performed on the high intensity IN6 spectrometer and the high resolution IN5 spectrometer. For each experiment the sample was press sealed with indium wire in a thin walled aluminium cylindrical can (i.d.= 7 mm). A compromise between high flux and reasonable resolution was chosen to search for the possible tunnelling transition on IN5. This resulted in choosing a wavelength of 6 Å and a resolution at the elastic line of 63 μeV . The maximum possible momentum transfer is 1.9 Å⁻¹. Data were collected at 1.5 K, 20 K and 50 K, being later summed over the entire Q range leading to an average Q of 0.84 Å⁻¹. Vanadium calibration was run at 100 K for 4 hours. For IN6 an incident neutron wavelength of 4.12 Å was used. The instrumental resolution at this wavelength is 0.14- 0.17 meV at the elastic line, increasing to 3.5 meV at 25 meV energy transfer. An 'orange' cryostat was used as sample environment with data

collection at 200, 152, 125, 100, 50 and 30 K. Data were collected over the full range of scattering angles with an average counting time of 5 hours. Empty aluminium can background runs were performed at 100 and 315 K for 8 hours each. A vanadium calibration at 295 K was done using a rolled sheet of vanadium in an identical cell. From initial on-line data analysis using LAMP[186], noisy detectors were identified and excluded from further analysis. The observed scattering law is corrected (average $Q = 1.41 \text{ \AA}^{-1}$) using INX[124] according to §2.5.4 with the parameters given in Tables 5.1 and 5.2 for IN5 and IN6, respectively. N.B. The effective radius of the vanadium is the radius it would have if it were a solid block within the can and is easily calculated given the density (6.11 g cm^{-3}) and mass in the beam. Cadmium shielding was used in all cases to exclude every part of the can that did not contain sample, so as to reduce aluminium contributions to the signal.

Table 5.1: INX Correction Parameters for $(\text{NH}_3)\text{K}_3\text{C}_{60}$ on IN5

Angular Range	8- 130°
Detectors	9-13 + 17-18 + 28-78 + 80-99
Can Radius	3.5 mm
Transmission	0.95
Sample Density	1.1 g cm^{-3}
Molecular Mass	854 g
Average Mass	12.75 g
σ_s	596 barns
σ_a at 1.8 Å	9.4 barns

Vanadium 100 K of effective radius 1.56 mm, with 0.8 transmission

Table 5.2: INX Correction Parameters for $(\text{NH}_3)\text{K}_3\text{C}_{60}$ on IN6

Angular Range	10-80 + 83-114°
Detectors	22-205 + 209-256
Can Radius	3.5 mm
Transmission	0.85
Sample Density	1.19 gcm ⁻³
Molecular Mass	854 g
Average Mass	12.75 g
σ_s	595 barns
σ_a	5.2 barns

Vanadium 295 K of effective radius 1.9 mm
with 0.8 transmission.

IN6 was again used to measure the INS spectra of $(\text{ND}_3)\text{K}_3\text{C}_{60}$ (mass 833 mg) using an identical sample environment as for the $(\text{NH}_3)\text{K}_3\text{C}_{60}$ case. Data were collected at 290, 200, 125 and 50 K with background runs at 100 and 200 K. Longer counting times were necessary for this non-hydrogenous sample, typically of 12 hours duration. Vanadium was run at 200 K. INX correction parameters are given in Table 5.3 with all angles summed for conversion to the generalised density of states so as to improve statistics (average $Q = 1.43 \text{ \AA}^{-1}$). To investigate the librational features common to fullerides, the scattering law was again summed over all scattering angles but excluding Bragg peaks resulting in the same average Q .

Time-of-flight data also contains information on the diffraction pattern of your sample, that is you sum the data across all energy transfers, and is an excellent way to confirm if your sample is what you expect. Fig.5.7 shows the integrated IN6 data, and even though there is limited resolution, comparison to data taken on D2B at the start of this chapter confirms the quality of the sample.

Table 5.3: INX Correction Parameters for $(\text{ND}_3)\text{K}_3\text{C}_{60}$ on IN6

Angular Range	12- 114°
Detectors	22- 256
Can Radius	3.5 mm
Transmission	0.8
Sample Density	1.19 gcm ⁻³
Molecular Mass	857 g
Average Mass	12.8 g
σ_s	373 barns
σ_a at 1.8 Å	8.4 barns

Vanadium 200 K of effective radius 1.35 mm, with 0.78 transmission
Normalised to time as monitor was broken.

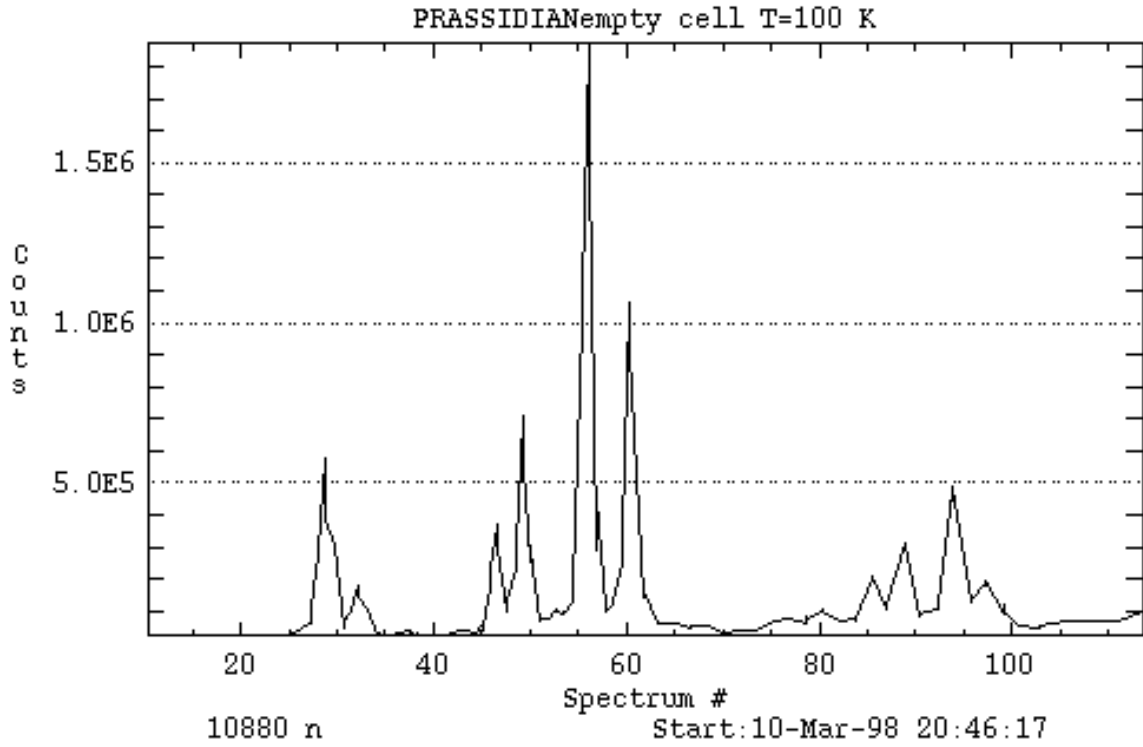


Figure 5.8: Neutron diffraction pattern of $(\text{ND}_3)\text{K}_3\text{C}_{60}$ at 100 K from a summation of IN6 time-of-flight data.

5.4.2 Rotational Tunnelling

Spectra taken at 1.5, 20 and 50 K for $(\text{NH}_3)\text{K}_3\text{C}_{60}$ on IN5 are shown in Fig.5.8. Tunnelling can be clearly seen at 1.5 K. The data cannot be completely corrected for using detailed balance as the intensity of the neutron energy gain peak is always larger than the mirror peak. This could be due to non-equilibrium conditions within the sample due to slow spin conversion and populations of higher rotational levels at this temperature. The broad distribution peaks at $270\text{ }\mu\text{eV}$ extending out to $700\text{ }\mu\text{eV}$ with a shoulder visible at around 0.6 meV . At 20 K the tunnelling peak has almost completely receded into the elastic line and the intensities on both sides of the elastic position are consistent with temperature and Boltzmann statistics. By 50 K, the complete collapse of the tunnelling peak has occurred and a quasielastic component remains. For a single site, we generally expect that the tunnelling peak broadens and shifts to lower energies before collapsing into a quasielastic peak as the temperature is raised.

It is difficult in the present circumstances to decide on the temperature dependencies of the width and intensities of the relevant peaks due to their partly resolved nature. The breadth of the main tunnelling peak at 1.5 K has not warranted beam-time on a higher resolution backscattering instrument so we can only speculate on the origins of this feature. Our observations of a broad peak, that has a decrease in intensity with increasing temperature is probably a reflection of the distribution of sites available within this compound. As the temperature is raised, the orientations of the NH_3 groups become increasingly disordered with a consequent loss of the tunnelling peak and development of a central quasielastic peak arising from diffusive rotational motion. The overall characteristics are in excellent agreement with those

obtained on $(\text{NH}_3)_{0.96}\text{Rb}_3\text{C}_{60}$ [187].

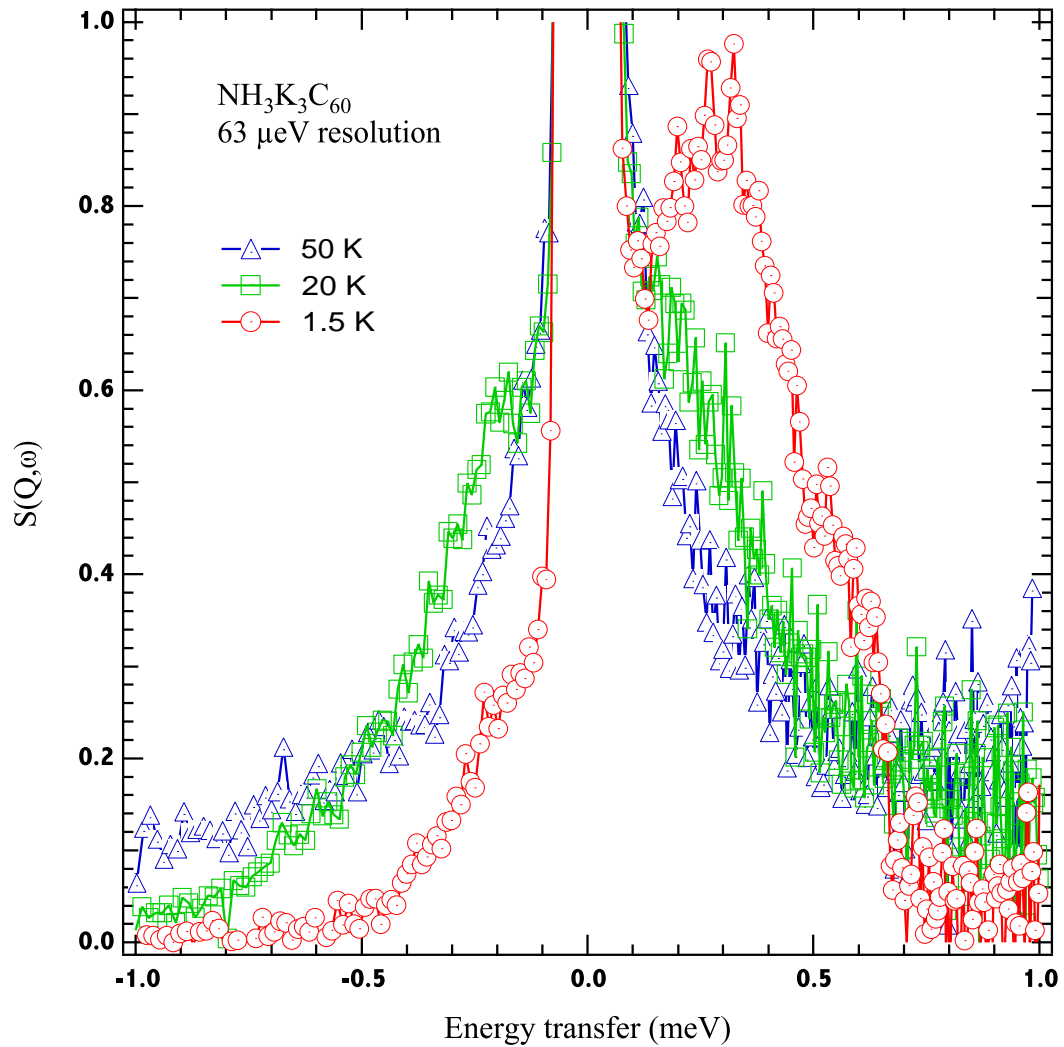


Figure 5.9: Neutron energy gain spectra of $(\text{NH}_3)\text{K}_3\text{C}_{60}$ at 1.5, 20 and 50 K. Scattering due to tunnelling is observable at $270 \mu\text{eV}$ at 1.5 K (red circles). The tunnelling transition is immediately suppressed with temperature as evidenced at 20 K (green squares) where the peak is now unresolved and lies within the elastic line. The intensities on energy gain and loss side of the elastic line are now comparable in accord with temperature and Boltzmann statistics. By 50 K the tunnelling feature is replaced by a quasielastic component that is indicative of diffusive motion (blue triangles).

The 600 μeV shoulder on the 1.5 K peak, though not seen in the rubidium equivalent, could be due to numerous factors. For instance, its energy is close enough to a multiple of the main peak to be caused by doubly inelastically scattered neutrons. Alternative, more interesting possibilities that would modify any simple energy level scheme are: a distribution of ammonia sites; coupling between sites; or precession of the NH_3 about its axis, as observed in the tetragonal Hoffmann clathrate[188] and lithium acetate dihydrate[189]. Taking into account the orthorhombic crystal structure of $(\text{NH}_3)\text{K}_3\text{C}_{60}$, we expect there to be three distinct ammonia environments characterised by different ammonia-fulleride contact distances. For the proposed structure of Rosseinsky *et al.*[60], the closest ammonia-fulleride contact distances vary between 3.186 Å and 3.474 Å, depending on the site. This is the most likely cause of the structure of the tunnelling peak, with the ammonia residing in the largest interstice being more free rotor like and contributing to the 600 μeV shoulder.

Tunnelling Barrier

The energy levels of the NH_3 rotor are derived from the solutions to the Schrödinger equation:

$$\hat{H}_r \psi_i = E_i \psi_i \quad (5.4)$$

where \hat{H}_r is the Hamiltonian of the NH_3 group which is given by

$$\hat{H}_r = \frac{\hbar^2}{2I} \frac{d^2}{d\phi^2} + V(\phi) \quad (5.5)$$

The simplest potential that one can use here comes from considering rotation about the threefold axis⁵. In principle, the potential could be three fold or a multiple

⁵It is expected that the nitrogen is constrained so an end-over nitrogen tumbling motion has a higher potential barrier

of threefold rotational symmetry. The one-dimensional torsional potential is then conventionally expressed as

$$V(\phi) = \sum_{n=1}^N \frac{V_{3n}}{2} [1 - \cos(3n\phi - \phi_{3n})] \quad (5.6)$$

with potential components V_{3n} and phases ϕ_{3n} . The solutions to the Schrödinger equation are available for $N=2$ (the Mathieu equation)[182]. We have observed tunnelling much reduced from $647.5 \mu\text{eV}$, the free rotor value, at $270 \mu\text{eV}$ indicating a substantial barrier to rotation. We can immediately discard the option of a sixfold potential as such a reduction in the $J=0 \rightarrow 1$ requires a very high potential barrier of $\sim 35 \text{ meV}$ that would also reduce $0 \rightarrow 2$ and $0 \rightarrow 3$ transitions to energies of around 1 meV in the classical librational limit. In contrast, the dependence of rotational energy states as a function of a threefold potential barrier is shown in Fig.5.9. The observed tunnelling frequency corresponds to a potential barrier, V_3 , of 7.35 meV . Predictions of other rotational transitions are: $0 \rightarrow 2$ at 4.38 meV , $0 \rightarrow 3$ at 6.64 meV , $0 \rightarrow 4$ at 7.65 meV , and $0 \rightarrow 5$ at 11.56 meV . This is consistent with the value of 12 meV obtained for V_3 in $(\text{NH}_3)_{2.5}\text{Rb}_3\text{C}_{60}$ [187] taking into account the smaller tunnelling transition ($214 \mu\text{eV}$) and the larger rotational constant ($883 \mu\text{eV}$) used here. Using our rotational constant, it would require a barrier height of $\sim 8.7 \text{ meV}$ to reproduce their tunnelling transition. The difference may be due to additional structural constraints from the higher concentration of ammonia in $(\text{NH}_3)_{2.5}\text{Rb}_3\text{C}_{60}$ compared to $(\text{NH}_3)\text{K}_3\text{C}_{60}$.

To distinguish a situation where there is a small addition of a six fold potential to the overall threefold potential, one needs more transitions to be observed with higher precision than at present.

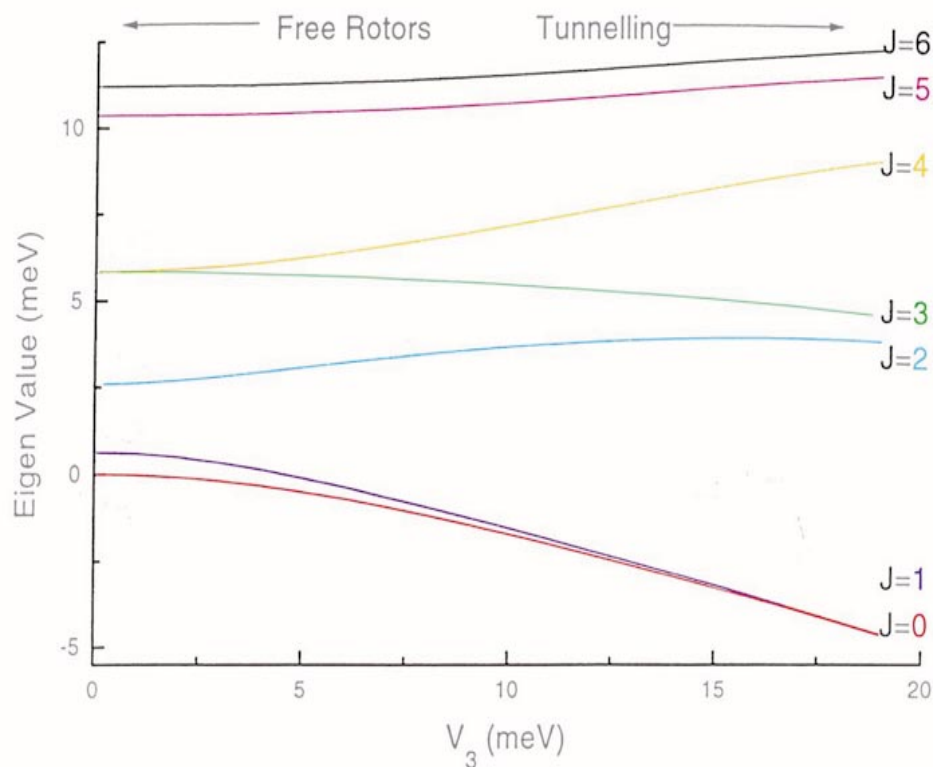


Figure 5.10: Rotational energy level dependence for a threefold potential for NH_3 groups. As the potential barrier is increased, wavefunction overlap is reduced resulting in an almost exponential dependence of the tunnelling transition on barrier height. In the classical limit of infinite barrier, the wavefunctions are discrete and librational transitions occur.

5.4.3 Molecular and Lattice Vibrations

This section refers to the IN6 data collected on these samples. The data were converted to the spectral distribution function, $P(\bar{\alpha}, \beta)$ and then to the generalised

phonon density of states, $G(\omega)$. The parameters used in the multiphonon correction stage are given in Tables 5.4 and 5.5 for $(\text{NH}_3)\text{K}_3\text{C}_{60}$ and $(\text{ND}_3)\text{K}_3\text{C}_{60}$, respectively.

Table 5.4: Multiphonon Correction Parameters used with the FITDEN5 program for $(\text{NH}_3)\text{K}_3\text{C}_{60}$.

Temperature/K	Parameter	Peak 1	Peak 2	Peak 3
30	Masses	12.75	12.75	12.75
	Frequency/meV	4.74	9.23	9.19
	Cutoff freq./meV	9.94	20.76	37.24
	Peak Width	0.88	1.11	0.989
	Concentration	0.26	0.31	0.43
50	Masses	12.75	12.75	12.75
	Frequency/meV	3.96	10.50	32.14
	Cutoff freq./meV	8.14	26.36	51.45
	Peak Width	0.88	1.03	1.25
	Concentration	0.12	0.22	0.66
100	Masses	12.75	12.75	12.75
	Frequency/meV	3.72	10.80	29.24
	Cutoff freq./meV	10.17	16.00	50.00
	Peak Width	1.00	1.01	1.25
	Concentration	0.12	0.44	0.44
125	Masses	12.75	12.75	12.75
	Frequency/meV	3.67	11.51	32.14
	Cutoff freq./meV	9.75	21.04	51.45
	Peak Width	1.13	1.05	1.25
	Concentration	0.11	0.40	0.49
152	Masses	12.75	12.75	12.75
	Frequency/meV	3.71	11.49	32.56
	Cutoff freq./meV	9.556	20.84	49.49
	Peak Width	1.15	1.09	1.03
	Concentration	0.097	0.314	0.589
200	Masses	12.75	12.75	12.75
	frequency/meV	3.81	11.29	33.03
	Cutoff freq./meV	9.94	20.76	51.89
	Peak Width	1.17	1.11	0.98
	Concentration	0.081	0.26	0.659

Table 5.5: Multiphonon Correction Parameters used with the FITDEN5 program for $(\text{ND}_3)\text{K}_3\text{C}_{60}$.

Temperature/K	Parameter	Peak 1	Peak 2	Peak 3
50	Masses	720	7	
	Frequency/meV	3.10	12.00	
	Cutoff freq./meV	6.00	15.00	
	Peak Width	0.82	1.24	
	Concentration	0.22	0.78	
125	Masses	720	7	12
	Frequency/meV	3.10	9.00	30.25
	Cutoff freq./meV	5.71	25.00	128.00
	Peak Width	1.30	1.18	0.91
	Concentration	0.072	0.330	0.598
200	Masses	720	7	12
	Frequency/meV	3.10	11.00	55.25
	Cutoff freq./meV	5.70	25.00	128.0
	Peak Width	1.29	1.17	0.91
	Concentration	0.025	0.140	0.835
290	Masses	720	7	12
	Frequency/meV	3.10	11.00	63.24
	Cutoff freq./meV	5.70	25.00	128.0
	Peak Width	1.29	1.17	0.91
	Concentration	0.018	0.11	0.872

The GDOS of $(\text{NH}_3)\text{K}_3\text{C}_{60}$ between 0 and 70 meV at 100, 125, 152 and 200 K are shown in the left hand side of Fig.5.10. The spectra are relatively simple with only three broad peaks present at ≈ 4.5 , 12 and 35 meV at high temperature. The main difference from the GDOS of other fullerenes is that in the present case, due to the large scattering cross section and low atomic mass of hydrogen, $G(\omega)$ is dominated by non- C_{60} vibrational modes involving hydrogen motion. Internal vibrations within the ammonia ligand that involve large amplitude hydrogen motion will occur outside our energy window. The lowest energy mode at 4 meV is ascribed to lattice vibrations,

while the feature at 12 meV is associated with ammonia torsions.

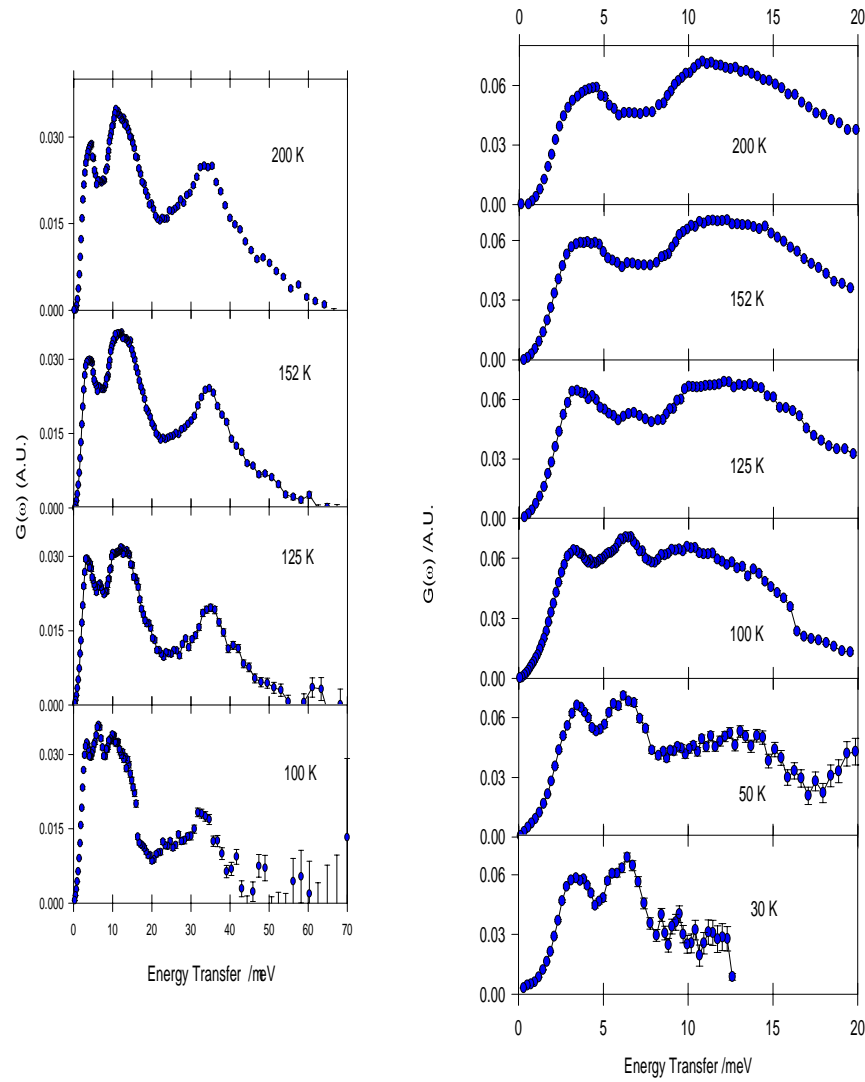


Figure 5.11: (Left) Multiphonon corrected generalised phonon density of states for $(\text{NH}_3)\text{K}_3\text{C}_{60}$ above 100 K showing the full energy transfer range. (Right) Low energy region between 0 and 20 meV showing the growth of a librational peak below 150 K.

The strong feature at 35 meV with possible structure at higher energy transfers is attributed to N-K-N δ bending modes whose presence provides direct evidence for the coordination of NH_3 to the K^+ ions forming an amine; a contribution from the $\text{H}_g^{(1)}$ intramolecular mode of C_{60}^{3-} is also expected in this region. These results are in excellent correspondence with those reported on the $(\text{NH}_3)_{2.5}\text{Rb}_3\text{C}_{60}$ sample[187]. Metal amine complexes exhibit the same bending modes in the same frequency range: e.g. $[\text{Cr}(\text{NH}_3)_6](\text{NO}_3)_3$ it is at 33.5 meV[190] and for $[\text{Co}(\text{NH}_3)_6](\text{Cl})_3$ it is at 37.5 meV[191]. For these compounds metal- NH_3 bond stretching frequencies occur at higher energies of 50- 60 meV and, we assume, contribute to our spectra in the same energy regions. No significant temperature dependence is observed for these modes down to 30 K, except for the worsening of the statistics at high energy, expected on cooling for neutron energy gain measurements.

However, what is immediately apparent from the right hand side of Fig.5.10, that shows the full temperature range for energy transfer up to 20 meV, is that below 150 K a sharp peak appears at 6.5 meV which grows in intensity with decreasing temperature. We associate this peak with the observed structural transition at ≈ 150 K and the appearance of superlattice peaks, associated with the ordering of the $\text{NH}_3\text{-K}^+$ pairs in the interstitial sites[176]. There is also an increase of intensity on the low energy side of the lattice modes at around 3.5 meV. Thus at high T, the ammonia molecules are disordered, possibly being able to perform tumbling type of motion and behave as free rotors. Below 150 K, the interaction between the K^+ and the ammonia molecules is strong enough to trap the molecules in a torsional potential and they now perform small-amplitude librational motion. We thus assign the 6.5 meV peak to ammonia librational modes. Considering the simple one-dimensional three-fold

torsional potential as in the previous section, the strong librational peak corresponds to the $J=0 \rightarrow 3$ transition. The slight shift of the 4 meV peak with decreasing temperature may reflect the structural ordering transition that may result in a less dispersed lattice mode or C_{60} libration. We also note that the three-fold rotational potential described above predicts a $J=0 \rightarrow 2$ at 4.38 meV that may contribute to this occurrence.

The corresponding data for $(ND_3)K_3C_{60}$ taken at 50, 125, 200 and 290 K are shown in Fig.5.11. There is a dramatic increase in structure within this spectrum compared to that of the hydrogenous sample. At 290 K there are four well distinguished peaks up to 15 meV after which we observe two peaks characteristic of intramolecular vibrations of the C_{60} molecule. The peak at 34 meV corresponds to the $H_g(1)$ breathing mode, while the energy of the 49 meV peak is typical for the first H_u mode. Any δ bending modes are expected to be reduced in frequency compared to the hydrogenous sample, though they may well be masked by the carbon scattering in this low resolution spectrum. The lowest energy peak at 3 meV is independent of temperature and so is ascribed to lattice modes with a shift to lower energy on deuteration that reflects the increased moment of inertia. Other peaks not evident in $(NH_3)K_3C_{60}$ are present at 6 meV, 7.5 meV and 11 meV.

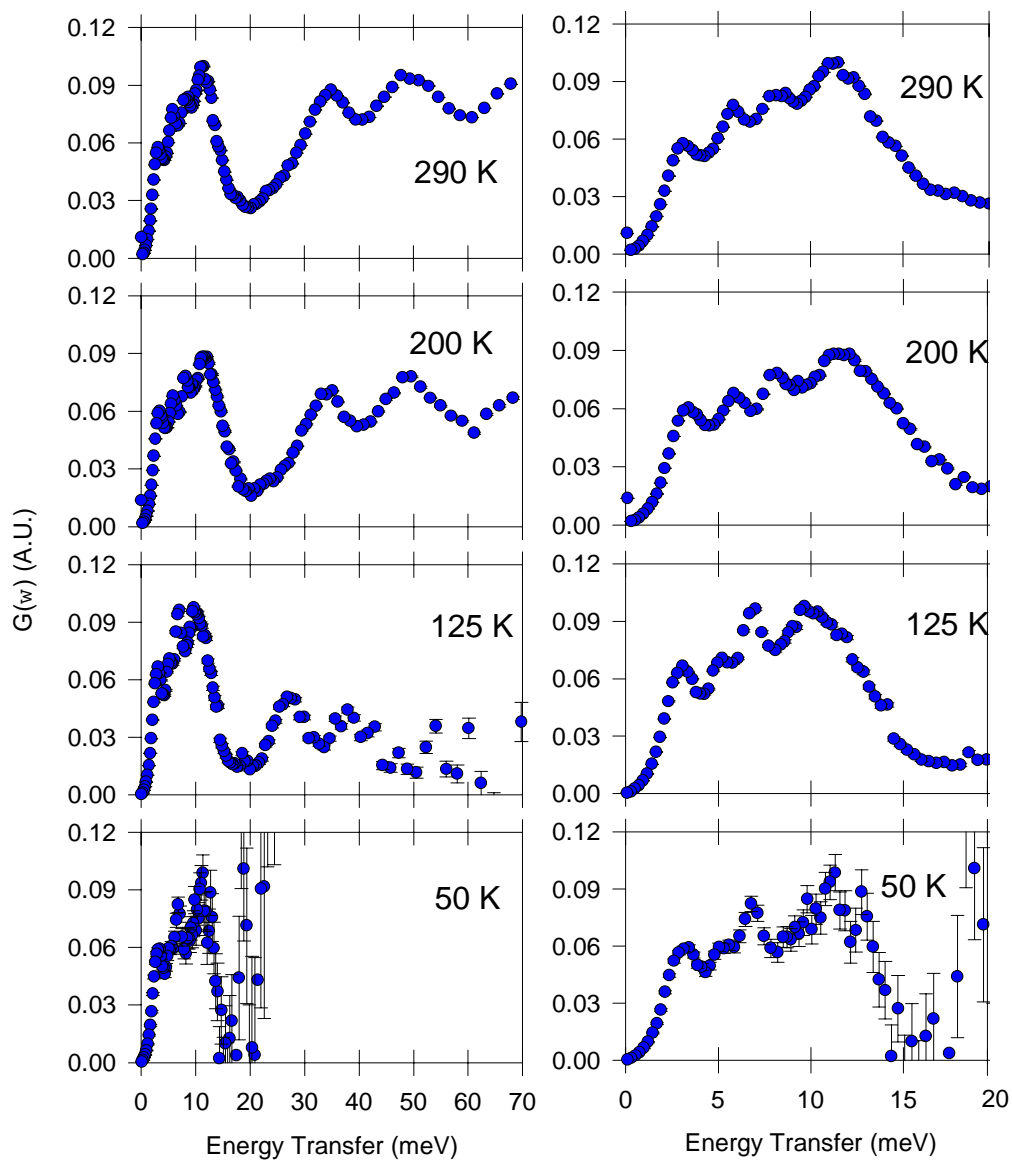


Figure 5.12: (Left) Multiphonon corrected generalised phonon density of states for $(\text{ND}_3)\text{K}_3\text{C}_{60}$ above 50 K showing the energy transfer range up to 70 meV. (Right) Low energy region between 0 and 20 meV, showing the detailed peak structure.

The origins of these peaks are somewhat unclear though comparison can be made between this spectral distribution and those obtained for pristine C_{60} and K_3C_{60} [192]. Lattice dynamic calculations have been used to decompose the observed generalised density of states into contributions from translational and librational phonons of the C_{60} as well as those from alkali atom vibrations. For K_3C_{60} , peaks due to C_{60} translations peak strongly at energies of 4, 6.5 and 8 meV with coincident librations at 4 meV. The octahedral potassium vibrations are encountered at 8 meV, while those of the tetrahedral lie at 14 meV. The octahedral metal vibration is expected to occur at a lower energy than that predicted by Renker *et al.*[192], due to the large temperature factor found in structural refinements which indicates off-site disorder. A direct correspondence of these peaks to ours is tempting even with the reduction in symmetry between the systems having an unknown effect on these modes. On the other hand, if we attribute these peaks to librations of the ND_3 group we require a larger V_ϕ potential barrier of 7.9 meV to assign the transitions as 4.26, 6.00, and 7.40 meV, to those between $J=0 \rightarrow 3$, $J=0 \rightarrow 4$ and $J=0 \rightarrow 5$ levels.

Decreasing the temperature through the phase transition at 150 K results in a jump of peak positions to 5.2, 6.8 and 10.5 meV. We notice that the 6.8 meV peak increases in intensity and is now sharper than before. It also seems that there is an increase of intensity for the ~ 3 meV peak when compared to the that of the ~ 5 meV peak. Just as with the spectra obtained on $(NH_3)K_3C_{60}$, we expect to see ammonia librational features appearing below the ordering temperature of 150 K. We can account for these two peaks by assuming a three-fold potential barrier of 6.5 meV. This predicts an assignment of a $J=0 \rightarrow 5$ transition occurring at 6.8 meV while a $J=0 \rightarrow 2$ would lie at 3.2 meV. This potential also predicts librations for $J=0 \rightarrow 3$

and $J=0 \rightarrow 4$ at 3.9 meV and 5.3 meV that fall within the other peak regions even though such a growth in intensity for these peaks is not observed. This adds supports to the view that the other peaks are probably not ND_3 related, but that they can be described as C_{60} librations and translations as with K_3C_{60} .

On cooling we also see a strange event at higher energy transfers where a possible splitting of the H_{g1} mode has occurred into two components at 27 and 38 meV. Such an observation has only been observed for one dimensional fullerene polymers[193, 194] where this breathing mode is constrained due to interfulleride bonding[195]. This feature here is not an artifact of data manipulation as it is visible in the raw data. We have no explanation for this, but it is certainly very unlikely that we are dealing with a polymer system.

The dependence of the scattering law, $S(Q, \omega)$ measured for $(\text{ND}_3)\text{K}_3\text{C}_{60}$ scaled by the relevant Bose occupation factors to make direct visual comparison with the data at 50 K, is shown in Fig.5.12. There are 4 excitations evident in the measured spectra at all temperatures. They can be adequately described by fitting with Gaussian peaks, convoluted with the instrumental resolution function. Also present is a Gaussian quasielastic component. At 50 K, the most intense peak is a product of C_{60} librational motion lying at -2.54(3) meV with a full width at half maximum (FWHM) of 1.68(4) (peak 1) with the mirror image (peak 2) constrained to have the same position and width. This is softer by 0.5 meV than that found using a triple axis spectrometer[196] (at a large Q of 5.5 \AA^{-1}) but having equivalent width, while it is similar to that of pristine C_{60} [7]. This position is temperature independent up to 290 K, though the FWHM increases to 1.98(4) meV. Two higher energy excitations are present at 50 K, at -4.80(7) and at -6.4(1) meV, hardening to -5.40(6) meV and

-7.7(1) meV at 290 K. These weak peaks are correspondingly strong in the phonon DOS. They broaden from 0.8(1) meV and 1.0(2) meV to 1.17(9) meV and 1.5(2) meV, respectively. We cannot use the Q dependence of these features to define their origin as the first maximum in the C_{60} form factor occurs at 3.5 \AA^{-1} and IN6 can only access a maximum of $Q \approx 2.5 \text{ \AA}^{-1}$. More surprisingly though is the presence of a quasielastic contribution at all temperatures that is characteristic of diffusive motion. This peak broadens from 2.3(7) meV at 50 K to 2.75(9) meV at 290 K, reflecting a faster diffusion with temperature. Interestingly the width is constant between 50 and 125 K while it decreases to 2.1(1) meV at 200 K, as the sample goes through the structural transformation. The source of the quasielastic peak should be the rotation of the deuterio-ammonia units.

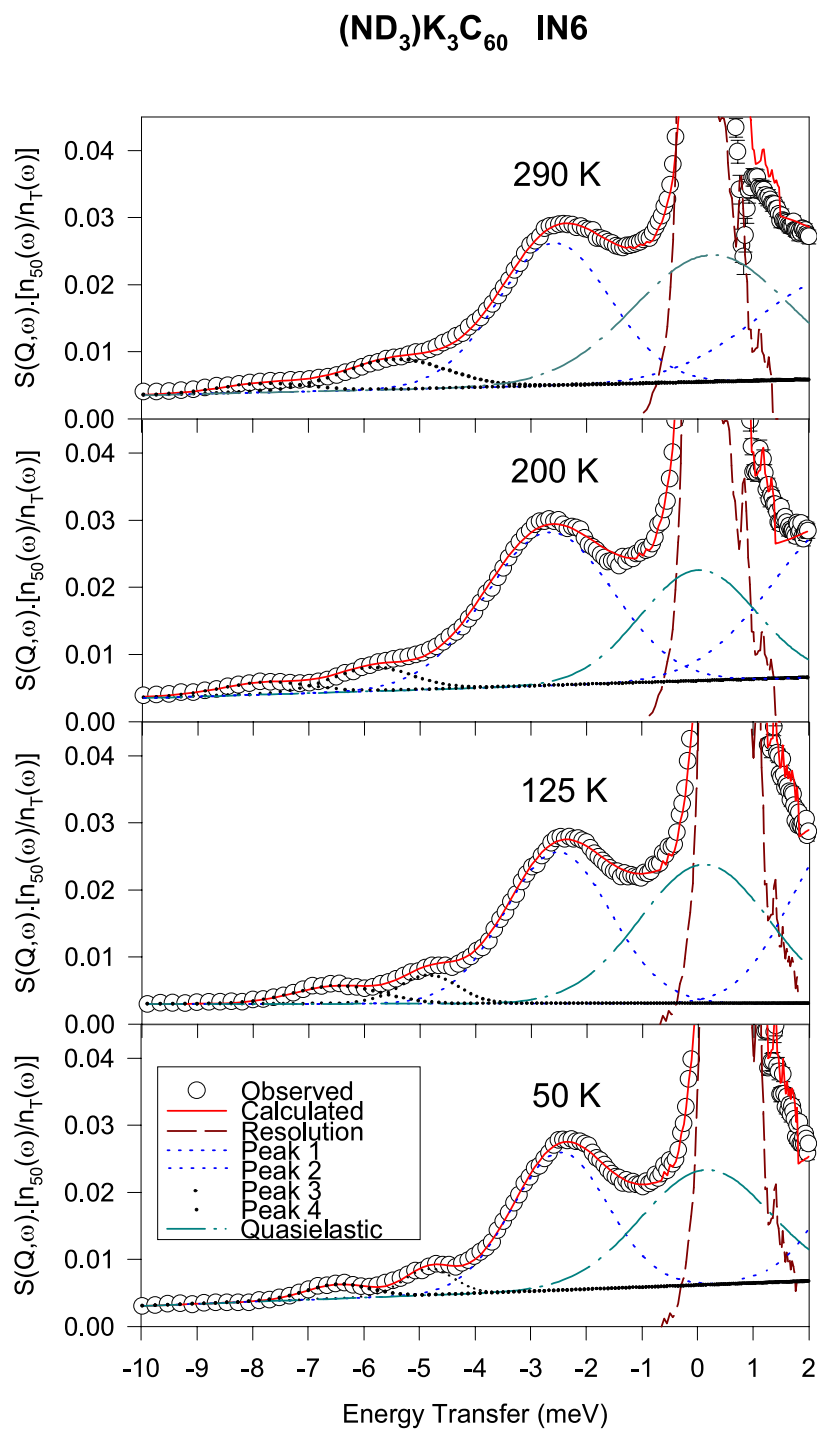


Figure 5.13: Temperature dependence of the normalised scattering law for (NH₃)K₃C₆₀. The observed points are plotted as open circles with a solid red line giving the calculated function. Each gaussian peak is convoluted with the resolution function, taken from the lowest temperature data, then summed to give the total plus a background.

5.5 Conclusions

In conclusion, we have shown *for the first time* that $(\text{NH}_3)\text{K}_3\text{C}_{60}$ shows a transition below 40 K to a long range ordered antiferromagnetic state, characterised by substantial spatially inhomogeneous effects. The observed local field at the muon site is consistent with an estimate of the magnetic moment per C_{60}^{3-} of the order of 0.1-0.2 μ_B . Such a small magnetic moment explains the absence of magnetic Bragg peaks in the neutron diffraction data. The importance of these experimental results for the understanding of superconductivity in C_{60}^{3-} compounds is far reaching. The suppression of superconductivity at large interfullerene spacings thus appears to be associated with effects of *magnetic* origin, providing an important analogy with the well-established phenomenology in high- T_c and organic superconductors. Recovery of the metallic/superconducting state upon application of external pressure may then be associated with the removal of the LRO AF state.

In addition, inelastic neutron scattering measurements reveal pronounced changes in the low-energy phonon DOS of $(\text{NH}_3)\text{K}_3\text{C}_{60}$, associated with the structural transition, as seen by powder neutron diffraction, at 150 K. A librational mode appears at 6.5 meV, growing in intensity on cooling and signifying the presence of a torsional barrier to ammonia motion of the order of 7.4 meV. Similiar features are observed for the rich spectrum of $(\text{ND}_3)\text{K}_3\text{C}_{60}$, that requires a somewhat smaller potential of 6.5 meV to describe the observed frequencies. Ideally tunnelling measurements are required to verify this potential and give additional information on any possible admixture of a sixfold potential. The librational spectra of the fulleride ions in $(\text{ND}_3)\text{K}_3\text{C}_{60}$ are much softer than in the parent K_3C_{60} . The disagreement between this measurement and that of the triple axis study may derive its basis in the limited

momentum transfer available here, as a temperature independent librational feature has also been extracted for $\text{Na}_2\text{CsC}_{60}$ on IN6 before[41]. The constant presence of a quasielastic component is the result of rotational diffusion of the deuterio-ammonia units. We can envisage a situation where, at high T, the ammonia molecules are disordered, and behave as free rotors. Upon cooling below 150 K, the interaction between the K^+ and the ammonia molecules is strong enough to trap the molecules in a torsional potential.

Chapter 6

Alkali Metal Fullerenes

6.1 Introduction

The study of superconductivity in alkali fullerenes with composition $A_2A'C_{60}$ ($A, A' = \text{Na, Rb, K}$)[23, 24, 197, 198] has been vigorously pursued. These systems invariably adopt cubic structures and their superconducting transition temperatures, T_c , increase monotonically with increasing lattice constant, a [28] up to a maximum of 33 K[24]. This behaviour can be rationalised in terms of increasing density-of-states at the Fermi level, $N(\epsilon_F)$, with increasing interfulleride separation and the concomitant decrease in molecular overlap that leads to band narrowing. For large cations (K^+, Rb^+) occupying the tetrahedral interstices, the structures are face-centered-cubic (space group $Fm\bar{3}m$)[25] and contain merohedrally disordered C_{60}^{3-} ions.

The T_c is affected in essentially identical ways by both physical and chemical pressure in these systems, with only a small deviation reported for Rb_3C_{60} [32]. A second structural family is encountered when Na^+ ions reside in the tetrahedral interstices; the crystal structure now changes from fcc at high temperatures to primitive cubic (space group $Pa\bar{3}$)[27, 42, 43, 199] near 300 K, as the spherically disordered C_{60}^{3-} ions

order orientationally. Evidently the primitive cubic family exhibits a much steeper dependence of the rate of change of T_c with interfullerene separation than that observed for the fcc systems[40, 43].

At the same time, magnetic susceptibility measurements at high pressure on $\text{Na}_2\text{CsC}_{60}$ have led to the conclusion that the effects of physical[49] and chemical[40] pressure on the superconducting properties of the $Pa\bar{3}$ phases are not identical, with chemical pressure suppressing T_c much faster than physical pressure. A further exception comes from the $\text{Li}_2\text{AC}_{60}$ ($A = \text{Rb}, \text{Cs}$) series that even though they possess the correct stoichiometry for superconductivity, none has been observed down to 50 mK[200]. This absence has been attributed to a strong $\text{Li}^+\text{-C}$ interaction that is prevalent in the crystal structure[9, 54] at all temperatures up to 473 K and up to pressures of ~ 6 GPa. The C_{60}^{3-} ions adopt a novel orientational disorder within space group $Fm\bar{3}m$ that is best described using quasi-spherical units of radius 3.567(4) Å with excess electron density in the [111] directions.

Even though no superconductivity has been encountered for other alkali fulleride compositions, a genus of the fulleride family with composition AC_{60} ($A = \text{K}, \text{Rb}, \text{Cs}$) has attracted considerable interest, principally because of the rich variety of structural forms encountered. Besides the formation of metastable cubic [67] and dimer structures[68, 69] formed by quenching at low temperatures, direct C-C bonding between the C_{60}^- ions can lead to polymer chain formation[64]. The resulting materials adopt a quasi-one-dimensional orthorhombic structure (space group $Pmnn$) with the shortest center-to-center interfullerene distance of the order of 9.10 Å, consistent with the formation of two C-C bridging bonds.

For a while, it seemed that formation of bridged fulleride ions was confined to

C_{60}^- and $C_{59}N$ (§3.3) units which contained a single unpaired electron in the lowest unoccupied molecular orbital (LUMO). However, recent work on alkali fullerides has led to the realisation that such systems are much more abundant than hitherto appreciated[201], as polymeric systems containing the C_{60}^{3-} and C_{60}^{4-} ions were synthesised and structurally characterised. For instance, Na_2RbC_{60} whose ground state structure was thought for a long time to be primitive cubic[42], was found to transform upon slow cooling to a monoclinic (space group $P2_1/a$) polymeric structure, distinctly different from that of the doubly bonded one, encountered in AC_{60} salts. The short fullerene centre-to-centre distance of 9.38 Å[69] implies a single C-C bridging bond[51, 52, 53] that agrees with the intradimer separations of 9.34 Å and 9.4 Å found in the singly C-C bridged AC_{60} dimer and $(C_{59}N)_2$ structures, respectively. Such a structure has also been found to form for other sodium C_{60}^{3-} salts, including the quaternary systems $Na_2Rb_{1-x}Cs_xC_{60}$ at ambient pressure[55] and Na_2CsC_{60} at elevated pressures[54]. The C_{60}^{3-} polymer of Na_2RbC_{60} has been shown to be non-superconducting. It has been conjectured that there may exist a connection between polymer formation and the reduced values of T_c for the primitive cubic alkali metal fullerides compared to the fcc fullerides[52]. Additionally, Na_4C_{60} is found to give rise to a two-dimensional polymer in which the interfulleride bonding is of single C-C bond order between four neighbours[74].

6.2 Sodium Fullerides

The crystal structures and dynamical behaviour of the superconducting alkali fullerides can be separated into two families. For the A_3C_{60} salts having large cations (K^+ , Rb^+) occupying the tetrahedral interstices, the structures are fcc. They are

best modelled in the space group $Fm\bar{3}m$ ($a = 14.24$ Å for K_3C_{60}) with a merohedral disorder of two equally populated standard fullerene orientations that are related by 90° rotations about $[100]$ axes. The alkali ions fill the available octahedral and tetrahedral interstices. Consideration of the sizes of the interstices in a cubic close-packed structure show that the tetrahedral hole is smaller than the ionic radii of K^+ , Rb^+ and Cs^+ . The mutual repulsion between the alkali ion and fulleride cage is reduced when the C_{60}^{3-} ion is oriented so as to present hexagonal faces to the tetrahedral cation, maximising the A^+-C distances. The restricted dynamics of the fulleride units have been measured by INS[26], where for K_3C_{60} , well-defined librational peaks are observed at 3.59(4) meV at room temperature. The Q dependence of the librational intensity indicated that the fulleride units undergo small-amplitude librations about their equilibrium positions. On cooling, the librations harden with the energy barrier (~ 500 meV) for reorientation estimated to be twice that of C_{60} . A monotonic relationship between the lattice constant and the superconducting transition temperature has been proposed for these fullerides[75]. The increase of T_c with increasing lattice constant, is explained by the narrowing of the conduction band with increasing fulleride separation.

The presence of the small Na^+ ion in the tetrahedral interstices has profound consequences on the structural and superconducting properties. While the Na_2CsC_{60} salt follows the experimental lattice constant dependence of T_c found in the case of the fcc fullerides, Na_2RbC_{60} and Na_2KC_{60} show anomalous behaviour and much lower T_c s than expected (3.5 and 2.5 K, respectively). These salts adopt fcc structures at high temperatures with a structural transition to a primitive cubic phase[42, 43] evident at ~ 300 K[199].

Evidently, the reduction of repulsive $A^+C_{60}^{3-}$ interactions is sufficient for interactions between the C_{60} ions to become significant. In this case, the salts are isostructural with pristine C_{60} , with the same optimisation of the primitive cubic fulleride orientations found in both cases. Inelastic neutron scattering experiments on Na_2RbC_{60} [27] reveal much softer librations (2.83(17) meV at 50 K) than those reported in K_3C_{60} . The intermolecular potential (~ 300 meV) is somewhat harder than that found in pristine C_{60} . The librations soften and broaden with increasing temperature until they collapse into a quasielastic line above the phase transition, signalling the occurrence of fulleride rotational diffusion. In the case Na_2CsC_{60} , a similar situation occurs but the energy of the librations, indicating reorientational jump motion, are temperature independent at 2.7(1) meV.

The modified dependence of T_c on lattice constant (Fig.1.6) cannot be attributed to differences between the lattice constant dependence of $N(\varepsilon_F)$ for the Na_2AC_{60} salts and the fcc alkali fullerides[44, 45, 46, 47]. Additionally, unlike for the fcc fullerides, chemical pressure suppresses T_c much faster than physical pressure. Structural work at elevated pressures for Na_2RbC_{60} [50] identified a low symmetry phase with short interball distances (~ 9.35 Å). Recent work has revealed a complicated situation where the properties of the sodium fullerides are found to be extremely sensitive to cooling protocols.

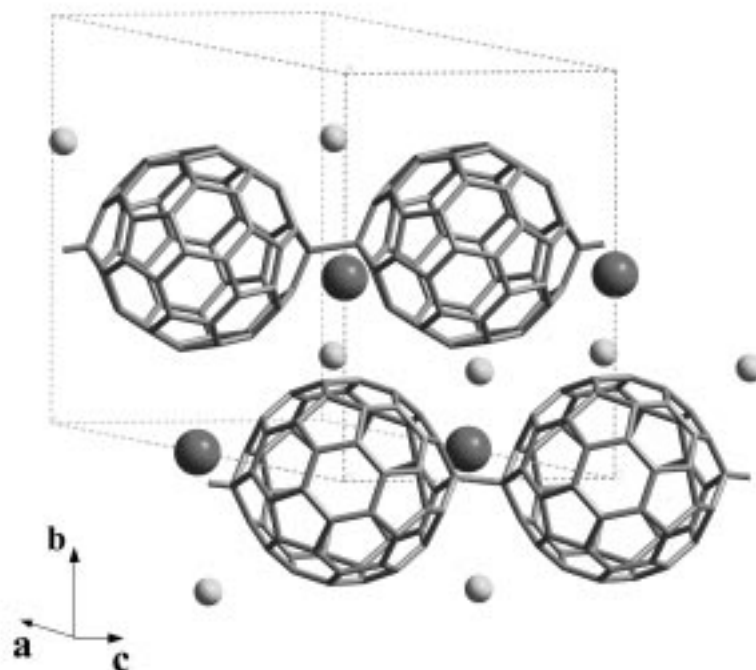


Figure 6.1: The unit cell of the polymeric phase of $\text{Na}_2\text{RbC}_{60}$.

While, upon rapid cooling, the salts remain strictly cubic, slow cooling stabilises the same low symmetry phase as that found at high pressures. Neutron powder diffraction experiments on quenched $\text{Na}_2\text{RbC}_{60}$ revealed the presence of non-cubic peaks in the temperature region between 190 and 260 K[202], but the quantity of this phase was insufficient to perform a structural refinement. Also observable in this data is a jump in the cubic lattice constants at ~ 310 K that is associated with the order-disorder transition from the pc to fcc phase.

High resolution powder diffraction measurements on slowly cooled $\text{Na}_2\text{RbC}_{60}$ allowed the structural solution of this low symmetry phase. The monoclinic structure has fulleride units linked via single bonds along the crystallographic c_m -axis. While

the length of these interfulleride bonds were fixed at 1.55 Å from the synchrotron work[53], our more recent neutron diffraction work[203], where we attempted to better define the distortions around the frontier carbons, increases this length to ~ 1.7 Å with an inclination of the bond to the c_m -axis of 7.7° while it remains in the $(bc)_m$ -plane (Fig.6.1). The polymerisation transition has been shown to occur under slow cooling conditions for $\text{Na}_2\text{Rb}_{1-x}\text{Cs}_x\text{C}_{60}$ ($1 \leq x \leq 0$) and $\text{Na}_2\text{KC}_{60}$ fullerides. The polymers are not superconducting[52, 55, 201], and the observed superconductivity is associated with the metastable $Pa\bar{3}$ phase.

It has been of particular interest that the metastable primitive cubic family, $\text{Na}_2\text{Rb}_{1-x}\text{Cs}_x\text{C}_{60}$ ($1 \leq x \leq 0$) displays a much steeper rate of change of T_c with interfullerene spacing. The origin of this effect could be empirically ascribed to the modified crystal structures and different orientational state of the fulleride ions. Indeed NMR measurements[48] have confirmed that the values of $N(\epsilon_F)$ for $\text{Na}_2\text{RbC}_{60}$ and $\text{Na}_2\text{KC}_{60}$ are strongly suppressed. However, EPR spectroscopy[45, 46] measurements find little difference between the lattice constant dependence of $N(\epsilon_F)$ for $\text{Na}_2\text{CsC}_{60}$ and fcc K_3C_{60} and Rb_3C_{60} . This implies that the changed orientational state in the $Pa\bar{3}$ phases may not be the factor responsible for the depressed T_c .

Powder neutron diffraction was employed to study in detail the transformation of the C_{60}^{3-} monomer phase to the polymer both as a function of temperature and time. Measurements taken on heating also reveal a strongly hysteretic behaviour associated with the breaking and forming of the C-C bonds. Neutron inelastic scattering measurements were used to characterise both the intramolecular vibrational spectrum of C_{60}^{3-} and to provide direct identification of the bridging C-C modes in the intermolecular energy region.

6.2.1 Polymeric $\text{Na}_2\text{RbC}_{60}$

$\text{Na}_2\text{RbC}_{60}$ was prepared (K. Kordatos) by reaction of stoichiometric quantities of C_{60} , Na and Rb, contained in a sealed Ta cell inside a sealed glass tube filled with He to 500 Torr at 480 K for 3 h, 570 K for 12 h, and 620 K for 72 h; after an intermediate regrinding, the sample was annealed at 673 K for 25 days. $\text{Na}_2\text{CsC}_{60}$ was also prepared by reaction of stoichiometric quantities of C_{60} , Na and Cs, contained in a sealed Ta cell inside a sealed glass tube filled with He to 600 Torr at 473 K for 12 h and at 703 K for 3 weeks with intermittent shaking. Both samples were characterised by solid state NMR, X-ray powder diffraction and SQUID magnetometry.

Neutron powder diffraction measurements on $\text{Na}_2\text{RbC}_{60}$ (mass= 1.2 g) were performed with the high-flux medium resolution powder diffractometer, D1B, at the ILL. The sample was placed in a cylindrical 4-mm diameter vanadium sample holder and was press-sealed with In wire. Data were collected in 5 min intervals throughout the experiment ($\lambda = 2.5242 \text{ \AA}$, $2\theta = 10^\circ - 90^\circ$). The applied heat treatment protocol comprised of cooling from 315 to 180 K at a rate of 5 K/h, remaining at 180 K for 12 h, and then cooling to 2 K at 72 K/h. Following optimisation of the diffracted intensity that provided a doubling of the observed counting rate, the sample was heated from 2 to 350 K at a rate of 16.5 K/h.

Table 6.1: The INX correction parameters used for the IN6 data of $\text{Na}_2\text{RbC}_{60}$.

Angular Range	10 80 + 84 115°
Detectors	22 205 + 209 256
Wavelength	4.12 Å
Can Radius	3.5 mm
Transmission	0.99
Sample Density	1.19 g cm ⁻³
Molecular Mass	851.51 g
Average Mass	13.5 g
σ_s	346.46 barns
σ_a at 1.8Å	1.68 barns
Vanadium of diameter 1.9 mm at 295 K with 0.9 transmission	
detectors used to exclude Bragg peaks	
24 52 + 90 124 + 179 202 + 242 256	

Neutron inelastic scattering measurements on $\text{Na}_2\text{RbC}_{60}$ (mass= 1.2 g) were performed with the IN6 spectrometer at the ILL. An incident neutron wavelength of 4.12 Å was used. The sample was placed inside a thin-wall cylindrical aluminium can (i.d.= 7 mm) and press-sealed with In wire. It was then cooled to 200 K at 8.7 K/h, where it remained for 24 h before further cooling to 100 K. Data were collected on heating at 100, 200 and 320 K over the full range of scattering angles (10°-115°), and later summed to improve statistics at the expense of momentum resolution. Corrections to the data were made for the aluminium can contribution, detector efficiency and geometry using the INX program (Table 6.1).

When converting to the phonon density-of-states, we performed a multiphonon correction based on four groups of peaks observable in the raw data (Table 6.2). At low energy transfers, there are fulleride cage motions and rubidium optic modes, while entirely C-C vibrations are found at higher energy transfers. Sandwiched between these distinct regions is a group of modes of mixed origin that have been attributed

a mass weighting intermediate between that of sodium and two carbon atoms.

Table 6.2: Multiphonon Correction Parameters used with the FITDEN5 program for $\text{Na}_2\text{RbC}_{60}$.

Temperature/K	Parameter	Peak 1	Peak 2	Peak 3	Peak 4
200	Mass	720.0	85.5	17.5	12.1
	Frequency/meV	3.92	4.81	10.28	86.68
	Cutoff freq./meV	6.95	12.04	17.38	100.67
	Peak Width	1.03	0.90	0.90	1.42
	Concentration	1.44×10^{-2}	5.8×10^{-3}	3.94×10^{-2}	0.940
320	Mass	720.0	85.5	17.5	12.1
	Frequency/meV	3.67	5.0	13.39	78.53
	Cutoff freq./meV	7.07	9.27	23.54	100.72
	Peak Width	1.03	0.90	0.90	1.39
	Concentration	1.49×10^{-2}	1.07×10^{-2}	1.99×10^{-2}	0.955

Neutron Diffraction Results

Fig.6.2 shows the evolution of the neutron diffraction profiles of $\text{Na}_2\text{RbC}_{60}$ between 150 and 350 K in the 2θ range 28° - 39° , as obtained on heating with the D1B diffractometer. The intensity is displayed in a logarithmic fashion in order to facilitate visualisation of the phase transitions which occur in this temperature range. At low temperatures, the patterns are dominated by low-intensity broad peaks. There is a drastic change in the profiles in the vicinity of 270-280 K, whence many peaks disappear, while others gain significantly in intensity. These changes are interpreted in terms of the established structural behaviour of $\text{Na}_2\text{RbC}_{60}$, namely that a transition from the low-symmetry monoclinic to the high-symmetry primitive cubic structure occurs at these temperatures[52, 53]. Shortly after this, a second transformation occurs to a fcc phase at ~ 299 K; this is accompanied by a shift in the position of the cubic peaks to lower 2θ , in agreement with the discontinuous lattice expansion at the transition temperature. The data were analysed by both single-phase and two-phase

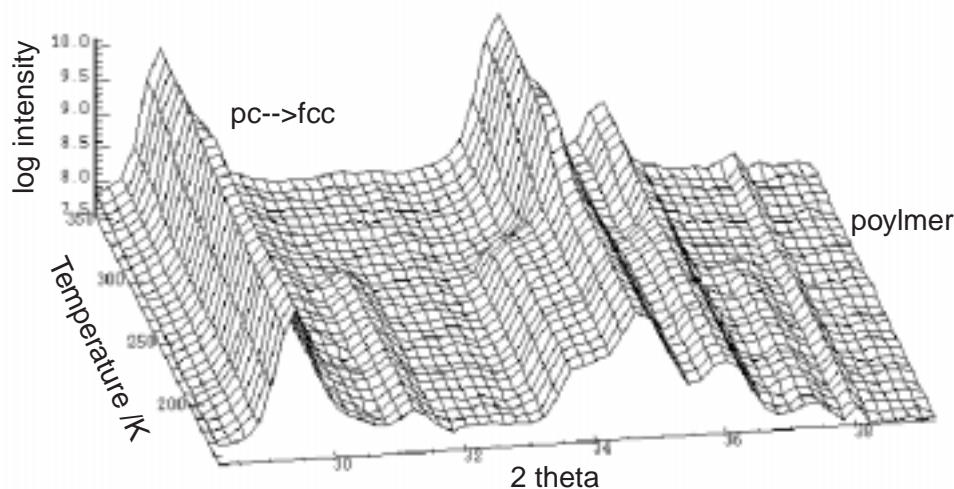


Figure 6.2: Selected region powder neutron diffraction patterns obtained on D1b. The intensity scale is logarithmic to highlight the phase transitions. Reflections corresponding to those of the polymer transform abruptly at ~ 280 K to those of the primitive cubic structure (labelled on the right hand side of the figure). A further change is apparent around 300 K where the cubic reflections jump to larger d -spacings and increase in intensity, as expected for the $pc \rightarrow fcc$ transition.

Rietveld profile analysis, in the 2θ range 10° - 60° , using the program FULLPROF[104] and employing the published structures for the monomer (fcc, space group $Fm\bar{3}m$ ¹ and pc, space group $Pa\bar{3}$ [43]) and polymer (monoclinic, space group $P2_1/a$ [53]) forms of Na_2RbC_{60} . Even though we now have a better representation of the monoclinic structure from neutron powder diffraction[203], this work has only recently been completed so we retained the X-ray structure throughout this analysis.

A two-phase Rietveld refinement between 10° and 60° 2θ , at 2.3 K is shown in Fig.6.3 with the structural and profile parameters listed in Table 6.3. Due to poorly

¹Modelled as quasi-spherical units of radius 3.55 Å.

resolved data, and the desire not to introduce too many parameters into the Rietveld analysis, we chose a *pc* form where one-third of the molecules are in the minor orientation (rotated by 38° about $[111]$ from the standard orientation) with the remainder being in the major orientation (rotated by 98°) which corresponds to the composition of primitive cubic C_{60} between ~ 150 and 250 K[12] and kept this relative fraction fixed for all refinements involving the *pc* phase. The fraction of the polymer phase is $64(2)\%$ while the primitive cubic phase adds $36(2)\%$ to the profile ($R_{wp} = 4.99\%$, $R_{exp} = 1.84\%$) with refined lattice parameters $a_m = 13.66(1)$ Å, $b_m = 14.420(8)$ Å, $c_m = 9.354(6)$ Å and $\beta_m = 133.57(6)^\circ$ and $a_c = 13.99(1)$ Å, respectively. The short $9.354(6)$ Å c_m -axis, is a direct result of the close proximity of the bonding fulleride units and much shorter than the fulleride centre-to-centre distance of $9.89(1)$ Å in the primitive cubic phase at the same temperature. Further comparison can be made to the doubly bridged polymer phase of CsC_{60} and the 2D singly bridged polymer Na_4C_{60} which exhibit closest centre-to-centre distances of $9.12[204]$ and 9.28 Å[74], respectively.

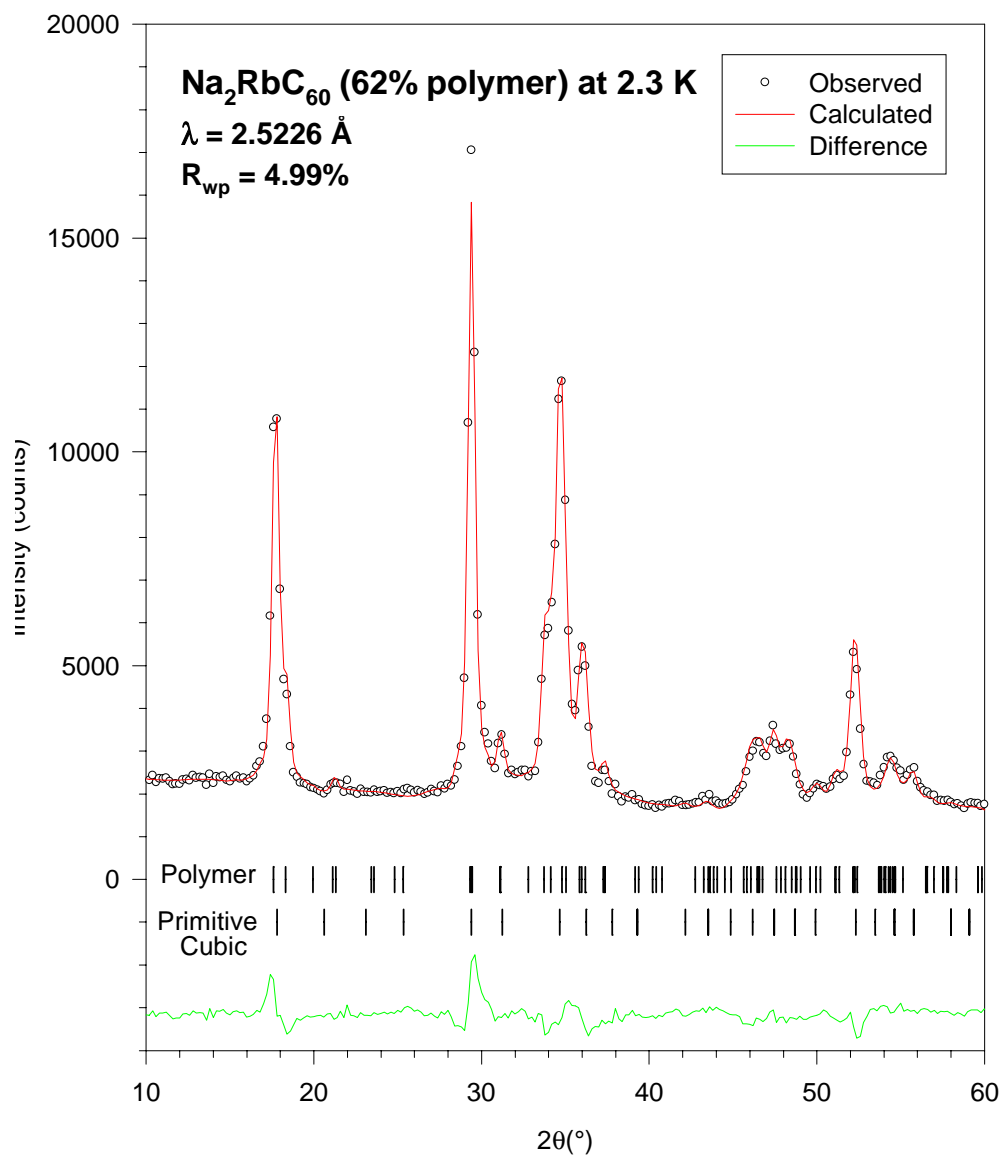


Figure 6.3: Rietveld refinement of D1B data at 2.3 K using a two-phase polymer/pc model as described in the text. Structural parameters can be found in Table 6.3.

Table 6.3: Structural parameters for two-phase Rietveld refinement of the powder diffraction profiles of $\text{Na}_2\text{RbC}_{60}$ (D1B, 2.3 K), as described in the text.

HISTOGRAM

R_{wp}	5.79%	R_p	4.57%	R_{exp}	1.84%	χ^2	9.86
$\lambda / \text{\AA}$	2.5226	U / $^\circ$	1.57(1)	V / $^\circ$	-0.27(1)	W / $^\circ$	0.20(1)
η	0.181(9)	$\Delta_{2\theta} / ^\circ$	-0.15(1)	Asymm.	0.01(1)		

PHASE 1: Polymer

Space group	$P2_1/a$		Weight Fraction		$62(2)\%$		
$a / \text{\AA}$	13.66(1)	$b / \text{\AA}$	14.416(9)	$c / \text{\AA}$	9.354(7)	$\beta / ^\circ$	133.59(6)
atom	x/a	y/b	z/c	atom	x/a	y/b	z/c
C1	-0.11735	0.22613	-0.19091	C2	0.02162	0.23949	-0.05100
C3	-0.01890	0.09325	0.32973	C4	0.00030	0.00000	0.41718
C5	-0.34882	-0.02404	-0.27843	C6	0.34509	0.04270	0.42021
C7	-0.18679	0.20486	-0.12862	C8	0.09713	0.23217	0.15724
C9	-0.10343	-0.20064	0.08204	C10	0.18050	-0.17333	0.36790
C11	-0.14497	0.12458	0.14069	C12	-0.10580	-0.06593	0.23967
C13	0.08958	0.14714	0.37684	C14	0.12875	-0.04338	0.47582
C15	-0.32215	0.06871	-0.20028	C16	0.28217	0.12683	0.40816
C17	-0.28980	-0.08868	-0.11850	C18	0.31453	-0.03055	0.48993
C19	-0.11441	0.19783	0.07097	C20	0.03055	0.21177	0.21691
C21	-0.04289	-0.15005	0.25171	C22	0.10207	-0.13610	0.39765
C23	-0.24664	0.06138	0.00794	C24	-0.22664	-0.03589	0.05847
C25	0.21272	0.10556	0.47043	C26	0.23272	0.00829	0.52096
C27	-0.29285	0.13892	-0.26712	C28	0.22559	0.18879	0.25486
C29	-0.22948	-0.16931	-0.10698	C30	0.28897	-0.11945	0.41500
Na	0.00000	0.25000	0.50000	Rb	0.50000	0.00000	0.00000

PHASE 2: Primitive Cubic

Space group	$P\bar{a}3$		Weight Fraction		$38(2)\%$		
$a / \text{\AA}$	13.99(1)	$b / \text{\AA}$	13.99(1)	$c / \text{\AA}$	13.99(1)	$\beta / ^\circ$	90
atom	x/a	y/b	z/c	atom	x/a	y/b	z/c
C1	0.22677	-0.03424	0.10663	C2	0.24579	-0.05817	0.00901
C3	0.20655	0.06207	0.13236	C4	0.20535	-0.14307	-0.03144
C5	0.16750	-0.09541	0.16370	C6	0.24439	0.01402	-0.06207
C7	0.20535	0.13466	0.06097	C8	0.14638	-0.20414	0.02613
C9	0.12745	-0.18032	0.12305	C10	0.22427	0.11083	-0.03624
C11	0.09281	-0.02733	0.23368	C12	0.12205	-0.11464	0.18923
C13	0.13496	0.06077	0.20525	C14	0.05196	-0.18472	0.16370
C15	-0.00651	-0.01031	0.25270	C16	0.19303	-0.11354	0.11694
C17	0.20635	0.06197	0.13266	C18	-0.04726	-0.16750	0.18302
C19	-0.07619	-0.08070	0.22717	C20	0.23548	-0.02503	0.08841
Rb1	0.50000	0.50000	0.50000	Na1	0.25	0.25	0.25

All isotropic temperature factors are fixed at 2.5 \AA^2

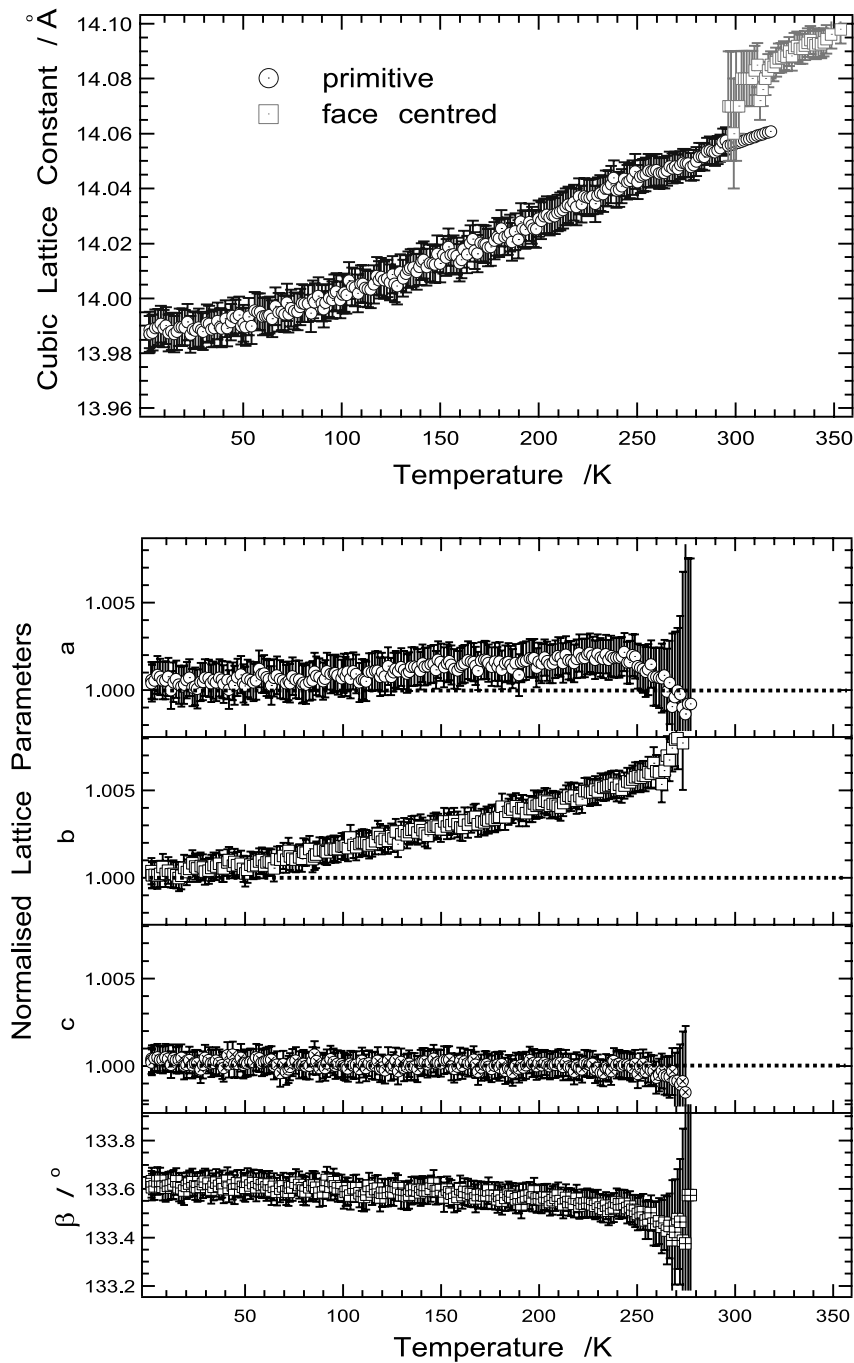


Figure 6.4: Temperature evolution of the lattice constant of cubic $\text{Na}_2\text{RbC}_{60}$ as extracted from the powder neutron diffraction data upon heating the sample to 350 K (upper panel): open black circles and grey squares refer to the pc and fcc phases, respectively. The monoclinic lattice parameters of polymeric $\text{Na}_2\text{RbC}_{60}$, normalised to the values 2.3 K, are shown in the lower panel with the key: a circles, b squares, c crossed-circles and angle β crossed-squares.

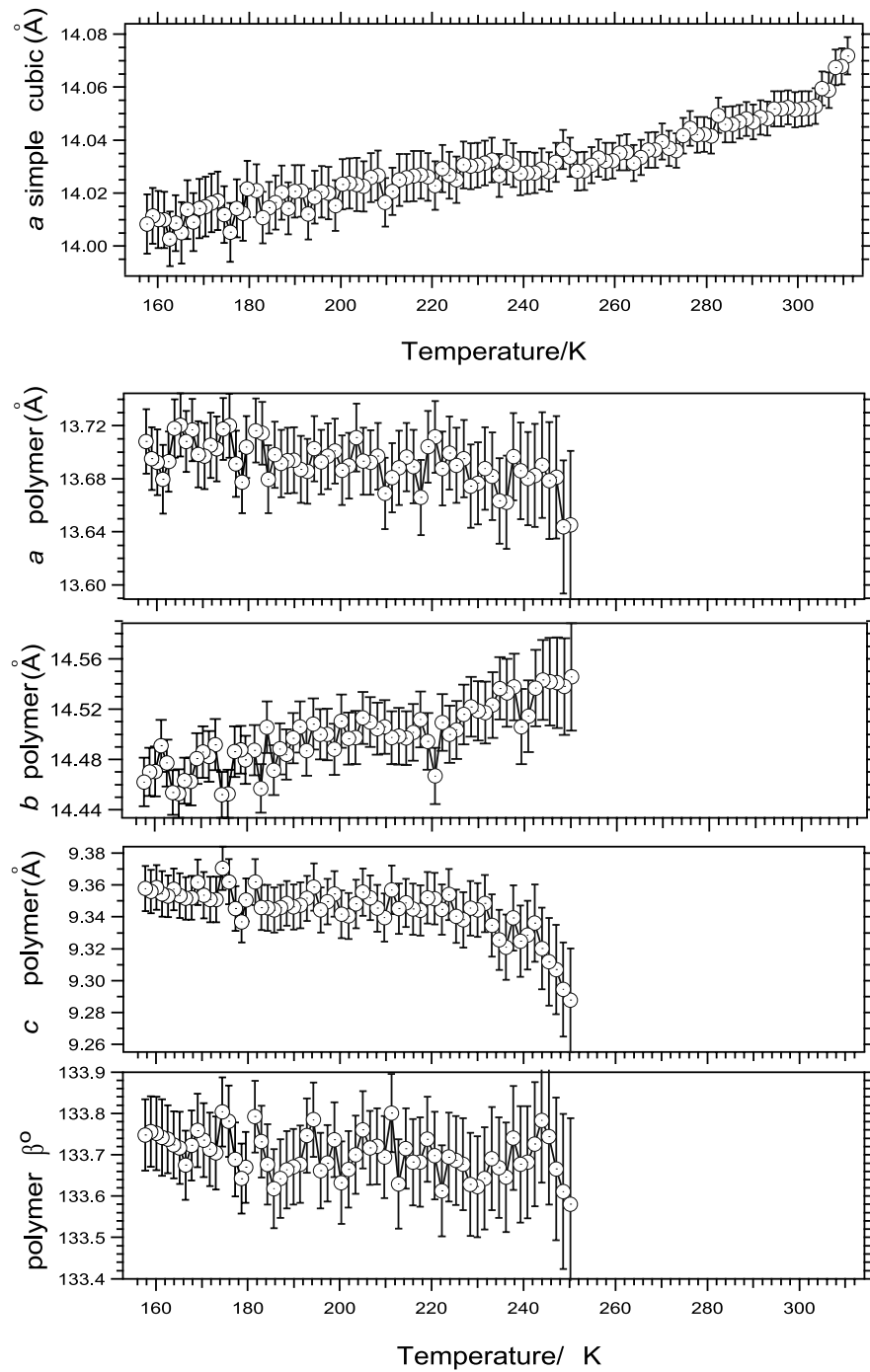


Figure 6.5: Temperature evolution of the lattice constant of cubic $\text{Na}_2\text{RbC}_{60}$ (upper panel) and the monoclinic lattice parameters a , b , c and angle β (lower panel) of polymeric $\text{Na}_2\text{RbC}_{60}$, as extracted from the powder neutron diffraction data upon cooling the sample to 155 K.

Fig.6.4 details the temperature evolution of the lattice parameters for all three phases obtained from the Rietveld analysis of the neutron data on heating - the results for the corresponding datasets measured on cooling are in excellent agreement and are shown separately in Fig.6.5 for clarity. On heating, a smooth evolution of all parameters occurs until 250 K when the gradual transformation of the polymer phase begins. The strong anisotropic bonding present in the polymer phase is clearly evidenced by the negligible - even slightly negative - thermal expansivity found along the chain axis, c_m ($d(\ln c_m)/dT = -2(1) \times 10^{-6} \text{ K}^{-1}$). This is in sharp contrast with the value of the expansivity along b_m ($d(\ln b_m)/dT = 2.4(1) \times 10^{-5} \text{ K}^{-1}$) which is comparable to those found in monomeric fulleride phases (e.g. in the primitive cubic phase $d(\ln a_c)/dT = 1.72(7) \times 10^{-5} \text{ K}^{-1}$). The expansivity of the a_m behaves in a somewhat intermediate manner and is a reflection on the tighter crystal packing in this direction enforced by the spatial distribution of rubidium ions. The cooling data exhibit the same trends as the heating data, albeit with poorer statistics.

The temperature dependence of the fraction of the primitive cubic phase, during both the cooling and heating cycles, is shown in Fig.6.6. The fractions of the monomer and polymer phases remain essentially temperature independent over a wide range of temperatures (2-230 K). Then the polymer fraction starts decreasing sharply until a complete disappearance of the polymer phase has occurred by 277 K, above which the data can be described in terms of the primitive cubic structure alone.

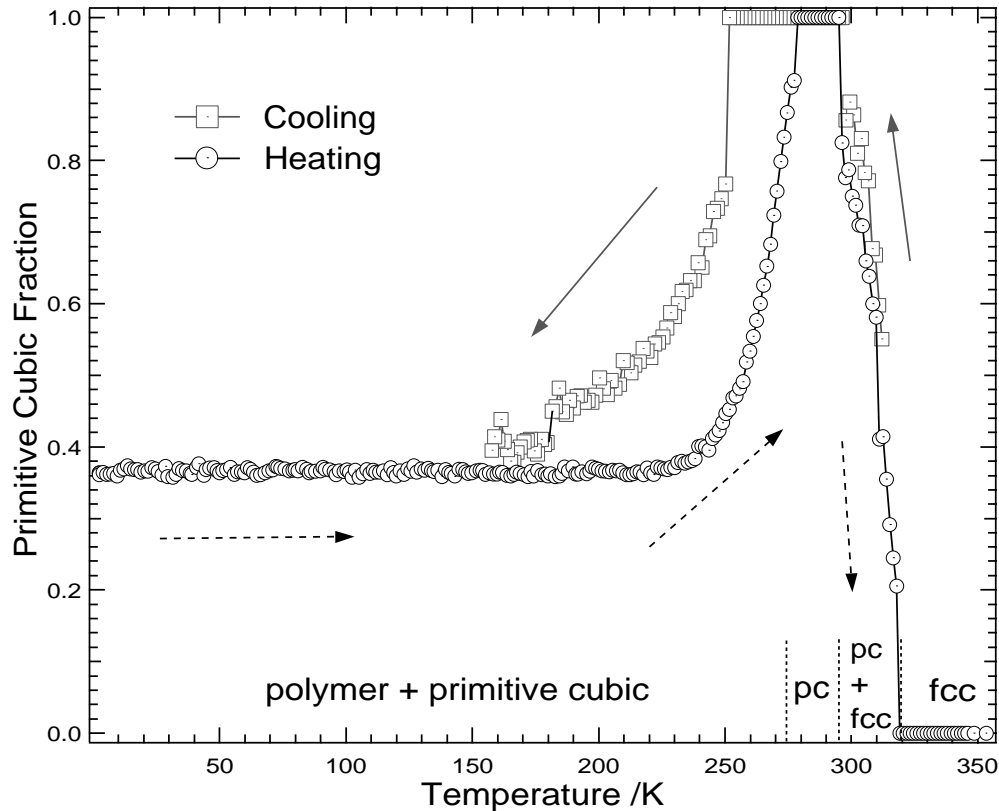


Figure 6.6: Volume fraction of the primitive cubic phase of $\text{Na}_2\text{RbC}_{60}$, as obtained from Rietveld analysis of the powder neutron diffraction profiles during the cooling (squares and full arrows) and heating (circles and dashed arrows) cycles. There are four different compositional regions as indicated: single phase fcc between 317 and 350 K, a phase coexistence region of pc and fcc phases between 296 and 317 K, single phase pc (278- 296 K), and the polymer and pc phase coexistence region.

A Rietveld refinement of the data at 285 K is shown in Fig.6.7 showing the goodness of fit ($R_{wp}= 8.24\%$, $R_{exp}= 1.81\%$) using the primitive cubic model only. The lattice constant of $14.053(5) \text{ \AA}$ is in good agreement with high resolution synchrotron X-ray data taken under similar cooling conditions[169] and D1B neutron data taken

on rapidly cooled $\text{Na}_2\text{RbC}_{60}$ [202]. A summary of the profile parameters is included in Table 6.4.

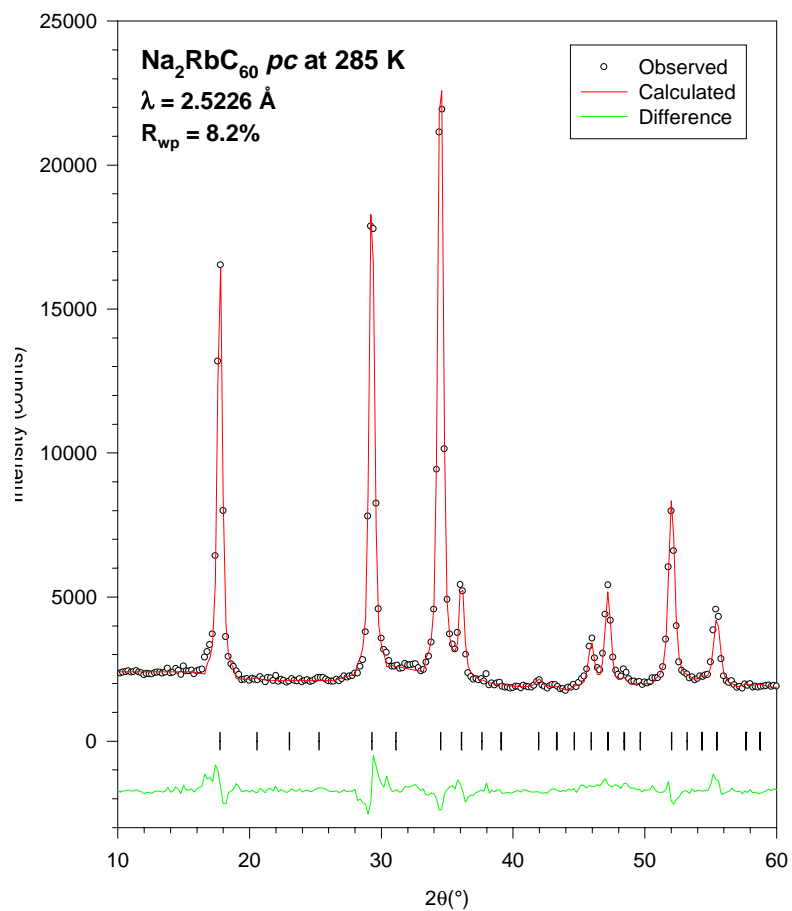


Figure 6.7: Rietveld refinement of D1B data at 285 K using a single *pc* phase. Structural parameters can be found in Table 6.4.

Table 6.4: Profile parameters for single phase refinement of $\text{Na}_2\text{RbC}_{60}$ (D1B 285 K).

Primitive Cubic $\text{Na}_2\text{RbC}_{60}$ at 285 K	
a / Å	14.053(5)
R_{wp} / %	8.24
R_p / %	6.11
R_{exp} / %	1.9
λ / Å	2.5226
U / °	1.5(4)
V / °	-0.6(3)
W / °	0.25(4)
η	0.61(3)
$\Delta 2\theta$ / °	-0.12(1)
asym	0.0122(9)
B_{iso} C	4.7(4) Å ²
B_{iso} Na	7(1) Å ²
B_{iso} Rb	6(1) Å ²

The evolution of the cubic lattice constant, a_c , with temperature is smooth up to 299 K when it becomes evident that a mixture of phases[52] is again present. However, the quality of the data is insufficient to precisely describe the transition boundary. As a consequence, refinements of the data between 299 and 317 K were performed repeatedly following various strategies. As single phase (either pc or fcc) refinements were clearly inadequate in this temperature range, two-phase refinements were attempted. In order to achieve convergence, the lattice constant of the pc component was extrapolated from the lower temperatures and kept fixed during refinement. In this way, a reasonable evolution of the fcc lattice constant and phase fraction was obtained up to 317 K. Above this temperature, satisfactory refinements of the diffraction profiles could be achieved by employing a model of a single fcc component (a_{fcc} = 14.085(5) Å at 317 K and a_{fcc} = 14.098(5) Å at 353 K).

The data obtained on cooling were not of sufficient quality to allow the precise determination of the transition temperatures, as above 250 K, the polymer fraction

is so small and peak overlap so extensive that it is not possible to refine its contribution independently. However, using an analogous approach to that employed in the refinement of the diffraction profiles obtained on heating, it was possible to extract the temperature evolution of the lattice constants and phase fractions. Fig.6.6 shows the presence of strong hysteretic behaviour for the formation and destruction of the polymer phase, as at all temperatures down to about 180 K the polymer fraction is greater during the cooling cycle.

A simple Arrhenius plot can be constructed from the fraction of simple cubic $\text{Na}_2\text{RbC}_{60}$ to extract the energy of activation for the formation/destruction of the polymer. For both heating and cooling, linear regions within plots of $\ln(\text{fraction})$ vs. $1/T$ were identified and the corresponding gradients extracted. On cooling, the data exhibits Arrhenius like behaviour from 250 to 219 K. The effective activation energy is 57(2) meV. On heating through 278 to 258 K an overall increase in activation energy is seen to 208(4) meV. The activation energy on heating is of the order of four times higher than the corresponding value on cooling. This seems to suggest the polymer is quite easy to form and is rather stable.

While waiting at 180 K in the cooling cycle, the slow transformation can be described as a linear equation of the rate of change of the polymer fraction, ϕ

$$\phi(t) = 55.6(2) + 0.0062(5) \times t(\text{min}) \quad (6.1)$$

where over ~ 12 hours the fraction of polymeric $\text{Na}_2\text{RbC}_{60}$ increases by just 4.4%. The extremely slow kinetics of the polymerisation reaction are clearly evident from these results and a complete transformation at this rate would necessitate 120 hours. This can be compared with X-ray powder data collected on the same sample under similar cooling conditions but allowing equilibration at 200 K. The fraction of the polymeric

phase reached $\sim 53\%$ when the temperature is 200 K and decreases by $\sim 7\%$ over ~ 7 hours. The extracted linear fit $\phi(t) = 53.0(2) + 0.0018(1) \times t(/min)$ [169] shows a large thermodynamic effect for the choice of equilibration temperature. Here a complete conversion to the polymer would require a mere 44 hours, approximately one third of the time needed at a temperature 20 K cooler.

Neutron Inelastic Scattering Results

The scattering law, $S(Q, \omega)$, was measured for $\text{Na}_2\text{RbC}_{60}$ with the IN6 spectrometer at an average $Q = 1.47 \text{ \AA}^{-1}$, at 100, 200 and 320 K. The data are normalised to the data at 100 K in order to facilitate comparisons and are shown in Fig.6.8. At both 100 and 200 K when the polymer and cubic phases coexist, there are two excitations evident in the measured spectra. The latter can be adequately described by fitting with two Gaussian peaks, convoluted with the instrumental resolution function. These are located at 3.30(5) and 2.92(8) meV with full widths at half maximum (FWHM) of 3.08(8) and 0.4(1) meV, respectively at 200 K. Similar broad features are present in the low-energy inelastic spectra of the doubly-bridged AC_{60} (A= Rb, Cs) polymers[78, 205]. They have been assigned to twisting modes of the polymer chains and it is tempting to make the same assignment in the present case. The weaker, narrow line is a librational peak resulting from non-transformed primitive cubic $\text{Na}_2\text{RbC}_{60}$. At 320 K, when the polymer phase has disappeared and the system adopts an orientationally disordered fcc structure, quasielastic scattering is present. This can be well-described by a broad Lorentzian line, centered at zero-energy transfer, of FWHM= 4.8(1) meV and implies the existence of diffusive rotational motion

in the high temperature fcc phase of $\text{Na}_2\text{RbC}_{60}$ [27, 41]. There is also a close rapport with the high temperature behaviour of $\text{Na}_2\text{CsC}_{60}$ where a similar coexistence of librational modes and quasielastic scattering is observed[41]. Comparison to the diffraction results where a coexistence of pc and fcc forms over a short temperature span around 310 K can also be made.

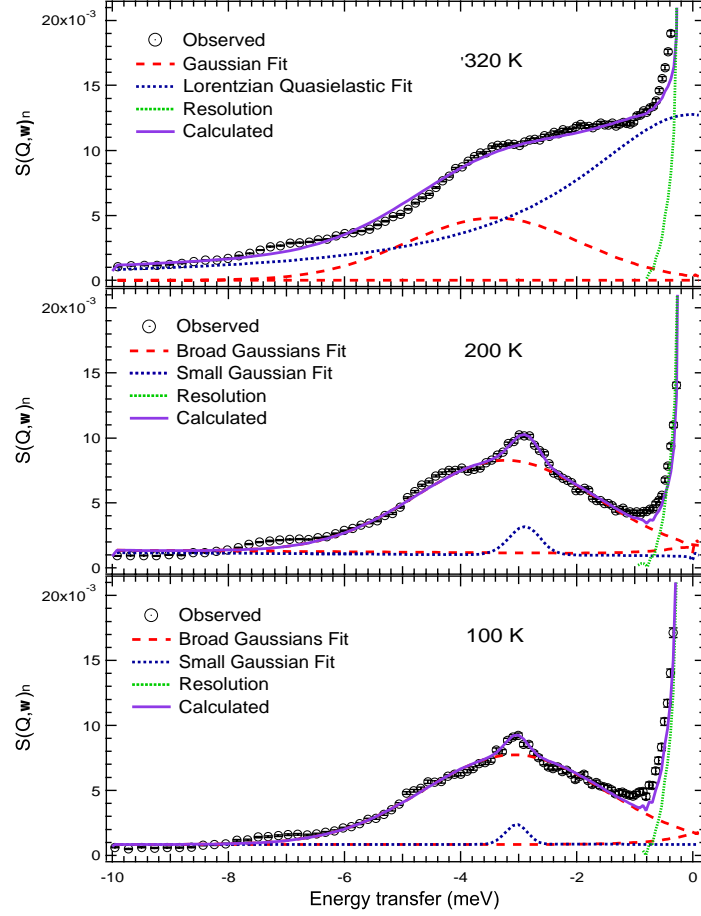


Figure 6.8: Near inelastic neutron scattering spectra ($Q_{av} = 1.42 \text{ \AA}$) of $\text{Na}_2\text{RbC}_{60}$ at 100, 200 and 320 K; the energy transfer shown is with respect to the sample. Data at 200 and 320 K have been scaled by the Bose factor so they are directly comparable to the 100 K spectrum. Each panel shows the normalised scattering law, $S(Q, \omega)_n$, as open circles with error bars. The data at 100 and 200 K were fitted by the convolution of a delta function at the elastic line, two broad Gaussians (one in neutron energy loss) and a weak Gaussian with the resolution function. The presence of quasielastic scattering is evident in the spectrum of the disordered fcc phase at 320 K and is modelled by a broad Lorentzian of width $2.8(1) \text{ meV}$.

The generalised phonon density-of-states, $G(\omega)$ was extracted from the full angular range of the data and is shown in Fig.6.9 for the energy range 0-38 meV at temperatures 200 and 320 K. In the energy transfer window shown, there are four

features of note at both 200 and 320 K. Three peaks at ≈ 4 , 7 and 34 meV, that remain almost unchanged by the transformation to the cubic phase and the broad peak between 8 and 25 meV that is strongly suppressed in intensity on going through the polymer-cubic transition.

In order to exemplify this situation further, the bottom panel of Fig.6.9 shows the difference curve obtained by subtracting the high temperature (cubic monomer phase) from the low temperature (two-phase mixture of polymer and monomer phases) data. The only feature which survives this subtraction is the broad peak at 8-25 meV which coincides with the intermolecular region of the vibrational spectra of fullerenes and their derivatives. The lowest lying modes are assigned to C_{60}^{3-} translational and librational modes and to Rb^+ optic modes. The observation of the peak at ~ 7 meV is in good agreement with the ~ 6 meV calculated for the octahedral rubidium ion in Rb_3C_{60} [192], the difference may be due to a more expanded fulleride lattice in Rb_3C_{60} that effectively reduces the force constant between Rb^+ and the fulleride ion. The highest energy mode at 34 meV is assigned to the lowest energy intramolecular mode, $H_g^{(1)}$ of C_{60}^{3-} [35].

A closer look at the lowest energy polymer modes shows an asymmetry and discernible kinks - a manifestation of the lowering in symmetry in the polymer phase. The details of the intermolecular modes are not quite like those seen in RbC_{60} so implying somewhat different van der Waals parameters for these bonds [78]. The overwhelming feature however, is the reduction in scattering for the 320 K spectra within the 8-25 meV region when compared to that of the polymer/pc system. Both spectra contain a substantial peak at ~ 15 meV that is due to sodium optic modes and so a direct subtraction of the two spectra gives the excess scattering found in

the polymer phase and is shown in the lower panel of Fig.6.9. While the error bars are quite large, a distinct maximum in the scattering is found between 8 and 18 meV and is evidence for the polymeric nature of the low symmetry system. This can be compared to the scattering found in RbC_{60} polymer (broad distribution from 12 to 23 meV) and dimer (3 sharp peaks at 10.4, 12.2 and 13 meV) phases[78]. Even though we witness the broad distribution of intensity characteristic of the double bonded polymer, we also see that the bulk of the scattered intensity has been softened by around 5 meV. This softening is indicative of weaker interfullerene bonding that is consistent with the presence of single C-C bonds as established by the X-ray profile refinements.

Further experiments have been performed on the TFXA spectrometer at ISIS. Data taken on TFXA has the advantage of having excellent, almost uniform resolution up to high energy transfers enabling the decomposition of C_{60} intramolecular modes into their individual components. Comparison of this data to that taken on pristine C_{60} , can be reconciled due to the symmetry reduction in polymeric $\text{Na}_2\text{RbC}_{60}$ along with the increased charge residing on the cage[206].

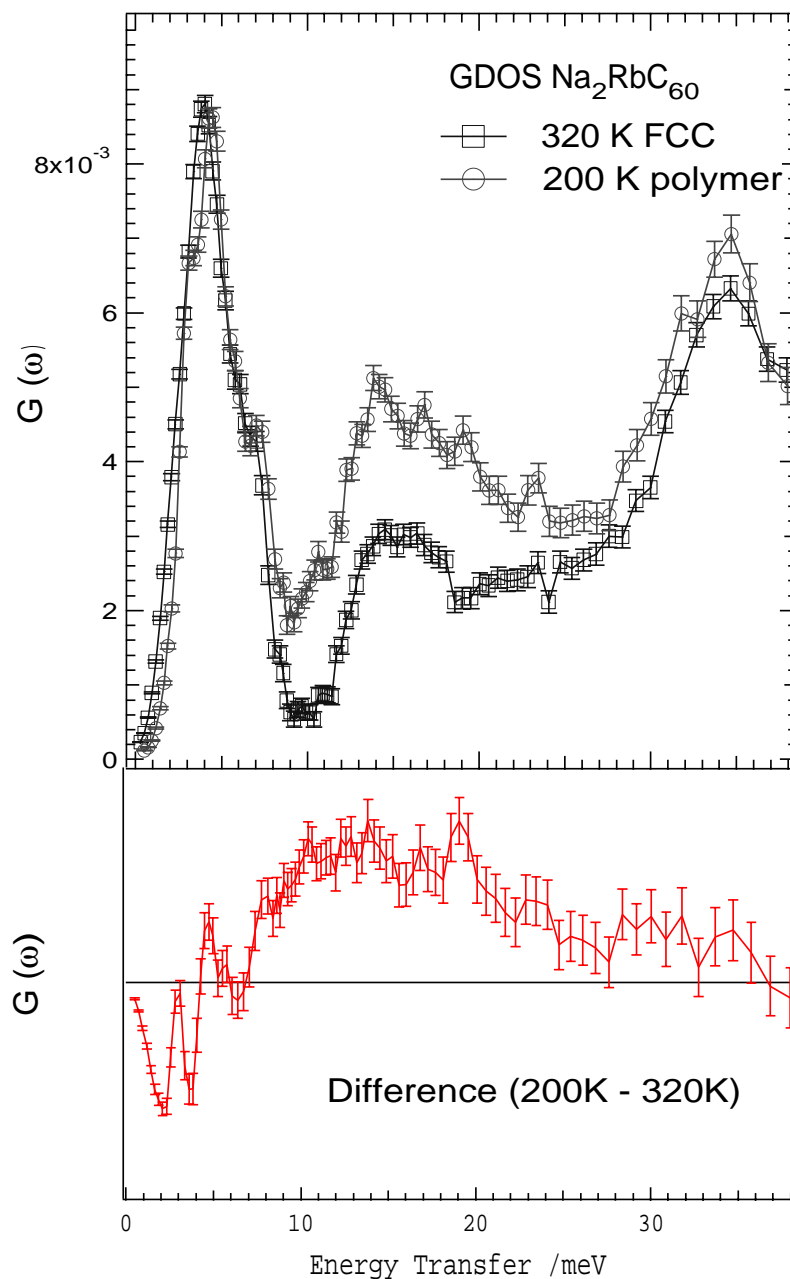


Figure 6.9: Above: low energy part of the generalised phonon density-of-states for $\text{Na}_2\text{RbC}_{60}$ at 320 K (squares - fcc phase) and at 200 K (circles - coexisting polymer and primitive cubic phases). Below: difference curve of the GDOS at 200 and 320 K, highlighting the additional phonon modes in the energy range 8- 25 meV that arise from the bridging C-C bonds in the polymer.

6.2.2 $\text{Na}_2\text{Rb}_{0.5}\text{Cs}_{0.5}\text{C}_{60}$

It has been shown that the effects of physical[49] and chemical[40] pressure on the superconducting properties of $\text{Na}_2\text{CsC}_{60}$ are not identical, with chemical pressure suppressing T_c much faster than physical pressure. In this section we wish to explore the T_c - a relationship in the cubic $\text{Na}_2\text{Rb}_{0.5}\text{Cs}_{0.5}\text{C}_{60}$ fulleride, relating the results to our current understanding of superconductivity and the occurrence of polymerisation transformations in the simple cubic fullerides. We performed detailed *ac* susceptibility measurements on the $\text{Na}_2\text{Rb}_{0.5}\text{Cs}_{0.5}\text{C}_{60}$ salt between ambient and 2.5 kbar applied pressure.

Phase purity of the $\text{Na}_2\text{Rb}_{0.5}\text{Cs}_{0.5}\text{C}_{60}$ sample was established by high resolution synchrotron X-ray powder diffraction measurements with the MAR Research circular image plate system on line A of the BM1 beamline at the ESRF at a wavelength of 0.873 Å. The sample to detector distance was 300 mm, with an exposure time of 2 minutes. The capillary containing the sample was rotated by 30° about its axis during data collection. A LaB_6 standard was used to calibrate the wavelength. The 2D images were integrated around the Debye-Scherrer circles to generate the 1D pattern using the FIT2D program[98]. The Le Bail pattern decomposition technique[120] was used to extract a lattice constant of 14.1137(5) Å. The pattern is well represented using the $Pa\bar{3}$ space group, as shown in Fig.6.10, though some small impurities are discernable at higher angles. The extracted parameters are listed in Table 6.5.

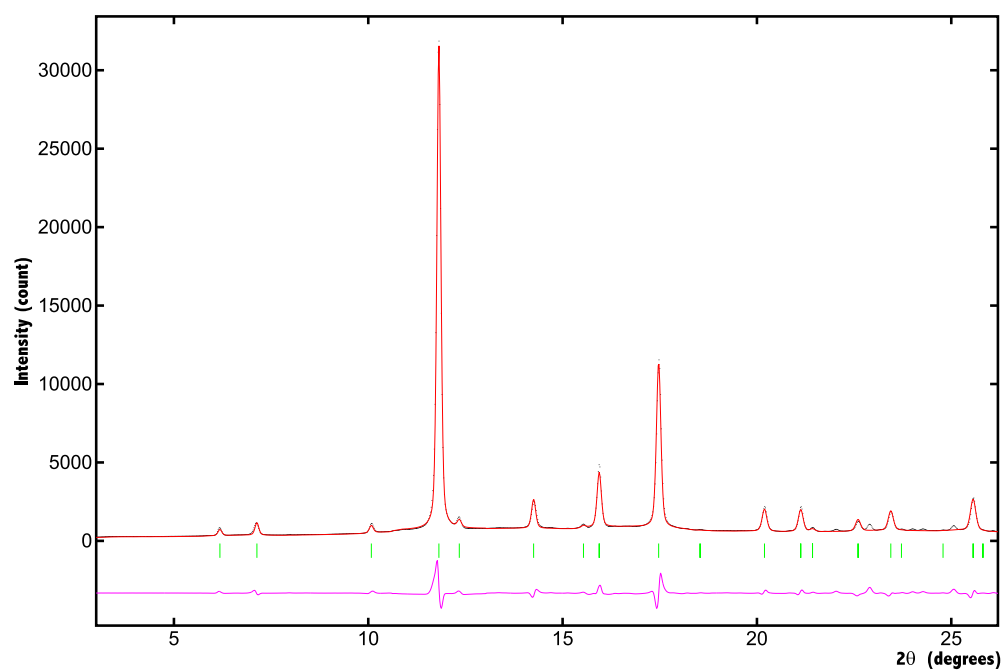


Figure 6.10: The synchrotron X-ray diffraction pattern of $\text{Na}_2\text{Rb}_{0.5}\text{Cs}_{0.5}\text{C}_{60}$. The measured data points are shown as black points, while the red line is a fit using the Le Bail pattern decomposition technique with the cubic $Pa\bar{3}$ space group. The green bars indicate the positions of the reflections and the solid pink line below the pattern, the difference between measured and calculated data.

Table 6.5: The Le Bail refinement parameters for the image plate data collected on $\text{Na}_2\text{Rb}_{0.5}\text{Cs}_{0.5}\text{C}_{60}$ at 295 K.

Space group	$Pa\bar{3}$
a /Å	14.1137(5)
R_{wp} , R_p /%	11.9, 3.03
χ^2	15.42
λ /Å	0.873
$\Delta_{2\theta}$ /°	0.042
2θ range /°	3 - 26
U /°	0.4(3)
V /°	-0.033(7)
W /°	0.014(5)
η	0.49(2)

For the *ac* susceptibility measurements the sample was introduced into a thin-walled glass capillary of 1.5 mm diameter inside a glove box. The sample height was ~ 0.5 cm and the capillary was sealed to a length of 1 cm. The sealed capillary was introduced into uniform *ac* pick-up (374 turns each) and field (440 turns) coils using copper wire of 0.05 mm diameter on a plastic base of 1.8 mm diameter. The coils together with a manganin pressure gauge were loaded into a Teflon cell filled with a degassed 1:1 mixture of Fluorinert FC70 and FC77. A Swenson-type brass piston-cylinder pressure cell was used with the aid of a retaining screw to apply and maintain pressure on the sample[207]. Sample temperatures down to 2.2 K were recorded by means of a platinum/cobalt thermometer, embedded in the brass cylinder near the sample. As the piston-cylinder apparatus allows the application of pressure only at room temperature, the present system was calibrated for the pressure drop which occurs on cooling using a K_3C_{60} sample. This entailed the performance of a series of experiments in which the pressure was first being increased at room temperature, the sample cooled and the T_c (defined as the *onset* of the appearance of diamagnetic

shielding) monitored until a decrease in its value was detected. The system has proven quite robust in that an applied pressure of 3.5 kbar at room temperature was repeatedly found to be equivalent to 'ambient pressure' at 20 K. The estimated error in pressure is of the order of ± 0.2 kbar. The use of a thin-walled glass capillary is not a limitation, as it shatters well below applied pressures of 1 kbar, thus allowing the sample to mix well with the pressure medium.

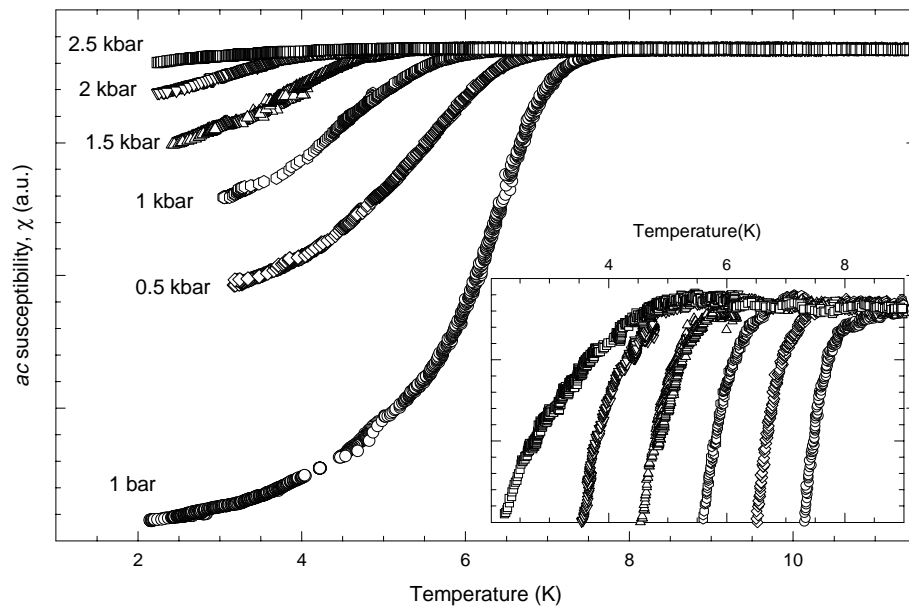


Figure 6.11: Temperature dependence of the *ac* magnetic susceptibility, χ of quenched $\text{Na}_2\text{Rb}_{0.5}\text{Cs}_{0.5}\text{C}_{60}$ at the indicated pressures. The inset shows an expanded view of the experimental data in the vicinity of T_c .

Detailed *ac* susceptibility measurements for $\text{Na}_2\text{Rb}_{0.5}\text{Cs}_{0.5}\text{C}_{60}$ were performed as a function of temperature at pressures up to 2.5 kbar. For these experiments, the

sample was heated above room temperature and after the pressure was applied, it was rapidly quenched in liquid nitrogen. Following completion of the susceptibility measurements, the sample was rapidly heated with the aid of a heat gun before the next cycle of measurements was initiated. Fig.6.11 summarises the *ac* susceptibility, χ of $\text{Na}_2\text{Rb}_{0.5}\text{Cs}_{0.5}\text{C}_{60}$ obtained in the pressure range 0.001 to 2.5 kbar. The ambient pressure *ac* susceptibility data show the onset of superconductivity in quenched $\text{Na}_2\text{Rb}_{0.5}\text{Cs}_{0.5}\text{C}_{60}$ at $T_c = 8.4$ K in agreement with the *dc* magnetisation data for the same sample[208]. Increasing the pressure to 0.5 kbar leads to a decrease in both the T_c to 7.6 K and the superconducting volume fraction by $\sim 50\%$. Increasing further the pressure in steps of 0.5 kbar to 2.5 kbar, results in a smooth decrease in T_c , as it is clearly evident from the inset of Fig.6.11. At the same time, the superconducting fraction also gradually decreases, implying that the superconducting primitive cubic phase of $\text{Na}_2\text{Rb}_{0.5}\text{Cs}_{0.5}\text{C}_{60}$ gradually transforms into the non-superconducting polymer phase with increasing pressure. The transformation is incomplete at these low pressures and the behaviour mimics what is encountered on cooling at ambient pressure. As the structural phase transition temperature, T_{tr} at ambient pressure is just below room temperature (in the temperature range 250-270 K), increasing pressure leads to a decrease in interfullerene separation, thus quickly driving T_{tr} to values above room temperature.

Fig.6.12 displays the pressure dependence of both T_c and the superconducting fraction which we identify with the volume fraction, ϕ of the primitive cubic phase of $\text{Na}_2\text{Rb}_{0.5}\text{Cs}_{0.5}\text{C}_{60}$. T_c varies linearly with pressure up to 2.5 kbar with a slope of $dT_c/dP = -1.22(2)$ K/kbar. This value is identical to that found before for the isostructural fulleride $\text{Na}_2\text{CsC}_{60}$ ($-1.25(2)$ K/kbar)[49], but considerably larger than

the values of -0.78 and -0.97 K/kbar, reported for the *fcc* fullerides K_3C_{60} and Rb_3C_{60} , respectively[29]. At present, there is no compressibility data available for $Na_2Rb_{0.5}Cs_{0.5}C_{60}$ and so the T_c dependence on the cubic lattice constant cannot be

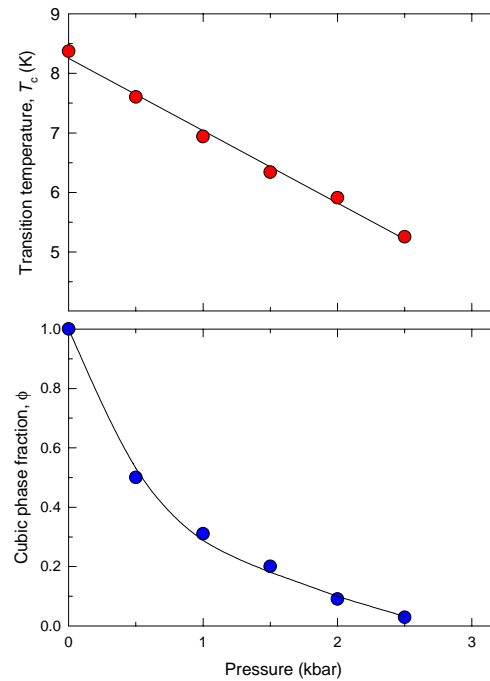


Figure 6.12: Pressure dependence of the superconducting transition temperature, T_c (top panel) and of the fraction of the cubic phase, ϕ (bottom panel) for quenched $Na_2Rb_{0.5}Cs_{0.5}C_{60}$. The lines are guides to the eye.

derived directly. However, the linear compressibility of the primitive cubic phase of Na_2CsC_{60} has been measured by both the powder neutron[45] and synchrotron X-ray[54] diffraction techniques. The measured values are $-d(\ln a)/dP = 1.8(2) \times 10^{-3}$

and $1.6(2) \times 10^{-3} \text{ kbar}^{-1}$, respectively, somewhat larger than that of the *fcc* fulleride K_3C_{60} ($1.2 \times 10^{-3} \text{ kbar}^{-1}$)[30]. Thus, to a good approximation, we can employ the linear compressibility value of $\text{Na}_2\text{CsC}_{60}$ to determine the relationship between T_c and the cubic lattice constant, a in $\text{Na}_2\text{Rb}_{0.5}\text{Cs}_{0.5}\text{C}_{60}$ as $dT_c/d(\ln a) \approx 0.7 \times 10^3 \text{ K}$, a value comparable to that of K_3C_{60} ($\approx 0.65 \times 10^3 \text{ K}$).

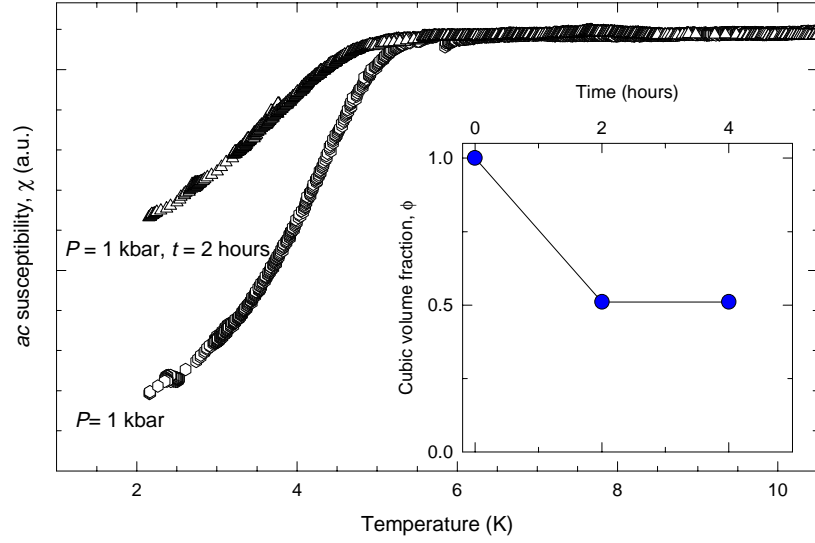


Figure 6.13: Temperature evolution of the *ac* susceptibility of $\text{Na}_2\text{Rb}_{0.5}\text{Cs}_{0.5}\text{C}_{60}$ at an applied pressure of 1 kbar. The two datasets shown correspond to equilibration times at room temperature before quenching of 0 and 2 hours as indicated. The inset displays the dependence of the superconducting fraction, ϕ , normalised to the value at 1 kbar with equilibration time.

We also performed measurements of the *ac* susceptibility, χ at elevated pressures,

in which the sample was first equilibrated at room temperature for various periods of time before quenching to low temperature. Some representative data of these experiments are shown in Fig.6.13 for an applied pressure of 1 kbar ($T_c = 6.9$ K). Following the return of the sample to room temperature and equilibration for two hours resulted in no detectable change in T_c . However, the superconducting fraction decreased by $\sim 49\%$. Repeating the heating/cooling cycle with an additional waiting period of two hours resulted in no further detectable changes in the *ac* susceptibility response. The detrimental effect on the fraction of the superconducting phase shown by extended periods of equilibration at room temperature (inset of Fig.6.13) can be understood in terms of the slow kinetics exhibited by the primitive cubic \rightarrow monoclinic phase transformation[52, 54](see §6.2.1).

Fig.6.14 depicts the relationship between T_c and lattice parameter, a [28, 45], for a variety of fulleride salts at both ambient and elevated pressures. The present high pressure results for the $\text{Na}_2\text{Rb}_{0.5}\text{Cs}_{0.5}\text{C}_{60}$ salt define a new branch in this diagram with a slope identical to that found for $\text{Na}_2\text{CsC}_{60}$ at high pressure[49] but about 5 to 6 times smaller than that encountered in the quaternary fullerides, $\text{Na}_2\text{Rb}_{1-x}\text{Cs}_x\text{C}_{60}$ ($1 \leq x \leq 0$) at ambient pressure[40]. Thus they reinforce the contrast in the behaviour of superconducting *fcc* and Na-containing primitive cubic fullerides. While in the former, the effects of chemical and physical pressure on the superconducting properties differ little, the latter show a clear differentiation with chemical substitution leading to a much faster suppression of T_c than application of pressure. The pressure dependence of the superconducting properties of individual members of the $\text{Na}_2\text{Rb}_{1-x}\text{Cs}_x\text{C}_{60}$ ($1 \leq x \leq 0$) family differs very little from the phenomenology established for the *fcc* fullerides in which the larger alkali ions K^+ , Rb^+ and Cs^+ reside in

the tetrahedral interstices. Thus the faster depression of T_c with interfullerene separation at ambient pressure, as x varies in $\text{Na}_2\text{Rb}_{1-x}\text{Cs}_x\text{C}_{60}$ appears to be metal-specific. Its origin still poses intriguing questions and has yet to be explained unambiguously. While the conjecture that the dependence of T_c on interfullerene separation is generally much steeper in the $Pa\bar{3}$ structure than in the $Fm\bar{3}m$ one can be now discarded, a number of additional possible explanations still remain. These include: (i) the existence of an as yet unidentified low-symmetry distortion of the primitive cubic structure; (ii) a very sensitive modulation of the degree of electron transfer between Na and C_{60} by the interfullerene separation which may lead to deviations from half filling of the conduction band and rapid suppression of superconductivity, in analogy with the situation encountered in non-superconducting $\text{Li}_2\text{CsC}_{60}$ [9]; and (iii) the presence of intergrowths, or co-existence at the microscopic level, of superconducting cubic and non-superconducting polymer domains, with the size of the latter growing as the lattice constant decreases with decreasing x in $\text{Na}_2\text{Rb}_{1-x}\text{Cs}_x\text{C}_{60}$.

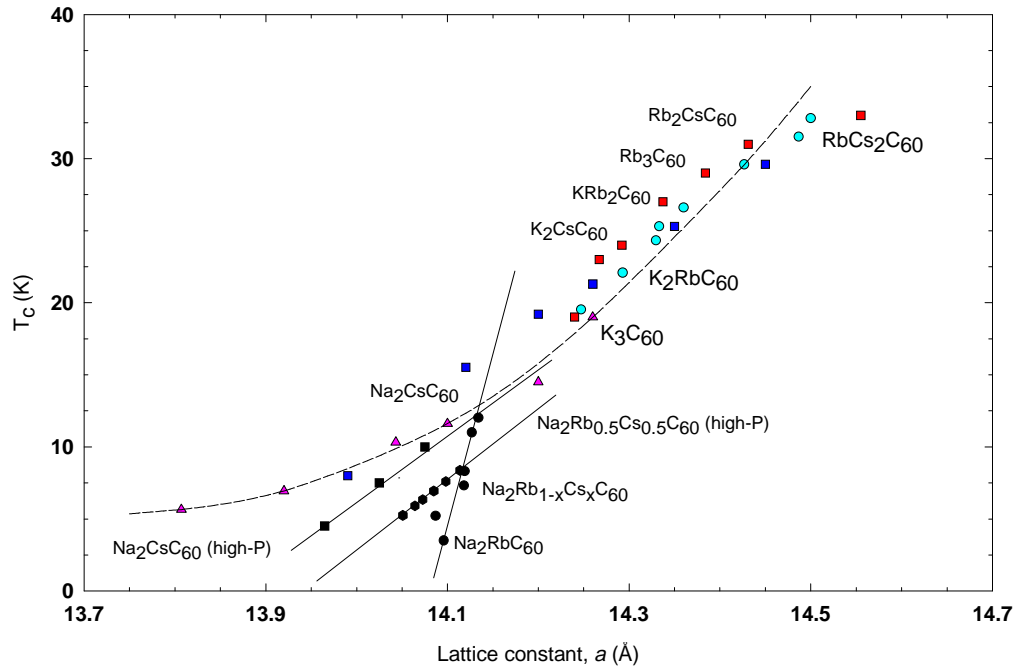


Figure 6.14: Relationship between the superconducting transition temperature, T_c , and the cubic lattice constants, a of fulleride salts over a wide range of values for a . Data indicated by coloured symbols are experimental measurements on fulleride salts with the $Fm\bar{3}m$ structure at both ambient and elevated pressures. Data indicated by black symbols are experimental measurements on fulleride salts with the $Pa\bar{3}$ structure at ambient (circles) and elevated (squares for $\text{Na}_2\text{CsC}_{60}$ and hexagons for $\text{Na}_2\text{Rb}_{0.5}\text{Cs}_{0.5}\text{C}_{60}$) pressures. The dotted line is the T_c - a relationship expected from the BCS theory using $N(\epsilon_f)$ values obtained by LDA calculations, while the straight lines are guides to the eye.

6.3 Lithium Fullerides

The $\text{Li}_2\text{AC}_{60}$ ($\text{A} = \text{Rb}, \text{Cs}$) salts adopt fcc (space group $Fm\bar{3}m$) disordered structures that have been modelled as containing quasi-spherical C_{60}^{3-} ions[9]. Unlike the sodium containing salts, the $\text{Li}_2\text{AC}_{60}$ fullerides exhibit no superconductivity, that is ascribed to a strong Li^+ -C interaction that is evident in the crystal structure. Despite $\text{Li}_2\text{CsC}_{60}$ having a smaller lattice constant (14.07 Å) than $\text{Na}_2\text{RbC}_{60}$, and presumably favourable interfullerene distances for polymerisation to occur, the structure remains fcc at all temperatures and to pressures as high as 6 GPa[54]. This has been interpreted as arising from the dominance of the Li^+ -C interaction so C-C bonding is precluded. On heating $\text{Li}_2\text{CsC}_{60}$ to 473 K, Rietveld refinements modelling the fulleride units in terms of SASH functions (§1.1) conclude that the strength of the Li^+ -C interaction is only marginally reduced[54].

This work was carried out with the aim of extracting more detailed information on the dynamical behaviour of the fulleride ions in $\text{Li}_2\text{CsC}_{60}$ and searching for evidence of a strong Li^+ -C interaction. We have used the INS technique to measure the generalised phonon density-of-states (GDOS) as a function of temperature for $\text{Li}_2\text{CsC}_{60}$ and for a sample with slight lithium deficiency, $\text{Li}_{2-x}\text{CsC}_{60}$. In principle, the GDOS is simple. For energy transfers up to ~ 10 meV the scattering is due to intermolecular vibrations, translations and librations that are characterised by weak van der Waals forces. A 'gap region' immediately follows this where usually no vibrational modes are found for the cubic fullerenes and fullerides. This region extends to ~ 30 meV. From ~ 30 meV to ~ 200 meV the scattering is from intramolecular phonon modes i.e. from deformations of the fulleride cage itself. It is the difference in energy scales between the van der Waals forces and the strong covalent C-C bonds that produce

the gap region. As we saw previously for the $\text{Na}_2\text{RbC}_{60}$ polymer, the gap region can contain vibrational modes with intermediate forces constants between these two extremes. A strong Li^+ -C interaction may give rise to vibrational modes that have not previously been seen in the GDOS of other alkali fullerenes.

6.3.1 Inelastic Neutron Scattering of $\text{Li}_2\text{CsC}_{60}$

To be able to access a wide range of temperatures and retain a low background signal for this weak scattering sample that was available only in small quantities (mass 520 mg), we employed the use of thin walled aluminium flatplate cells (1.2 mm deep) and a cryoloop sample environment. Data was typically collected for 11 hours per run at 100, 200, 280 and 350 K with a wavelength of 4.12 Å. Identical empty aluminium cans were measured at 200 and 350 K with a vanadium calibration performed at 300 K. The raw data were corrected using the INX parameters shown in Table.6.6, with all noisy detectors masked. The full data range was used to convert the corrected intensity to density-of-states with the correction parameters used in the FITDEN5 program given in Table.6.7. The corrected scattering law was calculated using a more restricted Q range from which the regions of Q contaminated by Bragg reflections were excluded.

Table 6.6: INX Correction Parameters for $\text{Li}_2\text{CsC}_{60}$ data collected at 4.12 Å on IN6.

Angular Range	10 - 44.33° , 46.67- 113.5°
Detectors	22 - 110 and 118 - 256
Wavelength	4.12 Å
Angle to beam	135°
sample depth	1.2 mm
sample mass	520 g
Transmission	0.99
Sample Density	0.96 g cm ⁻³
Molecular Mass	888.26 g
Average Mass	13.769 g
σ_s	339.7 barns
σ_a at 1.8 Å	170 barns

Detector groups used after exclusion Bragg Peaks:
22-59 76-110 118-121 176-202 212-223 245-256

Vanadium 1 mm thick at 300 K with 0.76 transmission

Table 6.7: Multiphonon Correction Parameters used with FITDEN5 for $\text{Li}_2\text{CsC}_{60}$.

Temperature/K	Parameter	Peak 1	Peak 2	Peak 3
200	Mass	888.26	720	12.06
	Frequency/meV	4.99	16.17	73.22
	Cutoff freq./meV	22.35	59.72	136.36
	Peak Width	0.84	1.26	0.86
	Concentration	0.037	0.061	0.902
280	Mass	888.26	720	12.06
	Frequency/meV	5.25	17.75	72.73
	Cutoff freq./meV	19.71	59.13	146.09
	Peak Width	0.72	1.25	0.80
	Concentration	0.044	0.053	0.901
350	Mass	888.26	720	12.06
	Frequency/meV	4.75	16.21	68.04
	Cutoff freq./meV	18.65	59.13	149.19
	Peak Width	0.74	1.25	0.70
	Concentration	0.038	0.056	0.906

Integration over all energy transfers results in a traditional powder diffraction profile as shown in Fig.6.15 for $\text{Li}_2\text{CsC}_{60}$ at 200 and 350 K. The full angular range

is shown in both patterns, corresponding to the data range used for analysis of the GDOS, while analysis of $S(Q, \omega)$ uses those regions with no elastic Bragg reflections.

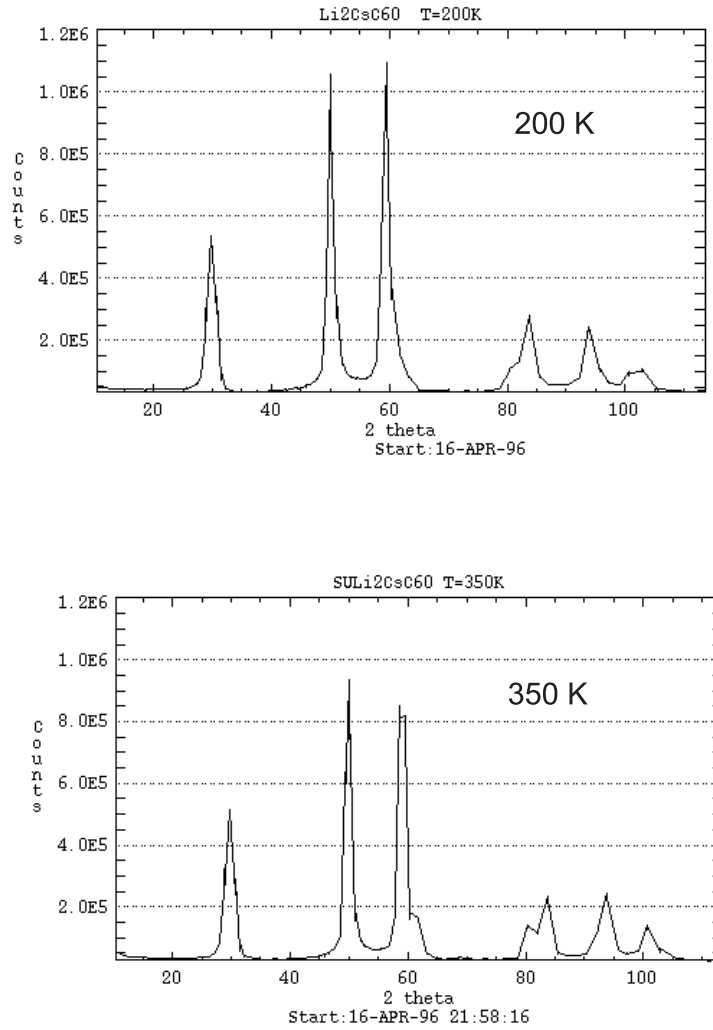


Figure 6.15: Energy transfer integrated time-of-flight data of $\text{Li}_2\text{CsC}_{60}$ at 200 and 350 K. The diffraction patterns clearly show a change on heating.

Even though the patterns are similar at this resolution, changes are observed in the relative maximum intensities of the major peaks at $\sim 50^\circ$ and 60° on heating. Indexing of the 200 K pattern to a $Fm\bar{3}m$ cubic cell with lattice constant of $a = 14.07 \text{ \AA}$ [9]

requires that the 50° peak indexes as (220) reflection, while the unresolved (311) and (222) reflections lie at 60° . This in effect explains the intensity reduction of the 60° peak on heating; these reflections become partly resolved.

The scattering law, normalised by the Bose factor to that of 200 K, is shown in Fig.6.16 at an average scattering vector of 1.23 \AA^{-1} . Fits to the data included a sum of a δ function at zero energy transfer and two Lorentzian peaks centred at $\pm\hbar\omega$, each convoluted with the instrumental resolution function. It was also found necessary that at 350 K a Gaussian quasielastic should be included. The fit results are summarised in Table 6.8. The well defined peaks at non-zero energy transfer can be assigned to librational modes of the fulleride ions by analogy to similar features in pristine C_{60} [209] and other alkali fullerides, whose Q dependence of the intensity and width leads to such an interpretation. The energy of the librational modes is strongly temperature dependent, softening from 2.985(2) at 200 K to 1.79(8) at 350 K. This is similar to the situation found in $\text{Na}_2\text{RbC}_{60}$ [27] where librations at ~ 2.2 meV at 300 K indicate a softer potential than that of K_3C_{60} [26] where librations occur at ~ 3.6 meV. The difference is attributed to arising from the influence of a small alkali ion residing in the tetrahedral interstice, so reducing the repulsive A^+-C interactions.

As expected for librational modes, softening is accompanied by broadening. The librations are already quite broad with a FWHM of 4.0(2) meV at 200 K, that is comparable to the width of the $\text{Na}_2\text{RbC}_{60}$ librations at ~ 350 K just before they collapse to give a quasielastic line. By 350 K, the librations have broadened by around 80% to 7.2(2) meV, thus giving the impression that a collapse into only a quasielastic peak is inevitable. This is also seen for C_{60} and $\text{Na}_2\text{RbC}_{60}$ [27]. It is worth noting the small quasielastic component at 350 K that coexists with the

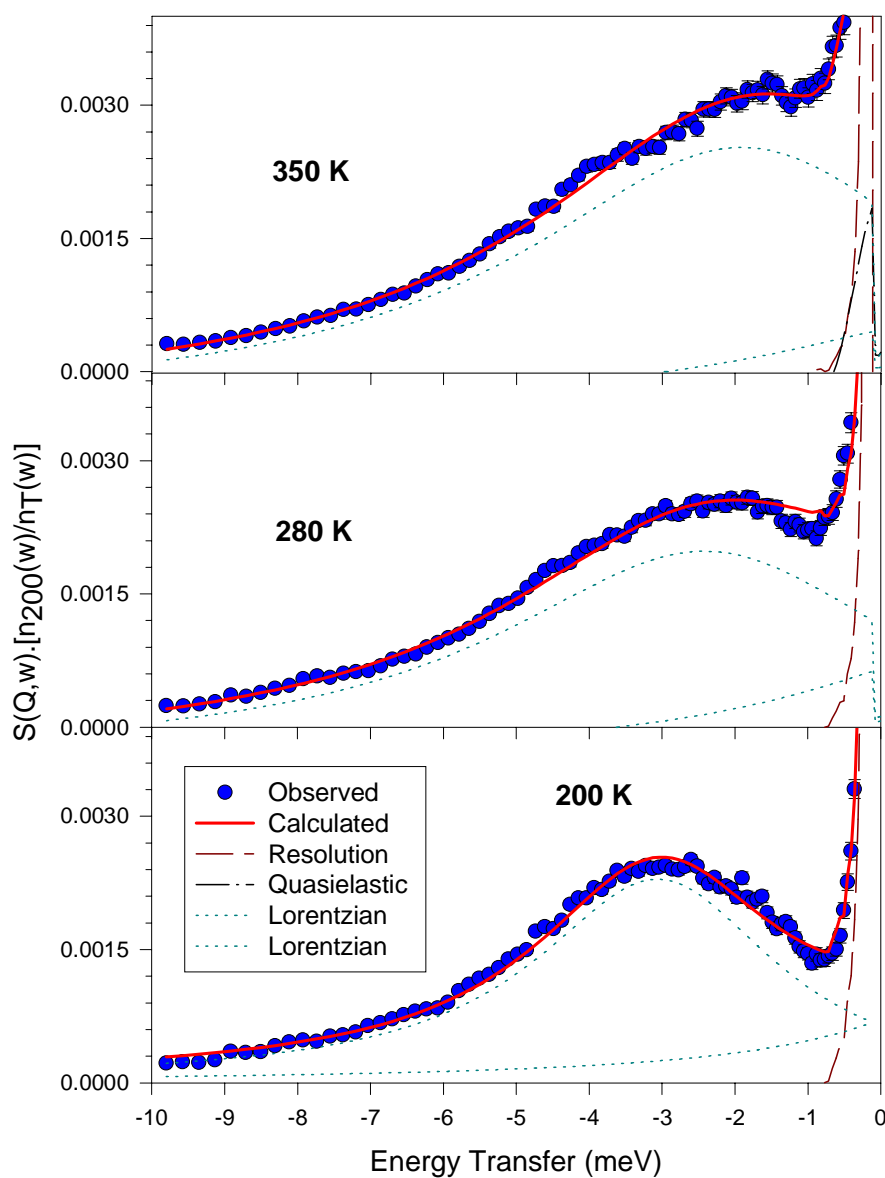


Figure 6.16: Development of the near inelastic spectrum of $\text{Li}_2\text{CsC}_{60}$ with temperature at an average Q of 1.23 \AA^{-1} . Blue circles are observed points while the red line is a best fit of two Lorentzian peaks mirrored on either side of the elastic line convoluted with the resolution function. By 350 K the librational peaks have softened and we observe a weak quasielastic component. The data have been scaled by the appropriate Bose factor to allow direct comparison of the spectra.

librational modes, indicating a diffusive rotational component in the sample. A co-existence has also been seen in the case of $\text{Na}_2\text{CsC}_{60}$ [41], while these features occur separately in pristine C_{60} [210]. It is interesting that for both $\text{Li}_2\text{CsC}_{60}$ and the high temperature fcc phase of $\text{Na}_2\text{CsC}_{60}$, X-ray structure analysis using symmetry adapted spherical harmonic functions, reveals essentially the same distribution of electron density on the fulleride cages with excess density pointing towards the tetrahedral sites[41]. The possibility of having a softening of a librational mode that gives way to a quasielastic component is quite unexpected here, given the structural analysis of $\text{Li}_2\text{CsC}_{60}$, where the disorder of the fulleride disorder essentially shows no temperature dependence between 295 and 473 K[54].

Table 6.8: Parameters extracted from fitting of the scattering law for $\text{Li}_2\text{CsC}_{60}$. The Lorentzians represent librational features, in both up- and down-scattering of neutrons. A Gaussian quasielastic component is necessary at 350 K.

Temperature/K	Peak	Position(meV)	Intensity	FWHM(meV)
200	Lorentzian 1	-2.985(2)	$1.32(5) \times 10^{-2}$	4.0(2)
	Lorentzian 2	2.985(2)	$1.4(2) \times 10^{-2}$	4.0(8)
280	Lorentzian 1	-2.28(9)	$3.41(7) \times 10^{-2}$	6.7(2)
	Lorentzian 2	2.3(3)	$2.3(1) \times 10^{-2}$	6.5(6)
350	Lorentzian 1	-1.79(8)	$5.71(9) \times 10^{-2}$	7.2(2)
	Lorentzian 2	1.8(3)	$2.3(2) \times 10^{-2}$	7.2(7)
	Gaussian Quasi-E	0	$4.4(7) \times 10^{-3}$	0.7(1)

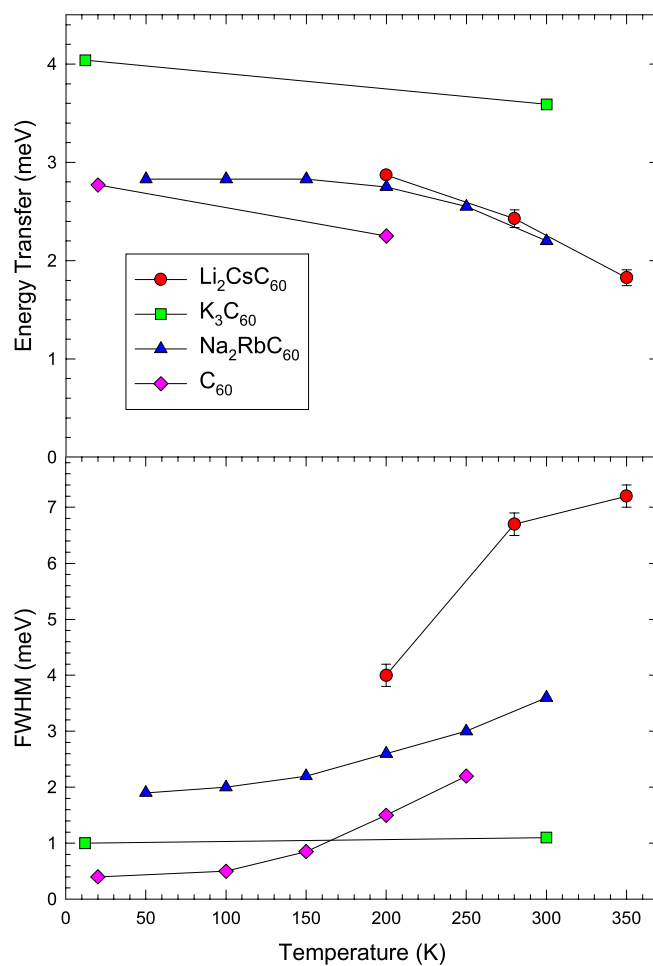


Figure 6.17: Temperature evolution of the librational energy (upper) and width of the librational peak for the cubic salts: $\text{Li}_2\text{CsC}_{60}$ (red circles), K_3C_{60} (green squares), $\text{Na}_2\text{RbC}_{60}$ (blue triangles) and C_{60} (pink diamonds). Adapted from Ref[27]: note that the markers used for K_3C_{60} , $\text{Na}_2\text{RbC}_{60}$ and C_{60} are used to distinguish the curves and are not data points.

A comparison of the temperature evolution of the energies and widths of the librational modes in $\text{Li}_2\text{CsC}_{60}$ with those reported for C_{60} , primitive cubic $\text{Na}_2\text{RbC}_{60}$ and K_3C_{60} is shown in Fig.6.17. It is now quite clear that the softening of the librational potential in $\text{Li}_2\text{CsC}_{60}$ is remarkably similar to that in $\text{Na}_2\text{RbC}_{60}$ in the temperature range studied. The width of the librational mode in $\text{Li}_2\text{CsC}_{60}$ has the characteristic temperature dependent behaviour of C_{60} and $\text{Na}_2\text{RbC}_{60}$, implying that the fulleride units experience similar orientational potentials. The librations in $\text{Li}_2\text{CsC}_{60}$ are much broader than is the case for the other fullerides, implying an increased anisotropy of the orientational potential. From this INS data we can say that at low temperatures the fulleride cages execute jump reorientations that give rise to librational modes. This jump motion gradually gives way to a diffusive motion and hence the appearance of the quasielastic feature with temperature. No such transition has been identified using X-ray diffraction.

Perhaps we can integrate the INS results with those of the X-ray diffraction analysis. Diffraction is a time averaged view of the crystal structure, smearing out the dynamics of the system. So, below 350 K, the fulleride ions are jumping between many orientations, whose distribution is not quite isotropic, or there is a preferred orientation of the fulleride ion. If this places electron density in the $\langle 111 \rangle$ direction, then the time averaged view of the C_{60}^{3-} ion derived from a diffraction experiment, will then be somewhat spherical but with excess scattering density seen in this direction. As the temperature is increased, a rotational diffusion regime begins marked by the corresponding appearance of a quasielastic component to the INS spectra. However, the rotational diffusion must result in almost the same time averaged view of the fulleride ion. For instance, a scenario can be envisaged starting with the fulleride ion

in the standard orientation: with three two-fold axis aligned with the lattice vectors and the hexagonal faces pointing towards the lithium ions in the tetrahedral interstices. If reorientations then take place about a random $[111]$ axis, a time averaged view will see excess density along that axis of rotation. As the temperature is raised, this motion may become more continuous and a uniaxial diffusion occurs, that essentially retains the the time averaged electron distribution. However, his does not take into account any role of the lithium ion. While this may be a possible mechanism for the librational and diffusive motion, to get a better picture would require more data taken as a function of Q and at temperature outside the current range studied.

The generalised density-of-states for $\text{Li}_2\text{CsC}_{60}$ is shown in Fig.6.18. The spectra at all temperatures are characterised by high backgrounds despite the removal of the multiphonon contributions. The peaks at ~ 35 , ~ 47 , and ~ 70 meV are typical of unresolved intramolecular vibrations of C_{60} and are consequently temperature independent. At lower energy transfers, up to 10 meV, we find contributions from lattice modes, librational modes of C_{60} and caesium optic modes. Of particular interest, is the observation of scattered intensity in the energy range 10- 20 meV. Even though this feature is in the energy range appropriate for aluminium phonon contributions (15- 25 meV), it also extends to lower energy transfers. This is confirmed by comparison of the raw data from the empty can with that of the sample *and* the can. Statistics in this region are poor and so a detailed description of the temperature evolution of this band is precluded, though it is better defined at 350 K. As to the origin of this broad band, one initially recalls that excess electron density is observed on the fulleride shells pointing towards the lithium containing tetrahedral interstices. It is very tempting indeed to make this conclusion but judgement shall be reserved

until the end of the next section.

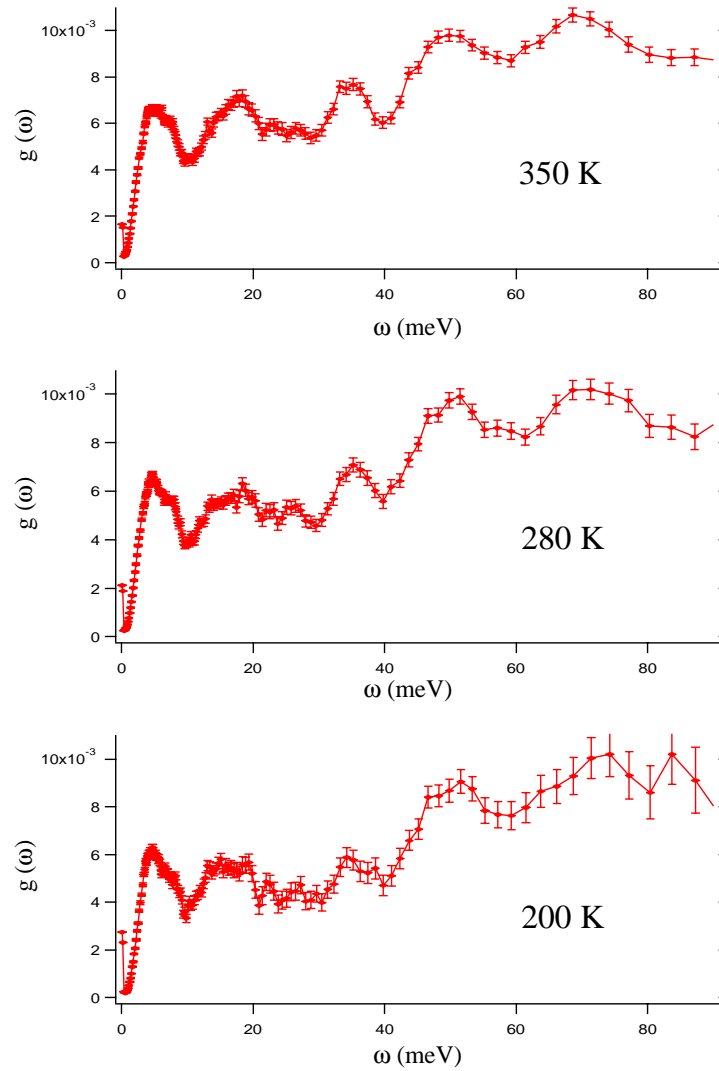


Figure 6.18: Temperature evolution of the generalised phonon density-of-states of $\text{Li}_2\text{CsC}_{60}$. Peaks at ~ 35 , ~ 47 and ~ 70 meV are due to intramolecular vibrations of the fulleride units.

6.3.2 Inelastic Neutron Scattering of $\text{Li}_{2-x}\text{CsC}_{60}$

With the intention of improving the quality of data and extending our measurements to higher temperatures, we performed an extension of the above experiment using a larger mass of sample. Alas, due to a miscalculation of lithium content, we actually have a $\text{Li}_{2-x}\text{CsC}_{60}$ sample that was somewhat deficient in lithium. It was *mixed* with the $\text{Li}_2\text{CsC}_{60}$ used previously. The resulting melange had a total mass of 1.25 g and shall be denoted as $\text{Li}_{2-x}\text{CsC}_{60}$ for the rest of this chapter.

The sample of $\text{Li}_{2-x}\text{CsC}_{60}$ was press sealed in an aluminium cylindrical can (i.d.= 7 mm) within a glovebox. Data were taken on IN6 at a wavelength of 4.12 Å, using a cryofurnace as sample environment. With a typical run time of 8 hours, spectra were recorded at 200, 315, 350, 420 and 520 K. A vanadium run was recorded at 300 K (4 hrs) and runs of the empty can at 300, 450 and 520 K. Corrections were routinely performed using the INX program with the parameters shown in Table 6.9.

Table 6.9: INX Correction Parameters for $\text{Li}_{2-x}\text{CsC}_{60}$.

Angular Range	12- 114°
Detectors	22- 256
Wavelength	4.12 Å
Can Radius	3.5 mm
Transmission	0.65
Sample Density	1.19 g cm ⁻³
Molecular Mass	888.26 g
Average Mass	13.769 g
σ_s	339.7 barns
σ_a at 1.8	170 barns

Vanadium of diameter 1.3 mm at 300 K with 0.9 transmission
excluding Bragg peaks: 22-58, 80-115, 182-202, 242-256

The full angular range was used for conversion to the spectral distribution function resulting in better statistics at the expense of momentum resolution. As before, Bragg peaks were excluded in the investigations of the scattering law, $S(Q, \omega)$. The FITDEN5 program was used to derive the multiphonon corrected generalised density-of-states. Two peaks were used in the correction, one covering lattice modes at low energies and the other broadly defining carbon based intramolecular vibrations at higher energy transfers, as shown in Table 6.10.

Table 6.10: Multiphonon Correction Parameters used with the FITDEN5 program for $\text{Li}_{2-x}\text{CsC}_{60}$.

Temperature/K	Parameter	Peak 1	Peak 2
200	Mass	888.26	12.06
	Frequency/meV	4.85	69.24
	Cutoff freq./meV	18.39	158.96
	Peak Width	0.59	1.02
	Concentration	0.127	0.873
315	Mass	888.26	12.06
	Frequency/meV	4.30	62.06
	Cutoff freq./meV	17.66	213.55
	Peak Width	0.59	0.95
	Concentration	0.118	0.882
350	Mass	888.26	12.06
	Frequency/meV	4.27	64.11
	Cutoff freq./meV	20.82	128.49
	Peak Width	0.56	1.01
	Concentration	0.126	0.874
430	Mass	888.26	12.06
	Frequency/meV	4.11	60.56
	Cutoff freq./meV	17.83	126.32
	Peak Width	0.56	0.98
	Concentration	0.128	0.872
520	Mass	888.26	12.06
	Frequency/meV	4.27	64.47
	Cutoff freq./meV	19.80	131.15
	Peak Width	0.56	0.97
	Concentration	0.118	0.882

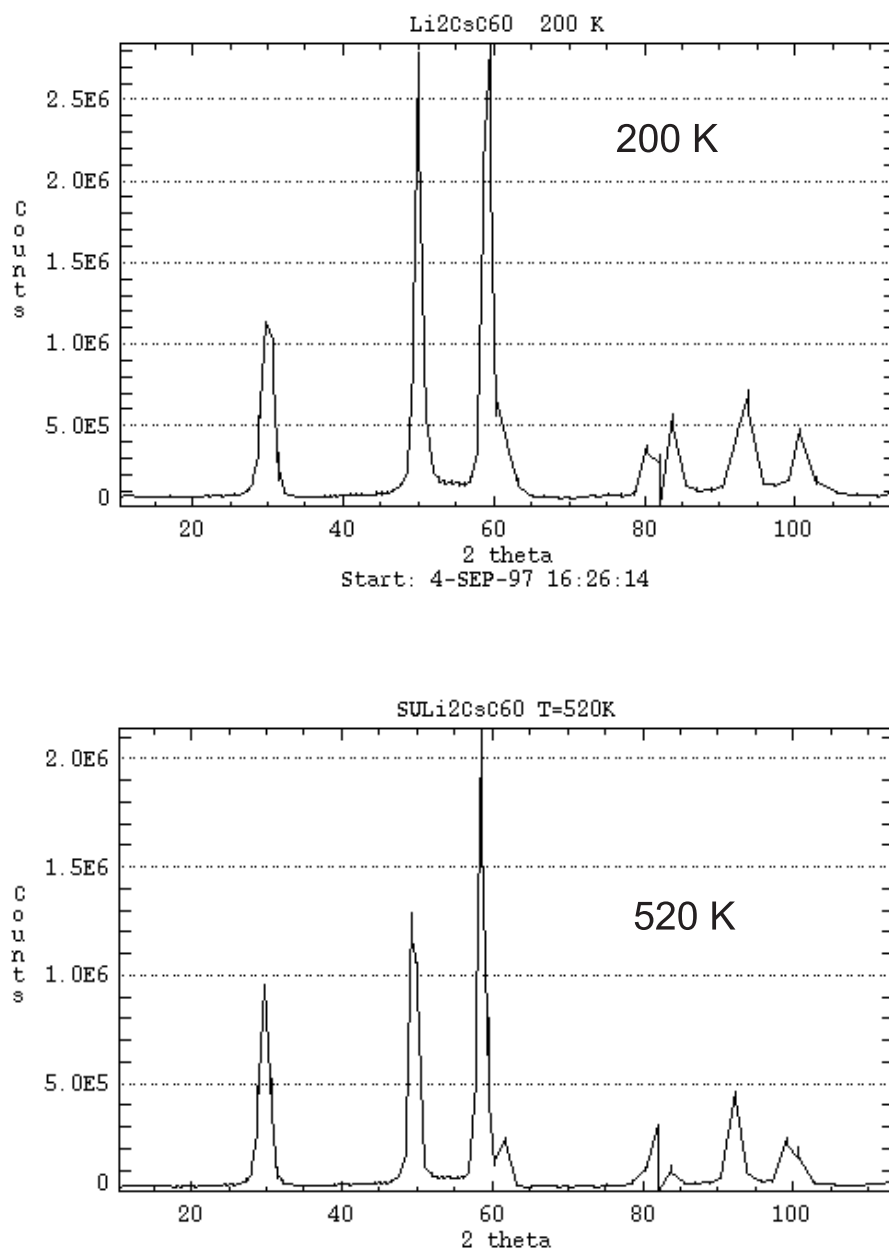


Figure 6.19: The integrated data of $\text{Li}_{2-x}\text{CsC}_{60}$ at 200 and 250K. On heating, the diffraction patterns show the positions of the Bragg reflections moving to lower 2θ values, consistent with the expanding unit cell.

Fig.6.19 shows the diffraction profile of $\text{Li}_{2-x}\text{CsC}_{60}$ at 200 and 520 K, following integration over ω of the scattering data. A small peak shift to lower 2θ is observable with increasing temperature that reflects an increase in unit cell volume. However, there are striking reductions in the intensities of some peaks that cannot be only attributed to an increased Debye-Waller factor. On heating to 520 K, we see again that the (311) and (222) reflections at $\sim 60^\circ$ are resolved. We also find that the intensity of the (220) reflection is much reduced, while the intensities of the reflections at about 80° are inverted. Such changes should be indicative of a structural transformation.

The scattering law, $S(Q, \omega)$, normalised by the Bose factor to that measured at 200 K, is shown in Fig.6.20 at an average scattering vector of 1.42 \AA^{-1} . Fits to the data included a sum of a δ function at zero energy transfer and two Gaussian peaks, each convoluted with the instrumental resolution function. It was also found necessary to include in the fits of the data at 200 K a sharp Lorentzian component. The fit results are summarised in Table 6.11.

Table 6.11: Parameters extracted from fitting of the scattering law for $\text{Li}_{2-x}\text{CsC}_{60}$. The peaks refer to the neutron energy gain side of the spectra.

Temperature/K	Peak	Position(meV)	Intensity	FWHM(meV)
200	Gaussian 1	4.12(9)	$6.0(7) \times 10^{-3}$	0.9(1)
	Gaussian 2	2.30(6)	0.176(2)	6.5(1)
	Lorentzian 1	2.75(3)	$1.65(9) \times 10^{-2}$	0.77(6)
315	Gaussian 1	3.8(1)	$6(1) \times 10^{-3}$	0.8(2)
	Gaussian 2	-0.39(4)	0.5556(5)	7.61(7)
350	Gaussian 1	3.7(1)	$6.7(9) \times 10^{-3}$	0.9(1)
	Gaussian 2	-0.41(4)	0.638(6)	7.60(6)
450	Gaussian 1	-3.56(7)	0.011(1)	0.8(2)
	Gaussian 2	0.0	0.759(6)	7.20(6)
520	Gaussian 1	3.50(6)	0.011(2)	0.6(1)
	Gaussian 2	1.28(3)	0.609(5)	5.87(6)

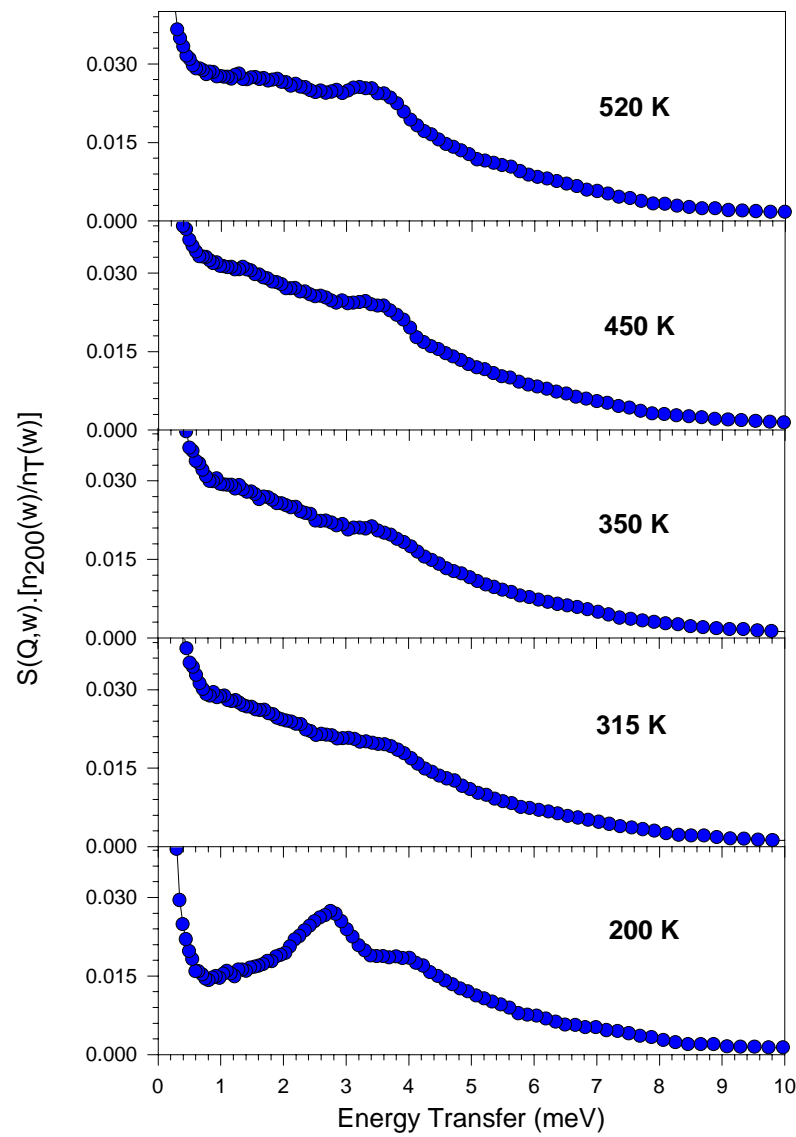


Figure 6.20: Temperature evolution of the scattering law at an average Q of 1.42 \AA^{-1} for $\text{Li}_{2-x}\text{CsC}_{60}$. A broad librational component broadens and softens with increasing temperature, collapsing into a quasielastic peak at 315 K. The sharp feature evident at 200 K disappears by 315 K. A peak at $4.12(9) \text{ meV}$ softens and increases in intensity, yet retains its width up to the highest temperature.

At 200 K a broad series of modes gives rise to a C_{60} librational feature centred at 2.30(6) meV with a coexisting peak of much weaker intensity at 4.12(9) meV and a Lorentzian at 2.75(3) meV. By 315 K the Lorentzian component has disappeared. We speculate that it has softened and broadened and is undistinguishable from the broad Gaussian now centred at the elastic line. Upon heating from 315 K to 520 K, the resulting spectra are simple with the trend being that the weak Gaussian component softens to 3.5 meV with almost a doubling in intensity, while its width remains unchanged. The broad nature of the quasielastic peak represent very fast diffusive motion or a very anisotropic orientational potential. There are very few similarities between the current spectra of $Li_{2-x}CsC_{60}$ and those obtained previously on Li_2CsC_{60} . The observation of a sharp librational mode at low temperatures, is at odds with our result in the previous experiment where we had broad librational modes. This can be rationalised by having an inhomogeneous distribution of fulleride environments in the present case. This may have arisen partly as a result of mixing two different sample stoichiometries prior to the experiment.

The most dramatic evidence for change as a function of temperature comes from consideration of the generalised phonon density-of-states that is shown for all temperatures in Fig.6.21. In this overall view of $Li_{2-x}CsC_{60}$ between 0 and 120 meV, no temperature dependence of the high-energy C_{60} intramolecular modes above 30 meV is observed. However, the observation of scattered intensity in the energy range between these modes and the lattice and caesium optic modes is quite surprising. It has been shown[195] that observation of scattered intensity in this so-called 'gap region' is indicative of interfulleride C-C bonds and has been observed in dimers[78] and polymers[78, 193, 205] alike. This has provided evidence for polymerisation of

$\text{Na}_2\text{RbC}_{60}$ under slow cooling as discussed in §6.2.

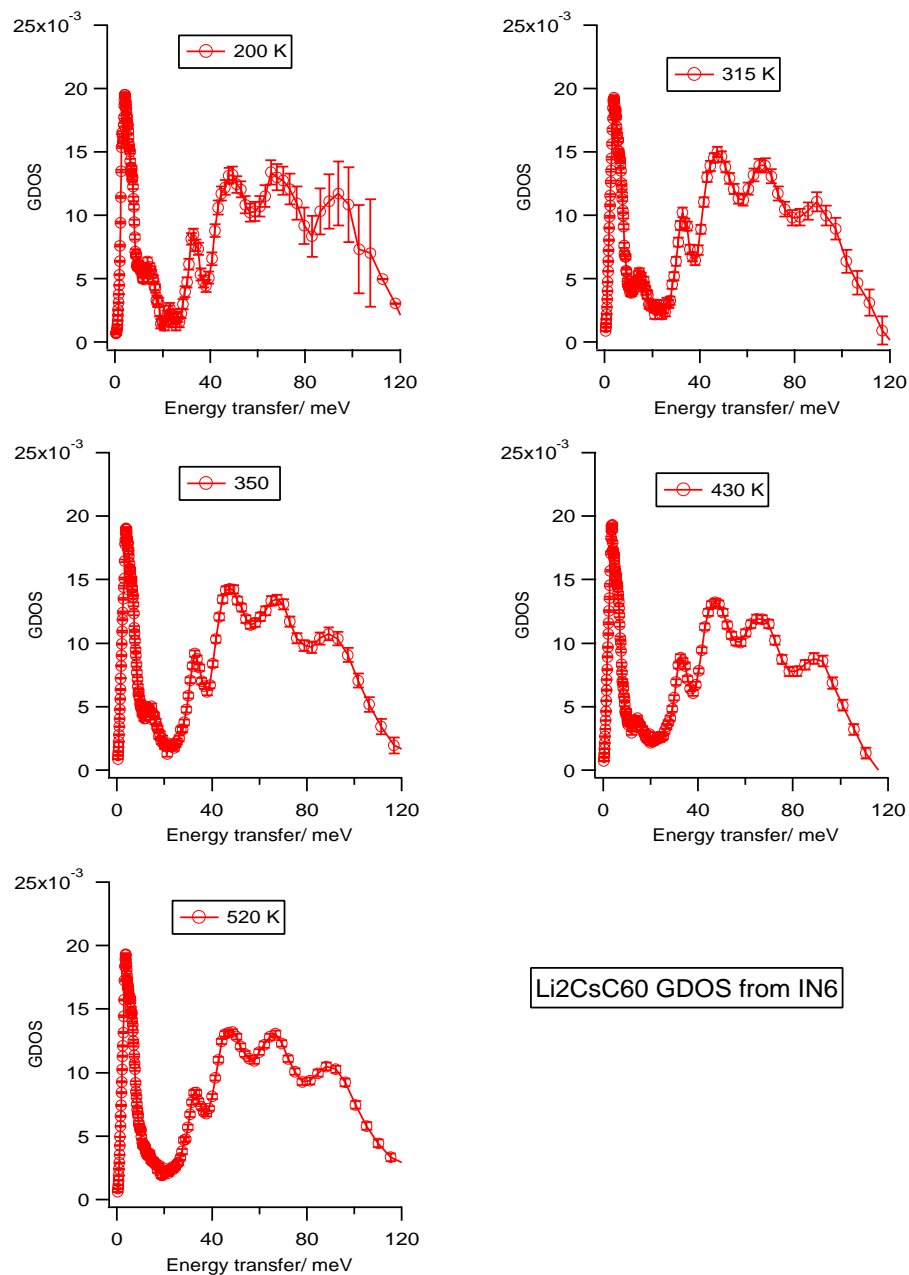


Figure 6.21: Generalised density-of-states for $\text{Li}_{2-x}\text{CsC}_{60}$ between 200 and 520 K. The spectra extend up to 120 meV with scattering above 30 meV arising from intramolecular C_{60} vibrations.

Fig.6.22 shows an expanded energy transfer view of the same spectra between 0 and 40 meV, shifted relative to each other for clarity. The lattice modes are relatively insensitive to temperature. The only feature which changes is the 3 meV shoulder evident for the data at 200 K that disappears with increasing temperature. The scattered intensity in the gap region is again present, though at a lower energy transfer of 14 meV compared to the previous experiment. The intensity of this band decreases with increasing temperature and by 520 K it collapses into the background. The origin of this mode is uncertain.

Perhaps this mode is due to a hindered optic vibration of the lithium ion. From a comparison with K_3C_{60} and Rb_3C_{60} fullerides whose optic modes for the tetrahedral ion occur at ~ 15 meV and ~ 10 meV[192], respectively, and in the harmonic approximation, a prediction of the energy of the Li^+ optic mode is ≈ 35 meV. The frequency may be reduced by decrease the force constant of the oscillator which is equivalent to decreasing the interaction of the Li^+ ions with the surrounding C_{60} units. This would be the case for a reduced electrostatic potential and decreased charge transfer levels between the alkali metal and the fulleride ions. Evidence of reduced charge transfer has been seen in $\text{Li}_2\text{CsC}_{60}$ via Raman spectroscopy where the frequency of the $A_g(2)$ fulleride vibration shows a monotonic shift of -6 cm^{-1} per unit charge accumulated[211]. This reduced charge transfer has been used in explaining the absence of superconductivity in $\text{Li}_2\text{CsC}_{60}$ where $\text{C}_{60}^{2.5-}$ ions are observed. Superconductivity is recovered for $\text{Li}_3\text{CsC}_{60}$ ($T_c = 10.5$ K) when C_{60} is further reduced to -3 [56]. While this may explain the reduction of the frequency of an optic mode, it does not explain the reduction of intensity with temperature.

Another option is found with analogy to the polymeric and dimeric alkali metal

systems where C-C bond motions are seen in the same energy region. If this mode derives from a lithium bond to the fulleride cage, then the reduction in intensity with temperature would reflect a gradual reduction over a temperature range of ~ 200 K, of the number of such bonds in the sample. It is not the strength of the bonds that is changing as the position of this mode is constant. This is consistent with the inhomogeneous, broad features in the librational spectra. We can imagine a situation where at low temperatures there exists a Li^+ -C interaction and the fulleride units perform small amplitude librations. As the temperature increases, some of the fulleride ions start to rapidly reorient, breaking the interaction with the lithium and reducing the intensity of the 14 meV mode. As the temperature increases to 520 K, the entire sample is characterised by a rotational diffusion of the fulleride units and no Li^+ -C bonds remain.

From the two options considered, the possibility of having a Li^+ -C bond is reasonable and consistent with both our measurements of the GDOS and the analysis of X-ray powder diffraction data. To be able to model the correct reorientational motion of the fulleride units, further work must be performed where the momentum transfer range is not as limited as in the present case.

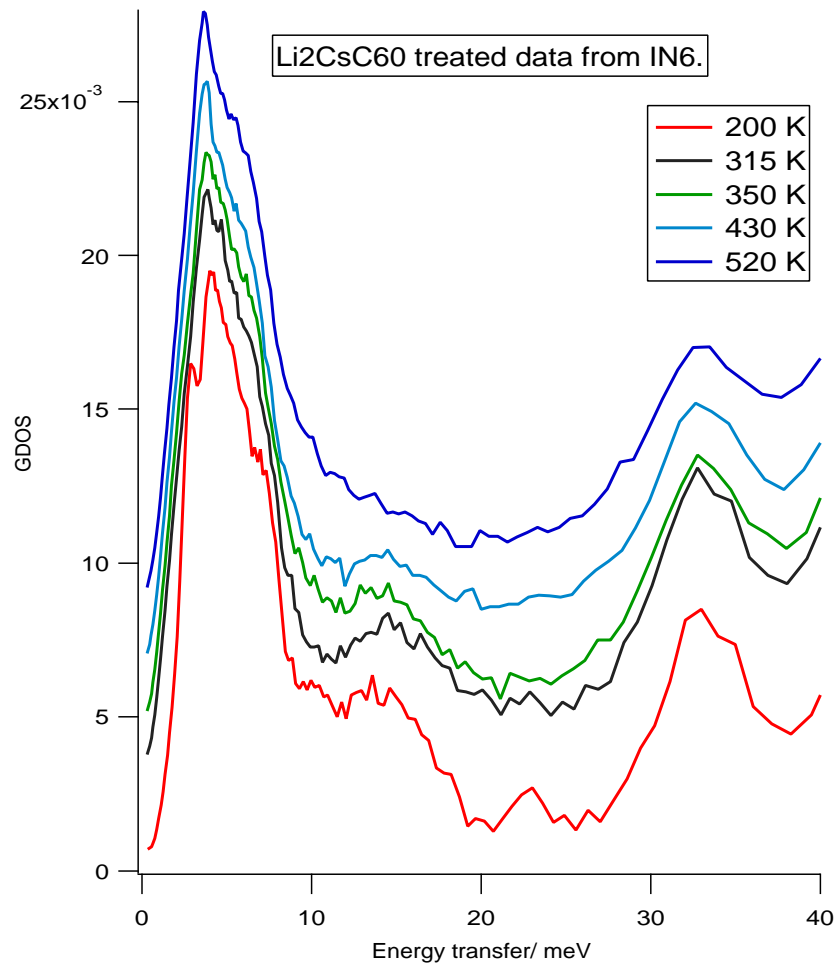


Figure 6.22: Low frequency part of the generalised density-of-states for $\text{Li}_{2-x}\text{CsC}_{60}$. The spectra are displaced from each other to facilitate viewing. No temperature dependence of the lowest energy C_{60} vibration is observed with limited softening in the group of peaks at 4 meV. Scattering density that lies in the gap region is seen to reduce in intensity with increasing temperature.

6.4 CsC₆₀

The discovery of KC₆₀[211] has generated a considerable amount of scientific interest in the AC₆₀ fullerenes, where A = K, Rb, Cs. Since this first observation of the high temperature phase by Raman spectroscopy, a plethora of different techniques have been employed to study this novel family. The most exciting feature of this series is the possibility of stabilising low dimensional phases from the high temperature cubic structure under differing cooling protocols. Short interfullerene contacts have been identified in these phases that has been interpreted in terms of bonding between neighbouring fullerene ions and leads to novel electronic and magnetic behaviour.

At high temperatures, the AC₆₀ family appears to be unexceptional, adopting a fcc structure[212], comprising of C₆₀⁻ monomers, in a similar manner to C₆₀ and the Na₂AC₆₀ compounds. Within the $Fm\bar{3}m$ space group, the large alkali ions rest in the octahedral interstices while the fullerene ion is disordered and reorients rapidly[193]. Below ~ 400 K, a structural transition to an orthorhombic phase occurs (space group $Pmnn$ with lattice constants of $a = 9.138(5)$ Å, $b = 10.107(5)$ Å, $c = 14.233(5)$ Å for RbC₆₀[64]), being characterised by short interball distances along the a axis[204]. The orthorhombic structure is related to the fcc parent via a compression along the cubic face diagonals. Rietveld analysis of X-ray[64] and neutron[202] powder diffraction data indicate the occurrence of one-dimensional polymer chains along the short orthorhombic axis, with neighbouring fullerene ions separated by a distance of ~ 9.11 Å[64]. These are much shorter than the ~ 9.95 Å found in the cubic phases.

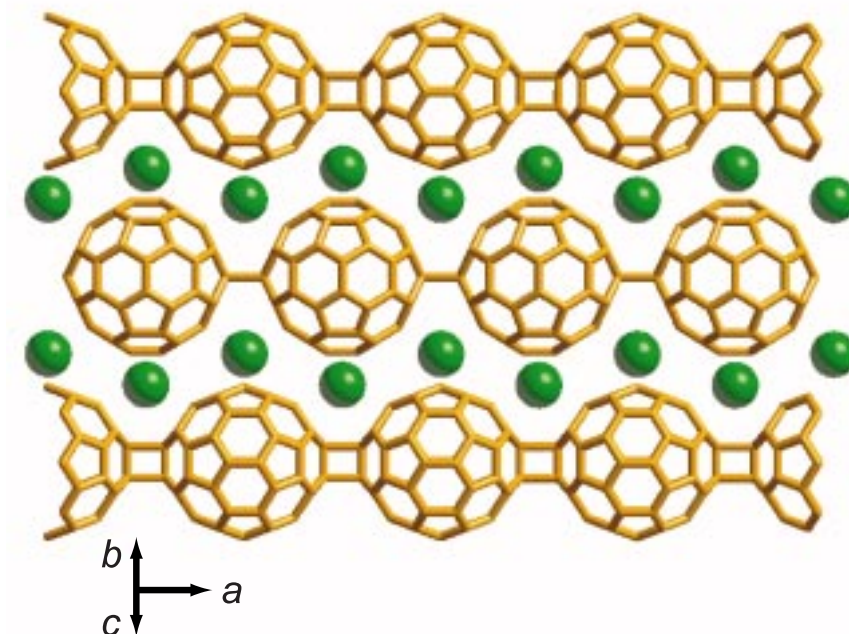


Figure 6.23: Polymeric chains formed in CsC_{60} . Spheres represent caesium ions that zig-zag in and out of the plane of the page along the chain directions.

In the polymeric structure, the fulleride units are connected by four membered rings comprising of C-C single bonds[64, 213]. It has been proposed that the mechanism for polymerisation is a $[2+2]$ cycloaddition reaction between neighbouring fulleride ions. This is similar to photo-polymerised C_{60} [214], where $[2+2]$ cycloaddition reactions are allowed by the Woodward-Hoffmann rules for the reaction between excited and groundstate molecules, but not between groundstate molecules themselves. For the case where charge transfer from the the alkali metal leads to formation of C_{60}^-

and the occupation of the LUMO t_{1u} orbitals, the reaction between two neighbouring anions is now thermally allowed.

The polymer is thermodynamically stable at room temperature and NMR measurements have shown that the fullerene molecules are not rotating in the orthorhombic phase[215]. Further cooling reveals a transition from a metallic[65] to a magnetic insulating phase below 40 K. The nature of the insulating phase has been the focus of many experiments. μ^+ SR results vary, with conclusions ranging from a spin-density-wave state[216], while others claim a more disordered magnetic structure[177, 217]. More recently it has been shown to be antiferromagnetic by the antiferromagnetic resonance technique[178].

From the high temperature fcc phase, further structural transitions are evidenced on quenching the sample and suppressing polymer formation. Initially, the formation of a dimeric monoclinic phase was reported to occur upon quenching below 270 K[68, 69, 70]. The singly bridged dimer (space group $C2/m$) is characterised by a short centre-to-centre separation of 9.34 Å, essentially the same as derived for $(C_{59}N)_2$ in §3.3. while the two dimers are structurally similar, calculations find that the $(C_{59}N)_2$ dimer is stable while the presence of the counter ion is necessary in the case of $(C_{60})_2^{2-}$ [134].

A complete characterisation of all the quenched phases of CsC_{60} has been performed using ESR, DTA (Differential Thermal Analysis) and DSC (Differential Scanning Calorimetry) measurements[66](Fig.6.24). Quenching CsC_{60} from high temperatures to below 160 K, stabilises a primitive cubic monomeric phase that is metallic, which transforms to a dimeric phase at 160 K. Following this, a transition to a pc phase at 220 K, and then to a fcc phase at 250 K is reported. The penultimate phase

transformation to the orthorhombic phase occurs at 270 K with the final fcc rotator phase formed above 370 K. The observation of a series of cubic phases separating the transition of the dimer to the polymer phase, may reveal the mechanism for polymerisation. In the dimer, the C_{60}^- units are connected by a single bond that is generated from the single free electron on two neighbouring molecules. Since no more electrons are available, a polymer structure connected by single bonds cannot occur, unlike the case of the ternary sodium salt where enough electrons are present to extend the 'dimer' into a polymer. To transform from the AC_{60} dimer phase to the polymer, it seems that the dimeric bond break at ~ 220 K, resulting in a monomeric structure. The polymer formation can then be understood by reorientation motion of fulleride units in the cubic intermediate phase. This presumably allows neighbouring fulleride units to have 6:6 bonds parallel such that they can bond.

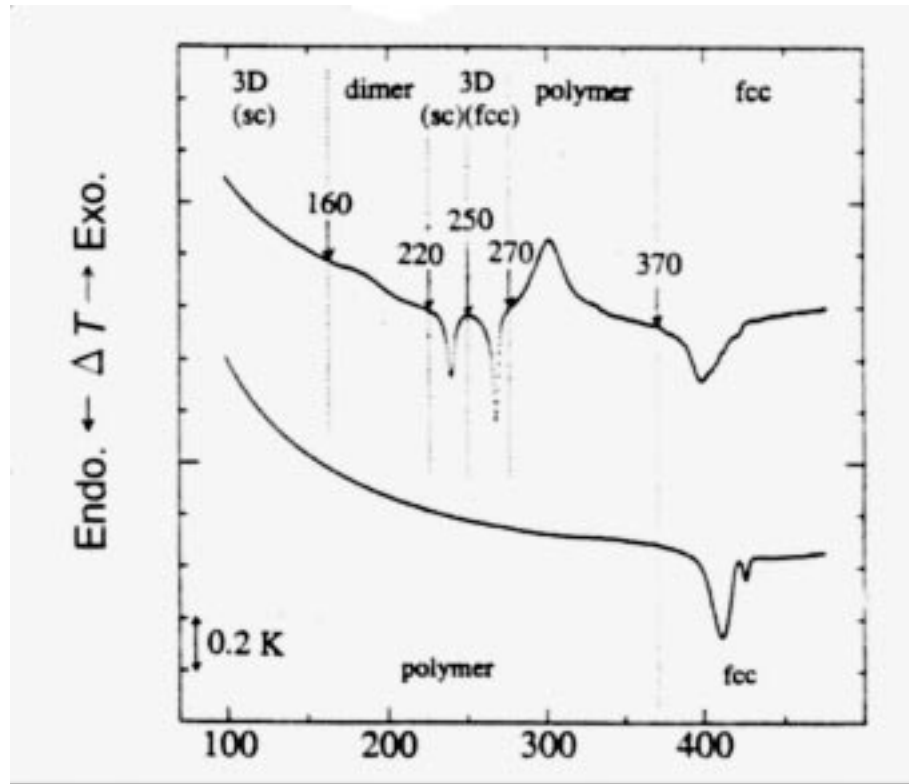


Figure 6.24: Differential thermal analysis of the (upper) deeply quenched (to 77 K) and slowly cooled (lower curve) CsC_{60} [66]. Results are obtained on heating.

6.4.1 Inelastic Neutron Scattering of CsC_{60}

Inelastic neutron scattering has proven to be a powerful tool for the investigation of the inter- and intra-molecular vibrations of fullerides. As we commented before, no vibrations of C_{60} origin appear in the energy region between 8 and 30 meV for pristine C_{60} [218, 219] and the alkali fullerides[35, 192]. Semi-empirical and *ab initio* calculations on the vibrational spectra of C_{60} have shown that the intermolecular interactions are dominated by van der Waals forces and the interball vibrations do not extend above 8 meV[220]. This can be explained considering that in solid fullerenes

the intermolecular forces are much weaker than the intramolecular ones, and hence vibrations have a disparate energy scale depending whether their origin is external (ending at 8 meV[219]) or internal (starting around 33 meV[218]). However, in the polymeric phase the fulleride units are connected through covalent C-C bonds and therefore interball vibration modes are now present. Calculations based on a first principles quantum molecular dynamics model[195] have predicted ball-ball chain modes in the energy range of 10-20 meV for the polymeric structure. Additionally, a splitting of the H_{g1} mode to a multiplet in the energy region of 28.5 to 32.5 meV is predicted. This splitting via symmetry lowering, formed the basis of an indirect observation of polymer formation using Raman and infrared measurements[221, 222].

Direct observation of the polymer modes has been seen using INS in CsC_{60} [193] with characterisation of low energy modes in both the polymer and dimer[205] systems, a detailed account of the transformations in RbC_{60} is given by Schober *et al.*[194]. Observation of anomalous softening in polymer modes on cooling through the metal-to-insulator transition has been reported for RbC_{60} and CsC_{60} [194]. The origin of this effect is uncertain.

The IN6 spectrometer at the ILL was used to perform inelastic neutron scattering experiments on CsC_{60} under differing cooling protocols. In all cases we used flat-plate aluminium cells with a small sample volume to accommodate our 310 mg of CsC_{60} sealed with lead wire. The wavelength was 4.12 Å. The following experimental procedures were used for the three cases under study.

Slowly cooled CsC_{60} : Data were taken on heating from 200 K when the polymer phase is stable to 580 K when the fcc phase is formed.

Deep quenching of CsC_{60} from the fcc phase to 77 K: The sample was attached

to the sample stick of the cryostat and heated, using a heat gun, to 450 K and kept at this temperature for 10 minutes to ensure full conversion to the cubic phase. Following quenching by dipping the sample holder in liquid nitrogen and allowing stabilisation at 80 K, the sample was transferred into an "orange" cryostat that was kept cold at 100 K. A thermocouple was attached to the sample stick and the temperature was monitored throughout this procedure. At no time during the transfer did the temperature rise above 100 K. Data were collected for ~ 10 hours at 100, 200, 250 and 300 K with empty can runs at 100, 200 and 300 K. Vanadium was used to normalise the detector efficiencies by performing a run at 300 K for 4 hours.

Quenching of CsC_{60} from the fcc phase to 200 K: The same experimental setup was used to quench the same sample to 200 K. The sample stick was removed from the cryostat and the sample was heated to 450 K for 10 minutes before dipping it into a slush bath made of acetone and solid CO_2 which was kept at ≈ 180 K. Initial counting rates for this series of experiments were approximately 10% higher than those in which the sample was quenched in liquid nitrogen, indicating retention of acetone on the surface of the cell that was gradually pumped away. With hindsight we should have employed deuterated acetone for the slush bath. Data were collected for ~ 10 hours at both 215 K and 250 K.

Data were analysed using the INX program with the following parameters (Table 6.12).

Table 6.12: The INX correction parameters used for the analysis of INS data collected on CsC₆₀ under different cooling protocols.

Angular Range	14- 114°
Detectors	26- 256
Wavelength	4.12 Å
Sample Depth	0.8 mm
Angle to Beam	135°
Transmission	0.97
Sample Density	0.86 g cm ⁻³
Molecular Mass	853.56 g
Average Mass	13.99 g
σ_s	337.2 barns
σ_a at 1.8Å	29.2 barns
Vanadium of thickness 1 mm at 300 K with 0.865 transmission	
Detectors used to mask Bragg reflections	
26-59 76-124 137-157 176-202 212-224 230-238 245-256	
Detectors used to mask Bragg reflections for polymer-fcc	
28-59 76-121 137-152 176-200 212-221 245-256	
with density= 1.26 g cm ⁻³ and 0.97 transmission.	

Since this is quite a complicated set of transformations, it is reasonable to organise the discussion of the results according to the different cooling treatments to which the CsC₆₀ sample was subjected.

Polymer to Cubic Phase Transition

The scattering law for slowly cooled CsC₆₀, taken on heating from 200 to 580 K is shown in Fig.6.25, with all data normalised to a Bose factor of 200 K. Fits to the spectra involve an elastic line, and appropriate Gaussian/Lorentzian combinations that are all convoluted with the instrumental resolution function (Table 6.13). Taking the 200 K spectrum initially, we only need a Gaussian component at $\pm 3.9(3)$ meV and a fairly broad Lorentzian component centred at the elastic line to reproduce the

data. We can assign the broad Gaussian to polymer derived modes by comparison to the polymeric CsC_{60} and RbC_{60} librational spectra of Schober *et al.*[194], with a similar feature present in the polymer state of $\text{Na}_2\text{RbC}_{60}$. This feature has been further resolved into three components using a triple axis instrument[205] where the structure factor development in Q allows their assignment to twisting modes of the chains. The presence of a broad quasielastic feature is probably due to remaining regions of monomeric C_{60}^- as also seen in RbC_{60} , where the actual proportion of monomers could be extracted from the temperature dependence of this quasielastic peak[194]. By 350 K, the only change occurs for the quasielastic peak which shows a slight increase in intensity.

On passing through the polymer \rightarrow fcc transition at 370 K, the spectra change dramatically, with a dominant quasielastic component evident at all subsequent temperatures. We modelled this quasielastic feature as a broad Gaussian and a Lorentzian component as just one quasielastic component did not fit the data well. An additional Gaussian was included in the fits to reproduce the feature at -3.7(3) meV. Assignment to C_{60} external modes is appropriate as the same feature is present in the spectra of RbC_{60} (≈ 3.5 meV) and agrees well with calculated translational and librational phonons at ~ 4 meV in Rb_3C_{60} and K_3C_{60} [192].

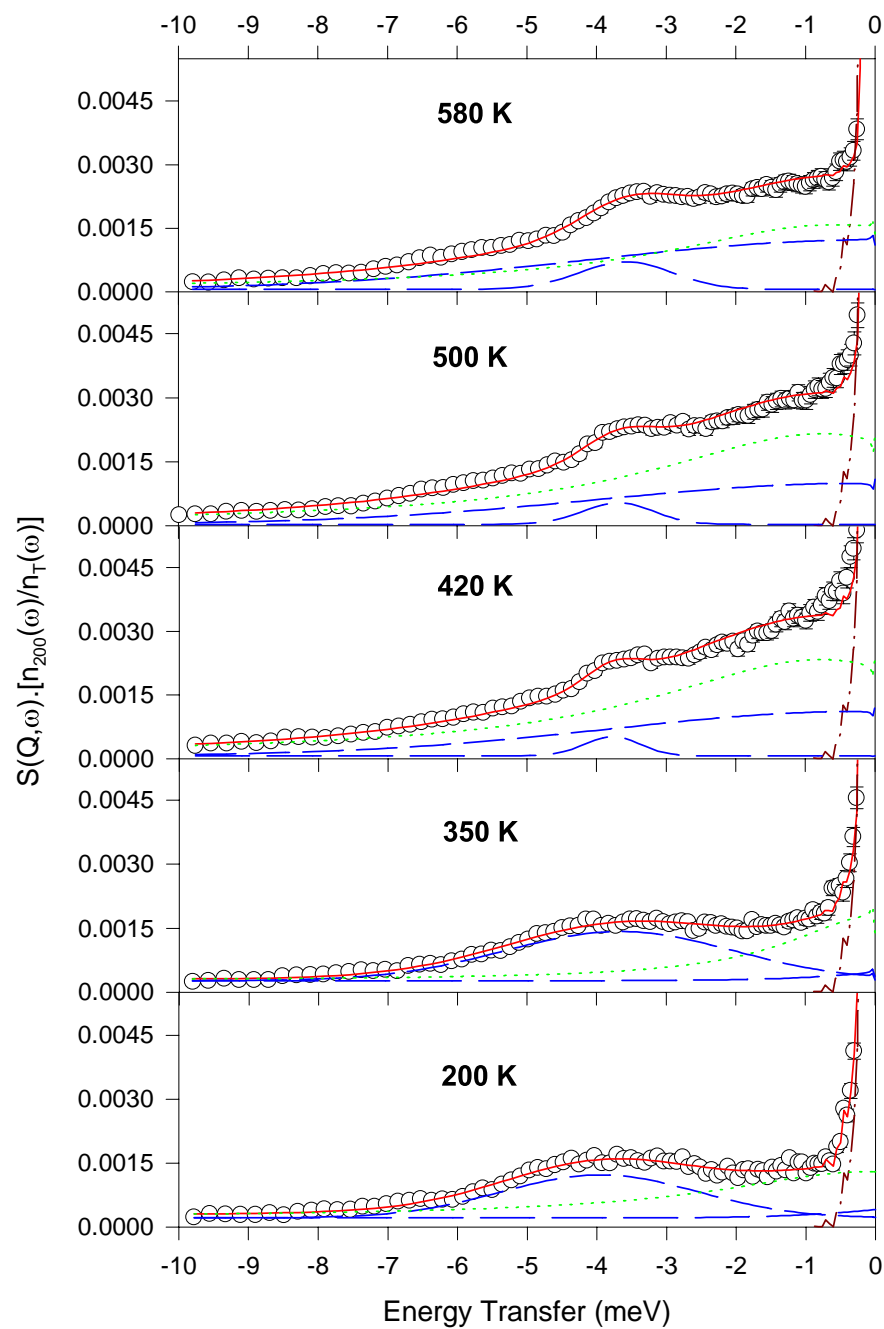


Figure 6.25: Temperature evolution of the normalised scattering law for the polymer→fcc transition in CsC₆₀. At each temperature, the observed data are shown as open circles, while the red line is the best fit. Dashed blue lines and dotted green lines are Gaussian and Lorentzian components, respectively.

Table 6.13: Results of the fits to the measured scattering law, $S(Q, \omega)$, across the polymer→fcc transition.

Temperature/K	Peak	Position(meV)	Intensity	FWHM(meV)
200	Gaussian 1	-3.9(3)	$4.0(6) \times 10^{-3}$	2.8(4)
	Lorentzian 1	0	$8(1) \times 10^{-3}$	3.0(12)
350	Gaussian 1	-3.6(2)	$9.8(9) \times 10^{-3}$	3.2(4)
	Lorentzian 1	0	$1.2(1) \times 10^{-2}$	3.0(6)
420	Gaussian 1	$-1(1) \times 10^{-5}$	$2.5(2) \times 10^{-2}$	7.2(6)
	Gaussian 2	-3.7(3)	$1.1(5) \times 10^{-3}$	0.8(4)
	Lorentzian 1	-0.7(2)	$4.4(2) \times 10^{-2}$	5.8(4)
500	Gaussian 1	$-1(1) \times 10^{-5}$	$2.8(2) \times 10^{-2}$	7.6(6)
	Gaussian 2	-3.7(2)	$1.9(6) \times 10^{-3}$	1.0(4)
	Lorentzian 1	-0.7(2)	$4.9(2) \times 10^{-2}$	5.8(4)
580	Gaussian 1	$-2(8) \times 10^{-5}$	$3.7(2) \times 10^{-2}$	8.4(6)
	Gaussian 2	-3.5(2)	$4.1(8) \times 10^{-3}$	1.4(4)
	Lorentzian 1	-0.6(2)	$4.4(2) \times 10^{-2}$	5.8(4)

Deep Quench of CsC₆₀ to 77 K

The aim of this part of the experiment is to by-pass all intermediate phases and form the metastable primitive cubic phase of CsC₆₀ via quenching of the sample to liquid nitrogen temperatures. Heating to 200 K should then lead to a transformation to the dimer phase. Further heating will take us successively to the intermediate cubic transition phase at 250 K and then to the polymer phase at 300 K. The renormalised scattering law for all temperatures is shown in Fig.6.26 along with fits that include a δ function at the elastic line, a broad pair of Gaussian and two smaller Lorentzians at finite energy transfer all convoluted with the resolution function (Table 6.14).

At 100 K, the data are well fit by a broad Gaussian distribution at 3.4(2) meV on both sides of the elastic line, and two weaker Lorentzians at -2.86(2) and -4.2(2) meV. Inspection of this data reveals a surprising similarity with the spectrum at

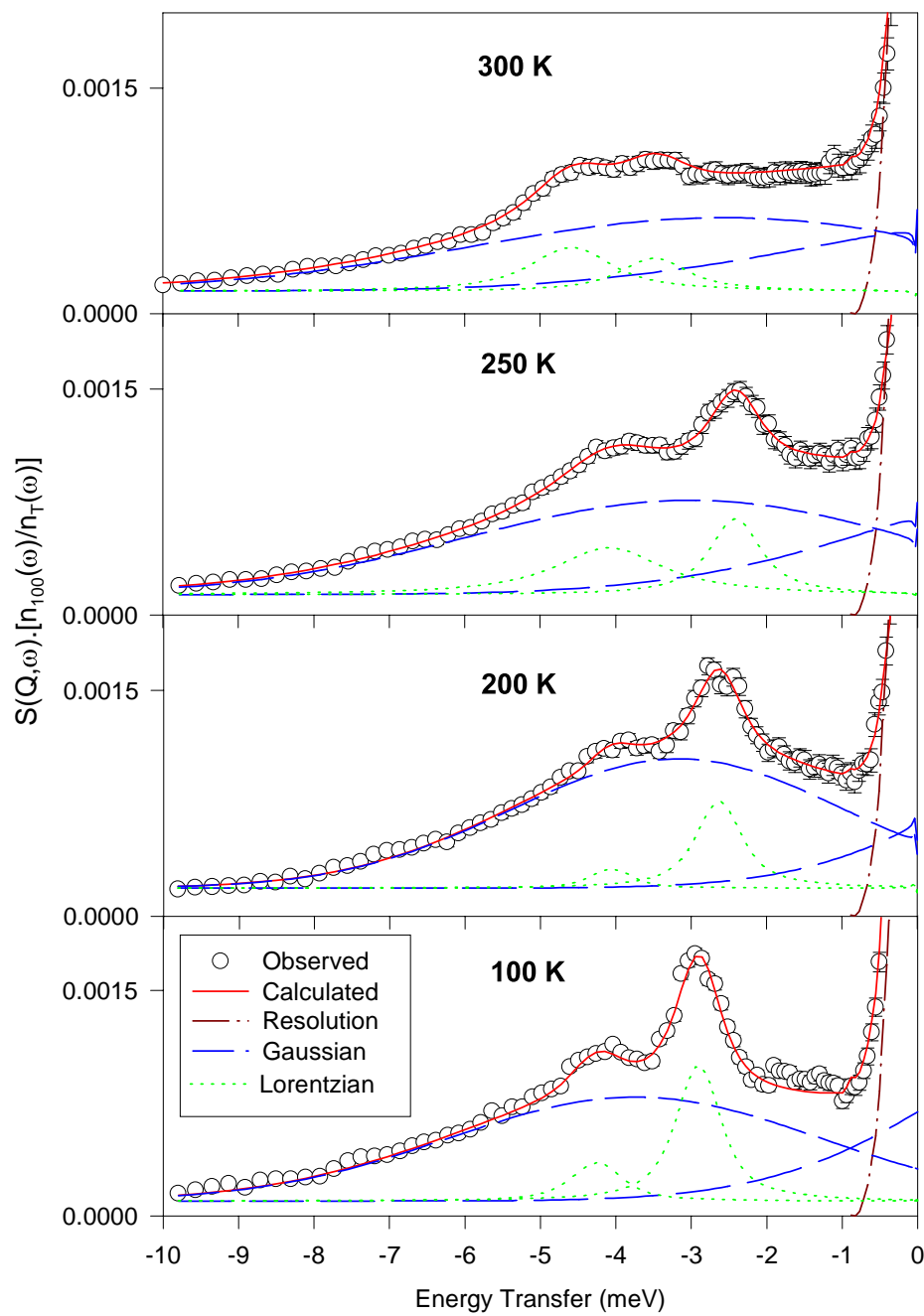


Figure 6.26: Temperature scaled scattering law for deeply quenched CsC_{60} . Observed data is shown by open circles with a fit as a solid red line. Contributions from Gaussian peaks are shown as dashed blue lines while Lorentzians are dotted green lines.

200 K for $\text{Li}_{2-x}\text{CsC}_{60}$. The origin of this should lie with the similarities in the structural/dynamic characteristics between the two fullerides. More explicitly, both are cubic with the fulleride cages librating about an equilibrium position giving rise to the intense peak at 2.86(2) meV. The position of this librational mode is in excellent agreement with the librations observed in $\text{Na}_2\text{RbC}_{60}$ [27] but somewhat softer than those of $\text{Na}_2\text{CsC}_{60}$. The weaker Lorentzian at -4.2(2) meV may be due to lattice phonons.

Table 6.14: Results of the fits to the measured scattering law, $S(Q, \omega)$, for CsC_{60} quenched to 77 K.

Temperature/K	Peak	Position(meV)	Intensity	FWHM(meV)
100	Gaussian 1	-3.4(2)	$4.4(3) \times 10^{-3}$	4.8(4)
	Lorentzian 1	-2.86(2)	$8(1) \times 10^{-4}$	0.5(1)
	Lorentzian 2	-4.2(2)	$2.3(9) \times 10^{-4}$	0.6(4)
200	Gaussian 1	-3.0(1)	$1.09(4) \times 10^{-2}$	4.4(2)
	Lorentzian 1	-2.60(9)	$1.2(2) \times 10^{-3}$	0.6(2)
	Lorentzian 2	-4.0(3)	$\times 10^{-4}$	0.4(4)
250	Gaussian 1	-2.8(3)	$1.36(5) \times 10^{-2}$	5.6(4)
	Lorentzian 1	-2.38(8)	$1.5(2) \times 10^{-3}$	0.7(2)
	Lorentzian 2	-4.0(2)	$1.9(3) \times 10^{-3}$	1.8(4)
300	Gaussian 1	-2.7(2)	$1.48(6) \times 10^{-2}$	6.6(4)
	Lorentzian 1	-3.4(2)	$1.0(3) \times 10^{-3}$	1.0(4)
	Lorentzian 2	-4.5(1)	$1.6(3) \times 10^{-3}$	1.0(4)

On heating to 200 K we expected to see distinct changes in the librational spectrum as the transformation to the dimer phase occurred. In fact, we see that the spectrum is dominated by remnants of the cubic fulleride librational peak, that has softened and broadened and its intensity has decreased. The intensity loss can partly be explained by an increase in the Debye-Waller factor. However, superposition of the 100 and 200 K spectra also reveals a slight increase in intensity at ~ 4 and ~ 1.5 meV.

The situation is extremely difficult to interpret due to the poor quality of the data after transformation to the generalised phonon density-of-states. In all cases, the spectra are heavily contaminated by aluminium phonons in the 15 to 25 meV region. Attempts at subtracting a larger contribution of the empty cell (i.e. changing the transmission factor in INX) have resulted in a situation where it seems impossible to remove these contributions and still retain a spectrum that resembles a fulleride internal mode spectrum at higher energy transfers.

Direct comparison of our librational spectrum with those published on CsC_{60} [205] and RbC_{60} [194] shows that little dimer phase is present. Triple-axis measurement on the dimer phase of CsC_{60} at 200K, have revealed peaks at ~ 1.6 , 2.9 and 4.3 meV. These occur at ~ 1.7 , 2.9 and 4.0 meV in the dimer phase of RbC_{60} (185 K) as measured by TOF experiments. The small intensity increases that we observe in our spectrum coincide well with the energy regions we would expect twisting modes of the dimer to appear. It seems that in CsC_{60} the cubic form was retained to 200 K with only a very small amount of dimer present. A similar situation to this has been reported for a deep quenching of CsC_{60} to the three-dimensional monomer phase and the subsequent heating of the sample into the dimer region. In this case, neutron powder diffraction could not identify any transformation from the cubic state[202]. The difference in the behaviour of samples synthesised in different laboratories may be due to different conditions and heat treatments in the experiments. Additionally, the exact composition of the sample may exert additional some influence on the phase transformations.

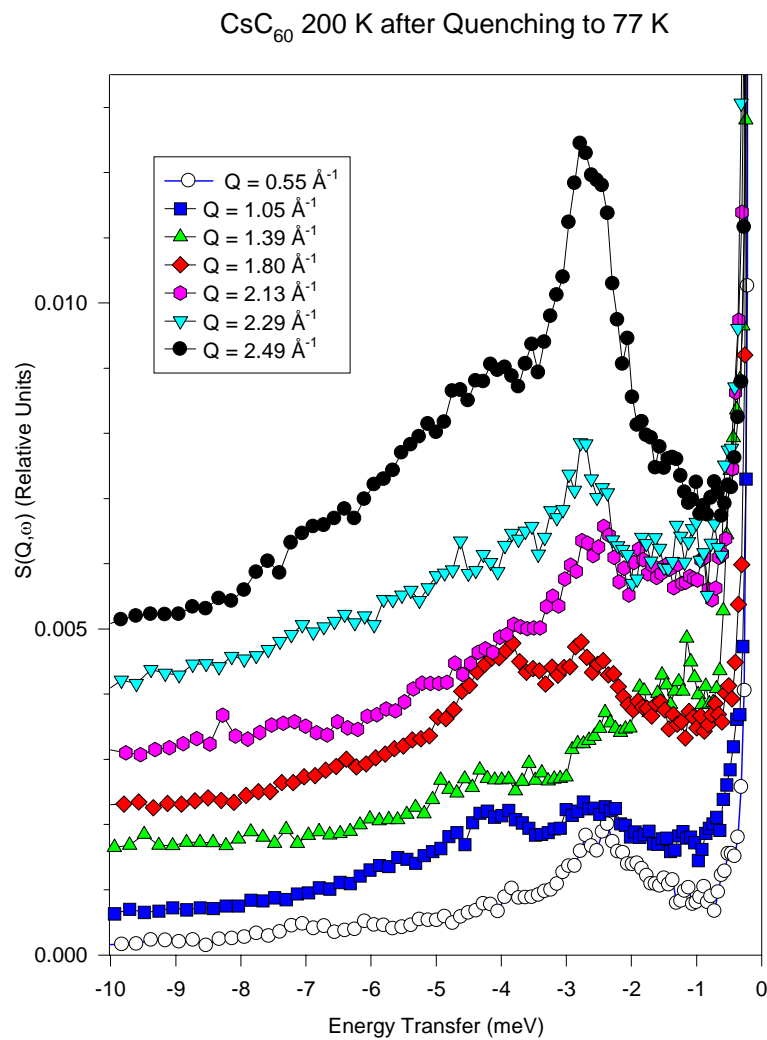


Figure 6.27: Q dependence of the scattering law for deeply quenched CsC₆₀ at 200 K. The spectra are displaced relative to one another.

The Q dependence of the spectra at 200 K are shown for various groupings in

Fig.6.27 where the strongest scattering comes from the highest Q region. It is worthwhile recalling that the maximum Q available on IN6 (2.5 \AA^{-1}) is still considerably smaller than the values at which the maxima in the form factor of C_{60} occur ($\sim 3.5 \text{ \AA}^{-1}$ and $\sim 5.8 \text{ \AA}^{-1}$). The effect of increasing Q on the measured scattering is quite astonishing with the sharp librational mode seen at 2.6 meV.

Following heating to 250 K, into the intermediate cubic phase temperature range, no further change in the spectrum occurs, besides the additional softening and broadening of the librational peak. Since very little dimer phase was present before, it is difficult to identify any other transformation to the expected cubic form. It is worth noting that the normalised spectra at 200 and 250 K are superposable except for the librational peak. A final heating to 300 K leads to the occurrence of transition to the polymer phase, as is reflected by the drastic change in the spectrum. The librational peak has completely collapsed, leaving only a broad series of modes. The decomposition of this peak is difficult, but the general characteristics are like those of the polymer phase in the previous experiment. A broad Gaussian component tails off between 4 and 6 meV, but we lack any defining cutoff nearer the elastic peak, a repeated feature throughout this quenching experiment. It is probable that the spectrum still comprises of polymer and cubic forms.

Quenching of CsC_{60} to 200 K

A final attempt to quench the high temperature phase of CsC_{60} into the metastable dimer form at 200 K was performed with an acetone slush bath. The affect of the strongly scattering hydrogenous acetone that remained frozen on the cell surface after the introduction of the sample stick in the cryostat, is clearly apparent in the recorded

spectrum at 215 K (Fig.6.28). An extremely broad and strong quasielastic peak arises from the influence of the hydrogen motion and was fitted by a combination of a broad Gaussian and a narrow Lorentzian peak. Also apparent in the scattering are two very weak features at -2.5(1) and -4.1(3) meV (Table 6.15). From their positions we can assign them to librational and lattice modes of the cubic phase, respectively. It is apparent that with time, pumping inside the cryostat led to a decrease in the scattering due to hydrogen and by the time we collected the spectra at 250 K, it had reduced to a minimum. This spectrum is qualitatively similar to that taken at 250 K after deep quenching, implying again that the majority phase is the primitive cubic form. It is indicated in the DTA curve of Fig.6.24 that around 250 K, a transition between the primitive cubic and fcc forms of the monomer may occur. We are not able to define a quasielastic component (due to hydrogenous scattering) in the 250 K spectrum that would be characteristic of the fcc phase, where the fulleride units undergo rotational diffusion.

Table 6.15: Results of the fits to the measured scattering law, $S(Q, \omega)$, for CsC_{60} quenched to 200 K.

Temperature/K	Peak	Position(meV)	Intensity	FWHM(meV)
215	Gaussian 1	2(2)e-4	$6.7(1) \times 10^{-2}$	7.3(1)
	Lorentzian 1	2(1)e-4	$4.26(8) \times 10^{-2}$	0.70(4)
	Gaussian 2	-2.5(1)	$6(2) \times 10^{-4}$	0.3(2)
	Gaussian 3	-4.1(3)	$1(1) \times 10^{-4}$	0.2(4)
250	Gaussian 1	-2.3(1)	$2.0(6) \times 10^{-2}$	6.6(2)
	Gaussian 2	-2.50(8)	$1.1(2) \times 10^{-3}$	0.6(2)
	Gaussian 3	-4.0(2)	$7(2) \times 10^{-4}$	0.8(4)

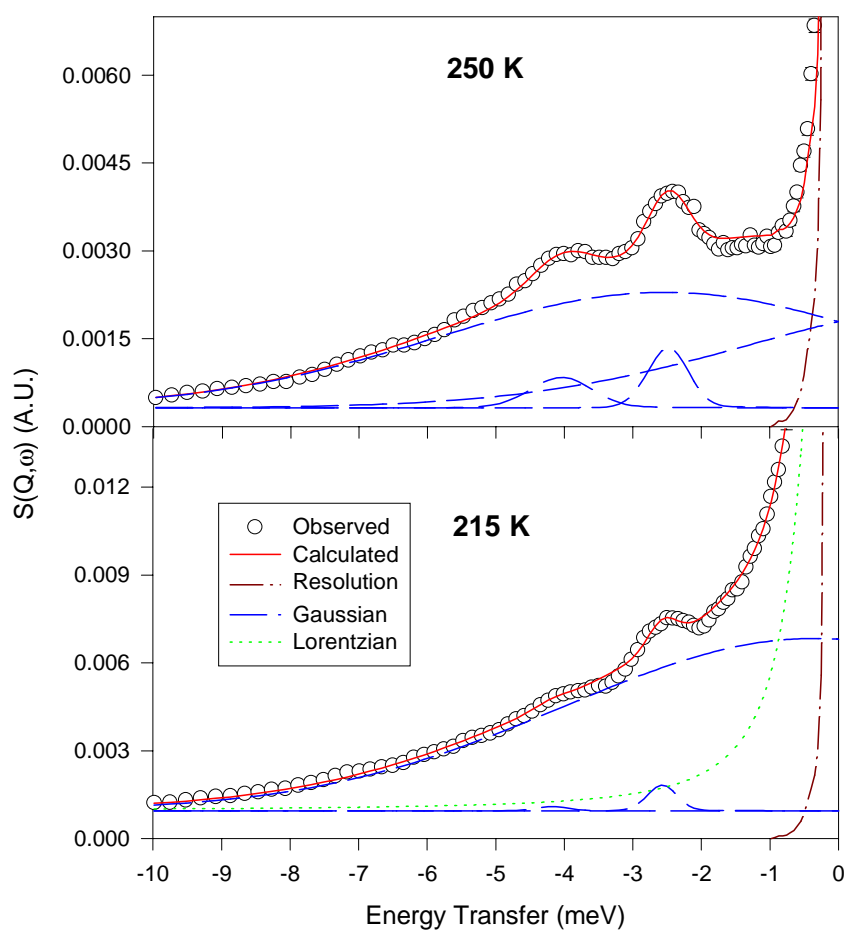


Figure 6.28: The scattering law for CsC_{60} after quenching in an acetone/ CO_2 mixture. Hydrogenous material is present as a time dependent quasielastic component.

In Fig.6.29 we collect together the energies and widths of the librational features

observed in $\text{Li}_2\text{CsC}_{60}$, CsC_{60} (quenched to 77 K) and CsC_{60} (quenched to 200 K). It can be seen that in all cases the temperature dependence of the librational energies are extremely similar. It has been noted before that the librational energies scale with size of the ion occupying the tetrahedral interstice. If the size of the ion is less than the size of the tetrahedral hole then the low temperature librational energy is roughly constant at ~ 2.8 meV. However, when the size of the ion is greater than the size of the interstice, the structure is fcc and the librational energy scales almost linearly with the ionic radius[18]. In the present case, $\text{Na}_2\text{RbC}_{60}$ and $\text{Li}_2\text{CsC}_{60}$ have small tetrahedral cations while CsC_{60} only has an octahedral ion. The conformity of behaviour reflects the dominance of the repulsive $\text{A}^+\text{-C}$ overlap in determining the orientational potential in these systems.

The variation of the librational width across fulleride families is not as easy to interpret. The width is determined by the anisotropic nature of the orientational potential. The narrow widths of the librations in CsC_{60} are almost temperature independent, following the development of the librations in K_3C_{60} . The exceptionally broad $\text{Li}_2\text{CsC}_{60}$ libration may reflect perturbations to the potential caused by $\text{Li}^+\text{-C}$ interactions.

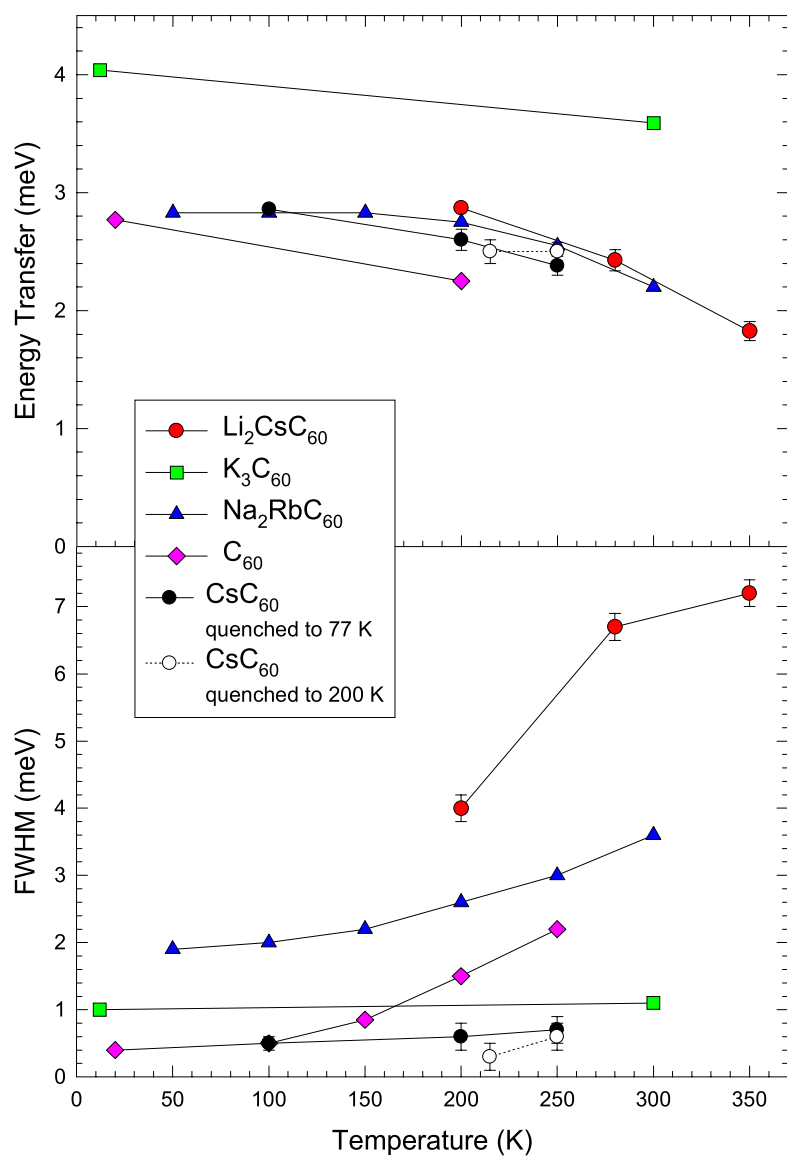


Figure 6.29: Temperature evolution of the librational energy (upper) and width of the librational peak for the alkali fulleride salts: $\text{Li}_2\text{CsC}_{60}$ (red circles), K_3C_{60} (green squares), $\text{Na}_2\text{RbC}_{60}$ (blue triangles), C_{60} (pink diamonds), CsC_{60} quenched to 77 K (black circles) and CsC_{60} quenched to 200 K (open circles). Adapted from Ref[27]

6.5 Conclusion

Neutron diffraction has been used to characterise the thermal evolution of the cubic-polymeric phase transition in $\text{Na}_2\text{RbC}_{60}$. The transformation to the monoclinic polymer from the primitive cubic phase occurs at ~ 250 K under slow cooling conditions. The rate of polymer formation is very slow and temperature dependent. Upon heating from 2.3 K, the volume fraction of polymer is constant, until 230 K after which the fraction is reduced with a concomitant increase in the amount primitive cubic. By 277 K, only the primitive cubic phase remains. This highlights the strong hysteresis observed in the cooling and heating cycles of polymer formation/destruction. The kinetics of the phase change play an important part in deciding how much of the polymer is formed in a given time. We note that, on slow cooling, the polymer forms below 250 K, while on heating the reduction of the polymer fraction occurs above 230 K. Hence, the logical temperature to maximise the polymer fraction should be just below 230 K. The thermal evolution of the monoclinic cell is characterised by anisotropy in the expansivity along the independent axes. Negligible expansivity is observed along the c axis that defines the polymer chain direction, while the expansivity along the monoclinic b_m axis is somewhat large at $2.4(1) \times 10^{-5} \text{ K}^{-1}$ than that obtained for the coexisting cubic phase ($1.72(7) \times 10^{-5} \text{ K}^{-1}$). On further heating, a coexistence of the primitive cubic and high temperature rotator phase is observed between 299 and 317 K.

Inelastic neutron scattering of slowly cooled $\text{Na}_2\text{RbC}_{60}$, shows excess scattering present between 8- 25 meV in the polymer phase when compared to the high temperature cubic phase spectrum. These new modes are in agreement with those observed for the doubly bridged AC_{60} polymers, though at slightly reduced energy transfers

consistent with the formation of a singly C-C bonded polymer. The librational spectrum of the polymer shows a broad distribution of modes centred at ~ 3.5 meV that arises from a twisting motion of the polymer chains about their axis. At 320 K the spectrum is characterised by the presence of a quasielastic peak that is indicative of rotational diffusion of the fulleride ions in the fcc phase.

The temperature variation of the *ac* susceptibility of $\text{Na}_2\text{Rb}_{0.5}\text{Cs}_{0.5}\text{C}_{60}$ was measured to pressures as high as 2.5 kbar. We established a rate of $-1.22(2)$ K/kbar for the decrease of T_c with increasing pressure. Combining this result with the linear susceptibility of the isostructural $\text{Na}_2\text{CsC}_{60}$ analogue, we derived the rate of change of T_c with cubic lattice constant as $dT_c/d(\ln a) \approx 0.7 \times 10^3$ K, comparable to that of K_3C_{60} . Thus the unusually steep dependence of T_c on interfullerene separation, encountered at ambient pressure for the $\text{Na}_2\text{Rb}_{1-x}\text{Cs}_x\text{C}_{60}$ family, was not apparent in the measurements on the individual members at high pressure. Rather each appears to revert back to the "normal" T_c - a dependence, exhibited by *fcc* fullerides. This dichotomy in the behaviour of Na-containing fullerides mitigates against early conjectures of the existence of a sensitive dependence of $N(\epsilon_F)$ on the orientational state of the fulleride ions and points towards metal-specific effects, perhaps associated with either the occurrence of polymerisation or the modulation of the $\text{Na}^+ - \text{C}_{60}^{3-}$ interaction with interfullerene spacing.

Neutron inelastic spectra have been collected for both $\text{Li}_2\text{CsC}_{60}$ and a mixture of $\text{Li}_{2-x}\text{CsC}_{60}$ and $\text{Li}_2\text{CsC}_{60}$ at various temperatures. Below 315 K, the fulleride ions undergo small amplitude librations about their equilibrium positions giving rise to librational peaks near 3 meV. These soften on heating in a similar manner to

$\text{Na}_2\text{RbC}_{60}$ but retain a small, coexisting quasielastic component at high temperatures, like $\text{Na}_2\text{CsC}_{60}$. This indicates the possibility of the existence of an order-disorder transition, that has not been seen using other techniques. The situation for $\text{Li}_{2-x}\text{CsC}_{60}$ is somewhat more difficult to interpret, but a change from librational motion to rotational diffusion above 350 K appears likely. This characteristic features in both experiments are in contrast to the absence of phase transitions in $\text{Li}_2\text{CsC}_{60}$ monitored using DCS and X-ray powder diffraction techniques. The GDOS for both compounds have scattering in the 10-20 meV region that is usually associated with C-C interfulleride bonding in fulleride dimers and polymers. While the spectra for $\text{Li}_2\text{CsC}_{60}$ have low statistics, the spectra of $\text{Li}_{2-x}\text{CsC}_{60}$ clearly define a mode at 14 meV. this feature reduces in intensity with increasing temperature and is no longer observable above 520 K. This mode may be related to a Li^+ -C interaction. No reduction in the strength of this interaction is seen with increasing temperature, though there is a reduction of number of the units that contribute to this peak.

INS has also been used to attempt to characterise the phase transitions within the complex CsC_{60} system. Successful experiments were only conducted where the cubic and polymer phases were concerned: we have no direct observation of the dimer form. This is difficult to understand given the fact that it has been observed by two different research groups. It may be related to different sample sizes and heating/cooling treatments. We confirm that a polymer \rightarrow fcc transition occurs between 350 and 420 K, with the fcc phase characterised by rotational diffusion of the fulleride units. Polymer twisting modes occur around 3.7 meV in excellent agreement with published data. On quenching to 77 K, we observe a sharp librational peak that occurs at an energy of 2.86(2) meV at 100 K. While we do not observe any transformation to the

dimer phase on heating, the temperature dependence of the librational energy follows that of the primitive cubic fullerenes and $\text{Li}_2\text{CsC}_{60}$. By 300 K, the libration has disappeared to be replaced by a broad feature characteristic of the polymer phase, in agreement with the expected phase transition. After heating CsC_{60} above the polymer \rightarrow fcc phase transition and subsequently quenching in an acetone slush bath, we observed a librational feature in $S(Q, \omega)$. This signifies the presence of the primitive cubic phase of CsC_{60} with no observation of dimer formation.

Chapter 7

Conclusion

7.1 Background

In this thesis, we have studied the structural and dynamical properties of fullerene based compounds. The initial interest in C_{60} resulted from the bulk production of the solid and its subsequent intercalation with alkali metals. In particular, the occurrence of superconductivity, as high as 33 K, motivated a systematic study of the structural and electronic properties of the alkali fullerenes as functions of the intercalant and the fullerene-alkali metal stoichiometry. As a result, a cubic structure was found for the superconducting fullerenes, while more expanded structures occur for higher doping levels. The superconducting characteristics of the C_{60}^{3-} phases are influenced strongly by the degree of fullerene molecular orbital overlap, and hence the cubic lattice constant. Efforts to increase T_c have focused on expanding the cubic lattice constants. One method of doing this is to intercalate neutral spacer molecules such as ammonia. However, it seems that there is a limit to the maximum interfullerene separation that can give rise to superconductivity.

Stoichiometries with less than three alkali metal atoms per fullerene molecule were

initially reported as unstable until the AC_{60} family was discovered, which displayed short interball distances that have been interpreted as a consequence of the fullerene molecules being connected by C-C bonds so forming monodimensional chains. Recent work has shown these polymer type structures are not confined to the C_{60}^- systems with evidence from X-ray diffraction studies indicating that sodium intercalated ternary also undergo polymerisation. In these cases the applied pressure or temperature, as well as the cooling or heating rate are crucial in determining the phase the fullerides will adopt.

The study of alkaline earth fullerides is not as developed as that of the alkali metal fullerides. The main reason for this stems from difficulties in production and purity control of these systems. These problems led to claims of superconductivity for the salts Sr_6C_{60} and Ba_6C_{60} . Only recently has superconductivity been attributed to the Ba_4C_{60} and Sr_4C_{60} phases where electrons populate the (LUMO+1)-derived C_{60} states. Photoemission studies and theoretical calculations on alkaline earth fullerides indicate that hybridisation of alkaline-earth s and d states and C_{60} π states is important in these systems. We have performed a detailed analysis of the structure of Ba_4C_{60} , as a function of temperature and pressure. We see evidence of a strong interaction between the barium ions and the fulleride cages. This is the first verified fulleride that is superconducting at ambient pressure and *not* cubic.

In the search for C_{60} variants that are expected to have interesting solid state properties, an alternatively method of 'doping' C_{60} can be envisaged by replacing a carbon atom in the cage with a nitrogen atom. As a consequence of exchanging a tetravalent carbon for a trivalent nitrogen, the monomer units are found to rapidly dimerise. We have performed the first X-ray structural analysis of the pristine $(C_{59}N)_2$

solid in combination with the optimised molecular dimer structure from density-functional calculations. The variety of bonding regimes within the solvated solid has been probed using X-ray diffraction to high pressures.

The next section describes in brief the significant points presented in this thesis and the studies that should follow in the future to answer questions arising from the present work.

7.2 Overview and Future Directions

We firstly probed the diverse bonding interactions present in the azafullerene solid. X-ray diffraction measurements were performed on the hexagonal form of $(\text{C}_{59}\text{N})_2$ upto 22 GPa at room temperature; these reveal a somewhat less compressible solid than pristine C_{60} . As with C_{60} , the individual quasispherical C_{59}N monomer units are seen to be much less compressible than the bulk solid. The lack of strong anisotropy can be rationalised in terms of nonalignment of the C-C bridging bonds of the dimer with the unit cell axes. We observe a faster compression of the interdimer distances than the those of the intradimer distances; at ~ 6.5 GPa, they are both of comparable magnitude, leading to a high pressure solid structure which appears to be characterised by almost isotropic bonding. Strong evidence for molecular dimerisation of the sublimed solid is obtained from synchrotron powder diffraction measurements. This is consistent with density functional theory-based calculations which confirm the stability of the dimer. We have used the optimised dimer structure to maximise the information extractable from the diffraction data.

When more of the sublimed material becomes available, it will be useful to collect neutron powder diffraction data and attempt a detailed refinement of the geometry

of the azafullerene cages. As with the polymer/dimer AC_{60} systems, inelastic neutron scattering would be an indispensable tool in probing vibrational properties of this solid. A systematic investigation of the properties of azafullerene intercalation compounds has been initiated at Sussex. Initially this has been using the solvated azafullerene. With the production of sublimed azafullerene, we can expect the production and characterisation of an entirely new series of azafullerides with unknown and potentially interesting properties. One can speculate on the occurrence of novel magnetic, electronic and structural properties arising from the nitrogen perturbation of the molecular potential. The development of this field of study may even parallel that of C_{60} itself.

We have performed a detailed Rietveld refinement of high resolution synchrotron powder diffraction data of Ba_4C_{60} collected at 295 K. We find that the best description of this structure is within the orthorhombic space group *Immm*. The structure is characterised by orientationally ordered anions with the barium ions occupying two distinct sites. The barium ions can be distinguished by their closest contacts distances to the fullerene cages; one barium site has a closest distance of ~ 3.3 Å while the other exhibits extremely close contacts of ~ 3.0 Å. No phase transitions are apparent on cooling with the crystal structure at 5 K being essentially identical to that at room temperature. The thermal expansivities for each axis are much reduced compared to the alkali metal intercalates, and a negligible expansivity of the short c axis is observed. X-ray studies of Ba_4C_{60} under high pressures reveal a solid that is much less compressible than the alkali metal intercalates. From the pressure dependence of the unit cell volume of Ba_4C_{60} , we obtain $d\ln(T_c)/d\ln(V) = 18.75$, implying that superconductivity in Ba_4C_{60} is more sensitive to changes in volume than K_3C_{60} .

and Rb_3C_{60} , where $d\ln(T_c)/d\ln(V) \sim 7$. The individual lattice constants of Ba_4C_{60} are anisotropic in compression with a small compressibility of $-1.16(4) \times 10^{-3} \text{ GPa}^{-1}$ extracted for the c axis. Compared to the alkali fullerenes, we expect a tighter crystal packing for the alkaline earth fullerenes due to an increased charge transfers and a concomitant increase in the electrostatic attractions between anions and cations. The lack of compression and thermal expansion along one axis as a function of pressure and temperature is associated with a short barium-carbon interaction distance along the same direction. We infer that there is a strong Ba-C interaction in this direction.

Future work should include re-performing the neutron diffraction experiment on Ba_4C_{60} , in order to search for any modifications of the structure that could be indicative of Ba-C bonding. In the structural work we have assumed a uniform length for the fullerene C-C bonds: it would be possible to test this assumption with neutron diffraction data. A more detailed study of the temperature dependence of the crystal structure is desirable to confirm the low thermal expansivities seen in this thesis, and to extend the measurements to higher temperatures to check for possible phase transformations. This work should not be just confined to Ba_4C_{60} , but is equally applicable to Sr_4C_{60} and the other stable alkaline earth phases. Of particular interest are the metallic AE_6C_{60} phases with Sr_6C_{60} having a larger density of states at the Fermi level than that of Ba_6C_{60} despite it also having a smaller lattice constant: this is the opposite trend from that found both experimentally and theoretically for the alkali metal fullerenes. With sufficient sample, neutron inelastic scattering can probe the fullerene rotational potential in an unmatched fashion. This technique can also give information on the intramolecular vibrations of the fullerene cage with possible differences between the alkali metal fullerenes and the alkaline earth fullerenes due to the

effects of electrons populating the (LUMO)+1 C_{60} derived states and hybridisation of the alkaline-earth s and d states and C_{60} π states.

Another charge transfer salt of C_{60} , whose novel properties have motivated our studies is $(NH_3)K_3C_{60}$. It has been reported that at ~ 40 K, a transition to an insulating state occurs. remarkably, upon application of pressure (> 10 kbar) superconductivity is observed at 28 K. In order to study the nature of the insulating phase, muon spectroscopy was used. The zero-field muon spin relaxation (ZF- μ^+ SR) technique provided direct evidence of spontaneous magnetic ordering below 40 K. The appearance of a precession signal indicates the spontaneous antiferromagnetic ordering of the electronic magnetic moments, with a frequency corresponding to a local field of $\langle B_\mu \rangle \approx 40$ G at the muon site at 7.2 K. This is the first time a long range ordered antiferromagnetic state has been verified for the C_{60}^{3-} salts. Furthermore, the width of the distribution of local fields has a value of $\sqrt{\langle \Delta B^2 \rangle} \approx 25$ G, only 1.6 times smaller than the $\langle B_\mu \rangle$ indicating spatial disorder and inhomogeneity effects that may be attributed to orientational disorder of the fulleride units or incommensurate order between the crystallographic and magnetic structures. Additional LF measurements have shown that even a small field of 100 G is able to decouple the μ^+ spin from the static fields and consequently enable the recovery of the asymmetry. This indicates that the spin relaxation is derived from static disordered internal fields. TF- μ^+ SR measurements have verified the above results by showing the onset of magnetic ordering below 40 K. The suppression of superconductivity at large interfullerene spacings thus appears to be associated with effects of *magnetic* origin. Recovery of the metallic/superconducting state upon application of external pressure may then be associated with the removal of the LRO AF state in direct analogy with

high- T_c and organic superconductors.

Inelastic neutron scattering has been used to observe rotational tunnelling of ammonia in $(\text{NH}_3)\text{K}_3\text{C}_{60}$ at an energy transfer of $270 \mu\text{eV}$ at 1.5 K. The position of the peak is temperature dependent: with increasing temperature the orientations of the NH_3 groups become increasingly disordered with a consequent softening of the tunnelling peak and development of a central quasielastic line arising from diffusive rotational motion at 50 K. The observation of a tunnelling peak that is broad and contains possible structure, indicates a possible distribution of ammonia sites that experience different potential barriers. Assuming that the ammonia dynamics is governed by a one-dimensional three-fold torsional potential, we require a potential barrier, V_3 , of 7.4 meV to reproduce the position of the $270 \mu\text{eV}$ tunnelling peak. Neutron powder diffraction data of $(\text{ND}_3)\text{K}_3\text{C}_{60}$ at 150 K, are consistent with a doubling along the b and c axes of the high temperature orthorhombic unit cell, giving rise to additional Bragg reflections that disappear above 150 K. Previously, this structural transition has been associated with ordering of the orientations of interstitial $\text{K}^+\text{-NH}_3$ pairs. In addition, INS measurements of $(\text{NH}_3)\text{K}_3\text{C}_{60}$ and $(\text{ND}_3)\text{K}_3\text{C}_{60}$ show changes in their low-energy phonon density-of-states associated with the structural transition. Below 150 K, strong librational peaks are observed at 6.5 meV and 6.8 meV for $(\text{NH}_3)\text{K}_3\text{C}_{60}$ and $(\text{ND}_3)\text{K}_3\text{C}_{60}$, respectively. For $(\text{NH}_3)\text{K}_3\text{C}_{60}$, this librational peak is consistent with a $J=0 \rightarrow 3$ transition for a three-fold torsional potential with the same barrier as derived from the tunnelling spectrum. A somewhat smaller potential of 6.5 meV is needed to satisfactorily predict the observed changes in the $(\text{ND}_3)\text{K}_3\text{C}_{60}$ spectra.

Future work on these systems include the solving of the low temperature structure and the analysis of the neutron diffraction data as a function of temperature,

that we have shown briefly in this thesis. Armed with the knowledge of the correct structure, a more detailed interpretation of the INS data can be attempted with rationalisation of the contributions from individual ammonia sites to the broad tunnelling spectrum. Tunnelling data for $(\text{ND}_3)\text{K}_3\text{C}_{60}$ is highly desirable, as this will provide information on the admixture of further rotational terms to the symmetry of the torsional potential. The tunnelling spectrum of $(\text{NH}_3)\text{K}_3\text{C}_{60}$ can also be better defined by increasing the counting statistics and resolution: try to separate the contributions to the current spectrum. Additionally, it will be of interest to see if there exists a global relation between the potential at the ammonia site and the characteristics of the $(\text{NH}_3)_x\text{NaA}_2\text{C}_{60}$ ($0.5 < x < 1$, A= K and Rb) salts.

Alkali metal fullerides have been subjected to intense research efforts in efforts to understand their novel conducting and structural properties. For instance, the ternary sodium containing fullerides are cubic at high temperatures and under slow cooling conditions they undergo a phase transformation to a mono-dimensional polymeric system. Under normal cooling conditions, the cubic phase can be quenched and exhibits superconductivity. As part of this thesis, we followed the temperature dependence of the structure of the slowly cooled polymeric $\text{Na}_2\text{RbC}_{60}$ system using powder neutron diffraction. On cooling, slow polymer formation begins at 250 K, the phase transformation being essentially frozen below 180 K. On heating, a smooth development of the polymer monoclinic unit cell is seen. The thermal expansivity is extremely anisotropic, with practically no expansion along the direction of the fullerene closest contacts. Polymer destruction begins to occur by 230 K with the process being complete by 277 K. From this temperature to 299 K the powder pattern can be well described by just a primitive cubic component. Between 299 and 317

K there is a co-existence region between the pc and fcc structures. Numerous studies on the vibrational properties of both monomeric and polymeric alkali fullerides have been reported in the literature. However, the identification of the polymeric phase of $\text{Na}_2\text{RbC}_{60}$ from diffraction techniques, should be supported by direct observation of the vibrational modes of the interfullerene C-C bonds. Therefore, employing inelastic neutron scattering measurements, we have identified excess scattering 8- 25 meV region for the polymer phase that is absent for the high temperature, three-dimensional monomeric fcc phase. These modes are in good agreement with those observed for the polymeric AC_{60} fullerides. The scattering law below 200 K, shows the co-existence of polymer and librational cubic modes, while at 320 K quasielastic scattering for the fcc high temperature phase. Further INS work should be performed on this sample, with the aim to eliminate all the cubic contribution to the GDOS. The application of lattice dynamical calculations to the structure of polymeric $\text{Na}_2\text{RbC}_{60}$ can be used to fit a calculated GDOS to the observed spectrum. In such a case additional information such as bond strengths and dispersion relations of the contributing modes can be extracted.

Within the same sodium containing alkali fullerides, we also tested the observation that chemical and physical pressure have dissimilar effects on the superconducting properties of the primitive cubic systems. We followed the *ac* susceptibility of the superconducting $\text{Na}_2\text{Rb}_{0.5}\text{Cs}_{0.5}\text{C}_{60}$ salt as a function of hydrostatic pressure. A monotonic shift of T_c with pressure ($dT_c/dP = -1.22(2)$ K kbar⁻¹) is observed that is essentially identical to that observed for $\text{Na}_2\text{CsC}_{60}$. Thus under high pressure, each member of the $\text{Na}_2\text{Rb}_{1-x}\text{Cs}_x\text{C}_{60}$ family appears to have a T_c dependence on interfullerene separation that is similar to that obtained for the fcc fullerides. The

superconducting fraction is also reduced upon the application of pressure. We have interpreted these results in terms of formation of the non-superconducting polymer at the expense of the superconducting cubic phase.

The lack of superconductivity in $\text{Li}_2\text{AC}_{60}$ was postulated to be due to strong $\text{Li}^+\text{-C}$ interactions evident in the analysis of X-ray powder diffraction. We have searched for enhanced alkali-fulleride interactions and characteristic bonding features in these systems using the INS technique. The temperature development of the librational spectra are similar to those measured for the primitive cubic systems, indicating that an order-disorder transition may occur above 350 K. Additionally, we have observed scattered intensity in the gap region of the GDOS. Scattering in this region is usually associated with interfullerene C-C bonding, as for the polymeric fulleride systems. It is too early to associate this scattering to bonding, though the appearance of a quasielastic diffusion term in $S(Q, \omega)$ occurs with the reduction of this additional intensity. This is consistent with a $\text{Li}^+\text{-C}_{60}^{3-}$ bond being broken due to rotational diffusion of the fulleride units. Future powder diffraction studies on homogeneous samples should be performed to higher temperatures than at present. Further, neutron powder diffraction may give additional information about the fulleride structure and orientation.

We have already discussed the significant role of the cooling rate on the structural behaviour of the sodium intercalated ternary fullerides. This rate is also of similar importance in the case of the AC_{60} compounds. While, upon slow cooling the well studied polymeric phase is formed in the low temperature region, upon quenching a sequence of monomer and dimer phases has been reported. We have studied the INS of CsC_{60} fulleride under different cooling protocols. The scattering law for the

slowly cooled CsC_{60} sample shows the characteristic features of the polymer phase. A broad distribution of modes centred around 3.7 meV arises from the unresolved polymer twisting modes. In agreement with DTA and powder diffraction experiments, a phase transformation to the high temperature cubic phase occurs between 350 and 420 K. The observation of quasielastic scattering confirms the transition to the orientationally disordered fcc phase. In the case of quenching CsC_{60} to 77 K, after being heated to high temperature and then being immediately immersed in liquid N_2 , a large component of the sample was primitive cubic. This gave rise to a librational mode at energies similar to those obtained for the cubic $\text{Na}_2\text{RbC}_{60}$ and $\text{Li}_2\text{CsC}_{60}$. No phase transitions were apparent on heating the sample to 250 K, though a spectrum identifying the polymer phase was observed at 300 K. Following a re-heating of the sample to temperatures above 400 K, we quenched the CsC_{60} sample to 200 K. Again, we observed no characteristic dimer twisting modes. The sharp libration which identifies the primitive cubic structure was again present in the measured scattering law.

Bibliography

- [1] R.C. Haddon, L. E. Brus and K. Raghavachari *Chem. Phys. Lett.*, **125**, 459, (1986).
- [2] P. A. Heiney, G. B. M. Vaughan, J. E. Fischer, N. Coustel, D. E. Cox, J. R. D. Copley, D. A. Neumann, W. A. Kamitakahara, K. M. Creegan, D. M. Cox, J. P. Jr. McCauley and A. B. III. Smith *Phys. Rev. B*, **45**, 4544 (1992).
- [3] C. S Yannoni, R. D. Johnson, G. Meigjer, D. S. Bethune and J. R. Salem *J. Phys. Chem.*, **95**, 9, (1991).
- [4] R. Tycko, G. Dabbagh, R. M. Fleming, R. C. Haddon, A. V. Makhija and S. M. Zahurak *Phys. Rev. Lett.*, **67**, 1886, (1991).
- [5] R. D. Johnson, C. S. Yannoni, H. C. Dorn, J. R. Salem and D. S. Bethune *Science*, **255**, 1235, (1992).
- [6] R. F. Kiefl, J. W. Schneider, A. MacFarlane, K. Chow, T. L. Duty, T. L. Estle, B. Hitti, R. L. Hitti, R. L. Lichti, E. J. Ansaldo, C. Schwab, P. W. Percival, G. Wei, S. Wlodek, K. Kojima, W. J. Romanow J. P. McCauley Jr., N. Coustel, J. E. Fischer and A. B. Smith III *Phys. Rev. Lett.*, **68**, 2708, (1992).
- [7] D. A. Neumann, J. R. D. Copley, R. L. Cappelletti, W. A. Kamitakahara, R. M. Lindstrom, K. M Creegan, D. M. Cox, W. J. Romanow, N. Coustel, J. P.

- McCauley Jr., N. C. Maliszewskyj, J. E. Fischer and A.B. Smith III *Phys. Rev. Lett.*, **67**, 3808, (1991).
- [8] Y. M. Jin, J. L. Cheng, M. Varmanair, G. H. Liang, Y. G. Fu, B. Wunderlich, X. D. Xiang, R. Mostovoy and A. K. Zettl *J. Phys. Chem.*, **96**, 5151, (1992).
- [9] I. Hirosawa, K. Prassides, J. Mizuki, K. Tanigaki, M. Gavaert, A. Lappas and J. K. Cockcroft *Science* **264**, 1294 (1994).
- [10] K. H. Michel, J. R. D. Copley and D. A. Neumann *Phys. Rev. Lett.* **68**, 2929 (1992).
- [11] P. C. Chow, X. Jiang, G. Reiter, P. Wochner, S. C. Moss, J. D. Axe, J. C. Hanson, R. K. McMullan, R. L. Meng and C. W. Chu *Phys. Rev. Lett.*, **69**, 2943, (1992).
- [12] K. Prassides, H. W. Kroto, R. Taylor, R. M. Walton, W. I. F. David, J. Tomkinson, R. C. Haddon, M. J. Rosseinsky and D. W. Murphy *Carbon*, **30**, 1277, (1992).
- [13] P. A. Heiney, J. E. Fischer, A. R. McGhie, W. J. Romanov, A. M. Denenstein, J. P. McCauley Jr., A. B. Smith III and D. E. Cox *Phys. Rev. Lett.*, **66**, 2911, (1991).
- [14] W. I. F. David, R. M. Ibberson, J. C. Matthewman, K. Prassides, T. J. S. Dennis, J. P. Hare, H. W. Kroto, R. Taylor and D. R. M. Walton *Nature* **353**, 147 (1991).
- [15] R. Sachidanandam and A. B. Harris *Phys. Rev. Lett.*, **67**, 1467, (1991).
- [16] J. E. Fischer and P. A. Heiney *J. Phys. Chem. Solids*, **54**, 1725, (1993).

- [17] W. I. F. David, R. M. Ibberson, T. J. S. Dennis, J. P. Hare and K. Prassides *Europhys. Lett.*, **18**, 219, (1992): and ammendum appears in *Europhys. Lett.*, **18**, 735, (1992).
- [18] D. A. Neumann, J. R. D. Copley, D. Reznik, W. A. Kamitakahara, J. J. Rush, R. L. Paul and R.M. Lindstrom *J. Phys. Chem. Solids* **54**, 1699 (1993).
- [19] E. Roduner, K. Prassides, R. M. MacRae, I. M. Tomas, C. Neidermayer, U. Binninger, C. Bernhard, A. Hofer and I. D. Reid *J. Chem. Phys. Solids* **54**, 1699 (1993).
- [20] J. R. D. Copley, D. A. Neumann, R. L. Cappelletti and W. A. Kamitakahara *J. Chem. Phys. Solids* **53**, 1353 (1992).
- [21] T. Matsuo, H. Suga, W. I. F. David, R. M. Ibberson, P. Bernier, A. Zahab, C. Fabre, A. Rassat and A. Dworkin *Solid State Commun.* **83**, 711 (1992).
- [22] R. C. Haddon, A. F. Hebard, M. J. Rosseinsky, D. W. Murphy, S. J. Duclos, K. B. Lyons, B. Miller, J. M. Rosamilia, R. M. Fleming, A. R. Kortan, S. H. Glarum, A. V. Makhija, A. J. Muller, R. H. Eick, S. M. Zahurak, R. Tycko, G. Dabbagh and A. F. Thiel *Nature* **350**, 320 (1991).
- [23] A. F. Hebard, M. J. Rosseinsky, R. C. Haddon, D. W. Murphy, S. H. Glarum, T. T. M. Palastra, A. P. Ramirez and A. R. Kortan *Nature*, **350**, 600 (1991).
- [24] K. Tanigaki, T. W. Ebbesen, S. Saito, J.S. Tsai, Y. Kubo and S. Kuroshima *Nature* **352**, 222 (1991).
- [25] P. W. Stephens, L. Mihaly, P. L. Lee, R. L. Whetten, S.-M. Huang, R. Kaner, F. Deiderich and K. Holczer *Nature* **351**, 632 (1991).
- [26] C. Christides, D. A. Neumann, K. Prassides, J. R. D. Copley, J. J. Rush, M. J. Rosseinsky, D. W. Murphy and R. C. Haddon *Phys. Rev. B* **46**, 12088 (1992).

- [27] C. Christides, K. Prassides, D. A. Neumann, J. R. D. Copley, J. Mizuki, K. Tanigaki, I. Hirose and T. W. Ebbesen *Europhys. Lett.* **24**, 755 (1993).
- [28] R. M. Fleming, A. P. Ramirez, M. J. Rosseinsky, D. W. Murphy, R. C. Haddon, S. M. Zuhurak and A. V. Makhija *Nature* **352**, 787 (1991).
- [29] G. Sparn, J. D. Thompson, S. -M. Huang, R. B. Kaner, F. Diederich, R. L. Whetten, G. Gruner and K. Holczer *Science* **252**, 1829 (1991).
- [30] O. Zhou, G. B. M. Vaughan, Q. Zhu, J. E. Fischer, P. A. Heiney, N. Coustel, J. P. McCauley and A. B. Smith, *Science* **255**, 833 (1992).
- [31] A. P. Ramirez, M. J. Rosseinsky, D. W. Murphy and R. C. Haddon *Phys. Rev. Letts.* **69**, 1687 (1992).
- [32] J. Diederichs, J. S. Schilling, K. W. Herwig and W. B. Yelon *J. Phys. Chem. Solids* **58**, 123 (1997).
- [33] O. Gunnarsson *Reviews of Modern Physics* **69**, 575 (1997).
- [34] W.L. McMillan *Phys. Rev.* **167**, 331 (1968).
- [35] K. Prassides, J. Tomkinson, C. Christides, M. J. Rosseinsky, D. W. Murphy and R. C. Haddon *Nature* **354**, 462 (1991).
- [36] S. J. Duclos, R. C. Haddon, S. H. Glarum, A. F. Hebard and K. B. Lyons *Science* **245**, 1625 (1991).
- [37] M. G. Mitch, S. J. Chase and J. S. Lannin *Phys. Rev. Letts.* **68**, 683 (1992).
- [38] A. P. Ramirez, A. R. Kortan, M. J. Rosseinsky, S. J. Duclos, A. M. Musjce, R. C. Haddon, D. W. Murphy, A. V. Makhija, S. M. Zahurak and K. B. Lyons *Phys. Rev. Letts.* **68**, 1058 (1992).

- [39] T. Yildirim, T. Barbedette, J. E. Fischer, C. L. Lins, J. Robert, P. Petit and T. T. M. Palsra *Phys. Rev. Letts.* **77**, 167 (1996).
- [40] T. Yildirim, J. E. Fischer, R. Dinnebier, P. W. Stephens and C. L. Lins *Solid State Commun.* **93**, 269 (1995).
- [41] L. Cristofolini, K. Vavekis, K. Prassides, A. J. Dianoux, M. Kosaka and K. Tanigaki *Physica B* **226**, 41 (1996).
- [42] K. Kniaz, J. E. Fischer, Q. Zhu, M. J. Rosseinsky, D. W. Murphy and O. Zhou *Solid State Commun.* **88**, 47 (1993).
- [43] K. Prassides, C. Christides, I. M. Thomas, J. Mizuki, K. Tanigaki, I. Hirosawa and T. W. Ebbesen *Science* **263**, 950 (1994).
- [44] K. Tanigaki, M. Kosaka, T. Manako, Y. Kubo, I. Hirosawa, K. Uchida and K. Prassides *Chem. Phys. Lett.* **240**, 627 (1995).
- [45] K. Tanigaki and K. Prassides *J. Mater. Chem.* **5**, 1515 (1995).
- [46] J. Robert, P. Petit, T. Yildirim and J. E. Fischer *Phys. Rev. B* **57**, 1226 (1998).
- [47] Y. Maniwa, D. Sugiura, K. Kume, K. Kikuchi, S. Susuki, Y. Achiba, I. Hirosawa, K. Tanigaki, and H. Shimoda *Phys. Rev. B* **54**, R6861 (1996).
- [48] Y. Maniwa, T. Saito, K. Kume, K. Kikuchi, I. Ikemoto, S. Susuki, Y. Achiba, I. Hirosawa, M. Kosaka and K. Tanigaki *Phys. Rev. B* **52**, R7054 (1995).
- [49] J. Mizuki, M. Takai, H. Takahashi, N. Mori, K. Tanigaki, I. Hirosawa and K. Prassides *Phys. Rev. B* **50**, 3466 (1994).
- [50] Q. Zhu *Phys. Rev. B* **52**, 723 (1995).

- [51] L. Cristofolini, K. Kordatos, G. A. Lawless, K. Prassides, K. Tanigaki and M. P. Waugh *Chem. Commun.* 375 (1997).
- [52] K. Prassides, K. Vavekis, K. Kordatos, K. Tanigaki, G. M. Bendele and P. W. Stephens *J. Am. Chem. Soc.* **119**, 834 (1997).
- [53] G. M. Bendele, P. W. Stephens, K. Prassides, K. Vavekis, K. Kordatos and K. Tanigaki *Phys. Rev. Lett.* **80**, 736 (1998).
- [54] S. Margadonna, C. M. Brown, K. Kordatos, A. Lappas, K. Prassides, M. Kosaka and K. Tanigaki *Recent Advances in the Physics and Chemistry of Fullerene and Related Material*, Eds., K. M. Kadish et al., Electrochemical Society, Pennington, NJ, **vol. 6**, 1998.
- [55] K. Prassides, K. Tanigaki and Y. Iwasa *Physica C* **282**, 307 (1997).
- [56] M. Kosaka, K. Tanigaki and K. Prassides *submitted* (1998).
- [57] T. T. M. Palstra, O. Zhou, Y. Iwasa, P. E. Sulewski, R. M. Fleming and B. R. Zegarski *Solid State Commun.* **93**, 327 (1995).
- [58] O. Zhou, R. M. Fleming, D. W. Murphy, M. J. Rosseinsky, A. P. Ramirez, R. B. van Dover and R. C. Haddon *Nature*, **362**, 433 (1993).
- [59] H. Shimoda, Y. Iwasa, Y. Miyamoto, Y. Maniwa and T. Mitani *Phys. Rev. B*, **54**, 653 (1996).
- [60] M. J. Rosseinsky, D. W. Murphy, R. M. Fleming and O. Zhou *Nature*, **364**, 425 (1993).
- [61] Y. Iwasa H. Shimoda, T. T. M. Palstra, Y. Maniwa, O. Zhou and T. Mitani *Phys. Rev. B*, **53**, 836 (1996).
- [62] K. M. Allen, S. J. Heyes and M. J. Rosseinsky *J. Mater. Chem.*, **6**, 1445 (1996).

- [63] O. Zhou, T. T. M. Palastra, Y. Iwasa, R. M. Fleming , A. F. Hebard, P. E. Sulewski, D. W. Murphy and B. R. Zegarski *Phys. Rev. B*, **52**, 483 (1995).
- [64] P. W. Stephens, G. Bortel, G. Faigel,, M. tegze, A. Janossy, A. Pekker, G. Oszlanyi and L. Forro *Nature* **370**, 636 (1994).
- [65] F. Bommeli, L. Degiorgi, P. Wachter, O. Legeza, A. Janossy, G. Oszlanyi, O. Chauvet and L. Forro *Phys. Rev. B* **51**, 14794, (1995).
- [66] M. Kosaka, K. Tanigaki, T. Tanaka, T. Atake, A. Lappas and K. Prassides *Phys. Rev. B* **51**, 12018, (1995).
- [67] A. Lappas, M. Kosaka, K. Tanigaki and K. Prassides *J. Am. Chem. Soc.* **117**, 7560, (1995).
- [68] Q. Zhu, D. E. Cox and J. E. Fischer *Phys. Rev. B* **51**, 3966 (1995).
- [69] G. Oszlanyi, G. Bortel, G. Faigel, M. Tegze, L. Granasy, S. Pekker, P. W. Stephens, G. Bendele, R. Dinnebier, G. Mihaly, A. Janossy, O. Chauvet and L. Forro *Phys. Rev. B* **51**, 12228 (1995).
- [70] G. Oszlanyi, G. Bortel, G. Faigel, L. Granasy, G. Bendele, P. W. Stephens and L. Forro *Phys. Rev. B* **54**, 11849 (1996)
- [71] M. J. Rosseinsky, D. W. Murphy, R. M. Fleming, R. Tycko, A. P. Ramirez, T. Siegrist, G. Dabbagh and S. E. Barrett *Nature* **356**, 419 (1992).
- [72] Q. Zhu, O. Zhou, N. Coustel, G. B. M. Vaughan, J. P. McCauley Jr., W. J. Romanov, J. E. Fischer and A. B. Smith III *Science* **254**, 545 (1991).
- [73] P. W. Stephens, L. Mihaly, J. B. Wiley, S. M. Huang, R. B. Kaner, F. Diederich, R. L. Whetten and K Holczer *Phys. Rev. B* **45**, 543 (1992).

- [74] G. Oszlanyi, G. Baumgartner, G. Faigel and L. Forro *Phys. Rev. Lett.* **78**, 4438 (1997).
- [75] R. M. Fleming, M. J. Rosseinsky, A. P. Ramirez, D. W. Murphy, J. C. Tully, R. C. Haddon, T. Siegrist, R. Tycko, S. H. Glarum, P. Marsh, G. Dabbagh, S. M. Zahurak, A. V. Makhija and C. Hampton *Nature*, **352**, 701 (1991).
- [76] C. A. Kuntscher, G. M. Bendele and P. W. Stephens *Phys. Rev. B*, **55**, R3366 (1997).
- [77] P. Dahlke, P. F. Henry and M. J. Rosseinsky *J. Mater. Chem*, **8**, 1571 (1998).
- [78] B. Renker, H. Schober and R. Heid *Appl. Phys. A*, **64**, 271, (1997).
- [79] D. W. Murphy, M. J. Rosseinsky, R. M. Fleming, R. Tycko, A. P. Ramirez, R. C. Haddon, T. Siegrist, G. Dabbagh, J. C. Tully and R. E. Walstedt *J. Phys. Chem. Solids*, **53**, 1321 (1992).
- [80] A. N. Kortan, N. Kopylov, R. M. Fleming, O. Zhou, F. A. Thiel, R. C. Haddon and K. M. Rabe *Phys. Rev. B*, **47**, 13070 (1993).
- [81] A. M. A. Bravais *Journal de l'Ecole polytechnique*, Paris, (1850).
- [82] D. Reidel *International tables for crystallography*, Vol. A, Space group symmetry, (1983).
- [83] C. Giacovazzo *Fundamentals of Crystallography*, Oxford Univ. Press, 1992.
- [84] S. W. Lovesey *Theory of Neutron Scattering from Condensed Matter*, Oxford Univ. Press, 1984.
- [85] I.L.L. web page <http://www.ill.fr>

- [86] D. Raoux *Neutron and Synchrotron Radiation for Condensed Matter Studies* ,
Vol.1, p.42, Eds., J. Baruchel, J. L. Hodeau, M. S. Lehmann, J. R. Regnard,
C. Schlenker, Springer-Verlag (1993).
- [87] C. S. Barrett, M. H. Mueller and L. Heaton *Rev. Sci. Instrum.*, **34**, 8, 121-124
(1963).
- [88] V. L. Sailor, H. L. Foote Jr., H. H Landon and R. E. Wood *Rev. Sci. Instrum.*,
27, 11, 26-34 (1956).
- [89] G. Caglioti and F. P. Ricci *Nucl. Instrum. Methods.*, **15**, 2, 155-163 (1962).
- [90] A. W. Hewat *Nucl. Instrum. Methods.*, **127**, 361-370 (1975).
- [91] G. Platbrood *J. Appl. Cryst.*, **16**, 24-7 (1983).
- [92] W. Soller *Phys. Rev.*, **24**, 158-167 (1924).
- [93] A. Freund *Neutron and Synchrotron Radiation for Condensed Matter Studies*,
Vol.1, p.79, Eds., J. Baruchel, J. L. Hodeau, M. S. Lehmann, J. R. Regnard,
C. Schlenker, Springer-Verlag (1993).
- [94] C. Niedermayer *Hyperfine Inter.*, **97/98**, 287-304 (1996).
- [95] L. Merrill and W. A. Basset *Rev. Sci. Instr.*, **45**, 290 (1974).
- [96] D. Schiferl, D. T. Cromer, R. R. Ryan, A. C. Larson, R. LeSar and R. L. Mills
Acta. Cryst., **C39**, 1151 (1983).
- [97] H. K. Mao, J. Xu and P. M. Bell *J. Geophys. Res.*, **91**, 4673 (1986).
- [98] A. Hammersley Program: *FIT2D*, E.S.R.F., Grenoble, France.
- [99] A. W. Hewat *High Resolution Powder Diffraction*, **Material Science Forum**,
(1986) **Vol. 9, p. 69**, Ed., C. R. A. Catlow, Trans Tech Publications Ltd.,
Switzerland.

- [100] P.S.I. web page <http://www.psi.ch>
- [101] P. Debye and P. Scherrer *Physik. Z.*, **17**, 277 (1916).
- [102] P. Thompson, D. E. Cox and J. B. Hastings *J. Appl. Cryst.*, **20**, 79 (1987).
- [103] A. C. Larson and R. B. Von Dreele Program: *GSAS*, LANSCE, Los Alamos national Laboratory, Los Alamos, U.S.A.
- [104] J. Rodriguez-Carvajal Program: *FULLPROF*, Laboratoire Leon Brillouin, Saclay, France.
- [105] T. M. Sabine *Austr. J. Phys.*, **38**, 507 (1985).
- [106] T. M. Sabine, R. B Von Dreele and J. E. Jorgensen *Acta. Cryst.*, **A44**, 374 (1988).
- [107] B. D. Cullity *Fundamentals of X-ray Diffraction*, **Vol.1**, p.209, Addison-Wesley (1978).
- [108] A. W. Hewat *Acta. Cryst.*, **A35**, 248, (1979).
- [109] K. D. Rouse, M. J. Cooper and A. Chakera *Acta. Cryst.*, **A26**, 682, (1970).
- [110] H. M. Rietveld *J. Appl. Cryst.*, **2**, 65 (1969)
- [111] W. A. Dollase *J. Appl. Cryst.*, **19**, 267, (1986).
- [112] A. March *Z. Kristallogr.*, **81**, 285, (1932).
- [113] G. K. Wertheim, M. A. Butler, K. W. West and D. N. E. Buchanan *J. Appl. Cryst.*, **12**, 107 (1974).
- [114] R. B. Von Dreele, J. D. Jorgensen and C. G. Windsor *J. Appl. Cryst.*, **15**, 581, (1982).

- [115] L. W. Finger, D. E. Cox and A. P. Jephcoat *J. Appl. Cryst.*, **27**, 892 (1994).
- [116] C. J. Howard *J. Appl. Cryst.*, **15**, 615 (1982).
- [117] J. K. Cockcroft Program: *DRAGON*, Birkbeck College, London, U.K.
- [118] J. K. Cockcroft Program: *PROFIL*, Birkbeck College, London, U.K.
- [119] G. S. Pawley *J. Appl. Cryst.*, **14**, 357, (1981).
- [120] A. Le Bail, H. Duroy and J. L. Fourquet *Mater. Res.*, **23**, 447, (1988).
- [121] G. L. Squires *Introduction to the theory of thermal neutron scattering*, Cambridge University Press (1978).
- [122] P. A. Egelstaff and P. Shofield *Nucl. Sci. Eng.*, **12**, 60, (1962).
- [123] M. Dobson *Multiphonon Corrections for Down Scattering Experiments*, ILL report 91DO17G, Grenoble, France.
- [124] F. Rieutord *Program: INX*, ILL report 90RI17T, Grenoble, France.
- [125] D. Richard, G. J. Kearley and M. Ferrand *Program: PROFIT*, ILL, Grenoble, France.
- [126] A. J. Dianoux and R. Currat *Program: FITDEN5*, unpublished.
- [127] C. M. Brown and S. Rols *Update of Program: FITDEN5*, unpublished.
- [128] A. Schenck *Muon Spin Rotation Spectroscopy*, Adam Hilger Ltd., U.K., 1985.
- [129] J. Brewer *Encyclopedia of Applied Physics, Vol 11, pp. 23-53*, VCH Publishers, Inc., 1994.
- [130] A. Hillier and R. Cywinski, *Applied Magnetic Resonance* **13**, 95 (1996).
- [131] A. Lappas, *D. Phil. Thesis* University of Sussex (1993).

- [132] R. Kubo and T. Toyabe *Magnetic Resonance and Relaxation*, ed. R. Blink, (Amsterdam: Holland).
- [133] J. C. Hummelen, B. Knight, J. Pavlovich, R. Gonzalez and F. Wudl *Science* **269**, 1554 (1995).
- [134] W. Andreoni, A. Curioni, K. Holczer, K. Prassides, M. Keshavarz-K, J. C. Hummelen and F. Wudl *J. Am. Chem. Soc.* **118**, 11335 (1996).
- [135] M. Keshavarz-K, R. Gonzalez, R. G. Hicks, G. Srdanov, V. I. Srdanov, T. G. Collins J. C. Hummelen, C. Bellavia-Lund, J. Pavlovich, F. Wudl and K. Holczer *Nature* **383**, 147 (1996).
- [136] K. Prassides, M. Keshavarz-K, E. Beer, C. Bellavia, R. Gonzalez, Y. Murata, F. Wudl, A. K. Cheetham and J. P. Zhang *Chem. Mater.* **8**, 2405 (1996).
- [137] W. Andreoni, C. Bellavia, C. M. Brown, L. Cristofolini, R. Gonzalez, M. Keshavarz-K, K. Kordatos, K. Prassides and F. Wudl *Recent Advances in the Physics and Chemistry of Fullerene and Related Material*, Eds., K. M. Kadish et al., Electrochemical Society, Pennington, NJ, 1996.
- [138] K. Prassides, M. Keshavarz-K, J. C. Hummelen, W. Andreoni, P. Giannozzi E. Beer, C. Bellavia, L. Cristofolini, A. Lappas, Y. Murata, M. Malecki, V. I. Srdanov, and F. Wudl *Science* **271**, 1833 (1996).
- [139] K. Kordatos, C. M. Brown, K. Prassides, C. Bellavia-Lund, P. de la Cruz, F. Wudl, J. D. Thompson and A. N. Fitch *Electronic Properties of Novel Materials*, Eds., H. Kuzmany et al., World Scientific Publ., Singapore, 1997.
- [140] J. C. Hummelen, M. Prato and F. Wudl *J. Am. Chem. Soc.* **117**, 7003 (1995).
- [141] C. M. Brown, E. Beer, C. Bellavia, L. Cristofolini, R. Gonzalez, M. Hanfland, D. Hausermann, M. Keshavarz-K, K. Kordatos, K. Prassides and F. Wudl *J. Am. Chem. Soc.* **118**, 8715 (1996).

- [142] S. J. Duclos, K. Brister, R. C. Haddon, A. R. Kortan, and F. A. Thiel *Nature*, **351**, 380 (1991).
- [143] C. M. Brown, L. Cristofolini, K. Kordatos, K. Prassides, C. Bellavia, R. Gonzalez, M. Keshavarz-K, F. Wudl, A. K. Cheetham, J. P. Zhang, W. Andreoni, A. Curioni, A. N. Fitch and P. Pattison *Chem. Mater.* **8**, 11335 (1996).
- [144] J. Arvanitidis, K. Papagelis, K. P. Meletov, G. A. Kourouklis, S. Ves, K. Kordatos, F. Wudl and K. Prassides *in press* (1998).
- [145] F. D. Murnaghan *Proc. Natl. Acad. Sci. U.S.A.*, **30**, 244 (1947).
- [146] J. R. Macdonald and D. R. Powell *J. Res. Natl. Bur. Stand. A*, **75**, 441 (1971).
- [147] C. Christides, I. M. thomas, T. J. S. Dennis and K. Prassides *Europhys. Letts.* **22**, 611 (1993).
- [148] S. Margadonna, C. M. Brown, T. J. S. Dennis, A. Lappas, P. Pattison, K. Prassides and H. Shinohara *Chem. Commun.* **10**, 1742 (1998).
- [149] Molecular Simulations Program: *CERIUS²*, Molecular Simulations Inc.
- [150] T. Pichler, M. Knupfer, M. S. Golden, S. Haffner, R. Friedlein, J. Fink M. Keshavarz-K, C. Bellavia-Lund, A. Sastre, J. C. Hummelen and F. Wudl *Phys. Rev. Letts.* **78**, 4249 (1997).
- [151] S. Haffner, T. Pichler, M. Knupfer, B. Umlauf, R. Friedlein, M. S. Golden, J. Fink, M. Keshavarz-K, C. Bellavia-Lund, A. Sastre, J. C. Hummelen and F. Wudl *Eur. Phys. J. B* **1**, 11 (1997).
- [152] W. Kratschmer, L. D. Lamb, K. Fstropoulos and D. R. Huffman *Nature*, **347**, 318 (1990).

- [153] A. R. Kortan, N. Kopylov, S. Glarum, E. M. Gyorgy, A. P. Ramirez, R. M. Fleming, F. A. Thiel and R. C. Haddon *Nature*, **355**, 529 (1992).
- [154] Y. Chen, F. Stepniak, J. H. Weaver, L. P. F. chibante and R. E. Smalley *Phys. Rev. B*, **45**, 8845 (1992).
- [155] A. R. Kortan, N. Kopylov, S. Glarum, E. M. Gyorgy, A. P. Ramirez, R. M. Fleming, O. Zhou, F. A. Thiel, P. L. Trevor and R. C. Haddon *Nature*, **360**, 566 (1992).
- [156] A. R. Kortan, N. kopylov, E. Ozdas, A. P. Ramirez, R. M. Fleming and R. C. Haddon *Chem. Phys. Lett.*, **233**, 501 (1994).
- [157] S. Saito and A. Oshiyama *Phys. Rev. Letts.*, **71**, 121 (1993).
- [158] S. Erwin and M. R. Pederson *Phys. Rev. B*, **47**, 14657 (1993).
- [159] B. Gogia, K. Kordatos, H. Suematsu, K. Tanigaki and K. Prassides *Phys. Rev. B*, **58**, 1077 (1998).
- [160] M. Baenitz, M. Heinze, K. Luders, H. Werner, R. Schlogl, M. Weiden, G. Sparn and F. Steglich *Solid State Comm.*, **96**, 539 (1995).
- [161] M. Kraus, M. Kanowski, M. Baenitz, H. Werner, R. Schlogl, E.-W. Scheidt, H.-M. Vieth and K. Luders. *Fullerene Sci. Technol.*, **3**, 115 (1995).
- [162] Th. Schedel-Niedrig, M. C. Bohm, H. Werner, J. Schulte and R. Schlogl *Phys. Rev. B*, **55**, 13542 (1997).
- [163] G. Sparn, F. Laube, A. Link, F. Steglich, M. Baenitz, K. Luders, H. Werner and R. Schlogl *J. Low Temp. Phys.*, **105**, 1703 (1996).
- [164] G. Sparn, J. D. Thomson, R. L. Whetten, S.-M. Huang, R. B. Kaner, F. Diederich, G. Gruner and K. Holczer *Phys. Rev. Lett.*, **68**, 1228 (1992).

- [165] J. E. Schirber W. R. Bayless, A. R. Kortan and N. Kopylov *Physica C*, **213**, 190 (1993).
- [166] O. Zhou and D. E. Cox *J. Phys. Chem. Solids*, **53**, 1373 (1992).
- [167] K. M. Allen, W. I. F. David, J. M. Fox, R. M. Ibberson and M. J. Rosseinsky *Chem. Mater.*, **7**, 764 (1995).
- [168] C. M. Brown, K. Kordatos, S. Margadonna, K. Prassides, K. Tanigaki, E. Suard, A. J. Dianoux, A. N. Fitch and K. D. Knudsen, in preparation.
- [169] S. Margadonna, C. M. Brown, A. Lappas, K. Kordatos, K. Tanigaki and K. Prassides *Electronic Properties of Novel Materials*, Eds., H. Kuzmany et al., World Scientific Publ., Singapore, 1998.
- [170] F. Gugenberger, R. Heid, C. Meingast, P. Adelman, M. Braun, H. Wuhl, M. Haluska and H. Kuzmany *Phys. Rev. Lett.*, **69**, 3774 (1992).
- [171] G. J. Burkhardt and C. Meingast *Phys. Rev. B*, **54**, R6865 (1996).
- [172] R. S. Ruoff and A. L. Ruoff *Appl. Phys. Lett.*, **59**, 1553 (1991).
- [173] S. Margadonna, C. M. Brown, A. Lappas, K. Prassides, K. Tanigaki, K. D. Knudsen, T. Le Bihan and M. Mezouar *Submitted J. Solid State Chem.* (1998).
- [174] J. E. Schirber et al., *Recent Advances in the Physics and Chemistry of Fullerene and Related Material*, eds., K. M. Kadish and R. S. Ruoff, Electrochemical Society, Pennington, NJ, **Vol. 94-24**, p.556, 1994.
- [175] *The Fullerenes*, Eds., H. Kroto, D. E. Cox and J. E. Fischer., Pergamon Press, Oxford, 1993.
- [176] K. Ishii, T. Watanuki, A. Fujiwara, H. Suematsu, H. Nakao, Y. Fujii, Y. Murakami, H. Kawada, Y. Iwasa, H. Shimoda and H. Mitani *unpublished*.

- [177] L. Cristofolini, A. Lappas, K. Vavekis, K. Prassides, R. DeRenzi, M. Ricco, A. Schenck, A. Amato, F. N. Gygax, M. Kosaka and K. Tanigaki *J. Phys. Condens. Matter* **7**, L567 (1995).
- [178] A. Janossy, N. Nemes, T. Feher, G. Oszlanyi, G. Baumgartner and L. Forro *Phys. Rev. Letts.* **79**, 2718 (1997).
- [179] A. Lappas, K. Prassides, K. Vavekis, D. Arcon, R. Blinc, P. Cevc, A. Amato, R. Feyerherm, F. N. Gygax and A. Schenck *Science* **267**, 1799 (1995).
- [180] F. Wudl and J. D. Thompson *J. Phys. Chem. Solids* **53**, 1449 (1992).
- [181] C. J. Carlile, I. M. Jamie, G. Lockhart and J. W. White *Molec. Phys.* **76**, 173 (1992).
- [182] W. Press *Single-Particle Rotations in Molecular Crystals* **p. 47**, Springer-Verlag, New York (1981)
- [183] G. J. Kearley, H. Blank and J. K. Cockroft *J. Chem Phys.* **86**, 5989 (1986).
- [184] C. J. Carlile, I. M. Jamie, M. Prager and W. Stead and J. W. White *Molec. Phys.* **87**, 73 (1991).
- [185] G. J. Kearley and H. Blank *J. Chem Phys.* **87**, 6809 (1987).
- [186] G. J. Kearley *Program: LAMP, ILL, Grenoble, France.*
- [187] C. J. Carlile, R. Durand, W. K. Fullagar, P. A. Reynolds, F. Trouw and J. W. White *Molec. Phys.* **86**, 19 (1995).
- [188] M. Neumann and G. J. Kearley *Chem. Phys.* **215**, 253 (1997).
- [189] P. Schiebel, G. J. Kearley and M. R. Johnson *J. Phys. Chem.* **108**, 2375 (1998).

- [190] K. L. Schmidt and A. Muller *J. Mol. Struct.* **22**, 343 (1974).
- [191] W. P. Griffith *J. Chem. Soc. A*, 899 (1966).
- [192] B. Renker, F. Gompf, H. Schober, P. Adelmann, H. J. Bornemann and R. Heid *Z. Phys. B* **92**, 451 (1993).
- [193] L. Cristofolini, C. M. Brown, A. J. Dianoux, M. Kosaka, K. Prassides, K. Tanigaki and K. Vavakis *Chem. Commun.* 2465, (1996).
- [194] H. Schober, A. Tolle, B. Renker, R. Heid and F. Gompf *Phys. Rev. B*, **56**, 5937, (1997).
- [195] G. B. Adams and J. B. Page, O. F. Sankey and M. O'Keeffe *Phys. Rev. B* **50**, 17471, (1994).
- [196] S. Margadonna, K. Prassides, D. A. Neumann, H. Shimoda and Y. Iwasa *Phys. Rev. B* in press (1998).
- [197] M. J. Rosseinsky, A. P. Ramirez, S. H. Glarum, D. W. Murphy, R. C. Haddon, A. F. Hebard, T. T. M. Palstra, A. R. Kortan, S. M. Zahurak and A. V. Makhija *Phys. Rev. Lett.* **66**, 2830 (1991).
- [198] K. Holczer, O. Klein, S. M. Huang, R. B. Kaner, K. J. Fu, R. L. Whetten and F. Deiderich *Science* **252**, 1154 (1991).
- [199] K. Tanigaki, I. Hirosawa, T. Manako, J. S. Tsai, J. Mizuki and T. W. Ebbesen *Phys. Rev. B* **49**, 12307 (1994).
- [200] K. Prassides, A. Lappas, W. Maser, I. Hirosawa, K. Tanigaki and J. Mizuki *Recent Advances in the Physics and Chemistry of Fullerene and Related Material*, Eds., K. M. Kadish and R. S. Ruoff, Electrochemical Society, Pennington, NJ, **p.530**, 1994.

- [201] K. Prassides, *Current Opinion Solid State Materials Science*, **2**, 433 (1997).
- [202] K. Vavekis, *D. Phil. Thesis* University of Sussex (1998).
- [203] A. Lappas, C. M. Brown, K. Kordatos, E. Suard, K. Tanigaki and K. Prassides
J. Phys. Cond. Matter in press (1998).
- [204] O. Chauvet, G. Oszlanyi, L. Forro, P. W. Stephens, M. Tegze, G. Faigel and A.
Jannosy *Phys. Rev. Lett.* **72**, 2721 (1994).
- [205] J-L, Sauvajol, E. Anglaret, R. Aznar, D. Bormann and B. Hennion *Solid State
Commun.* **104**, 387 (1997).
- [206] K. Kordatos, *D. Phil. Thesis* University of Sussex (in preparation).
- [207] J. D. Thompson *Rev. Sci. Instrum.* **55**, 231 (1984).
- [208] C. M. Brown, T. Takenobu, K. Kordatos, K. Prassides, Y. Iwasa and K. Tani-
gaki submitted enphPhysica B, (1998).
- [209] D. A. Neumann, J. R. D. Copley, W. A. Kamitakahara, J. J. Rush, R. L.
Cappelletti, N. Coustel, J. E. Fischer, J. P. McCauley Jr., A. B. Smith III, K. M.
Kreegan and D. M. Cox *J. Chem. Phys.* **96**, 8631 (1992).
- [210] J. R. D. Copley, D. A. Neumann, R. L. Cappelletti, W. A. Kamitakahara, E.
Prince, N. Coustel, J. P. McCauley, N. C. maliszewskyj, J. E. Fischer, A. B.
Smith III, K. M. Creegan and D. M. Cox *Physica B* **180**, 706 (1992).
- [211] J. Winter and H. Kuzmany *Solid State Commun.* **84**, 935 (1992).
- [212] Q. Zhu, O. Zhou, J. E. Fischer, A. R. McGhie, W. J. Romanow, R. Strongin,
M. A. Cichy and A. B. Smith III *Phys. Rev. B* **47**, 13948 (1993).
- [213] S. Pekker, L. Forro, L. Mihaly and A. Janossy *Solid State Comm.* **90**, 349
(1994).

- [214] A. M. Rao, Z. Ping, W. Kai-An, G. T. Hager, J. M. Holden, Y. Wang, W. -T. Lee, B. Xiang-Xin, P. C. Eklund, D. S. Cornett, M. A. Duncan and I. J. Amster *Science* **259**, 955 (1993).
- [215] R. Tycko, G. Dabbagh, D. W. Murphy, Q. Zhu and J. E. Fischer *Phys. Rev. B* **48**, 9097 (1993).
- [216] Y. J. Uemura, K. Kojima, G. M. Luke, W. D. Wu, G. Oszlanyi, O. Chauvet and L. Forro *Phys. Rev. B* **52**, 6991, (1995).
- [217] W. A. MacFarlane, R. F. Kiefl, S. Dunsiger, J. E. Sonier and J. E. Fischer *Phys. Rev. B* **52**, 6995, (1995).
- [218] K. Prassides, T. J. S. Dennis, J. P. Hare, J. Tomkinson, H. W. Kroto, R. Taylor and D. R. M. Walton *Chem. Phys. Lett.* **187**, 455, (1991).
- [219] L. Pintschovius, B. Renker, F. Gompf, R. Heid, S. L. Chaplot, M. Haluska and H. Kuzmany *Phys. Rev. Lett.* **69**, 2662, (1992).
- [220] F. Negri, G. Orlandi and F. Zerbetto *Chem. Phys. Lett.* **144**, 31, (1988).
- [221] J. Winter and H. Kuzmany *Phys. Rev. B* **52**, 7113, (1995).
- [222] M. C. Martin, D. Koller, A. Rosenberg, C. Kendziora and L. Mihaly *Phys. Rev. B* **51**, 7115, (1985).